Determining the Influence of Surface Preparation on Transient Liquid Phase Bonding of Inconel 718/BNi-2

by

Joel Mark Chapman

Submitted in partial fulfilment of the requirements

for the degree of Master of Applied Science

at

Dalhousie University

Halifax, Nova Scotia

October 2019

Dedications

This thesis is dedicated to my parents Mark and Virginia Chapman, as well as my grandparents James and Rita McLean. I simply could not have completed this journey without them. I can not thank them enough for everything they have done for me. I would also like to thank my brothers and friends for providing a support network for me over the course of my graduate studies. They certainly helped me believe in myself and showed me I could do anything I put my mind to.

I also need to give great thanks to my supervisor Dr. Stephen Corbin. He was a great mentor to me along this journey and has taught me a great deal about research and experimentation. I have been given so many opportunities as a result of being a part of his team and I am thankful for that. His guidance along this process has been so helpful and I am forever grateful to have been a student of his.

Table of Contents

List of Tables

List of Figures

Abstract

Transient liquid phase bonding is a high-performance brazing process used to join superalloys. Alloys that contain stable oxide layers present on the faying surface require surface preparation in order to be successfully brazed.

This work examined the effects of different Ni based superalloy surface treatments on TLPB. Differential scanning calorimetry was used in combination with other materials characterization techniques to determine how surface preparation influences the kinetics of the isothermal solidification process, as well as the wetting and spreading of a molten filler metal on a superalloy surface.

Surface pre-treatments that included a Ni plating exhibited superior wetting and spreading behaviour. DSC coupled with optical metallography was successful in quantifying the wetting process. The presence of a Ni plating step resulted in an increased rate of isothermal solidification and reduced isothermal solidification due to initial boron uptake.

List of Abbreviations and Symbols Used

***NOTE:** Chemical symbols, as well as symbols used in equations presented in Chapter 1 are omitted from the list below.

FM	Filler metal
TLPB	Transient liquid phase bonding
BM	Base metal
IS	Isothermal solidification
IN718	Inconel 718
γ	Austenitic matrix phase in nickel superalloys
γ'	Secondary precipitate phase in nickel superalloys
γ"	Secondary precipitate phase in nickel superalloys
AWS	American Welding Society
T_B	The brazing temperature
wt.%	Weight percent
MPD	Melting point depressant
S/L	Solid/liquid
IBU	Initial boron uptake
C_L	Solute composition of liquidus
C_S	Solute composition of the solidus
t_{IS}	Time required for completion of isothermal solidification

ISZ	Isothermally solidified zone
DAZ	Diffusionally affected zone
ASZ	Athermally solidified zone
FE-SEM	Field emission scanning electron microscope
DSC	Differential scanning calorimetry
TA	Thermal analysis
ISP	In-house surface prepared
P&WC	Pratt & Whitney Canada
AC	Acid cleaned
NiCr	Nicroblast ™
Ni(F)	Nickel flash plating
Ni(B)	Nickel brush plating
ICP-OES	Inductively coupled plasma-optical emission spectrometry
MBC or $2w_{ISZ}$	Maximum brazing clearance or width of isothermally solidified zone
OM	Optical microscopy
EDS	Energy dispersive spectroscopy
LSCM	Laser scanning confocal microscopy

ΔH_t	Enthalpy of solidification for BNi-2 foil measured from each cycle during half-joint DSC
ΔH_o	Enthalpy of solidification for BNi-2 foil from diffusion barrier experiment
$2w_t$ (w_t)	Full liquid width (half)
$2w_o$ (w_o)	Full gap width (half)
L_f	Liquid fraction
LR	Linear regression
$2w_i$	Liquid width present at zero minutes liquid duration
$2w_{ISZ,\,o}$	Width of isothermally solidified zone present at zero minutes liquid duration
γ	Dimensionless constant for migrating interface
$D_{B\text{-}IN718}$	Diffusion coefficient for boron in Inconel 718
C_M	Solute concentration in the base metal
N	Spreading index

Acknowledgements

The author would like to acknowledge the funding support provided by National Sciences and Engineering Research Council of Canada (NSERC) through the Industrial Research Chair in Structural Brazing and Processing of Powder Metallurgy Superalloys, with additional funding provided by Pratt & Whitney Canada. The author would also like to acknowledge the technical support of the following people: Julian O'Flynn, Cathy Whitman, Clare MacIsaac, Daniel Cluff, Addison Rayner, Colin Tadgell, Eric Moreau, Patricia Scallion.

The author acknowledges the support of the Canada Foundation for Innovation, NSERC, and other partners which fund the Facilities for Materials Characterization, managed by The Clean Technology Research Institute (CTRI), formerly The Institute for Research in Materials (IRM).

CHAPTER 1 Introduction

1.1 Background

There exists a motivation amongst researchers in the aerospace industry to develop processes that produce more energy efficient and sustainable components. One area of focus is the use of near net shape manufacturing techniques for nickel (Ni)-based superalloys used in gas turbine engine components. Compared to traditional processing routes, a near net shape approach can reduce the need for costly machining steps, resulting in reduced energy usage and material waste. The near net shape approach involves brazing together several simpler parts produced via powder metallurgy or additive manufacturing to make a more complex shaped part. Brazing is an umbrella term for a group of joining processes that uses a filler metal (FM) insert to join two parent materials at temperatures above the liquidus of the FM (at least 450°C) [1].

One brazing technique that has been applied for almost half a century is known as transient liquid phase bonding (TLPB) [2]. TLPB is a brazing process that makes use of capillary force to fill a gap with liquid FM to join two components together. By heating a fixed assembly of base metal (BM) components and FM within a vacuum furnace, a strong bond of uniform properties and higher melting point can be formed at a single temperature above the liquidus of the FM. This phenomenon is also known as isothermal solidification (IS), because the FM solidifies at a single temperature.

One TLPB couple commonly employed in structural brazing of turbine engine components is Inconel 718 (IN718) and BNi-2. A series of surface pre-treatment steps are required prior to brazing IN718. These pre-treatments involve cleaning, roughening, and plating processes. IN718 is more susceptible to oxidation due to the presence of stable oxide formers such as aluminum (Al) and titanium (Ti). The presence of stable oxide films can inhibit wetting and spreading of the FM during brazing compared to other Ni-based superalloys [3]. The Ni plating is known to enhance wetting of the FM, but the overall effects of the plating on the TLPB process are not entirely understood. Therefore, motivation exists to investigate the effects Ni plating has on the TLPB of IN718 using BNi-2, to effectively optimize the brazing process.

1.2 Superalloys

High-temperature engineering requirements have been a driving force for innovation in alloy development for quite some time. Applications demanding materials with high strength and corrosion resistance at an elevated service temperature led to the development of superalloys. Superalloys are heat resistant alloys capable of retaining their strength at high temperatures [4]. These alloys have excellent corrosion/oxidation resistance, high strength, and resistance to creep and rupture at elevated temperatures. Ni-base superalloys have become the material of choice for high temperature applications requiring superior high strength under static, fatigue, and creep conditions [5]. The three classes of superalloys are Ni-, iron (Fe)-Ni- and cobalt (Co)-based superalloys.

Various shapes can be produced from superalloys through appropriate processing methods such as forging or rolling. More complex assemblies can be built up through brazing or welding methods.[6]. The largest application of superalloys is in aircraft and industrial gas turbines, but they are also used in production of petrochemical equipment, rocket engines, space shuttles, steam power plants, and nuclear reactors [4]. Table 1.2.1 contains the compositional ranges for major alloying additions present in the three classes of superalloys. Note that the remainder of any given alloy would be Ni in Table 1.2.1.

Table 1.2.1 - Compositional ranges of major alloying elements in superalloys [6]

Element	Range of Composition [wt.%]	
	Fe-Ni & Ni-based	Co-based
Cr	5-25	19-30
Mo, W	0-12	0-11
Al	0-6	0-4.5
Ti	0-6	0-4
Co	0-20	…
Ni	…	0-22
Nb	0-5	0-4
Ta	0-12	0-9
Re	0-6	0-2

1.2.1 Microstructure of Superalloys

The microstructure typically found in superalloys consists of an austenitic FCC matrix phase plus a variety of secondary phases. The secondary phases include an assortment of carbides and Ni-rich intermetallic precipitates. Figure 1.2.1 shows the various phases commonly found in the microstructure of commercial superalloys.

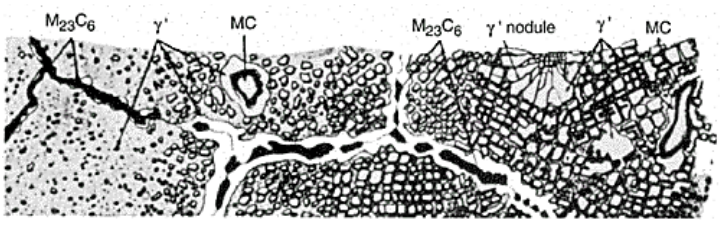

Figure 1.2.1 - Schematic depicting the microstructure present in an Fe-Ni-based superalloy [6]

The austenitic FCC matrix is known as the gamma phase (γ), and is a Ni-rich, non-magnetic phase containing high amounts of solid solution strengtheners such as tungsten (W), Co, molybdenum (Mo), Fe, and chromium (Cr). High temperature creep occurs at temperatures above $0.6T_{melt}$, meaning that strengthening is diffusion dependent. Slow diffusing species such as W and Mo are most beneficial for prevention of high-temperature creep failure [4].

The major precipitate phase found in most superalloys is the gamma prime phase (γ'). γ' improves strength in superalloys and is produced through controlled heat treatments. γ' is an Al and Ti rich intermetallic precipitate that is coherent with the γ matrix. In a Ni-base superalloy, the chemical composition of γ' is Ni_3(Al, Ti). The Ni matrix present in superalloys favours precipitation of γ' as the mismatch between precipitate and the matrix is only 0.1 percent. γ' has tremendously long-term stability and can nucleate homogeneously with low surface energy. Tetragonal distortion maintains the coherency between the γ' precipitates and the matrix [4].

The shape of γ' precipitates present in Fe-Ni-base superalloys is spherical, whereas in Ni-based superalloys the shape is cuboidal. The morphology of the γ' precipitate can be controlled by altering the Mo content and the ratio of Al/Ti. The morphological sequence that γ' goes through is as follows: spherical, globular, blocky, cuboidal. The mismatch between the γ and γ' lattices determines the morphology of the γ' precipitate. γ' is spherical

when the mismatch is low, and becomes cuboidal with {100} faces as the mismatch increases between the precipitate and the matrix [4]. It is even possible to form a γ-γ' eutectic in heat treated cast alloys. Alloys that contain higher amounts of Al and Ti form cuboidal γ' precipitates. After prolonged exposure above 700°C, undesirable phases such as η and δ can form when the lattice mismatch between γ and γ' is high [6].

Another important strengthening phase found in Fe-Ni superalloys with high niobium (Nb) contents is the gamma double prime phase (γ''). This is an ordered intermetallic precipitate phase with BCT crystal structure and a chemical composition Ni_3Nb. γ'' has an orientation relationship with the γ matrix phase, such that $\langle 100\rangle_{\gamma''}//\langle 100\rangle_{\gamma}$ and $\langle 001\rangle_{\gamma''}//\langle 001\rangle_{\gamma}$ [5].

The morphology of the γ'' precipitate is disk-shaped, and it is coherent with the matrix phase. The dimensions of the discs are approximately 50 nm in diameter and 10 nm in thickness. γ'' has high coherency strains, usually several percent. The combination of limited number of slip systems in γ'' and high coherency strains contribute to the excellent high-temperature properties displayed by Fe-Ni alloys. γ'' can become overaged and form the deleterious δ phase. This phase is incoherent with the matrix and does not provide strengthening. The δ phase forms in the temperature range 650 to 980°C [5].

Carbide phases also contribute to strengthening in superalloys. The presence of carbon results in the formation of metallic carbides both within grains and at grain boundaries. The common types of carbides found in superalloys are shown in Figure 1.2.1, and they are M_6C, MC, and $M_{23}C_6$ (M= carbide former element). These carbides are extremely stable and primarily form as part of the solidification process [4].

The presence of carbides in the grain boundary serve as a grain growth inhibitor by pinning the grain boundaries in place. The high-temperature properties of a superalloy will be affected by the size and distribution of the carbides within the alloy. The presence of a continuous chain of carbides at the grain boundary results in a least resistance fracture pathway for dislocation movement, due to the their harder and more brittle nature. This will impact the properties of the alloy severely. Without the presence of carbides at the grain boundary, excessive grain boundary sliding will occur due to coalescence of voids at the grain boundary [4].

1.2.2 Alloying Additions and Microstructural Effects in Superalloys

The variety of elements present in superalloys is among the widest of all classes of metallic alloys. The addition of each of these elements has significant effects on the microstructure that develops, and in-turn the high-temperature properties of the alloy [6]. Table 1.2.2 lists the major alloying elements found in superalloys and their associated effects on the microstructure and properties of the superalloy. It should be noted that not all alloys within a given class will possess those effects from a given alloying addition [6].

Table 1.2.2 - Role of various alloying elements in superalloys [6]

Effect	Fe-Ni-based	Ni-based	Co-based
Forms γ'	Al, Ni, Ti	Al, Ti	---
Retards γ' coarsening	---	Re	---
Raises solvus temperature of γ'	---	Co	---
Hardening precipitates or intermetallics	Al, Nb, Ti	Al, Ti, Nb	Al, Mo, Ti, W, Ta
Retards formation of η	Al, Zr	---	---
γ stabilizer	C, W, Ni	---	Ni
Solid solution strengthener	Cr, Mo	Co, Cr, Fe, Mo, W, Ta, Re	Nb, Cr, Mo, Ni, W, T
Oxidation resistance	Cr	Al, Cr, Y, La, Ce	Al, Cr
Facilitates working	---	---	Ni_3Ti
Improves creep properties	B	B, Ta	---
Increases rupture strength	B	B	B, Zr
Grain boundary refiners	---	B, C, Zr, Hf	---
Carbide formers	Mo, Cr, Ti	Ti, Cr, Mo, W	W, Ta, Ti, Mo, Nb, Hf, Cr

1.2.3 Iron-Nickel-Based Superalloys

Since the main superalloy used as a base material in the work completed during this thesis was IN718, an Fe-Ni-based superalloy, this subsection will briefly describe some of the metallurgical background relevant to Fe-Ni-based superalloys.

Fe-Ni-based superalloys contain from 25 to 45 wt.% Ni and 15 to 60 wt.% Fe. Fe-Ni-based superalloys can't be used at as high of temperatures as Ni-based superalloys due to their

reduced Ni content but are inherently cheaper due to substitution of a portion of the Ni for Fe. The addition of more exotic alloying additions, such as Cr, Mo, Al, Ti, and Nb, greatly improve the various properties that make superalloys so widely used in environmentally aggressive high-temperature applications. Typical applications for these alloys include manufactured components in steam turbines (fasteners, disks, blades), gas turbine and jet engines, heat exchangers, and furnaces [4].

The matrix phase present in Fe-Ni-based superalloys is the FCC austenite phase. Due to added Mo and Cr (ferrite stabilizers), the Ni content required to stabilize the austenite phase at room temperature is above 25 wt.%. The addition of austenite stabilizers such as Co can decrease this minimum Ni content. Higher amounts of Ni make the alloy more resistant to oxidation but increase cost. Increasing the Fe content in the superalloy can improve ductility and cost, but results in decreased elevated temperature oxidation resistance [4].

Mo is the most important solid solution strengthening element as it increases the lattice parameter of the austenite matrix, and also enters into solid solution with carbides and γ' precipitates. Small additions of carbon and boron can also act as solid solution strengtheners. Although the primary function of Cr is to improve oxidation resistance, it also provides some solid solution strengthening effect [4].

Perhaps the most widely used and relied on alloys within the Fe-Ni-based superalloy class, are those that are strengthened by intermetallic compound precipitation in an FCC matrix [6]. Despite the solid solution strengthening effect provided by Al, Nb, and Ti, their main purpose is their participation in very important precipitation strengthening reactions. These elements combine with Ni to form various intermetallic phases that can greatly influence the mechanical and physical properties of a superalloy [4]. Table 1.2.3 contains a summary of the important precipitating phases commonly found in Fe-Ni-based superalloys [4].

Table 1.2.3 - Important precipitating phases in Ni-Fe-based superalloys [4]

Phase	Chemical Formula	Structure
γ'	$Ni_3(Al, Ti)$	Ordered FCC
γ''	Ni_3Nb	Ordered BCT
η	Ni_3Ti	HCP
δ	Ni_3Nb	Orthorhombic

1.2.4 Inconel 718

IN718 is an Fe-Ni-based superalloy that is strengthened via precipitation of Nb rich γ''. This alloy also contains amounts of Al and Ti, meaning that it is strengthened by the presence of both γ' and γ''. The strength of IN718 is also attributed to solid-solution strengthening due to presence of elements such as Mo and Cr [4]. Fe-Ni-based superalloys strengthened by presence of γ' can be used up to 650°C, while alloys with greater Ni contents can be used to about 815°C. This class of superalloys have considerably lower rupture stress at elevated temperature than Ni-based superalloys, again due to reduced Ni content [4].

Superalloys that contain high amounts of Al and Ti such as IN718 are susceptible to detrimental metallurgical effects when they are joined by welding. These alloys are susceptible to heat affected zone cracking during welding [7]. Welding also causes segregation of Nb during non-equilibrium solidification of the fusion zone. This results in the formation of very problematic Nb-rich Laves phase. The presence of this phase causes depletion of alloying elements from the adjacent matrix that are crucial to precipitation hardening. The Laves phase is also detrimental to mechanical properties and acts as a site for crack nucleation and growth [8]. Brazing with high-temperature Ni-based FM developed into an effective technique used to join superalloys while avoiding problems introduced by welding. TLPB became the method of choice for joining/repair of aerospace engine components manufactured from superalloys [7].

1.3 Brazing

The American Welding Society (AWS) defines brazing as “a group of joining processes that produce coalescence of materials by heating them to the brazing temperature in the presence of a brazing FM that has a liquidus above 450°C and below the solidus of the base materials” [3]. Brazing began as an ancient art as early as 3400 B.C and developed over

centuries into a widely used and well-established commercial joining process. The first edition of the *Brazing Manual* was published in 1955 by AWS, where joint strength was merely described qualitatively, and acceptance criteria only went as far to say if joint was "good" or "bad". By the 1950's, brazing was being introduced in the repair of aircraft engines. A standard for the testing of brazed joints titled AWS C3.2-63, Standard Method for Evaluating the Strength of Brazed Joints, was introduced by the AWS Committee of Brazing and Soldering in 1963 [3].

During a brazing process, a leak tight, and structural bond is created between two parent materials through the melting, flow, and solidification of a brazing FM. The molten FM is distributed between a relatively narrow gap existing between the two base metal faying surfaces through capillary action. Faying surface is the term used to describe the surfaces of the base metal that the molten FM will wet and spread over, and eventually solidify upon.

The phenomena of wetting and capillary action are crucial physical processes to obtaining a strong joint [9]. The driving forces behind capillary action and wetting are characterized by thermodynamic concepts of free energy resultant from phase transformations occurring during brazing, as well as surface free energy [3]. The degree to which both wetting and spreading occur are affected by interfacial chemical reactions, the geometry of the joint, and reaction within the FM [3].

The FM selected for a particular brazing application must demonstrate full wettability of the base metal and spreading into the joint clearance, as the final properties of the joint are strongly influenced by these two phenomena [9]. Wetting and spreading will be treated in greater detail in Subsection 1.5.

The cleanliness of the faying surfaces, as well as the FM is very important in terms of obtaining a joint with the desired properties. Surface preparation is required in many brazing procedures to ensure good wetting and capillarity is achieved. Contamination of the faying surface results in poor wetting and spreading conditions, resulting in reduced joint integrity [3].

The type of base metal being joined has a great effect on the strength of a brazed joint. Thus, the base metal microstructure and associated properties must be taken into careful

consideration. Metallurgical interaction between the FM and BM can play a vital role in determining the strength of a brazed joint. Phenomena that is associated with the base metal that could affect strength includes embrittlement (due to hydrogen, phosphorus, or sulfur), alloying between the FM and BM, oxidation, stress cracking, and carbide precipitation. Joints that use hardenable base metals have less predictable strengths due to the complex metallurgical reactions that occur between the FM and BM. In cases where dissimilar metals are to be joined, the difference in coefficient of thermal expansion becomes of great importance [9].

There exist several requirements for selecting an appropriate FM for a given brazing procedure. The FM must be able to alloy with the BM to form an alloy with a much higher melting temperature. The FM should demonstrate good wettability against the faying surfaces of the BM and should possess high fluidity so that full alloy distribution into the joint clearance can occur via capillary flow. The base metal erosion caused by the FM should be minimized or avoided if possible. The penetration of FM elements into the base metal is governed by the intensity of the mutual diffusion processes. Diffusion plays a vital contribution in producing high quality braze joints in the case of brazing high-temperature metals with Ni-based FM [9]. FM come in a variety of different forms including rods, wires, strips, preforms, powders, pastes, and tapes [3].

The brazing temperature (T_B) is ultimately determined by the phase equilibria between the base and filler metal. The first and most obvious requirement is that the FM should be fully melted at T_B. Another important consideration is that the dissolution of the base metal will also be affected by T_B [3]. Most brazing alloys melt over a temperature range, and this range is rarely a narrow one. In the case of filler metals that possess a narrow melting range, the tendency to liquate or to coexist as a mixture of solid and liquid is low. This type of FM flows very well and should be used in small joint gaps. When the FM has a wider melting range the tendency to liquate is increased. T_B should also be below the solidus of the base metal and may need to be tailored to avoid deteriorating properties such as strength and oxidation resistance [9].

Many different heating methods exist in brazing including infrared, electrical resistance, induction, furnace, and torch. Many factors go into selecting the appropriate heating

method, including required production rate, assembly size, quantity of assemblies required, tolerable heating rate, external/internal cooling rates and differential thermal gradients. Different heating methods will also inevitably possess tremendously different effects on structural integrity, distortion, and dimensional stability of the joint produced [9]. Heating can also be accomplished in a vacuum or inert gas atmosphere to reduce or prevent oxidation of the brazing components. In the case of torch brazing, a flux is used "to hinder or prevent formation of oxides and other undesirable substances in the molten metal and on solid metal surfaces and to dissolve or otherwise facilitate the removal of such substances" [3].

Many different brazing techniques exist for joining a multitude of materials including metals and ceramics. These brazing techniques include diffusion, resistance, dip, torch, furnace, and induction brazing. As mentioned earlier, TLPB is a diffusion brazing process used to join superalloys components in the production of gas turbine engines for aerospace. Thus, the following chapter will briefly introduce and discuss important aspects related to the TLPB process.

1.3.1 Transient Liquid Phase Bonding

TLPB is a capillary joining process that was derived from fluxless vacuum brazing. TLPB, like many joining processes, functions under the main concept of the addition of a FM between the two BM substrates and application of thermal exposure. Duvall et al. [2] were the first to introduce the process to improve the bonding techniques applied in joining superalloys. The composition of FM is typically engineered to contain approximately similar weight percent (wt. %) of chemical constituents as the BM. The key difference between FM and BM chemical composition is the introduction of a certain amount of one or more elements known as melting point depressants (MPD) [3].

During TLPB, significant diffusion of the MPD occurs during an elapsed time at T_B. "Diffusion induces significant compositional changes at the bond line, which, increases the melting temperature of the bond and results in re-solidification during holding at a constant bonding temperature."[10] These are the two characteristics of TLPB that make it an economic solution to materials joining problems in a multitude of industries. The increase in melting temperature of the bond region is one of the main advantages of TLPB.

The term isothermal solidification derives from the fact that solidification occurs at a constant temperature as opposed to happening over a temperature range during "equilibrium" cooling conditions, known as athermal solidification. The term TLPB derives from the fact that after enough time at T_B the liquid is completely consumed through MPD diffusion (i.e. is transient in nature).

TLPB is generally used in high-temperature applications requiring high strength and strong resistance to degradation due to other environmental issues such as corrosion or creep. Applications for TLPB include heat exchanger, aerospace, semiconductor and automotive industries [2], [11]–[13]. TLPB is often used when welding and other brazing techniques can't be used [14].

1.3.2 Stages of Transient Liquid Phase Bonding

Conceptually, TLPB can be treated as a four stage process, where each stage is related to different composition regimes on the binary phase diagram [15]. Figure 1.3.1 is a series of diagrams depicting the various stages of TLPB using a hypothetical material 'A' joined with an interlayer consisting of 'A' plus an MPD element 'B' added.

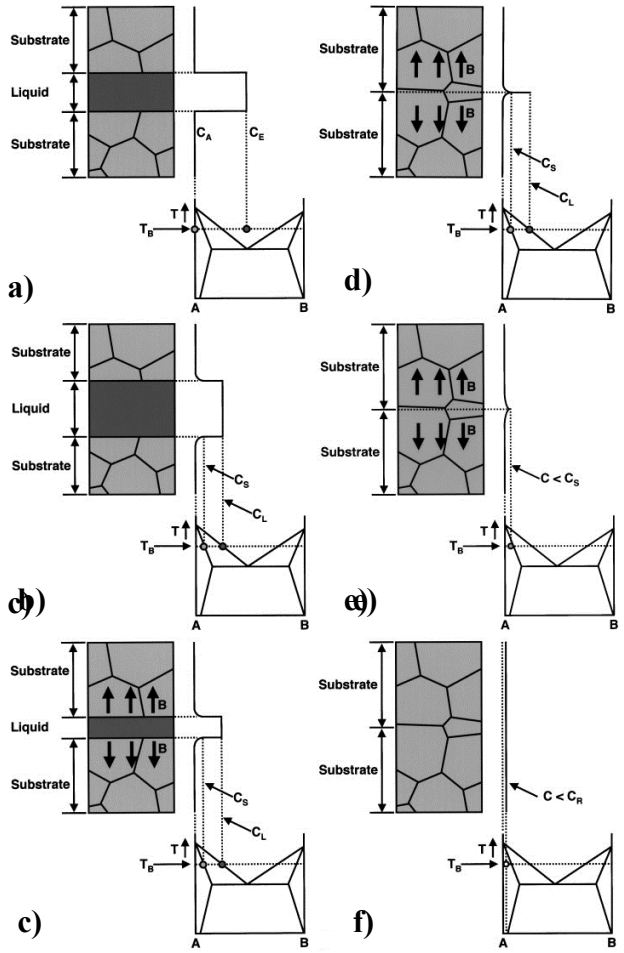

Figure 1.3.1 - TLPB stages: a) initial condition; b) dissolution; c) IS; d) completion of IS; e) SSH; f) final condition [10]

Stage I involves heating the assembly to the melting point of the FM. During the initial heating it may be possible that interdiffusion between the FM and BM may occur. As temperature increases, the interdiffusion between the FM and BM results in shifting of the solute concentration at the solid/liquid (S/L) interface along the solvus line as indicated by Figure 1.3.1. The extent to which diffusion occurs during heating to the melting temperature depends on the diffusivity of the solute within the BM, the heating rate, and whether good contact with the base metal faying surface exists [14]. The occurrence of diffusion during heating is especially important in cases where a thin gap width is used.

Most TLPB of Ni superalloys uses boron (B) as the MPD solute addition to the FM and the rapid diffusion of B into the base metal during heating to T_B is termed initial boron

uptake (IBU). This results in a reduction of the initial liquid layer thickness upon melting, and some diffusional solidification before T_B is reached [16].

Once the melting point of the FM is reached, heating is continued to T_B. T_B is generally higher than the liquidus temperature of the FM. The diffusion of the BM elements into the liquid is required to reach the liquidus composition, C_L. This causes melt back of a portion of the solid BM to conserve mass. This is known as Stage II and is termed the dissolution stage as the base metal dissolves into the liquid. Dissolution of a portion of the base metal results in an increase in the liquid width and the direction of the S/L interface displacement is away from the centerline. The movement of the solid–liquid interface continues until T_B has been reached; at this point the liquid has attained its maximum width. Close examination of Figure 1.3.1 b) indicates that some solute from the FM must diffuse into the BM during the dissolution stage in order to establish the equilibrium composition in the solid, C_S. This can be considered early diffusional solidification and will limit the extent of gap widening achieved once the braze temperature is reached. Depending on the system this diffusional solidification process could be negligible or significantly impact the extent of gap widening.

The amount of dissolution that occurs depends on the liquidus and solidus compositions at T_B [14]. Dissolution needs to be monitored, as it can have detrimental effects on the mechanical and physical properties of the final joint if a large degree of BM dissolution occurs [14]. The most obvious disadvantage related to excessive dissolution is the increase in liquid width, which is inevitably associated with an increase in time required for completion of isothermal solidification (t_{IS}). The extent of dissolution can be controlled to some degree by using a thin interlayer, tailoring FM composition to be similar to BM, or ensuring FM is of a eutectic composition [14].

Once the temperature has reached T_B, local equilibrium at the S/L interface is established once the solute composition of liquidus (C_L) and solidus (C_S) are reached. At this point, the dissolution stage is terminated. Dissolution is typically completed after a short hold at T_B, since the activation energy for dissolution is generally low relative to interstitial, substitutional, or self-diffusion [10].

Upon reaching T_B, Stage III is initiated, and the BM/FM/BM assembly undergoes IS. Stage III involves solidification of the molten FM region at T_B due to the diffusion of MPD into the BM. Solute concentrations at the interface remain constant during this stage in order to maintain local equilibrium. This means that as solute continues to diffuse into the BM, the liquid width shrinks in order to conserve mass. The width of the liquid zone decreases continuously with increasing hold time at T_B, until complete IS has been achieved [10]. Stage III is often considered the most important stage in the TLPB process, as it is ultimately the most limiting step in terms of achieving a successful TLPB joint [14]. A large degree of research has focused on this aspect of the TLPB process, including t_{IS}. The success of Stage III (i.e. whether IS reaches completion) is also dependent on FM composition, gap width, and solute diffusivity in the BM [10].

Bond microstructure can be homogenized by prolonging isothermal hold or applying a post braze heat treatment [14]. The solid-state homogenization (SSH) treatment is usually considered as Stage IV. SSH is usually carried out such that the solute concentration at the bond line is below the solid solubility of the solute in the BM at room temperature. This way, precipitation of undesirable second phases during cooling from T_B is prevented [10].

1.3.3 Advantages and Disadvantages of Transient Liquid Phase Bonding

Likely one of the largest advantages offered by TLPB is the large increase in bond melting temperature that can occur. Ultimately, this means that joining via TLPB can occur at a temperature below the intended service temperature. This is beneficial in terms of retaining the carefully tailored microstructures that exist within materials intended for high-temperature service [14]. Other advantages offered by the TLPB process are listed below.

The bond formed after completion of TLPB often has similar mechanical properties to the BM. In some cases, the strength of the bond can even be raised high enough, such that failure occurs in the BM as opposed to the joint region. Compared to fusion welding or other joining processes, the melting of the substrates is minimal. Unlike many other joining procedures, the TLPB process is tolerable to the presence of a faying surface oxide layers and does not require as much joint preparation or the use of fluxes. Although this does depend very heavily on the stability of the oxides on the surface. Overaging of temperature-sensitive materials such as Fe-Ni-based superalloys can be avoided [14].

It should be kept in mind that TLPB can be both expensive and time consuming compared to other joining techniques, and these factors must also be considered when selecting an appropriate joining method for a given application. The required t_{IS} can be uneconomical and unfeasible. TLPB should be avoided if dissolution is going to be excessive, specifically while joining materials with a sensitive microstructure. If the growth of brittle intermetallics will occur in the bond region as a result of the joining process, TLPB should be used extremely cautiously. Intermetallics in the bond region can lower the ductility and lead to catastrophic failure due to the brittle nature of the intermetallics.

1.3.4 Modelling of Transient Liquid Phase Bonding Process

Modelling TLPB has been based around Fick's laws and mass balance arguments. Modelling has primarily focused on the dissolution and IS stages [12]. Only modelling efforts focused on Stage III (IS) will be discussed in the following chapter since the work completed in this thesis was concentrated on the IS process.

The analytical solutions developed over time have typically had a couple of assumptions associated with them. First off, the influence of grain boundaries is not considered. The effect of surface oxides inhibiting diffusion across interfaces is absent in the models. Generally, it assumed that mass conservation applies, and that no loss of MPD occurs from edges of the bond region. It is also assumed that contact between the components (FM and BM) is established by collapsing any asperities through appropriate stress, resulting in rapid initiation of surface contact. The BM is considered to demonstrate a semi-infinite surface at the interface of the joint. The FM and BM are assumed to be homogeneous. Finally, the classical Fick's diffusion equations are assumed to be applicable in all scenarios [17].

In 1979, Ikawa et al. [18] studied the TLPB of Ni-base materials (pure Ni and Alloy 713C) using a Ni-base FM that contained phosphorus as an MPD. This work was successful in obtaining a complete analytical solution to describe the kinetics of the TLPB process, as well as an expression for the solute concentration at the center of the FM interlayer. Ikawa et al. [18] modelled the IS stage and homogenization stages separately. Ultimately, they found that the solidification of the liquid FM was controlled by the diffusion of MPD

phosphorus into the parent metal substrates. It was also determined that the solute concentration at the center of the joint can be modelled as a function of time.

As previously mentioned, once the hold at T_B commences, a liquid phase with solute concentration C_L is in equilibrium with a solid phase possessing a solute concentration C_s. This results in a constant solute concentration in both the solid and the liquid phase at the interface. The diffusion of solute, in this case phosphorus, from the liquid into the solid means that the S/L interface must move towards the centerline to ensure a constant solute concentration at the interface [18].

A one-dimensional diffusion model was adopted, since the liquid width at the bond region was significantly smaller than the width of the two parent materials. According to Ikawa et al. [18], the flux of solute atoms, J, per unit area of the S/L interface and unit time can be expressed as in Equation 1.3.1;

$$\boldsymbol{J = -\left(\frac{D}{V_s}\right)\left(\frac{dC}{dx}\right)} \qquad \textbf{Eq. (1.3.1)}$$

where V_s is the molar volume of solid at T_B, dC/dx is the gradient of solute concentration in the x direction and D is the diffusion coefficient of the solute into the solid phase.

The diffusion flux of solute can be expressed by Equation 1.3.2 if the S/L interface moves a distance dx within a given time dt due to diffusion of solute into the solid phase at the interface;

$$\boldsymbol{J = -\left(\frac{dx}{dt}\right)\left(\frac{C_l}{V_l} - \frac{C_s}{V_s}\right)} \qquad \textbf{Eq. (1.3.2)}$$

where V_l is the molar volume of liquid at T_B, and C_s and C_l are the mol fraction of solute at the interface in the solid and liquid respectively.

The solute concentration at a position x within the solid phase can be expressed by Equation 1.3.3, where C_s is constant;

$$\boldsymbol{\left(\frac{C}{V_s}\right) = \left(\frac{C}{V_s}\right)\left[1 - erf\left\{\frac{(x-h)}{2\sqrt{Dt}}\right\}\right]} \qquad \textbf{Eq. (1.3.3)}$$

where h is equal to half of the initial thickness of the liquid phase.

From Equation 1.3.3, the concentration gradient at x=h is expressed as;

$$\left(\frac{dC}{dx}\right)_{x=h} = -\left(\frac{C_s}{\sqrt{\pi Dt}}\right) \qquad \textbf{Eq. (1.3.4)}$$

From Equations 1.3.1, 1.3.2 and 1.3.4, the thickness of the liquid film, 2x, at time t is expressed as;

$$2x = 2h - \left(\frac{4C_s}{\sqrt{\pi V_s}}\right)\left(\frac{C_l}{V_l} - \frac{C_s}{V_s}\right)^{-1}\left(\sqrt{Dt}\right) \qquad \textbf{Eq. (1.3.5)}$$

If the slope of the linear relationship in Equation 1.3.5 is denoted m, then the natural logarithm of m can be written as follows;

$$ln(m) = ln\left\{\left(\frac{4C_s}{\sqrt{\pi V_s}}\right)\left(\frac{C_l}{V_l} - \frac{C_s}{V_s}\right)^{-1}\right\} + \left(\frac{ln(D_0)}{2}\right) - \left(\frac{Q}{2RT}\right) \qquad \textbf{Eq. (1.3.6)}$$

where D_0 is the frequency factor, T is the absolute temperature, R is the gas constant and Q is the activation energy for solute diffusion in the solid phase.

Three temperatures were selected for bonding experiments under vacuum atmosphere. Ikawa et al. [18] cited difficulty in measuring the S/L interface at room temperature, and opted to measure the width of eutectic solid remaining at the centerline. This eutectic thickness was converted into a thickness of liquid film. An inverse linear relationship between the eutectic width and the square root of bonding time was observed at each temperature [18].

The natural logarithm of m was plotted against the inverse of absolute temperature, and again a linear relationship was observed. From this plot, an estimation of the activation energy of solute diffusion into the solid could be obtained by determining the slope of the ln(m) vs. 1/T plot. The frequency factor can then be calculated using the y-intercept of the linear approximation obtained from the ln(m) vs. 1/T plot. After obtaining the frequency factor and activation energy, Equation 1.3.7 can be used to calculate the diffusion coefficient of solute into the solid at the interface for a given temperature.

$$D = D_0 exp\left(\frac{Q}{RT}\right) \qquad \textbf{Eq. (1.3.7)}$$

The diffusion coefficient is required in expressions developed for predicting t_{IS}.

Another important derivation came out of the study completed by Ikawa et al. [18], and that was an expression to describe the solute concentration in the bonding region as a function of both space and time. The expression suggested by Ikawa et al. [18] is shown in Equation 1.3.8. An expression for the solute concentration at the centerline, x=h, is given in Equation 1.3.9;

$$\boldsymbol{C(x,t) = C_0 - \left(\frac{C_0}{2}\right)\left\{erf\left(\frac{h-x}{2\sqrt{Dt}}\right) + erf\left(\frac{h+x}{2\sqrt{Dt}}\right)\right\} + C_i} \qquad \textbf{Eq. (1.3.8)}$$

$$\boldsymbol{C(t) = C_0\left\{1 - erf\left(\frac{h}{2\sqrt{Dt}}\right)\right\} + C_i} \qquad \textbf{Eq. (1.3.9)}$$

where C_b is the solute concentration of the base metal, C_i is the initial solute concentration of the interlayer, and C_0 is (C_b-C_i).

In a later study conducted by Nakao et al. [19], an expression to predict t_{IS} was presented. During this study [19], several Ni-base alloys were joined using commercially available amorphous FM, and the kinetics of the melting and IS processes were examined. The interlayer width was held constant via spot-welded Ni spacers. The expression for the time required for complete IS, t_f, is written as follows;

$$\boldsymbol{\sqrt{t_f} = \left(\frac{C_l}{V_l} - \frac{C_s}{V_s}\right)\left\{\left(\frac{\sqrt{\pi V_s}}{4C_s}\right)\left(\frac{2h}{\sqrt{D}}\right)\right\}} \qquad \textbf{Eq. (1.3.10)}$$

They found that since the term (C_l/V_l-C_s/V_s) $\left(\sqrt{\pi V_s}/4C_s\right)$ is essentially independent of temperature within the experimented range of T_B, that the square root of t_f was directly proportional to $2h/\sqrt{D}$.

Another expression for t_{IS} was developed by Tuah-Poku et al. [20]. In this study, pure silver was joined to itself using a copper foil insert as the FM. It was established that the final maximum liquid width, W_{max}, could be estimated via a mass balance approach, shown in Equation 1.3.11. Equation 1.3.12 shows the mass balance rearranged to provide an expression for the maximum liquid width. Note that the densities of A and B are assumed to be equal in Equation 1.3.12.

$$W_0 C^B \rho_B = (W_{max} - W_0)(C^{L\alpha} \rho_A) + W_0 C^{L\alpha} \rho_B \quad \textbf{Eq. (1.3.11)}$$

$$W_{max} = W_0 \left[\frac{C^B}{C^{L\alpha}}\right] \quad \textbf{Eq. (1.3.12)}$$

where W_0 is the initial interlayer width, C^B is the weight fraction of solute in the interlayer, and $C^{L\alpha}$ is the weight fraction of solute in the liquid at the interface, ρ_A and ρ_B are the densities of A and B respectively[20].

If the assumption that the density of A and B are equivalent is valid, the mass balance at any time during the IS stage can be written as follows;

$$WC^{L\alpha} = W_{max} C^{L\alpha} + 2 \int_0^t D_s^\alpha \frac{dC}{dy} dt \quad \textbf{Eq. (1.3.13)}$$

where W is the liquid width at time t, $W_{max}C^{L\alpha}$ denotes the initial mass of the interlayer and $WC^{L\alpha}$ represents the actual mass of the interlayer [20]. The integral represents the migration of solute atoms across the interface. The solution of the Fick's equation is shown in Equation 1.3.14.

$$C(y,t) = C^{L\alpha}\left[1 + erf\left(\frac{y}{\sqrt{4D_s^\alpha}}\right)\right] \quad \textbf{Eq. (1.3.14)}$$

Integration of over time yields [20];

$$\int_0^t D_s^\alpha \frac{dC}{dy} = -C^{L\alpha}\left(\frac{4D_s^\alpha}{\pi}\right)^{0.5} \quad \textbf{Eq. (1.3.15)}$$

Upon inserting Equation 1.3.15 into Equation 1.3.13, and setting W=0 and t=t_f, the following expression for t_f is obtained;

$$t_f = \frac{\pi {W_0}^2}{16 D_s^\alpha}\left(\frac{C^B}{C^{L\alpha}}\right)^2 \quad \textbf{Eq. (1.3.16)}$$

Tuah-Poku et al. [20] found that Equation 1.3.16 greatly overestimated t_{IS} determined experimentally. It was postulated that the overestimation was a result of the inherently complex phenomena occurring at the migrating S/L interface [20].

As previously mentioned, the IS process is governed by diffusion and the progression of IS can be modelled using time dependent diffusion expressions derived from Fick's second law. Analytical solutions for Fick's second law can be written as expressed in 1.3.8. By substituting $W_0/2 = h$, $x = 0$, and $C(x, t) = C_S$ into 1.3.8, the following expression is obtained;

$$\frac{C_S - C_{BM}}{C_{FM} - C_{BM}} = erf\left(\frac{W_0}{4\sqrt{Dt_{IS}}}\right) \qquad \textbf{Eq. (1.3.17)}$$

where C_S is the equilibrium composition of the solid at the interface, C_{BM} is the solute concentration in the BM, C_{FM} is the solute concentration in the FM , W_0 initial thickness of the FM , D is the diffusion coefficient, and t_{IS} is the holding time required for completion of IS [21]. This particular approach has been referred to as the solute distribution model, or in the case of TLPB using Ni-based superalloys the B diffusion model [7]. The solute distribution model is a continuum approach that treats the liquid homogenization and IS stages as simultaneous rather than discrete [22]. This simultaneous behaviour was demonstrated in the Ni-P system by Nakagawa et al. [23]

Another common approach used to model IS during TLPB is termed the migrating S/L interface model [7]. The solution for unsteady state linear diffusion can be expressed as follows;

$$C(x_S, t) = A_1 + A_2 erf\left(\frac{x}{2\sqrt{Dt}}\right) \qquad \textbf{Eq. (1.3.18)}$$

where $C(x_S, t)$ represents the solute concentration in the solid phase, x is the location of the S/L interface along the x direction, D is the diffusion coefficient, t is time, and A_1 and A_2 are constants determined via substitution of boundary conditions into Equation 1.3.18 [7]. A semi-infinite assumption is applied to this diffusion scenario, and the following expression is obtained;

$$C(\infty, t) = A_1 + A_2 = C_m \qquad \textbf{Eq. (1.3.19)}$$

where C_m is the solute concentration in the BM [7]. If the S/L interface is displaced to $x=x_S$ after time t, Equation 1.3.18 is written as follows;

$$C(x_s, t) = A_1 + A_2 erf\left(\frac{x_s}{2\sqrt{Dt}}\right) = C_s \quad \textbf{Eq. (1.3.20)}$$

where C_s is the solute concentration of the solid phase at the S/L interface [7]. Since Equation 1.3.20 is true for all values of t, x_s must be proportional to the square root of time, and thus;

$$x_s = \gamma\sqrt{4Dt} \quad \textbf{Eq. (1.3.21)}$$

where γ is a dimensionless constant that accounts for movement of the S/L interface [7]. γ has also been represented with the symbol K elsewhere in the literature [15], [24]. Mass balance applied to the S/L interface results in Equation 1.3.22.

$$(C_L - C_S)\frac{dx_s}{dt} = D\left(\frac{\partial C(x,t)}{\partial x}\right)_{x=x_S} \quad \textbf{Eq. (1.3.22)}$$

where C_L is the solute concentration of the liquid phase at the interface [7]. Equation 1.3.23 can be obtained through manipulation of Equations 1.3.18 - 1.3.22. Equation 1.3.23 can be utilized to determine the value of the dimensionless moving boundary constant.

$$\frac{C_S - C_M}{C_L - C_S} = \gamma\sqrt{\pi}exp(\gamma^2)\left(1 + erf(\gamma)\right) \quad \textbf{Eq. (1.3.23)}$$

Through rearrangement of Equation 1.3.21, t_{IS} can be estimated as follows;

$$\sqrt{t_{IS}} = \frac{2h}{16\gamma^2\sqrt{D}} \quad \textbf{Eq. (1.3.24)}$$

where 2h is the final maximum liquid width [7].

As indicated by Arafin et al. [7], these analytical modelling efforts do not take into account chemical and physical uncertainties associated with the TLPB process. Due to this, a single set of kinetics parameters (D_0 and Q) would not be very practical. These chemical and physical uncertainties (shown in Table 1.3.1) affect the kinetics associated with the TLPB process and therefore the assumption of unidirectional diffusion of solute atoms. Diffusion of solute atoms needs to be modeled taking the random diffusion of solute atoms into account [7]. Random Walk Modeling is a modeling technique that uses a random number

based on the statistical distribution profile obtained through several sets of experimental diffusion data. Arafin et al. [7] applied this technique to model the transport of B to account for chemical and physical uncertainties present. The cumulative probability distribution and probability density function of predicted t_{IS} were calculated for different process conditions. Experimental data was verified to have good agreement with predicted t_{IS}. Through this work, Arafin et al. [7] determined that t_{IS} for the IN718/BNi-2 system was much less than other Ni superalloy/Ni based FM couples. It was also found that increasing T_B and decreasing gap width resulted in reduction of hold time with no significant grain growth [7].

Table 1.3.1 - Physical & Chemical Uncertainties Associated with TLPB Process [7]

Physical & Chemical Uncertainties
Chemical heterogeneity in the FM and BM compositions
Variation in solute composition in the FM along gap length
Heterogeneous wetting behavior displayed by FM on BM
Joint configuration variation
Faying surface waviness
Uncertainty associated with measurements (length, temperature, and time)

1.4 Transient Liquid Phase Bonding of Nickel-Based Superalloys

1.4.1 Nickel-based Filler Metals

Joining Ni-based and high-Ni-containing alloys using TLPB generally uses a Ni-based FM. The classes of FM used for brazing are categorized in the AWS publication *Specification for Filler Metals for Brazing and Braze Welding*, AWS A5.8M:2004 [25]. The types of FM are classified based on the principal chemical element present in the composition of the FM. Ni-based FM 's are listed under the BNi classification, and are typically used in joining assemblies that require high-temperature service properties (strength, corrosion and oxidation resistance) [3]. Some common types of BNi FM used as well as their chemical composition can be found in Table 1.4.1. Note that in each of the BNi filler alloys, Ni makes up the remainder of the chemical composition. It is also worth noting, that only elements present in amounts greater than 0.1wt.% are listed in Table 1.4.1**,** other elements are present but are of less importance. Therefore, the wt.% listed in Table 1.4.1 do not sum

to one hundred. If a single value for an element is listed, it represents a maximum amount for that element in the alloy composition.

Table 1.4.1 - Chemical composition requirements for select Ni-based brazing FM [3].

AWS Classification	Chemical Composition [wt.%]				
	Cr	**B**	**Si**	**Fe**	**Other**
BNi-2	6.0-8.0	2.75-3.50	4.0-5.0	2.50-3.50	---
BNi-3	---	2.75-3.50	4.0-5.0	0.5	---
BNi-5	18.5-19.5	---	9.75-10.50	---	---
BNi-7	13.0-15.0	---	---		P: 9.7-10.5
BNi-8	---	---	6.0-8.0	---	Mn: 21.5-24.5; Cu: 4.05-5.0
BNi-10	10.0-13.0	2.0-3.0	2.0-4.0	2.5-4.5	W: 15.0-17.0; C: 0.40-0.55
BNi-13	7.0-9.0	2.75-3.50	3.8-4.8	0.4	Mo: 1.5-2.5; Nb: 1.5-2.5; Cu: 2.0-3.0

As indicated in Table 1.4.1, the chemical composition of BNi FM contains at least one of the following alloying additions; Ni, silicon (Si), B, and/or phosphorus. These elements act as a MPD in Ni, and therefore when these MPD elements are added to Ni, a suitable brazing alloy that will result in little to no base metal erosion is produced [3]. The binary Ni-B phase diagram shown in Figure 1.4.1 demonstrates that the melting point of Ni can be significantly reduced with addition of the B.

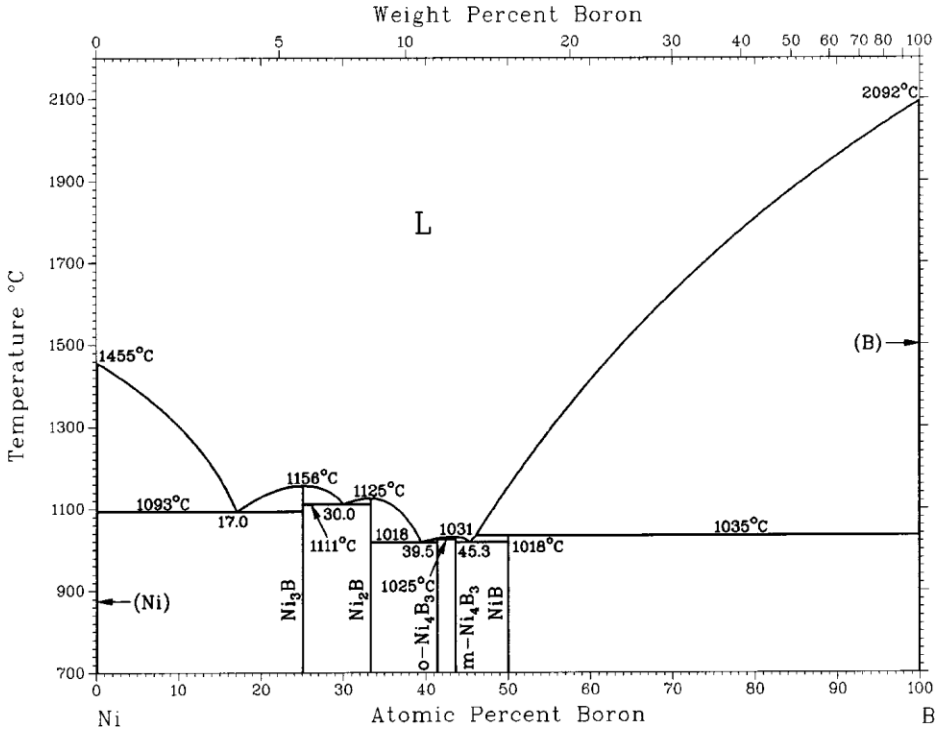

Figure 1.4.1 - Binary phase diagram for Ni-B system [26]

1.4.2 Investigating the Kinetics of Isothermal Solidification During Transient Liquid Phase Bonding of Nickel-based Filler and Base Materials

As previously mentioned, TLPB has been applied to join various Ni-based alloys using a Ni-based FM. The TLPB process is fairly complex, and has several physical and chemical uncertainties associated with it [7]. These uncertainties have made it rather problematic to obtain a comprehensive understanding of the TLPB process. Verification of analytical models using experimental results has been hindered by these uncertainties. Approaches generally taken by other researchers involved experimental validation of previously mentioned analytical approaches, particularly the solute distribution and migrating interface models. The way in which experimental confirmation was accomplished usually involved measuring the reduction in the eutectic liquid width over brazing hold time. This was done by heating several joints to T_B and increasing the amount of isothermal hold time for each successive joint. Once the joints were cooled to room temperature, the width of the eutectic liquid width that solidified at the centerline as a result of insufficient holding at T_B was measured metallographically.

Table 1.4.2 summarizes important information extracted from a selection of interesting papers that investigated the TLPB of Ni-based superalloys using a Ni-based FM. All of the tests listed in Table 1.4.2 were performed under a vacuum atmosphere. It is also worth mentioning that the rate was never explicitly mentioned in these papers as the focus was measuring the time for complete IS for a given starting gap or filler insert width $2w_o$. In addition, most studies did not consider the influence of dissolution and a $2w_{max}$ value. For the purposes of this work the rate was calculated by dividing the original gap width cited ($2w_o$) by the square root of experimentally determined t_{IS}.

Table 1.4.2 - Summary table of experimental investigations selected from literature studying TLPB using Ni-based materials and Ni-based FM

BM	FM	$2w_0$ [µm]	T_B [°C]	k_{IS} $\left[\frac{\mu m}{\sqrt{min}}\right]$	t_{IS} [min]	Reference
IN625	**BNi-2**	77*	1052	9.20	70	[7]
Ni	**BNi-3**	51	1065	4.66	120	[22]
IN718 (Cast)	**BNi-2**	50	1050	7.91	40	[27]
Waspaloy	**Nicrobraz 150**	100	1145	5.27	360	[28]
GTD-111	**BNi-3**	25	1100 1150	2.89 3.73	75 45	[29]
IN713	**BNi-9**	40	1100	2.76	210	[30]
Haynes282	**Nicrobraz 150**	80	1100	10.32	60	[31]
IN738	**Nicrobraz 150**	100	1100 1150	4.56 5.77	480 300	[32]
Mar-M247	**BNi-9**	40	1120	5.16	60	[33]
IN600	**BNi-9**	40	1100	2.39	281	[30]
CMSX-2 (Single Crystal)	**BNi-9**	40	1100	2.22	326	[34]

*This paper used a wedge-type gap that allowed for a variable $2w_o$.

In all cases listed in Table 1.4.2, there was a linear relationship observed between the reduction of the liquid width and the square root of time. The IS process was observed to be a diffusion-controlled process, where after prolonged holding at a specified T_B, the liquid present eventually completely isothermally solidifies. These authors also often compared experimental results to predictions obtained using various previously mentioned analytical models. Despite the widespread use of these common approaches, there are a couple of main issues with this method. Due to the requirement of multiple samples held for varying times and temperatures, the approaches taken in literature are susceptible to a relatively large degree of variability and can be fairly time consuming. A more recent development is the use of DSC to study the kinetics and microstructural evolution present within a TLPB couple. These thermal analysis approaches will be discussed briefly in Subsection 1.6.1.

1.4.3 Microstructural Evolution During Transient Liquid Phase Bonding of Nickel-based Superalloys Using BNi-2 (Ni-Fe-Si-Cr-B) Filler Metal

In a fundamental study completed by Tung et al. [35], the solidification pathway observed during brazing of pure Ni using various Ni-based FM was investigated. Although BNi-2 was not directly studied, a very similar alloy, BNi-1a was investigated. BNi-1a has a higher Cr content (14 wt.%) than BNi-2 (7 wt.%). Firstly, γ-(Ni) isothermally solidified from the faying surface. The direction of the growth was into the melt from the faying surface. Upon cooling to room temperature, any residual molten FM will solidify according to traditional equilibrium alloy solidification theory. The athermal solidification begins with growth of nodular pro-eutectic γ-(Ni) dendrites at the S/L interface [35]. The growth of the primary phase results in enrichment of the melt with B, Si, Cr. Binary eutectic solidification of γ-(Ni) and Ni boride occurred with continued cooling. The formation of the binary eutectic enriched the melt with Cr and Si. This resulted in the growth of another binary eutectic consisting of γ-(Ni) and Cr boride. The remaining portion of the melt was enriched with Si, and therefore a ternary eutectic composed of γ-(Ni), Ni boride, and Ni silicide formed with subsequent cooling [35].

Pouranvari et al. [36] investigated the microstructural development during diffusion brazing of IN718/BNi-2/IN718 couples (see Figure 1.4.2). It was determined that four

distinct microstructural regions developed during the brazing process. One such region is termed the isothermal solidification zone (ISZ). Interdiffusion between the FM and BM during the hold period at T_B results in a compositional change at the interface. This driving force results in migration of the S/L interface, and the liquid begins to freeze at T_B [36]. The solid-state diffusion of B into the BM results in the precipitation of borides in the BM. This region where the BM has formed secondary intermetallic phases is known as the diffusion affected zone (DAZ) [36]. When insufficient holding time at T_B is allotted, the solidification of the residual liquid results in the formation of the athermal solidification zone (ASZ). The ASZ contains intermetallic phases with eutectic morphology [36]. The final microstructural region is known as the base metal region. This region has not been affected by the brazing process, aside from some grain growth due to time at elevated temperature [36].

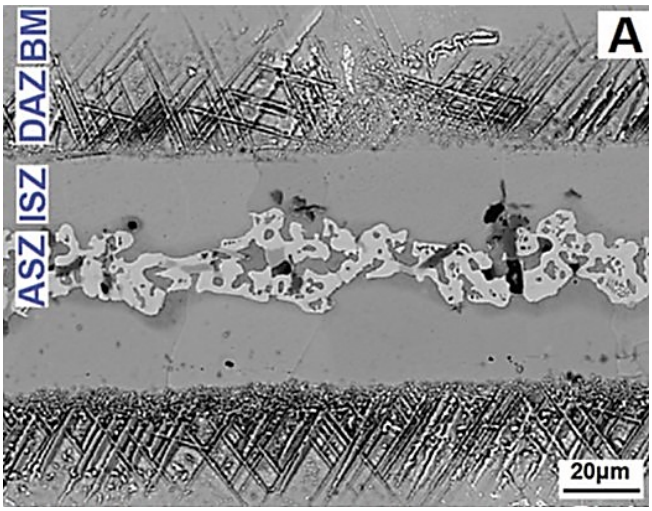

Figure 1.4.2 - Backscattered electron micrograph of joint cross section subjected to partial IS indicating various microstructural regions of interest [36]

Through a combination of optical and field emission scanning electron microscopy (FE-SEM), the identity of the various intermetallic compounds forming in the ASZ was determined. Pouranvari et al. [36] also used distribution and partition coefficient arguments to complement their conclusions. The distribution coefficient, k, represents the direction and extent of elemental segregation that occurs during the cooling and solidification of the residual liquid. Elements that possess $k<1$ have the tendency to segregate to interdendritic regions from dendrite cores, whereas $k>1$ indicates the opposite behaviour. It is a generally

accepted theoretical assumption that the first solid to form from the liquid has composition of kC_0, where C_0 is the nominal concentration of the element of interest within the alloy [36]. The distribution coefficient can be calculated as the ratio between dendrite core composition and C_0. This interpretation of the distribution coefficient is valid for equilibrium conditions, when solid-state back diffusion and undercooling are neglected. Figure 1.4.3 contains the calculated distribution coefficients for the various elements contained within IN718. Note that Pouranvari et al. [36] also determined that B would have a tendency to segregate to the liquid during cooling due to the low solubility of B within Ni indicated by Figure 1.4.1.

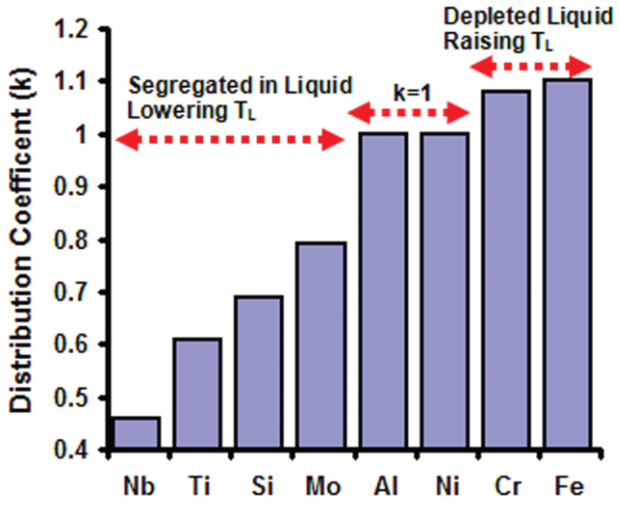

Figure 1.4.3 - Calculated distribution coefficient of alloying elements present in IN718 [36]

It was determined that the solidification pathway begins with the formation of primary γ-(Ni). The residual liquid becomes enriched with elements that have a k<1 (See Figure 1.4.3). The growth of binary eutectic Ni-rich boride and γ-(Ni) was found to follow the primary γ-(Ni) solidification. The primary γ-(Ni) growth is halted once the liquid composition at the S/L interface satisfies the three phase noninvariant eutectic reaction of L→ γ-(Ni) + Ni-rich boride [36]. It was determined that the Ni-rich boride was Ni_3B. The formation of Ni-rich boride enriches remaining melt with Si, Cr, and Mo (Figure 1.4.3). The enrichment of the melt results in a shift in the liquid composition such that the formation of a pseudo-binary eutectic of Cr-rich boride and γ-(Ni) occurs. This Cr-rich boride was enriched in Mo and based on the Cr content was determined to be CrB [36].

The remaining liquid at this point was enriched with Si, as Si tends to segregate to the liquid and has low tendency to dissolve into Ni- and Cr-rich borides. It was determined that a ternary eutectic of Ni-rich boride, γ-(Ni), and Ni-rich silicide forms. It was also found that a fine Ni_3Si phase precipitated via solid-state precipitation. This was deduced due to the decreasing solid solubility of Si in Ni at lower temperatures [36]. The phases present within the DAZ were determined to be rich in Cr, Mo, and Nb. Two different morphologies were observed in the DAZ, needle-like and blocky precipitates [36].

1.5 Wetting & Spreading

The wettability of the molten interlayer on the substrate material is an important requirement for achieving high quality braze joints. Thermodynamic and kinetic phenomena dictate the extent to which a FM /BM material system is successfully joined. The following sections will provide a brief overview of physical and chemical concepts related to the wetting and spreading of a liquid over a solid surface.

1.5.1 Surface Energy and Surface Tension

Surface energy and surface tension are two important concepts that are related to wetting and spreading, and brazing. Figure 1.5.1 can be used to illustrate the concepts of surface energy and surface tension. Particles at the solid free surface have missing "neighbors" adjacent to one side of the free surface, meaning that atoms at the surface have unsaturated bonds. Due to missing neighboring atoms, the potential energy of atoms at the surface is higher than for atoms in the bulk. The difference between the potential energies of surface and bulk atoms is defined as the surface energy, γ_{sv} [37]. The tendency of liquids to contract initiates a tensile force at the free surface known as the surface tension and is equivalent to the surface energy under isothermal conditions. Metallic materials have high surface tension due to their strongly bonded and highly coordinated metallic structures. For example, liquid water has a surface tension of 0.059 N/m, whereas liquid mercury has a value of 0.480 N/m [37]. The magnitude of the surface tension is important as it controls capillary action, and can be a controlling factor in determining the time required for wetting [38].

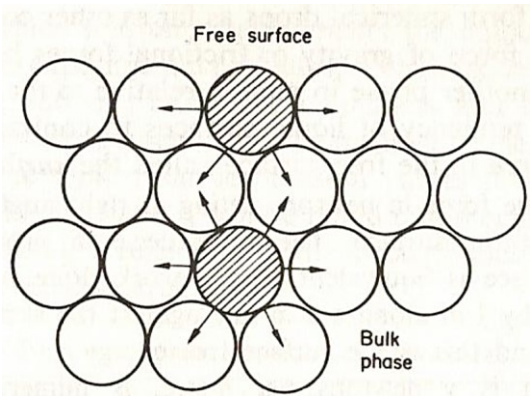

Figure 1.5.1 - Section normal to free surface of a solid phase [37]

1.5.2 Contact Angle

Wetting refers to the physio-chemical interaction between a liquid and a solid surface. From a brazing perspective, wetting refers to the interaction between the faying surface and the molten brazing alloy [39]. Figure 1.5.2 is a schematic representation of the balance of surface tensions at each interface.Young's contact angle, θ_Y, can be used to describe the equilibrium of the surface tensions of a solid-liquid-vapor system [40]. θ_Y is the angle subtended by the S/L interface and the liquid surface and can be seen in Figure 1.5.2.

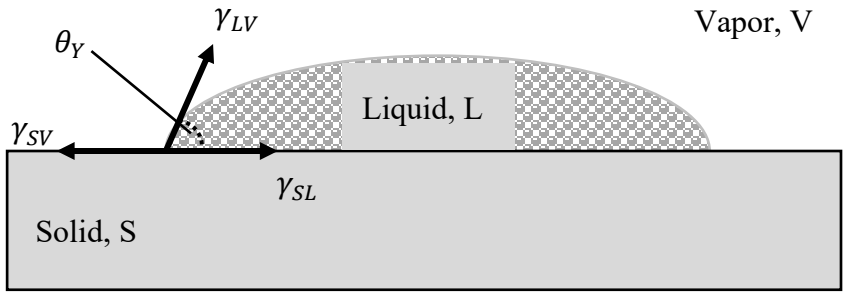

Figure 1.5.2 - Schematic of classical wetting model depicting balance of surface tension existing at solid-liquid-vapor triple point [40]

Young's equation represents the inherent ability of a non-reactive liquid to wet a flat, smooth, and chemically homogeneous solid surface, and is shown in Equation 1.5.1.

$$\gamma_{LV} cos\, \theta_Y = \gamma_{SV} - \gamma_{SL} \qquad \textbf{Eq. (1.5.1)}$$

where γ_{LV} is the surface tension between the liquid and vapor, γ_{SV} is the surface tension between the solid and vapor, and γ_{SL} is the surface tension between the solid and liquid.

Contact angles are generally measured through what is termed the sessile drop test, which involves observing and measuring the contact angle at a specified temperature.

When θ_Y is greater than 90°, the value of $\cos\theta_Y$ is negative, and the surface tension between the liquid and solid is greater than the surface tension between the vapor and the solid. This indicates that the attraction of liquid particles for solid particles is not as strong as the attraction of liquid particles to other liquid particles, meaning that the liquid does not wet the solid. If the value of θ_Y is less than 90°, the opposite is true and the liquid wets the solid [37]. Complete wetting occurs when the contact angle is equal to zero. Whereas a contact angle of 180° indicates no attraction between liquid and solid and this situation probably does not occur in real metallurgical systems [37].

According to Equation 1.5.1, decreasing θ_Y, increasing γ_{SV}, and decreasing either γ_{LV} or γ_{SL} can lead to increased wettability. γ_{LV} is related to the atmospheric pressure, and use of a vacuum atmosphere results in a reduction in the partial pressure of oxygen (O_2), and therefore a reduction in the surface tension between the liquid and the vapor [17]. γ_{SV} is related to the cleanliness of the solid surface, thus it is vital that the faying surfaces be cleaned thoroughly prior to brazing. The surface tension between the solid and liquid decreases with increasing temperature [17].

1.5.3 Wetting During Joining

Chapters 1.5.1 and 1.5.2 have dealt with wetting and spreading using classical approaches. These classical treatments of wetting and spreading are most valid for situations where the fluid flow is laminar, the surfaces are free from foreign contaminants and perfectly smooth, and that no interaction between the liquid and solid occurs. These ideal situations rarely arise during brazing of two metallic surfaces [17]. Brazing processes comprise a degree of chemical reaction between the FM and BM which leads to departures from the classical situations previously discussed. The following subsection will briefly address the concept of reactive wetting, as well as the influence of surface roughness and oxidation on wetting and spreading.

Interfacial reactions between the FM and BM result in a reaction layer with altered surface tension compared to the substrate prior to the reaction. The two most common types of interfacial reactions that occur in brazing are the formation of a new compound and

dissolution. A modified Young's equation exists to incorporate the change in Gibbs free energy associated with the formation of a reaction product layer between the FM and BM and is presented below. It is worth noting that Equation 1.5.2 is of little practical use, but serves as a good theoretical basis [17].

$$\boldsymbol{cos\theta_Y = cos\,\theta_Y^0 + \frac{\gamma_{SL} + \gamma_{SL}^0}{\gamma_{LV}} - \left(\frac{\Delta G_r}{\gamma_{LV}}\right)} \qquad \textbf{Eq. (1.5.2)}$$

where θ_Y^0 represents the contact angle after the reaction, γ_{SL}^0 is the surface tension after the reaction, and ΔG_r is the change in Gibbs free energy associated with the reaction [17].

In terms of the topography of the substrate material, the surface roughness can have an impact on the extent to which the liquid spreads out across the solid surface. For each parent material an optimum surface roughness exists where the wettability of the molten FM is maximized [17]. The roughening of surfaces has two main impacts on wetting and spreading and they are the pinning of the solid-liquid-vapour triple line due to presence of sharp defects and an increase in surface area [40].

From the perspective of triple line pinning, sharp defects can pin the triple line at location that is significantly removed from its equilibrium position. When wetting on the smooth surface is poor to begin with, the surface roughness impact on wetting is dominated by the triple line pinning phenomena [40]. In terms of the increase in surface area, this can have either positive or negative effects depending on the composition of the FM and BM to be used in the brazing process. An increase in surface area can result in increased wettability if the Young's contact angle is already low between the FM and BM [40]. If there is a large degree of interaction between the FM and BM, then an increased roughness can have adverse effects on the wetting and spreading [17]. In a system where wettability on the smooth substrate results in low contact angles much less than 90°, the surface roughness effect on wetting is dominated by the increased surface area [40]

The preferential roughening of a surface can result in formation of fine grooves that act like capillary channels. The presence of these fine grooves can result in an increased capillary force. Furthermore, the flow of molten FM will be parallel to the direction of the fine grooves if the roughening is done such that the grooves are unidirectionally oriented

[17]. An increase in surface roughness can also result in a reduction of the effective contact angle, θ^*. θ^* is determined by multiplying the Young's contact angle by the roughness factor S_r, which is the ratio of the actual area to the planar area [40].

Lastly, oxidation of both the interlayer and the substrate material can have a drastic effect on the extent to which the molten FM wets and spreads the BM faying surface. In a review of TLPB written by Gale and Butts [10], it is stated that liquid metals generally have very poor wettability on oxide surfaces. It turns out that very few brazing materials can wet oxides. Despite TLPB being carried out in vacuum furnaces, in some cases the O_2 content present in commercial furnaces is much greater than the partial pressure of O_2 at which the oxide layers would decompose [41]. Thus, in order to achieve a sound braze joint where the FM fills the gap completely, the process must be designed such that oxide films are disrupted, destabilized, or removed all together [40].

Oxide layers that form on the FM act as a "container" and restrict the wetting of the interlayer [10]. However, it has been shown by Gale and Wallach [22] that in the case of Ni-based interlayers, that the volume change associated with melting is sufficient to fragment the thin oxide skin and the flow of liquid metal continues. Another possibility is that the oxide layer can be entrapped at the S/L interface, which can act as a diffusion barrier and inhibit any reaction-driven spreading [10].

In terms of substrate oxide layers, a low surface energy oxide is present as the molten droplet attempts to spread. Two mechanisms associated with the promotion of spreading of molten metal on a substrate oxide are reduction and undermining. The reduction is the chemical reaction that reverses the oxidation process and results in formation of a new metallic surface. Dissolution of the BM can release reactive elements into the melt that can promote the reduction of surface oxide layers [10]. The undermining process consists of penetration of the molten FM into defects present in the oxide layer and subsequent spreading along the substrate-oxide/substrate-metal interface [41].

1.5.4 Surface Preparation Used in Brazing

The previous subsection placed great emphasis on the importance of FM wettability on the BM substrate, it also stressed that oxidation and other surface characteristics can influence the success and strength of the braze joint. It is common practice in joining procedures to

conduct a series of surface preparation steps prior to the actual brazing procedure to alleviate or prevent the adverse effects that a poorly prepared surface can have on a braze joint.

The ASM Handbook: Vol. 5 Surface Engineering defines the term surface engineering as "treatment of the surface and near-surface regions of a material to allow the surface to perform functions that are distinct from those functions demanded from the bulk of the material." [42]. According to *AWS C3.6M/C3.6:2016, Specification for Furnace Brazing*, "the faying surfaces and adjacent areas of components to be brazed shall be free of oil, grease dirt, oxides, paint, scale, or other foreign substances that can interfere with the brazing process or contaminate the braze joint" [43]. The presence of foreign contaminants on the faying surface can lead to FM wetting and spreading complications, which can have detrimental effects on the quality of joint achieved [3]. Surface preparation methods are utilized in brazing to remove contaminants and prevent oxidation. These surface preparation steps can be divided into three main categories which are; cleaning, roughening, and plating.

The purpose of the cleaning step is to prepare the surface for subsequent treatment. Clean surfaces are required to ensure that a strong joint of uniform properties is formed. The cleaning process is responsible for removing contaminants such as dirt, grease, oil, and mill scale from the faying surface. These contaminants are undesirable as they can potentially hinder molten FM wetting and spreading. Many different cleaning methods are commonly employed during brazing operations such as solvent cleaning, vapor degreasing, emulsion cleaning, aqueous cleaning, electrolytic cleaning, and acid cleaning and pickling. The combination of cleaning methods chosen depends on the nature of the contaminant as well as the base material to be cleaned [3]. Generally, more than one type of contaminant will be present on the surface, and thus a combination of cleaning steps is required to successfully remove all the contaminants present.

Acid cleaning will be focused on as it was the cleaning method used for the purposes of the experiments carried out in this study. Acid cleaning removes surface contaminants through the means of chemical reactions. Acid cleaning involves soaking in mixtures of

mineral acids and acid salts to remove oxides and light metals. This method is an aggressive disrupter of oxides and contaminants [3].

Once the removal of all organic contaminants and oxides is complete, the roughening stage is performed. Roughening is usually achieved through means of a blasting process where spherical metallic or ceramic particles impact and roughen the faying surface. Blasting serves to clean the BM faying surface and impose a surface roughness on the BM substrate which can improve wetting and spreading of molten FM and help facilitate subsequent plating operations. Blasting is also an effective way to further remove any remaining oxide on the faying surface that the initial cleaning process did not eliminate [3].

Once the faying surface has been cleaned and roughened, the last step is to treat the surface. This stage involves modifying the surface of the BM to contain a layer of different chemical composition. Surface treatments in general are beneficial to the brazing process because of the induced adherence of the liquid FM film and improved wetting. Pre-coatings are applied through methods such as electrodeposition, hot dipping, thermal spraying, and cladding. For materials containing stable oxide formers, such as Al and Ti in IN718, pre-coatings are applied to ensure wetting and spreading during TLPB [3]. According to *AWS C3.6M/C3.6:2016, Specification for Furnace Brazing*, "nickel plating is recommended on the braze joint areas of stainless, corrosion-, or heat-resistant alloys having equal or greater" than 0.40 wt.% Al or Ti (0.7 wt.% Al and Ti) [43].

1.6 Differential Scanning Calorimetry

Differential scanning calorimetry (DSC) is a thermal analysis (TA) technique capable of detecting and quantifying transformations in materials occurring due to an increase in temperature. The most common use for DSC instruments is to characterize energy associated with material transformations as a function of time and temperature. These transformations are thermally activated and are known as thermal events. A variety of thermal events can be studied while consuming small quantities of material and time using TA instruments [44]. Examples of analysis capabilities that can be studied using DSC include melting, recrystallization, solidification, phase transitions, phase diagram determination, specific heat capacity, and solid-solid transitions.

There exist different DSC instrument designs, but the heat flux type DSC will be the focus of this thesis [44]. Figure 1.6.1 shows a schematic of a typical heat flux DSC instrument. Where S and R denote the sample and reference crucible/material respectively.

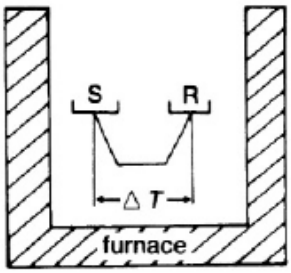

Figure 1.6.1 - Schematic of a heat flux DSC [45]**.**

The material of interest is placed into a crucible and exposed to a programmed thermal profile. An identical crucible to the sample crucible is also placed within the furnace of the instrument and is known as the reference crucible. In a heat flux DSC instrument, the thermocouple is situated within a stage or a sample carrier and measures the difference in temperature as shown in Figure 1.6.1.

Figure 1.6.2 contains a schematic that illustrates how a signal is generated within a heat flux DSC instrument. Through application of a constant power source, the heat flux instrument maintains a relatively linear increase in temperature with time, and the sample and reference are heated and cooled at approximately the same rates. Since the thermocouple is connected to the sample and reference sensor areas, the temperature of the sample and reference, as well as the temperature difference, can be measured. Due to the thermal mass being larger in the sample side, the temperature rise in the reference side is generally faster than the sample side during heating of the DSC furnace. As seen in Figure 1.6.2, the sample and reference exhibit parallel behaviour until the occurrence of a thermal event. During the thermal event, the temperature of the sample remains constant while the reference side continues to increase at a constant rate. Upon termination of the thermal event, the temperature of the sample side continues to increase at a constant rate. The lower portion of Figure 1.6.2 shows the differential thermal signal of the two temperature curves. In the case shown in Figure 1.6.2, the area of the peak represents an endothermic melting process [46].

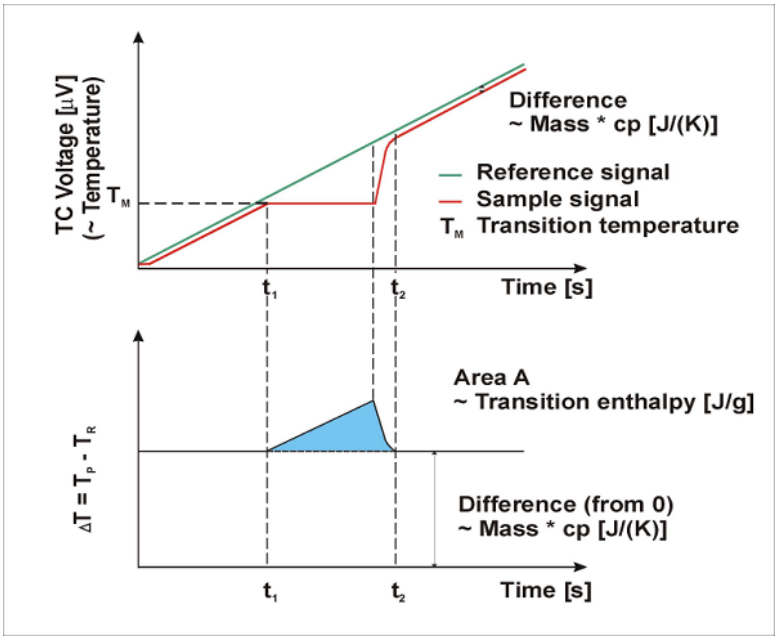

Figure 1.6.2 - Schematic depicting signal generation within a heat flux DSC [46]**.**

Figure 1.6.3 is a hypothetical thermogram that could be generated by a DSC. Thermograms have heat flux on the y-axis and temperature or time on the x-axis. The thermal baseline is the natural thermal drift present within the heat flux DSC instrument without the sample [47]. The thermal baseline is extrapolated over thermal events to serve as an aid in interpreting results and obtaining meaningful conclusions. When the resultant heat flow is zero, the thermal baseline of the thermogram is relatively flat due to a minimal increase in power to maintain sample and reference at the same temperature. During the melting of a material, an input of heat is required and thus the process is endothermic, and a positive peak can be observed on the thermogram. Whereas during solidification heat is released and the process is exothermic.

There may be a slight fluctuation about a certain heat flow value, or the baseline may have a slight endothermic or exothermic drift depending on the combined thermal characteristics of both the DSC and thermal masses within it. Correction files are used to subtract the thermal baseline of the system from the DSC signal. Correction files are obtained through a similar process used for calibration, except the test is performed without the material in the sample crucible [44].

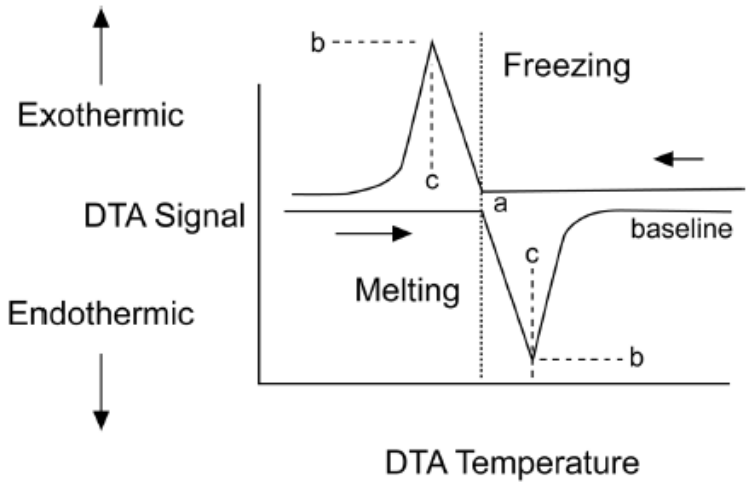

Figure 1.6.3 - Schematic of Thermogram from a Heat-Flux DSC [47]

For accurate and reliable DSC results, it is vital that appropriate calibrations have been completed using the exact experimental conditions and setup to be used for the study. Calibration of the DSC is done through use of standard reference materials. The standard reference needs to be a material that is well characterized, has high purity, and possesses a thermal event occurring over approximately the temperature range of interest. It is widespread practice to make use of multiple standard references offered by the instrument manufacturer. Indium, zinc, bismuth, and tin are some common materials used as standard reference materials [48]. By melting a set of standard reference materials, the relationship between temperature and thermal offset in the instrument can be determined [44].

The interpretation of thermograms output from DSC instruments can be greatly influenced by sample characteristics, purge gas, crucible material. A larger sample mass produces a larger peak signal but also results in shifting the temperature that the signal returns to baseline to higher temperatures [47]. Cylindrical disks of approximately 1 mm thickness with flat surfaces are the ideal sample geometry characteristics. Good contact between sample and the base of the crucible is vital for quantitative enthalpy analysis [49]. High purity inert gas is generally used to reduce the effects of oxidation present in the atmosphere of the DSC furnace. In some cases, a zirconium getter is used during DSC tests to further reduce the O_2 content within the atmosphere. The choice of the purge gas impacts the thermal transport within the DSC based on the thermal conductivity of the fluid. Many crucible types are available such as high purity alumina, zirconia, and yttria. An oxide

crucible manufactured from a material that is negligibly reduced by the sample is the ideal choice. The shape of the peak is influenced by the mass and heat conductivity of the crucible. [49] Crucible lids are effective in preventing radiation losses and maintaining a constant temperature within the crucible [47].

1.6.1 Using Differential Scanning Calorimetry to Study Isothermal Solidification During TLPB

Ruiz-Vargas et al. [50], [51] made use of TA to investigate the microstructural development in TLPB of Ni using BNi-2. The results showed that brazing kinetics can be studied using TA. They also found that a linear relationship exists between residual liquid at the end of brazing and the square root of the surface of the exothermal peak detected on cooling [50]. Many other TLPB systems have been studied by other research groups including Ag BM with Ag-Au-Cu FM , Ag BM with Ag-Cu FM, Cu with Ag-Cu FM, and Ni BM with Au-Ge FM [52]–[54]. Weyrich and Leinenbach [54] used a cyclic DSC method which allowed for greatly improved experimental conditions.

A DSC technique capable of quantifying the TLPB of Ag-Cu binary system was developed by Kuntz et al.[53]. The eutectic solidification enthalpy on cooling was measured as function of isothermal braze time. The rate of IS (k_{IS}) and t_{IS} were successfully determined, but this approach still required the use of multiple samples. Corbin et al. [55] developed a similar TA technique to investigate Al furnace brazing. This method made use of a single TLPB sample, that was exposed to a cyclic thermal profile. The determined k_{IS} and t_{IS} were validated through a series of interrupted DSC tests. It was found that the information obtained from the cyclic DSC method can be used to effectively measure kinetics of the TLPB process using a single sample. By implementing a cyclic TA approach with one sample, experimentation time and sample to sample variability can greatly be reduced.

Murray et al. [56] applied the cyclic method to the IN625/BNi-2 system. This study was successful in developing an IS curve for the system using one DSC experiment and a single sample. The IS curve was used to determine the TLPB kinetics of the investigated system. DSC analysis also revealed that rapid diffusional solidification during heating results in formation of solid solution Ni before T_B is reached. As previously mentioned, this phenomenon is termed initial solute uptake, or in the case of Ni-based superalloy brazing,

IBU. Initial solute uptake was also observed by other researchers [16], [23], [51], [57]. The importance of considering solute diffusion during the initial heating stage was emphasized in review papers written by Zhou et al. [15] and MacDonald et al.[12]. The IBU occurs due to the high diffusivity of interstitial MPD elements such as B.

CHAPTER 2 Research Scope & Objectives

Despite the importance of surface preparation to Ni-based superalloy brazing, it has generally not been studied in the scientific literature. Almost all authors that have studied the details of superalloy TLPB presented in Table 1.4.2 have used surface grinding and solvent cleaning to prepare BM for brazing. While this approach generally leads to good wetting by the molten FM, it does not represent the commercial/industrial method of surface preparation as described as described in Section 1.5.4. Arafin et al [7] did examine the TLPB behaviour of BM with an industrial surface preparation. However, without comparison to other surface preparation stages and types, it was not possible to isolate the influence of surface preparation on the details of the TLPB process.

IN718 is more susceptible to oxidation and therefore experiences greater wetting issues during brazing compared to other Ni-based superalloys. Therefore, motivation exists to investigate the surface preparation of IN718 to effectively optimize the brazing process. Further examination of how surface preparation influences spreading and wetting of molten BNi-2 is anticipated to give insight of surface reactions that potentially promote IBU. Despite their effectiveness, aerospace manufacturers still do not have a comprehensive knowledge of the true reasoning behind the relationship between surface preparation and TLPB of IN718 with BNi-2.

One of the primary goals of this study was to determine if the TA approach used by Murray and Corbin [56] can capture the effect Ni plating has on the TLPB process. To develop an understanding of the plating's effect, the TLPB behavior of wrought IN718 also had to be quantified. TA used in parallel with microstructural examination can be a powerful tool to help develop a fundamental understanding of how Ni plating influences the TLPB process.

The cyclic DSC approach was employed to determine the k_{IS}, extent of IBU, and t_{IS}. This approach also gave insight on how Ni plating affects the development of metallurgical contact between IN718 and BNi-2; the magnitude of initial B uptake (IBU), and the spreading and wetting of molten BNi-2 on BM surface.

The main goals of the thesis were to develop a fundamental understanding of how surface preparation influences a) the development of metallurgical contact between IN718 and

BNi-2, b) magnitude of IBU, and c) the kinetics of IS, and d) spreading and wetting of molten BNi-2 on IN718 BM surface. Extensive efforts were made to achieve these goals using TA techniques coupled with a variety of other metallurgical investigation methods.

CHAPTER 3 Experimental Procedure

The work completed for this thesis is divided into three sets of experiments. SET I is a general study using DSC to determine the kinetics of the TLPB process of IN718 (AMS 5596) BM using BNi-2 FM and a standard lab-based surface preparation commonly used by other researchers (Chapter 4). SET II investigated the effects of base metal surface preparation on the wetting and spreading of molten BNi-2 using an undersized FM (Chapter 6). The final group of tests, SET III, involved using the DSC to study the influence of surface preparation on the kinetics of the IS process (Chapter 7).

3.1 Materials

BM used in SET I was IN718 sheet metal obtained from McMaster Carr. Base metal ingots used in SET I will be referred to as in-house surface prepared (ISP) ingots. Cylindrical ingots with a diameter of approximately 4.76 mm were sectioned from a rolled sheet of IN718 (1.64 mm thick) via wire electrical discharge machining. The average mass of the BM ingots was 232.71 ± 2.50 mg. Disks of equivalent diameter were punched from a sheet of amorphous BNi-2 foil (50 μm thick). The average mass of FM discs was 6.12 ± 0.10 mg.

The base metal ingots used in SET II and III were obtained from Pratt & Whitney Canada (P&WC). Six different surface preparation routes were studied to examine the effects of BM surface preparation on the TLPB of IN718 with BNi-2 FM. Surface preparation of the BM was performed on-site at the P&WC facility. The different processing routes are outlined in Table 3.1.1.

Table 3.1.1 - Base metal surface preparation legend

Sample I.D #	Surface Preparation Processing Route		
	Cleaning	**Roughening**	**Ni Plating**
1	Acid Cleaned (AC)	---	---
2	AC	Nicroblast™ (NiCr)	---
3	AC	NiCr	Nickel Flash (Ni(F))
4	AC	NiCr	Nickel Brush (Ni(B))
5	AC	---	Ni (F)
6	No Prep		

Square samples (3.9 X 3.9 mm) of surface prepped IN718 were sectioned from the provided stock sheet (1.92 mm thick) using a Struers slow speed saw equipped with a cubic boron nitride blade. Areas approximately 1 mm from the edge of the IN718 sheets were not used for brazing as the thickness of the sheet was tapered. A mineral oil-based coolant was used to act as a lubricant to mitigate microstructural damage and reduce wear on the blade. This sectioning procedure was successful in preserving the engineered surface of the base materials. Surface prepared samples were always handled with gloves and stored in a desiccant cabinet to preserve the surface condition imposed by the various pre-treatment routes. The average mass of BM ingots in SET II was 228.81 ± 7.79 mg. While the average mass for the BM ingots used in SET III was 220.80 ± 3.80 mg.

SET II used undersized FM foils sectioned from the BNi-2 foil using a pair of handheld sheet metal shears. The average mass of these FM squares was 0.97 ± 0.06 mg. For experiments in SET III, FM squares of approximately the same cross-sectional area as the base metal were sectioned using the same shears. The average mass of these FM squares was 5.00 ± 0.20 mg.

Acid cleaning was accomplished in accordance with AWS C3.6M/3.6:2016. Some samples were subjected to a roughening step using a NiCr blast media. NiCr is a commercial blasting grit composed of Ni, Fe, and Cr. Finally, plating procedures were accomplished in one of two ways, a flash or brush procedure. The Ni(F) operation is an electrolytic deposition of a thin layer of Ni onto the base metal faying surface. Whereas, the Ni brush operation is a more localized coating of Ni that was applied using a brush to paint the Ni onto the surface.

The chemical compositions of the materials used in this study are listed in Table 3.1.2. BM composition was determined via EDS, and the FM composition was determined via inductively coupled plasma optical emission spectroscopy (ICP-OES). The chemical compositions listed in AMS 5596 (IN718) and AMS 4777 (BNi-2) are also included in Table 3.1.2 for reference.

Table 3.1.2 - Chemical composition of materials used in TLPB couples

Material	Chemical Composition [wt.%]								
	Ni	**Fe**	**Cr**	**Al**	**Ti**	**Nb**	**Mo**	**Si**	**B**
ISP	54.0	18.4	17.7	0.5	0.9	5.3	3.1	---	---
P&WC	53.9	18.0	18.3	0.4	0.9	5.1	3.4	---	---
BNi-2	82.2	3.3	7.4	---	---	---	---	4.0	3.2
AMS 5596	50.0-55.0	Balance	17.0-21.0	0.4-0.8	0.6-1.1	5.0-5.5	2.8-3.3	---	0.006
AMS 4777	Balance	2.5-3.5	6.0-8.0	---	---	---	---	4.0-5.0	2.75-3.5

3.2 DSC Experiments

DSC was the primary investigation method employed in this study to simulate the TLPB process. TLPB of IN718/BNi-2 was simulated using a Netzsch DSC 404 F1 Pegasus® (see Figure 3.2.1). It comes equipped with a platinum furnace and can operate within the temperature range of 20 - 1500 °C. Optimum atmosphere is achievable through use of a purge gas, vacuum pump, and O_2 trap system. The purge gas can be supplied at various rates to the instrument via a mass flow control system.

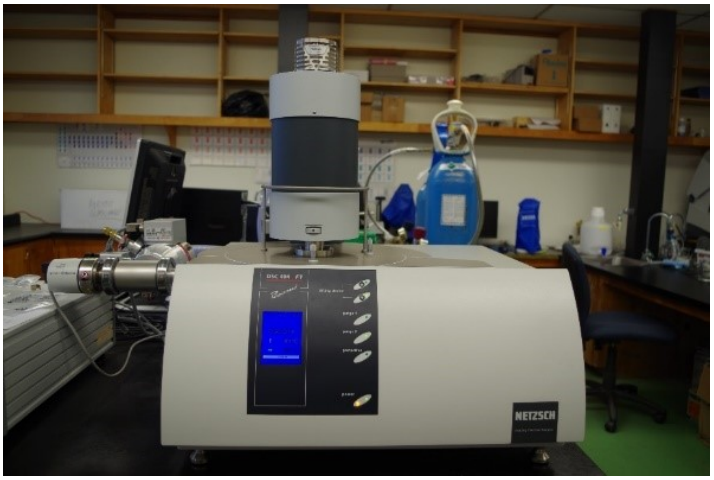

Figure 3.2.1 - Netzsch DSC 404 F1 Pegasus® used for thermal analysis experiments

Two different approaches were employed for the DSC experiments in SET I, a cyclic and an interrupted method. The first method was a DSC test using a cyclic heating profile (shown in Figure 3.2.2). The selected maximum temperature is sufficiently high enough to ensure that the FM completely melts and effectively spreads over the BM surface. The maximum and minimum temperatures are 50 ℃ below measured liquidus and solidus temperatures of BNi-2 foil respectively.

Each cyclic test in SET I was carried out for 20 cycles (N=19 in Figure 3.2.2) in an attempt to completely isothermally solidify the FM. Six trials were completed for the cyclic runs to determine the variability. The interrupted method involved heating a FM foil in contact with a BM ingot to 1050°C and varying the isothermal hold time period (between 0-210 minutes). Two trials per isothermal hold time were completed to investigate the repeatability. The purpose of the isothermal hold experiments was to confirm the validity of using the cyclic method.

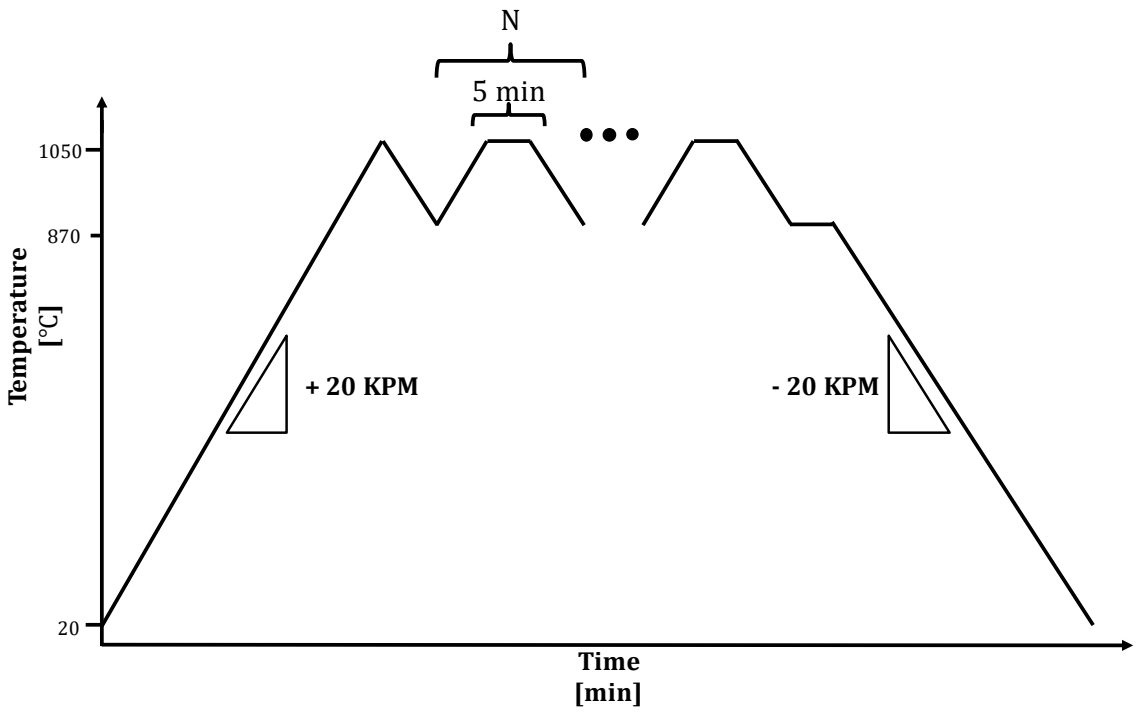

Figure 3.2.2 - Temperature profile used for cyclic DSC experiments

The sample was arranged within the crucible as shown in Figure 3.2.3. The use of an alumina sample crucible was previously shown to prevent chemical interaction with brazing materials and wetting with the FM [56]. This setup is referred to as the half-joint configuration, and it has been shown that the kinetics of a full TLPB joint can be determined using this experimental setup [52], [53], [56], [58]. Simulation of the phenomena observed in a full TLPB joint can be achieved with this configuration. Also, by placing the FM on the bottom, optimization of the DSC signal is accomplished. As previously discussed, the crucible holder is placed directly above the thermocouple responsible for measuring the temperature difference between reference and sample crucibles. Therefore, it is ideal to have the FM as close as possible to the thermocouple to reduce thermal lag. Increased thermal lag within the system can add difficulty into separating instrumental artifacts from real thermal events.

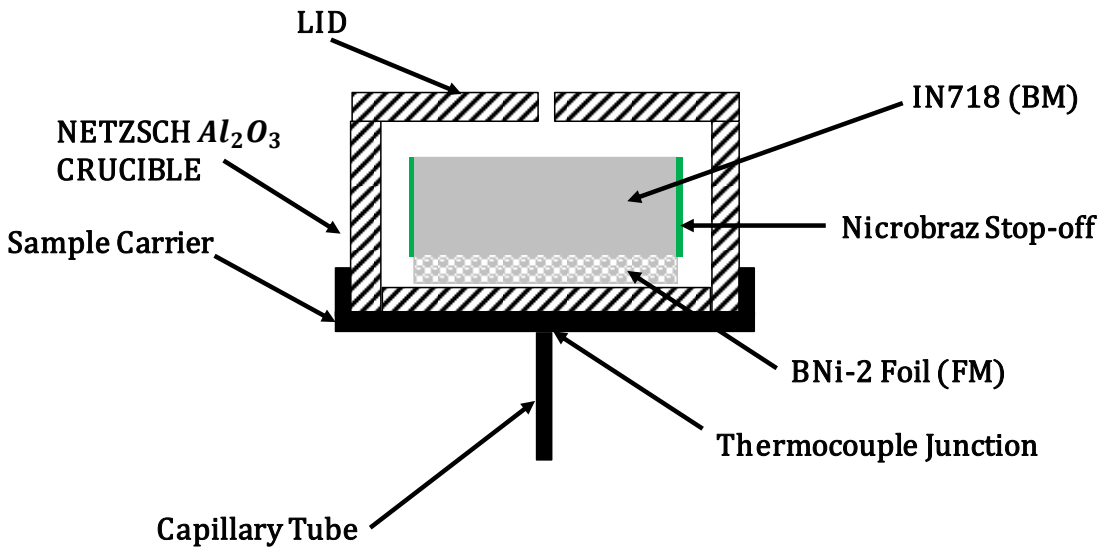

Figure 3.2.3 - Schematic of half-joint configuration used in full foil coverage DSC experiments

An alternative sample arrangement was adopted for SET II. For this alternative arrangement, the foil was placed on top of the surface prepared IN718 ingots. The main objective of this arrangement was to observe the difference in wetting and spreading of BNi-2 against the various surface prepared IN718 faying surfaces. Only a cyclic DSC approach was used in SET II, using the same thermal profile in Figure 3.2.2. Two trials were done for each surface preparation type using 2 cycles (N=1 in Figure 3.2.2). A third test was done using up to 8 cycles (N=7 in Figure 3.2.2) in an attempt to reach completion of IS. A stereoscopic image was taken before and after brazing to document the change in coverage area, which was a quantification of the extent of wetting and spreading experienced by the FM on the various surface preparations.

SET III used the same thermal profile shown in Figure 3.2.2, using 20 cycles (N=19). The same sample arrangement shown in Figure 3.2.3 was used for the surface preparation experiments.

No correction file was required since the peaks were large and sharp, such that they were easily discernible from the relatively stable thermal baselines during the DSC experiments. Appropriate instrument calibrations were completed prior to testing for both the temperature and sensitivity. This was accomplished by melting different pure metals (In,

Sn, Bi, Al, Ag, Au, and Ni) using the DSC. It is important to note that the calibration was conducted using the same experimental conditions used in this study (heating/cooling rate, sample/reference crucible material, atmosphere, etc.).

For SET I only, the faying surface of the base metal was ground using 500 grit SiC papers (Struers). This was done to remove a degraded surface layer that resulted due to the machining process. SET II and III were not ground with the SiC paper in order to preserve the commercially prepared surface treatments. The following steps were completed prior to DSC testing in all experiments (SET I – III). The sample crucible, base metal, and FM were cleaned using acetone in an ultrasonic agitation cleaner. The aim of this basic surface preparation was to remove surface oxide layers present and provide a clean surface for the liquid FM to wet. A commercial stop-off agent, known as Nicrobraz Stop-off ™, was applied to the sides of the BM ingots. This stop-off agent is a solvent-based ceramic suspension that inhibits wetting of the molten FM. By applying this coating to the sides of the ingot, the interaction between the filler and base metal is restricted to the faying surface.

The mass of the FM was input into the software as the sample mass. The heating chamber of the DSC was evacuated using a turbo vacuum pump to a pressure of approximately 1.9 E-5 mbar, and subsequently backfilled using dynamic 99.999 % argon (max flow rate of 244 ml/min). The test was conducted under a dynamic argon atmosphere, with a gas flow rate of 50 ml/min used during testing. A zirconium "getter" ring combined with a radiation shield improves removal of residual O_2 (below 2ppm) in the gas atmosphere.

One of the main tools that can be obtained through using DSC to study IS are isothermal solidification growth rate plots. These plots can also be referred to as maximum brazing clearance (MBC) plots when they are applied to practical brazing conditions. An MBC plot allows one to obtain an understanding of the magnitude of IBU, k_{IS}, and t_{IS} in a Ni-based TLPB couple.

The heating and cooling segments are separately analysed in Proteus® Software for Thermal Analysis created by Netzsch. During melting and solidification of BNi-2, an endothermic and exothermic peak is registered on the DSC signal. The solidification enthalpy for each cycle is measured in Proteus®, and is the first piece of information provided by the DSC required to generate an MBC plot.

Next, the liquid duration time for each cycle is required for the MBC plot. The liquid duration is determined in Proteus® by calculating the time elapsed from the onset of the melting peak until the termination of the solidification peak, as shown in Figure 3.2.4.

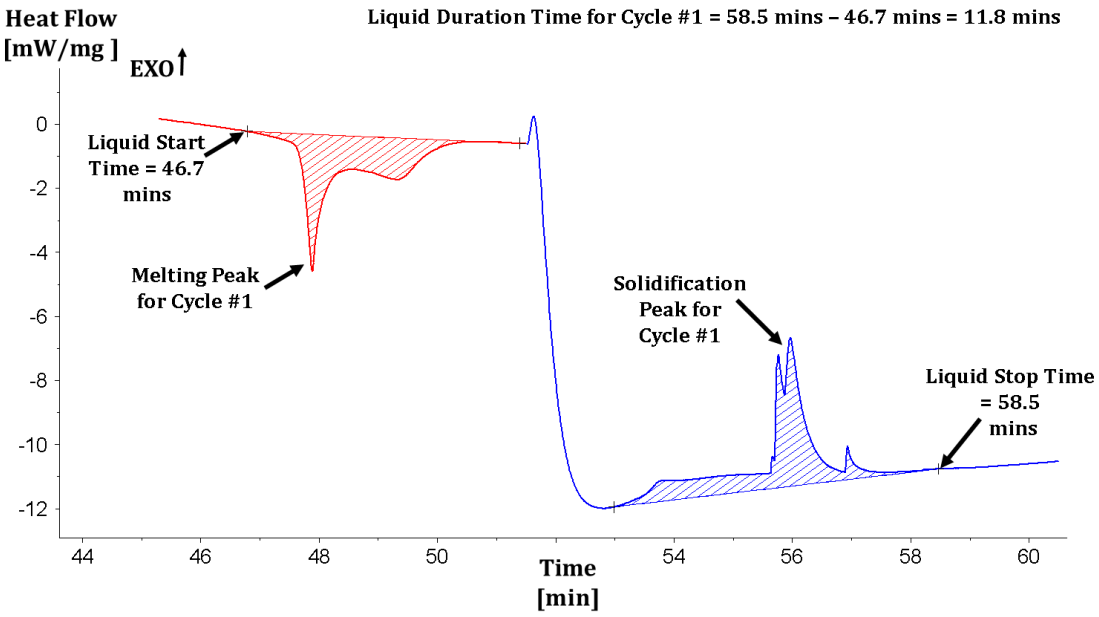

Figure 3.2.4 – Determination of liquid duration from a DSC trace

Once the solidification enthalpy and liquid duration is determined for each cycle, the first steps towards generating an MBC curve are completed and optical microscopy (OM) must be conducted to complete the analysis. Details on how the MBC plot is generated will be further explained in Chapter 4.

3.3 Metallographic Analysis

Initial surface characterization of the as received pretreated IN718 samples was completed using FE-SEM, EDS, OM, and surface profilometry. An initial study of the surface imposed by the various preparation methods is critical to ensuring that the results collected are not potentially biased due to poorly prepared surfaces. The post DSC TLPB half-joints were also examined using FE-SEM, EDS, and OM.

Prior to observation under the various microscopes, sample preparation was conducted in order to properly observe the microstructure. The following steps were conducted prior to capturing images with either the OM or the FE-SEM. Post DSC tested samples were

mounted in a conductive resin (Struers PolyFast) using a Struers automatic mounting press. Prior to mounting, samples were rinsed in acetone. Once mounted, the samples were ready for subsequent grinding and polishing steps using a semiautomatic machine produced by Struers. First, samples were ground using SiC grinding paper of increasingly higher grit number (#220, #320, #500 grit size FEPA P). Samples were ground approximately halfway into the ingot, so that the cross section examined would have maximum FM wetting across the faying surface.

Next, samples were polished using various Struers diamond suspensions (9 μm, and 3 μm) and the appropriate polishing disk. Final polishing was accomplished using a colloidal silica suspension (0.04 μm) and an oxide polishing cloth made from porous neoprene. In some cases, samples were etched using waterless Kalling's No. 2 reagent, which is a common general-purpose etchant used for Ni-based superalloys. The components of Kalling's are a mixture of hydrogen chloride, ethanol, and cupric chloride. It will be indicated within the figure caption if a particular micrograph contains a sample that was etched.

Once the samples were properly prepared, the cross section of both as received BM and post DSC TLPB half-joints were examined using a Zeiss Axiotech 100 HD reflected light optical microscope. This microscope uses 5x, 10x, 20x, 50x, and 100x objective lenses to achieve magnifications of up to 1000x. Proper calibration for the objective lenses was achieved using a laser etched stage micrometer. Various measurements were made on the obtained micrographs using an image analysis software called ImageJ. Post processing of obtained micrographs was also accomplished using Image J. The post processing steps applied to images included sharpen, adjustment of brightness and contrast (if required), scale bar application, and stitching. Sharpen simply increases the contrast and accentuates detail within the image. Stitching is a macro that automatically stiches multiple images together to create a composite image capturing a larger field of view.

In certain cases, samples were examined using a Hitachi S-4700 FE-SEM, equipped with an Oxford X-max (80 mm^2) energy dispersive spectrometer (EDS). This system is capable of qualitative and quantitative chemical analysis of elements with atomic number of B and higher. The X-ray radiation detector was a Si drift detector. Calibration of operating

parameters was accomplished by using the IN718 BM and confirming that the nominal composition was determined to be within the range cited by the supplier. The accelerating voltage and emission current used for the EDS analysis was 15 keV and 15 µA respectively. In cases where EDS mapping for B was conducted, a lower accelerating voltage of 5 keV was used.

Profilometry was accomplished using a VK-X1000 laser scanning confocal microscope (LSCM) manufactured by KEYENCE. ASME B46.1: Surface Texture (Surface Roughness, Waviness, and Lay) was followed for the procedures and analysis methods for surface profilometry.

In order to measure the surface roughness of the various pretreated IN718 BM, 10 micrographs were randomly captured using the LSCM. The micrographs were taken with the LSCM using the 50x objective lens which results in magnification of 1000X. The area of each micrograph was roughly 1.2 mm^2. Areas approximately 1 mm from the edge of the IN718 sheets were not analysed as the thickness of the sheet was tapered and not used for brazing purposes. Post processing of micrographs and surface roughness determination was accomplished in Multifile Analyzer software created by KEYENCE. In terms of post processing, each image was subject to a filtering process where the "reference plane" was determined and set to be the horizontal plane that is at 0 µm. All the "height" data collected from the instrument is converted to a surface roughness measurement with respect to the reference plane. The surface roughness measurement of interest was an area parameter, and is termed the average roughness, S_a. According to ASME B46.1, S_a represents "the arithmetic average of the absolute values of the measured height deviations from the mean surface taken within the evaluation area" [59].

CHAPTER 4 Using Differential Scanning Calorimetry to Study the Transient Liquid Phase Bonding Behaviour of IN718/BNi-2

4.1 Thermal Analysis

4.1.1 BNi-2 Foil Alone and Diffusion Barrier Experiments

To establish the behavior of the FM, the BNi-2 foil was heated to 1050°C and cooled to room temperature (±20 kelvin per minute) using the DSC. The DSC trace for the heating segment is shown in Figure 4.1.1.

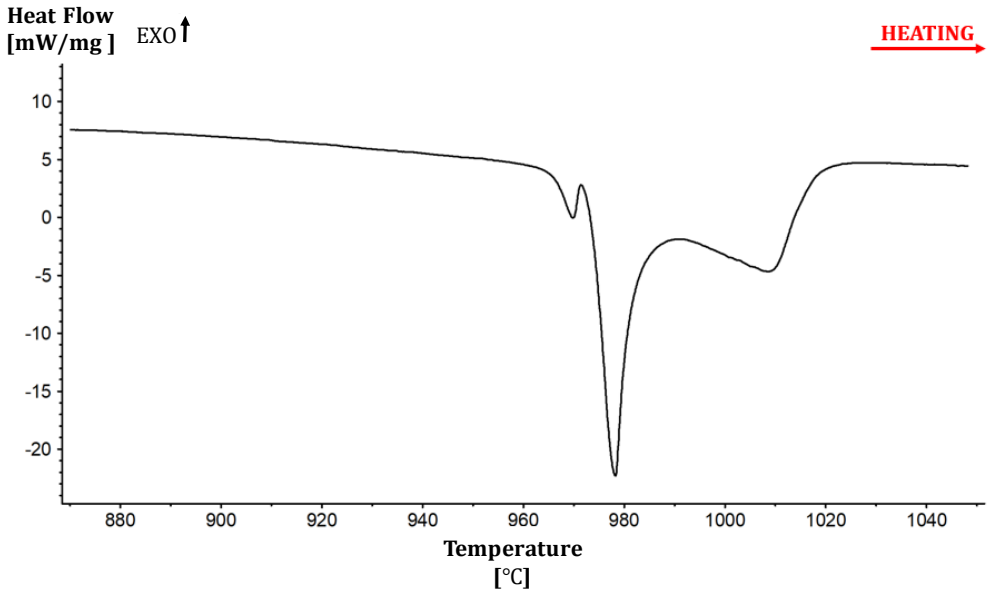

Figure 4.1.1 - DSC thermogram depicting melting endotherm associated with BNi-2 foil

Three endothermic peaks were present on the DSC trace during the first heating segment. These peaks are associated with the melting of the BNi-2 foil. The onset temperature of the first melting event was measured as approximately 965°C. Endothermic peak temperatures were determined to be 969°C, 978°C, and 1010°C. Interrupted DSC testing conducted by Murray et al. [56] determined that a large degree of melting occurs after the second peak (approximately 978°C). Three exothermic peaks are observed on the DSC trace during cooling to room temperature. These peaks are associated with the solidification of the molten BNi-2 foil.

The enthalpy of solidification is an important measurement that is required when using DSC to study the kinetics of TLPB. Under the current experimental conditions, the average enthalpy of solidification for the BNi-2 foil was measured to be 279 ± 12 J/g (six trials). As pointed out by Kuntz et al. [53] and Murray and Corbin [56] , the heat sink effects of the base metal can alter the enthalpy measurements of the FM. A diffusion barrier experiment was conducted to obtain an enthalpy of solidification value for BNi-2 in thermal contact with an IN718 base metal ingot. The faying surface of the ingot was coated with a thin layer of Nicrobraz^{TM} stop-off pen to act as a diffusion barrier and allow for a corrected measurement of the FM solidification enthalpy. An average value of 221 ± 17 J/g was measured for the solidification enthalpy during three diffusion barrier experiments. Figure 4.1.2 shows typical DSC traces on cooling for the FM alone and diffusion barrier experiments. Note that the curves have been shifted in the y-axis for clarity. This will be the case when more than one DSC trace is shown on a thermogram in the preceding chapters.

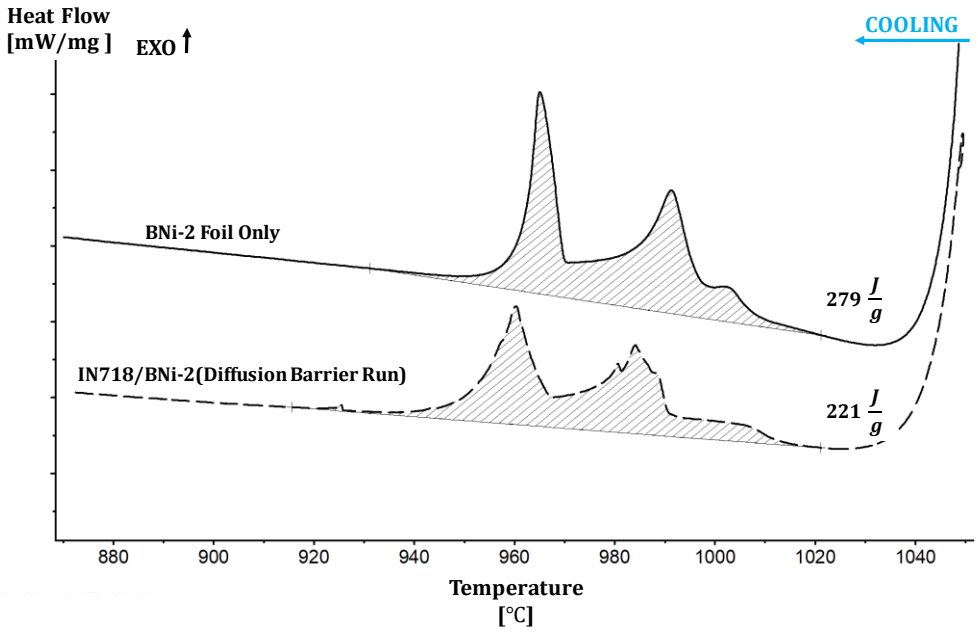

Figure 4.1.2 - DSC cooling trace of BNi-2 only & diffusion barrier experiment

The general shape of the DSC trace on cooling was consistent in both types of experiments and consists of three exothermic peaks related to the solidification of the BNi-2 braze ball.

The high temperature peak for the diffusion barrier run was broader than in the case of the foil only. The details regarding how the solidification peaks relate to the joint microstructure will be discussed in Chapter 4.2. There was a 21% reduction in the solidification enthalpy in the diffusion barrier experiments, consistent with values observed in other systems [53], [56]. The average solidification enthalpy measured in the diffusion barrier experiments was used as the value associated with 100% liquid formation in the TLPB couple.

4.1.2 Inconel 718/BNi-2 Transient Liquid Phase Bonding Couple

Figure 4.1.3 shows a stereo image of one of the cyclic half-joints after brazing. In both sets of experiments (cyclic and isothermal hold times), the faying surface had varying degrees of FM coverage. In fact, the FM was not successful in completely wetting the faying surface in either of the DSC approaches. This was despite a high purity Ar gas atmosphere used within the DSC, where the O_2 content was measured to be between 2 - 10 ppm. This behaviour supports the importance of specialized surface preparations for IN718. The average FM coverage area was approximately 85% ± 8% of the base metal for the cyclic samples, and 85% ± 5% for the interrupted tests. A method that accounts for the different degrees of wetting in these samples is described below in Chapter 4.3.

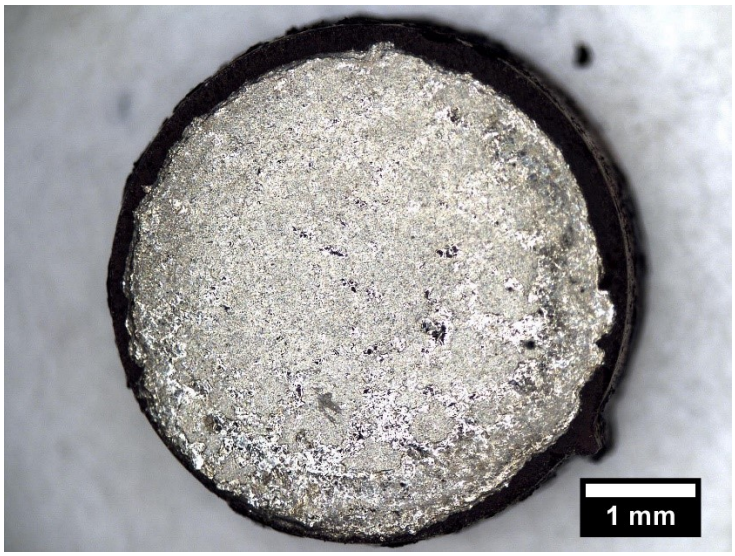

Figure 4.1.3 - Stereo image of IN718/BNi-2 TLPB half-joint after cyclic DSC testing

Figure 4.1.4 is an example of the first five cooling traces from a cyclic DSC test using an IN718/BNi-2 TLPB half-joint. An example of the complete set of heating and cooling traces from a cyclic TLPB half-joint DSC experiment are found in Appendix A. The values of solidification enthalpy determined for each cycle are located in the bottom left hand corner of Figure 4.1.4. Examination of the DSC cooling traces revealed that with increasing liquid duration, the magnitude of the solidification enthalpy decreased. This was evidence that diffusional solidification had occurred with elapsed time at T_B. Another observation was that only two peaks were present after the second cycle (approximately 25 minutes liquid duration). The enthalpy of solidification and liquid duration were measured for each cycle. The enthalpy was measured as the area under the exothermic peak present on the cooling segment from 1050°C to 870°C.

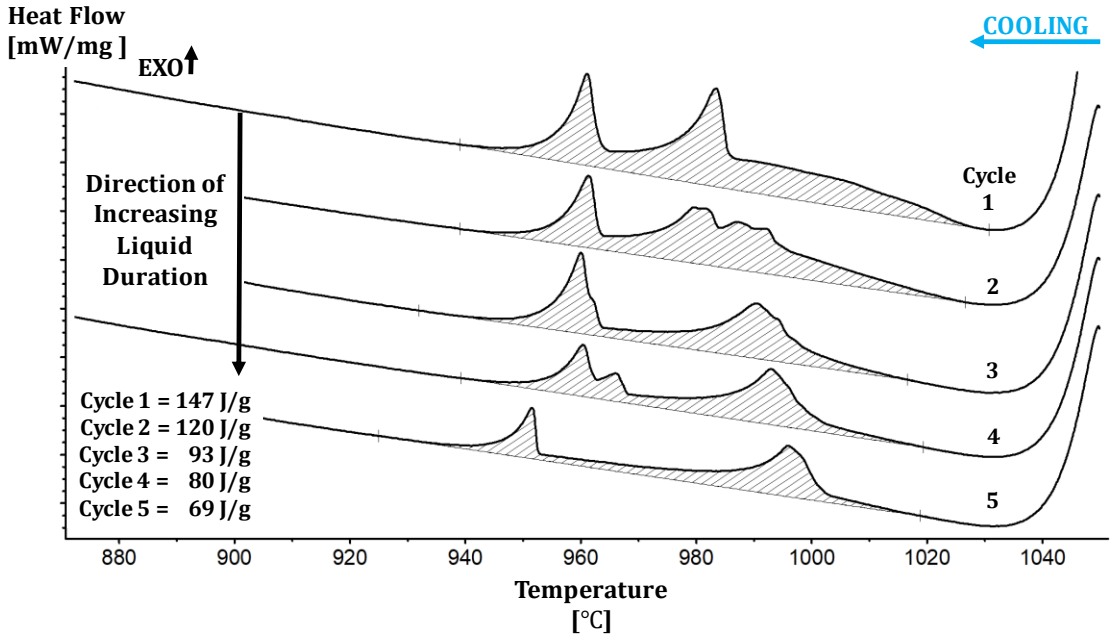

Figure 4.1.4 - First five cooling segments obtained after cyclic DSC testing of IN718/BNi-2 TLPB half-joint

The average enthalpy of solidification measured for both the cyclic and interrupted DSC tests is plotted against the square root of liquid duration in Figure 4.1.5. The liquid duration for each cycle was determined as described in Section 3.2. The error bars represent the standard deviation in the measured solidification enthalpy amongst the different trials for each DSC approach. Relatively good agreement between the cyclic and interrupted

enthalpy data measured from the DSC experiments was achieved, particularly at short and long liquid duration times. Discrepancy that does exist, was partly due to the different degrees of wetting mentioned above and the use of multiple samples in the case of the interrupted data set.

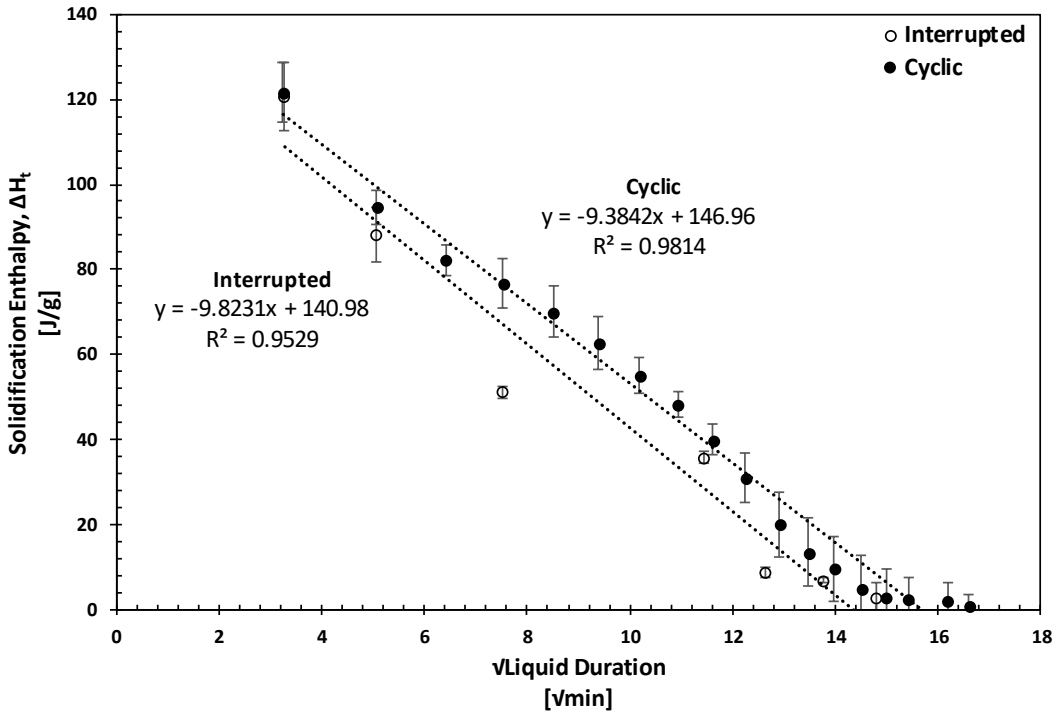

Figure 4.1.5 - Average solidification enthalpy vs. square root liquid duration for IN718/BNi-2 TLPB couple

Since TLPB is a diffusion-controlled process, there was a linear relationship between the solidification enthalpy on cooling and the square root of liquid duration. With the progression of liquid duration, there was a decrease in solidification enthalpy measured for the liquid present. Figure 4.1.5 showed that the initial enthalpy measurement was significantly lower than the diffusion barrier value of 221 J/g for both cyclic and interrupted DSC testing. This result indicated that diffusional solidification occurred in tandem with initial melting due to IBU. Upon reaching 1050°C and immediately cooling, (a liquid duration of 9 minutes), a significant portion of the liquid FM had already been isothermally solidified.

4.2 Microstructural Analysis

Figure 4.2.1 contains a micrograph of one of the IN718/BNi-2 half-joint samples held at 1050°C for 15 minutes. This micrograph was selected for discussion as it contains all the possible microstructural regions of interest. As indicated in the micrograph, there existed three distinct microstructural zones when a half-joint was held at T_B for an insufficient amount of time to reach completion of IS. The three regions are termed as follows: athermally solidified zone (ASZ), isothermally solidified zone (ISZ), and diffusionally affected zone (DAZ). There was also a region of unaltered BM microstructure.

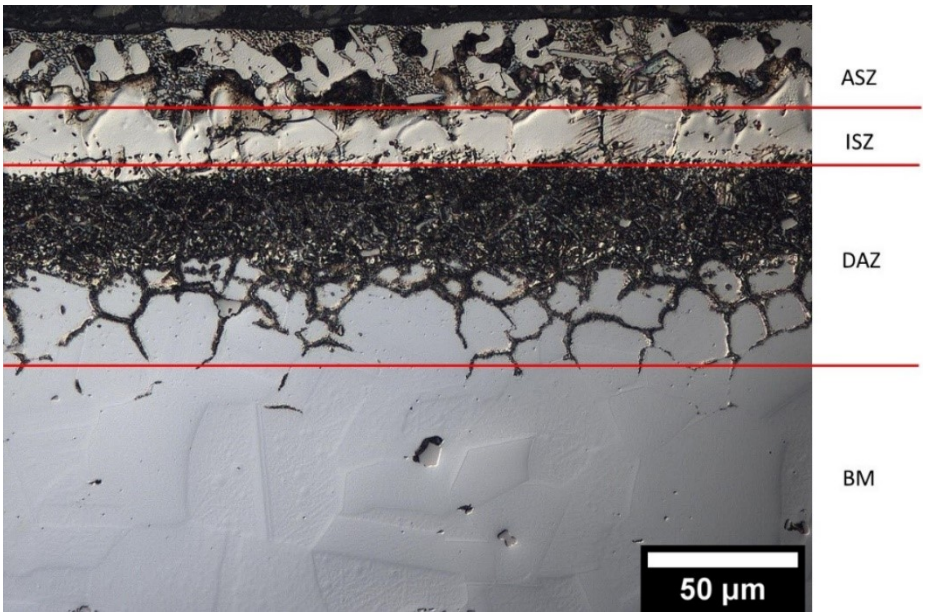

Figure 4.2.1 - Optical micrograph of IN718/BNi-2 half-joint after 15 minutes of isothermal hold time at 1050°C (etched)

During diffusion brazing of IN718 with BNi-2 at 1050°C, Arafin et al. [7] reported a dissolution thickness of approximately 7 µm after holding for 60 minutes at 1050°C for a wedge-type joint using an initial gap of 75 µm. Since IN718 samples did not fully wet, the initial position of the S/L interface was easily tracked, and it was determined that the dissolution thickness was approximately 4 ± 1 µm for the cyclic DSC tests. The dissolution was measured by superimposing a line on the micrograph that started at the left-hand side of the BM and ran across the entire BM. This line serves as a marker for the original BM/FM interface prior to dissolution. Dissolution results in an increased liquid width and thus the position of the interface moves away from the centreline. The thickness of ISZ

below the superimposed line would have been BM regions prior to dissolution, and thus that thickness can be interpreted as the dissolution thickness.

As seen in Figure 4.2.1, the DAZ region formed in the base metal adjacent to the ISZ. The DAZ forms because of solid-state diffusion of B into the IN718 base metal during IS. The microstructure of this region was characterized by both inter- and intragranular secondary phase boride precipitates within the BM. The morphologies of these precipitates were blocky and Widmanstätten/needle-like. Due to the low solubility of B in Ni-based alloys, the in-situ precipitation of borides in the base metal occurs [8]. EDS maps of the DAZ for two different IN718/BNi-2 half-joints are found in Figure 4.2.2. Upon analysis of Figure 4.2.2 a) and b), it was determined that the inter- and intra-granular borides present were Nb-Mo-borides and Cr-Mo-Nb borides respectively.

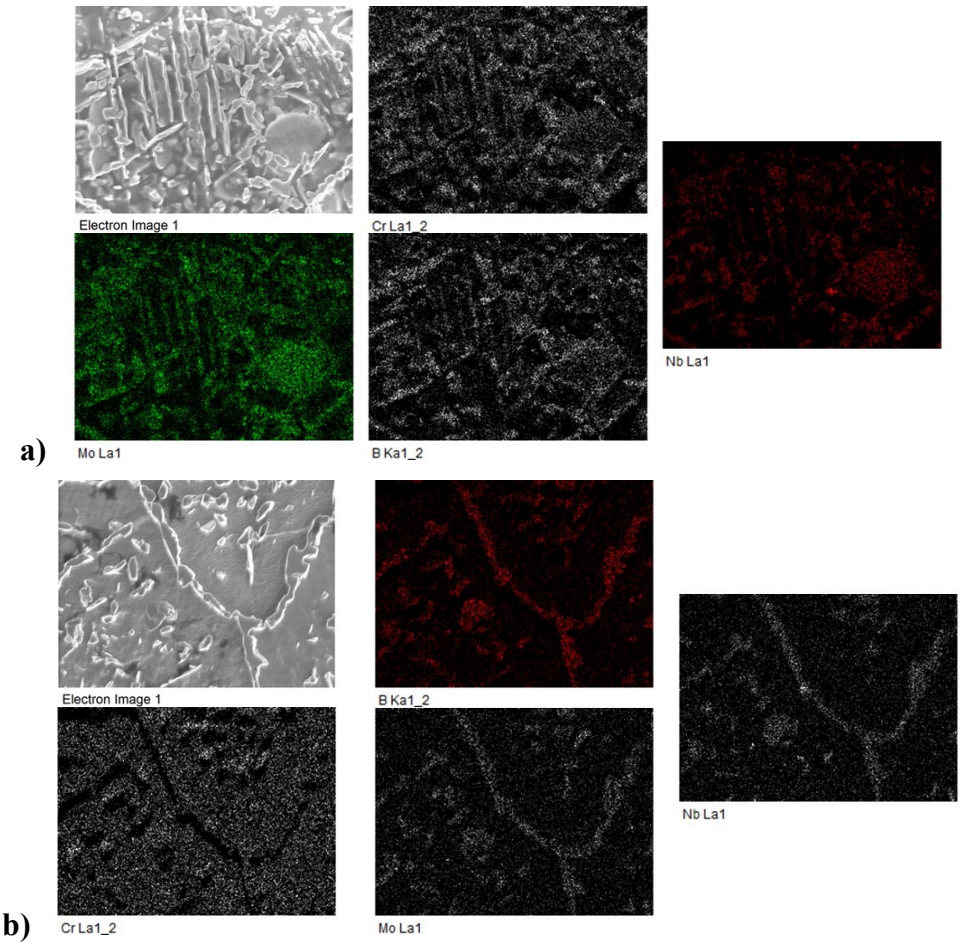

Figure 4.2.2 - EDS map of the DAZ for the IN718/BNi-2 half-joint subject to: a) 15-minute isothermal hold at 1050°C, b) 90-minute isothermal hold at 1050°C

Other researchers have confirmed from electron probe micro analysis line scans that the fine precipitates are likely Cr-Mo-Nb-based borides [8]. The presence of these secondary boride precipitates in the DAZ deplete the surrounding matrix of Cr, Mo, and Nb. This Nb depletion can influence the corrosion resistance, as well as the aging response of the alloy Post braze heat treatments have been used to decrease the width of the DAZ and homogenize the microstructure of TLPB joints to alleviate this effect. [60]

The ASZ is located at the joint centerline adjacent to the ISZ, as indicated in Figure 4.2.1. When insufficient brazing time is allotted, an ASZ forms from re-solidification of the liquid phase remaining during cooling from T_B. The three exothermic peaks observed in Figure 4.1.2 are associated with the athermal solidification of any remaining liquid during cooling. It is well understood that the presence of an ASZ is detrimental to mechanical properties of the joint, due to the formation of coarse, continuous brittle boride compounds. Studies have confirmed that boride compounds present at the centerline act as favourable sites for crack initiation and propagation [50], [60]–[63].

A higher magnification FE-SEM micrograph is shown in Figure 4.2.3. The various boride compounds expected to be present within the ASZ are labelled in Figure 4.2.3 with different shapes.

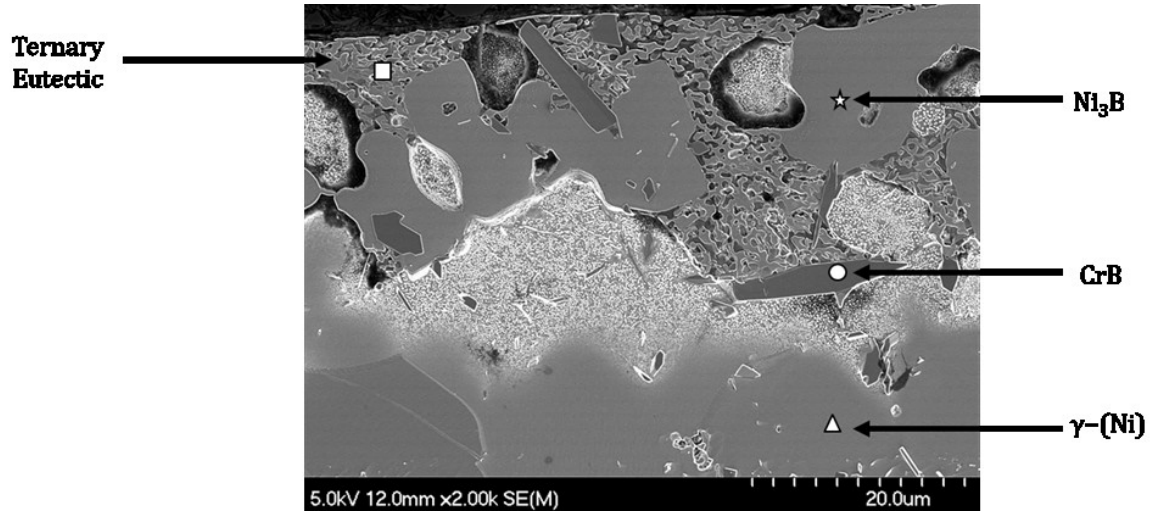

Figure 4.2.3 - FE-SEM micrograph of IN718/BNi-2 half-joint after 15 minutes of isothermal hold time at 1050°C (etched)

The approximate chemical compositions determined via EDS of the aforementioned phases are found in Table 4.2.1. The column titled “Spectrum” in Table 4.2.1 corresponds to the shaped labels in Figure 4.2.3. It should be noted that due to absorption effects associated with measuring B using EDS, that the analysis conducted in Table 4.2.1 is of a semi-quantitative nature.

Table 4.2.1 - EDS scans of ASZ phases present in IN718/BNi-2 half-joint after 15 minutes of isothermal hold time at 1050°C

Spectrum	Chemical Composition [at%]						
	B	**Si**	**Cr**	**Fe**	**Ni**	**Nb**	**Mo**
△	---	5.2	9.5	9.0	76.3		
○	59.4	---	39.1	---	---	---	1.5
☆	28.3	---	---	---	71.7	---	---
□	23.7	6.4	1.0	2.7	66.2	---	---

The first phase to freeze was solid solution γ-(Ni) in the form of epitaxial nodular dendrites extending into the melt from the ISZ/liquid interface. During this primary solidification, the melt becomes enriched with solute elements because of solute rejection. The approximate chemical composition of the ISZ/primary zone was close to the nominal FM composition (not including B). It is worth nothing that Fe, Cr, and Si values are higher than expected. This could be a result of either dissolution or diffusion of BM elements into ISZ. The complications of studying a multi element system such as IN718, while also attempting to measure light elements such as B could also be affecting the semi-quantitative data. During this primary solidification, the melt becomes enriched with solute elements because of solute rejection. Due to this rejection, the solute concentration of the melt eventually exceeds the solid solubility limit of the primary (pro-eutectic) γ-(Ni), and any liquid BNi-2 remaining freezes into various intermetallic compounds during cooling [62].

As primary solidification continues, B is rejected into the melt, as it has a low partition coefficient in Ni and has lower solubility limit in both Ni and Cr than Si does. This rejection of B into the melt results in shifting of the composition to eutectic amounts, and two eutectic reactions occur simultaneously. The two eutectic microconstituents are Cr-rich boride + γ-(Ni), and Ni-rich boride + γ-(Ni) [62]. The presence of these phases are confirmed in Table 4.2.1. Pouranvari et al. [36] measured the chemical composition of these eutectic phases using EPMA equipped with line scan wavelength dispersive

spectrometer, and determined that the Ni-rich boride was likely Ni_3B, while the Cr-rich boride was likely CrB.

Once the binary eutectics have formed, the melt becomes concentrated with Si, due to limited solubility of Si in borides. Si also has a low partition coefficient in Ni, and therefore rejection of Si into melt is favourable. The bulk composition of the ternary eutectic region is found in Table 4.2.1. The composition of the phases within the ternary region could not be confirmed due to spatial resolution of the FE-SEM-EDS equipment. Upon reaching the eutectic composition, the remaining liquid solidifies into a ternary eutectic product comprised of γ-(Ni)+ Ni-rich boride + Ni-rich silicide [35]. A. Davoodi Jamaloei et al. [60] have measured the chemical composition of these ternary eutectic regions using EDS and confirmed that the volume fraction of Si, Ni, and B present were adequate to form a ternary eutectic Ni-Si rich boride. According to the Ni-Si-B ternary phase diagram, the Ni-Si-rich boride is Ni_6Si_2B [27]. Researchers have confirmed the presence of fine β-Ni_3Si precipitates within the γ-(Ni) phase, which formed via a solid-state precipitation reaction on cooling [35], [60].

The exothermic peaks present on the DSC traces in Figure 4.1.2 and Figure 4.1.4 are associated with the athermal solidification of BNi-2 into the various eutectic compounds described above. It is assumed that the two binary eutectic reactions occur simultaneously, and that the FM exhibits three distinct stages of melting and solidification [56]. The first high temperature peak is related to the solidification of the initial primary solid solution Ni nodules. The second peak is linked to the binary eutectic reactions, while the final peak is the solidification of the ternary eutectic component. This three stage melting/solidification sequence is shown in Figure 4.1.1, Figure 4.1.2, and Figure 4.1.4.

Figure 4.2.4 shows a series of micrographs taken of samples subject to various isothermal hold times. The microstructure of the TLPB half-joint held for zero minutes (Figure 4.2.4 a)) consists of all three microstructural zones (ASZ, ISZ, and DAZ). It is interesting to note that there exists an ISZ, approximately 20 ± 5 μm (on a half-joint basis), despite the absence of an isothermal hold period at T_B. This observation serves as further evidence for ISZ growth in parallel with initial melting due to IBU. Note that this ISZ measurement likely contains some of the primary γ-(Ni) as it was difficult to visually separate this portion of

the ASZ from the ISZ. The width of the ISZ increased with increasing hold time at T_B (Figure 12 b)). The width of the ASZ decreased with increasing holding time and was eventually completely absent from the microstructure in the sample held for 180 minutes (Figure 4.2.4 c)). The conclusion from the DSC enthalpy traces, that the liquid fraction decreased with increased hold time is further supported by the gradual decrease in the width of the ASZ shown in Figure 4.2.4. Figure 4.2.4 also illustrates that the extent of B diffusion into the base metal also increased with longer hold time, extending from approximately 26 ± 6 μm for a zero-minute hold sample to 135 ± 38 μm for a 180-minute hold sample.

a)

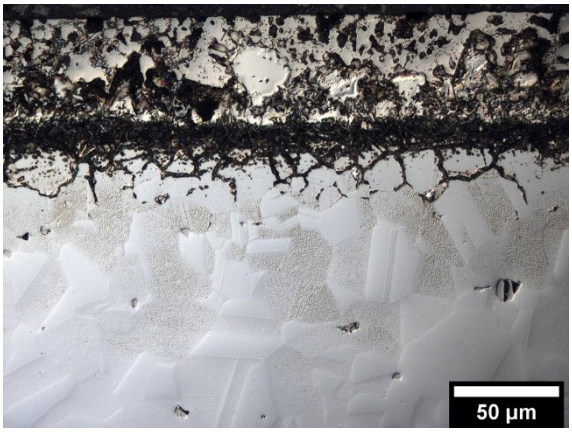

b)

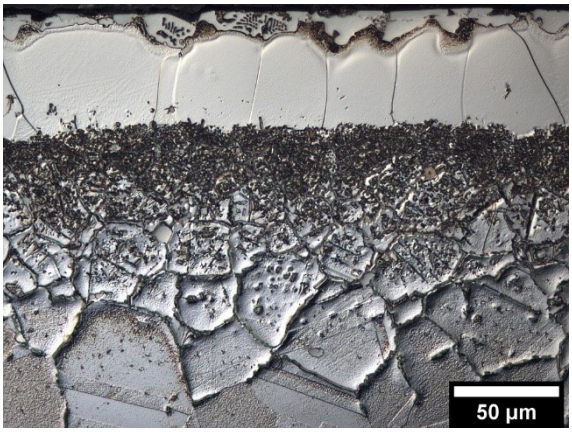

c)

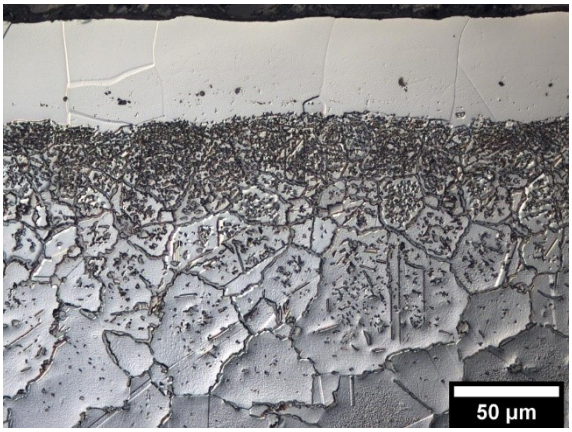

Figure 4.2.4 - Microstructural progression in IN718/BNi-2 half-joint with increased hold time at 1050°C: a) 0 min hold, b) 90 min hold, c) 180 min hold (etched)

Figure 4.2.5 displays the chemical composition (wt.%) of the ISZ developed after two different hold times. EDS bulk scans were conducted within the ISZ of two DSC samples

using the FE-SEM. One sample was subject to a 15-minute isothermal hold at 1050°C, while the other sample was held for 210 minutes. Interestingly, both the chemical compositions for the 15-minute and 210-minute samples approach the nominal composition of the FM (excluding B). The amount of Fe and Cr present in the two DSC samples was higher than the nominal composition value, indicating that dissolution and interdiffusion of the base metal occurred. One notable difference between the two DSC samples was that approximately 0.2 wt.% Ti was present in the ISZ of the 210-minute sample. The presence of Ti also indicates that base metal dissolution occurred to some extent, as Ti was not present within the FM initially. Also, with increased hold time the amount of Nb and Mo present within the ISZ increased.

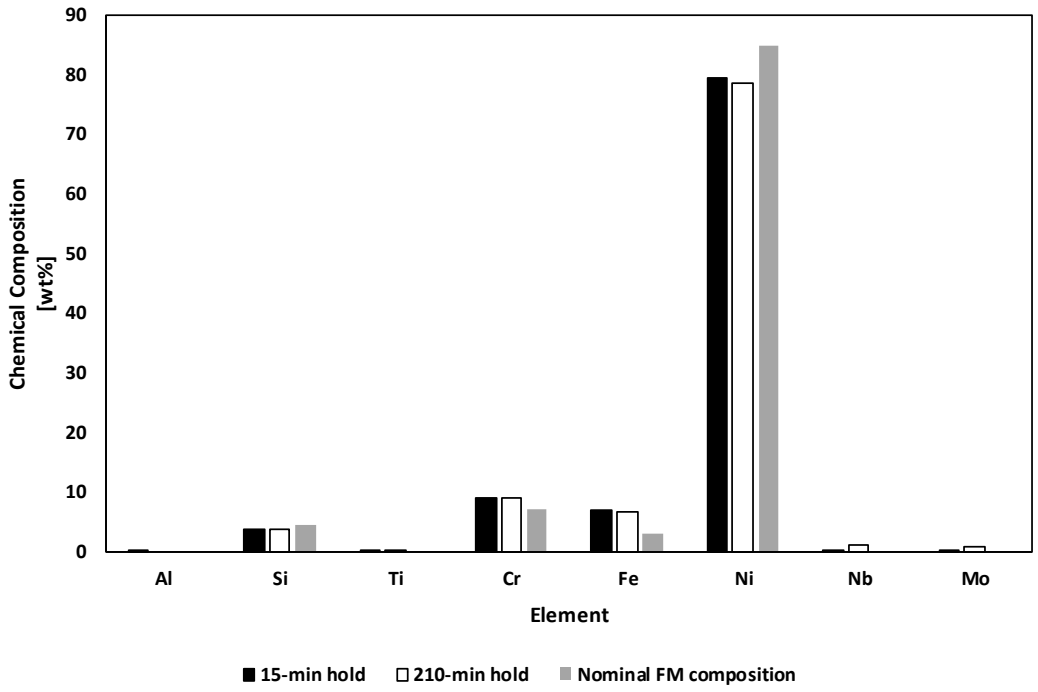

Figure 4.2.5 - Bulk chemistry of ISZ determined via FE-SEM-EDS for IN718/BNi-2 half-joint TLPB couple held isothermally at 1050°C for 15 and 210 minutes

Figure 4.2.6 a) contains an FE-SEM micrograph taken of an IN718/BNi-2 TLPB half-joint after a 15-minute isothermal hold at 1050°C. An EDS line scan was conducted on the sample, represented by the white line on the micrograph in Figure 4.2.6 a). The results of the EDS line scan across the ISZ grain are plotted as chemical composition vs. distance

from the DAZ/ISZ interface in Figure 4.2.6 b) and c). After 15 minutes there was a shallow positive Ni gradient (from 77 to 82 wt.% Ni) across the ISZ moving from the DAZ/ISZ interface towards the centerline. There was a shallow negative gradient for both Cr and Fe as the distance away from the DAZ/ISZ interface increased. In terms of the Si content, there was the presence of a shallow positive gradient away from the interface.

a)

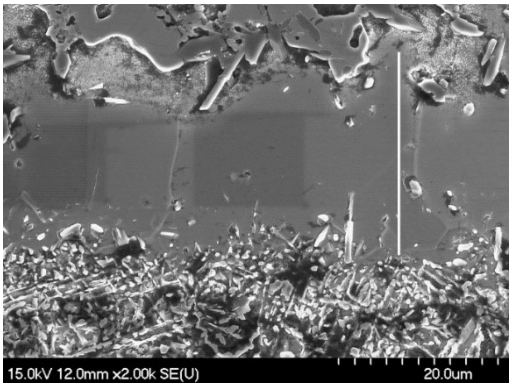

b)

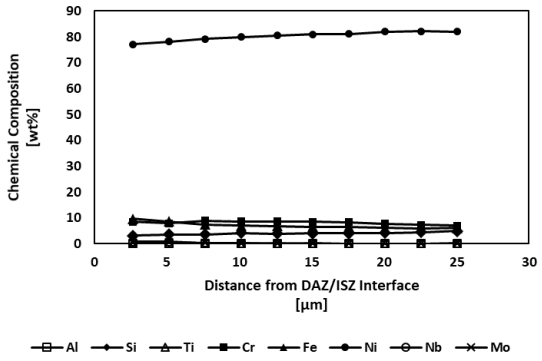

c)

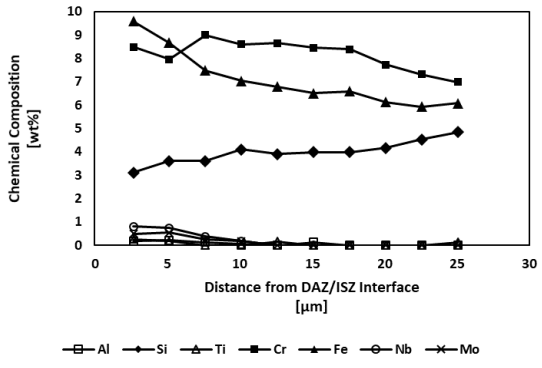

Figure 4.2.6 - a) FE-SEM micrograph of IN718/BNi-2 half-joint held isothermally at 1050°C for15 minutes, b) plot of chemical composition vs. distance from DAZ/ISZ interface, c) Ni data removed (etched)

4.3 Maximum Brazing Clearance

While the solidification enthalpy vs. square root of liquid duration plot can provide a good understanding of t_{IS}, a much more meaningful manner to display DSC data from a TLPB couple is in the form of an MBC plot. MBC is the $2w_o$ value that is free from centerline eutectic and is related to brazing time and joint clearance [64]. Analysing the DSC data in this way allows determination of the extent of IBU and a quantitative measure of the kinetics of IS that is independent of the gap size.

The first step to convert enthalpy data obtained from the DSC to an MBC plot was to produce a liquid fraction plot (Figure 4.3.1). The error bars represent the standard deviation in the liquid fraction amongst the different trials for each DSC approach. The liquid fraction was calculated by dividing the enthalpy of solidification measured from each cycle (ΔH_t) by the diffusion barrier enthalpy (ΔH_o). The trends observed in the liquid fraction plot are much the same as those observed in an enthalpy plot. Both plots can serve as an indicator of the extent of IS with progressing braze time, by observing the initial liquid fraction and the rate that the liquid is consumed.

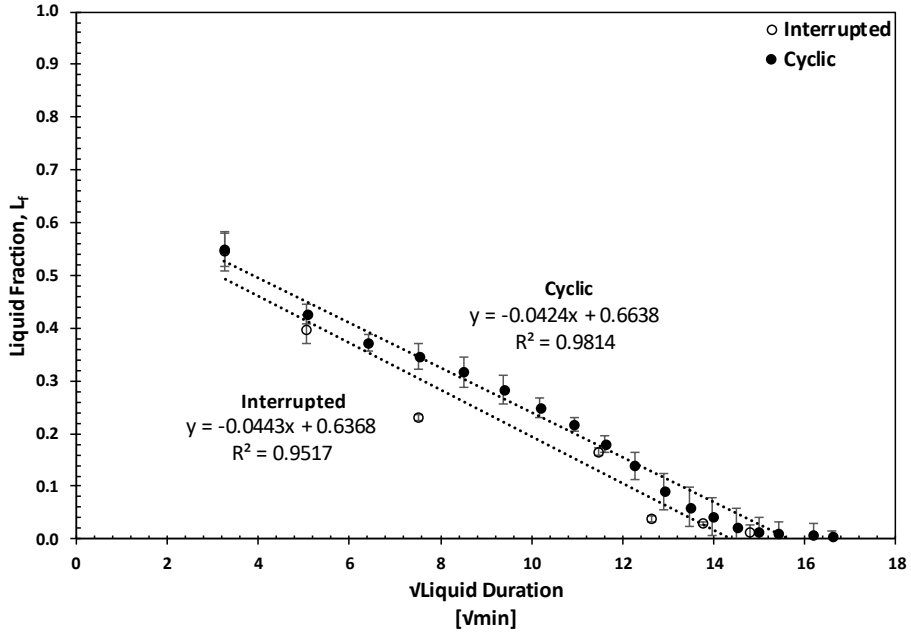

Figure 4.3.1 - Liquid fraction vs. square root of liquid duration for IN718/BNi-2 TLPB couple

A more industrially relevant manner to display this information is through a liquid width plot, as shown in Figure 4.3.2. The liquid width of the half-joint (w_t) can be obtained by simply multiplying the liquid fraction by the initial half-gap width (w_o for a half-joint, or $2w_o$ for a full joint). The average w_o was measured for each sample as the distance from the DAZ to the centerline (location where the ASZ ended). This average w_o was obtained through 30 equidistant measurements across the length of the joint on polished cross sections of the DSC samples. The average w_o for each cyclic test varied between 54 – 61 µm depending on how well the FM was able to fully wet the faying surface. The standard deviation of the average w_o also varied (between 3 – 13 µm) due to differences in the wetting behaviour. In general, samples that exhibited poor wetting resulted in increased w_o and were subject to more variation along the length of the joint. The average $2w_o$ value was determined by simply multiplying the average w_o by two.

Equation 4.3.1 expresses the liquid width ($2w_t$) in terms of the liquid fraction obtained from DSC (L_f) and $2w_o$. The average w_o measured on samples from the cyclic tests was 57 ± 3 µm, resulting in an average $2w_o$ value of 114 ± 5 µm. The average w_o measured on samples from the interrupted tests was 57 ± 6µm, resulting in an average $2w_o$ value of 114 ± 11 µm. The value of $2w_o$ was larger than 100 µm in both cases due to a combination of dissolution and incomplete wetting, which would both contribute to increasing the initial liquid width.

$$\mathbf{2w_t = \frac{\Delta H_t}{\Delta H_o} 2w_o = L_f 2w_o} \qquad \textbf{Eq. (4.3.1)}$$

Figure 4.3.2 plots the resultant variation in $2w_t$ versus the square root of liquid duration. The error bars represent the standard deviation in $2w_t$ amongst the different trials for each DSC approach.

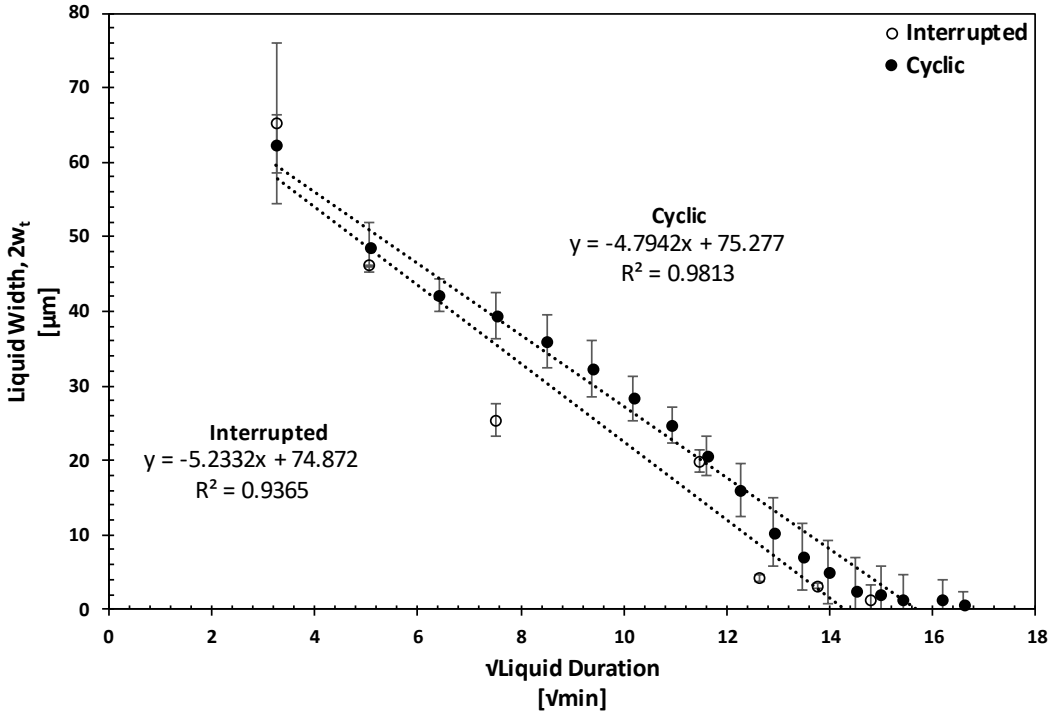

Figure 4.3.2 - $2w_t$ vs. square root of liquid duration for cyclic and interrupted DSC tests

Linear regression (LR) analysis can be conducted on the $2w_t$ data. The LR equation takes the following form;

$$2w_t = -k_{IS}\sqrt{t_{IS}} + 2w_i \qquad \textbf{Eq. (4.3.2)}$$

where k_{IS} is the rate constant for IS and $2w_i$ represents the liquid width present at zero minutes liquid duration. Table 4.3.1 contains relevant LR parameters from the $2w_t$ plot in Figure 4.3.2 for the cyclic and interrupted data sets.

Table 4.3.1 - Comparison of LR parameters extracted from $2w_t$ plot

Experiment Type	R^2	k_{IS} $\left[\frac{\mu m}{\sqrt{min}}\right]$	% Difference	$\sqrt{t_{IS}}$ $[\sqrt{min}]$	% Difference	$2W_i$ [µm]	% Difference
Cyclic	0.98	5.2	8.8	15.7	9.2	75	0
Interrupted	0.94	4.8		14.3		75	

t_{IS} can be estimated using Figure 4.3.2, by simply determining the square of the x-intercept of the LR equation for the $2w_t$ plot. t_{IS} estimated by Figure 4.3.2 was 247 mins and 205 mins for the cyclic and interrupted data sets respectively

The y-intercept of the $2w_t$ plot, $2w_i$, can be interpreted as liquid width present at zero minutes liquid duration. The initial full liquid width extrapolated from Figure 4.3.2 was approximately 75 μm for both the cyclic and interrupted tests respectively. The y-intercept of the LR equation from Figure 4.3.2 can be used to estimate the width of ISZ that had grown before melting started to occur. By subtracting the y-intercept from the measured $2w_o$, the approximate width of ISZ due to IBU can be predicted. Using the LR parameters in Table 4.3.1 and a $2w_o$ of 114 μm, the estimated width of ISZ grown due to IBU was 38 μm and 39 μm for the cyclic and interrupted data sets respectively. In general, good agreement between the LR parameters of the cyclic and interrupted data sets was achieved. In fact, the slope, y-intercept, and x-intercept all agreed within 10%.

While the ISZ present at the onset of melting is easily determined through LR, no ISZ growth or B diffusion occurs until the BNi-2 solidus temperature has been reached [51], [56], making the y-intercept value have little physical meaning. However, as previously mentioned rapid growth of the ISZ during initial melting and heating to the peak braze temperature of 1050°C was observed and has been reported by other researchers [16], [23], [51], [57]. The IBU process is thought to grow at a rapid nonlinear rate during heating from the solidus to T_B. Once T_B is achieved, and the filler has completely melted, the ISZ growth continues at the linear rate indicated by the MBC plot [65].

As pointed out by Moreau and Corbin [65], the width of ISZ present once T_B is first achieved represents a more physically meaningful prediction for the growth of the ISZ due to IBU [65]. To determine the width of ISZ present upon first reaching 1050°C using Figure 4.3.2, the liquid width present at 2.2 $\sqrt{\text{min}}$ predicted using the LR equation is subtracted from $2w_o$. The liquid width at the peak braze temperature predicted by Figure 4.3.2 was determined to be 65 μm and 63 μm for the cyclic and interrupted data sets respectively. Thus, it can be inferred that 49 μm and 51 μm of ISZ had grown by the time the peak braze temperature was first reached for the two testing approaches. This is equivalent to approximately 44% of $2w_o$ being solidified due to IBU.

One disadvantage with plotting $2w_t$ is that its value depends on $2w_o$, making it difficult to compare samples with different degrees of spreading. Moreau and Corbin [65] have recently developed a method which converts the DSC enthalpy data and $2w_t$ to an isothermally solidified solid width ($2w_{ISZ}$). The following expression is used to convert the DSC data to an MBC plot;

$$\textbf{MBC or } 2w_{ISZ} = 2w_o(1-L_f) \qquad \textbf{Eq. (4.3.3)}$$

where $2w_{ISZ}$ is the width of the ISZ, $2w_o$ is the average gap width measured from the polished cross section, and L_f is the liquid fraction obtained from the DSC data. Multiplying the solid fraction ($1-L_f$) by the average $2w_o$ allowed for analysis of samples where the faying surface of the BM was not completely wetted by the FM. Using a $2w_o$ value measured from a polished cross section instead of the nominal FM thickness accounts for variabilities in the initial liquid width introduced through dissolution and incomplete wetting. Figure 4.3.3 displays the average MBC plots for both the cyclic and interrupted sets of DSC experiments. The error bars represent the standard deviation in the MBC amongst the different trials for each DSC approach.

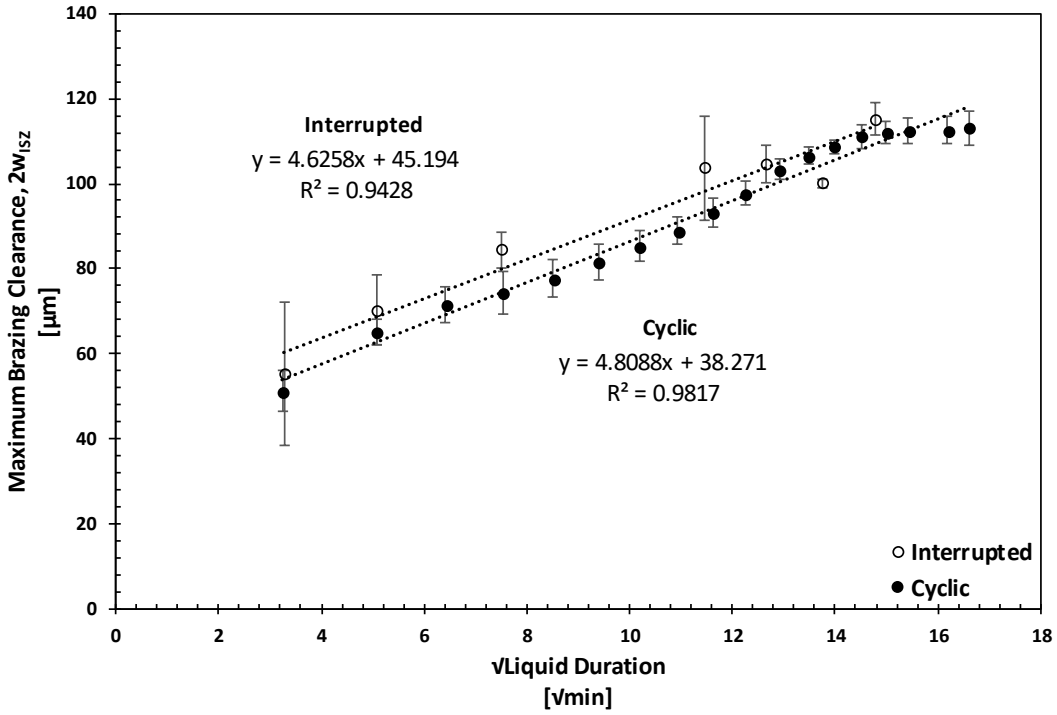

Figure 4.3.3 - MBC vs. square root of liquid duration for cyclic and interrupted DSC testing using IN718/BNi-2 TLPB half-joints

The LR line can be expressed in terms of the MBC in the following manner;

$$\textbf{MBC or } 2w_{ISZ} = k_{IS}\sqrt{t_{IS}} + 2w_{ISZ,o} \qquad \textbf{Eq. (4.3.4)}$$

where $2w_{ISZ}$ is the MBC, k_{IS} is the rate of IS, $\sqrt{t_{IS}}$ is the IS time and $2w_{ISZ,o}$ is the width of ISZ present at zero minutes liquid duration (i.e. onset of melting). Table 4.3.2 contains a comparison of the LR parameters obtained from both sets of DSC experiments.

Table 4.3.2 - Comparison of LR parameters extracted from MBC plot

Experiment Type	R^2	k_{IS} $\left[\frac{\mu m}{\sqrt{min}}\right]$	% Difference	$\sqrt{t_{IS}}$ $[\sqrt{min}]$	% Difference	$2W_{ISZo}$ [μm]	% Difference
Cyclic	0.98	4.8	3.7	15.7	5.9	38	17
Interrupted	0.94	4.6		14.8		45	

t_{IS} can also be estimated using an MBC plot such as that found in Figure 4.3.3. Using an MBC of 114 μm and the LR equations found in Figure 4.3.3 , t_{IS} estimated by Figure 4.3.3 was 247 mins and 219 mins for the cyclic and interrupted data sets respectively.

The y-intercept of the LR equations extracted from the MBC plots in Figure 4.3.3 can be interpreted as the width of ISZ grown due to IBU prior to melting of the foil. The predicted width of ISZ due to IBU present at the onset of melting was determined to be 38 μm and 45 μm for the cyclic and interrupted data sets respectively.

As in the case of the liquid width plot, a more physically relevant value for quantifying the IBU is determining the ISZ width present at T_B (2.2 $\sqrt{min}$ liquid duration) using the LR equation for the MBC curve. This results in an MBC of 49 μm and 55 μm once 1050°C is first reached for the cyclic and interrupted tests respectively.

The zero-minute hold sample in Figure 4.2.4 a) can be used to verify the ISZ width predicted by Figure 4.3.2 and Figure 4.3.3. The zero-minute hold sample corresponds to a liquid duration of 3.2 $\sqrt{min}$ and is the first data point on any of the plots related to DSC data previously shown. The liquid width from the DSC data in Figure 4.3.2 at 3.2 $\sqrt{min}$ was 62 ± 4 μm for the cyclic series, and 65 ± 11 μm for the interrupted series. This implies an ISZ growth of 52 ± 4 μm for the cyclic series, and 49 ±11 μm for the interrupted series.

The MBC from the DSC data in Figure 4.3.3 at 3.2 $\sqrt{\text{min}}$ was 51 ± 5 μm and 55 ± 17 μm for the cyclic and interrupted data sets respectively. The ISZ width determined from both Figure 4.3.2 and Figure 4.3.3 agreed well with the measured ISZ width of 20 ± 5 μm (40 ± 10 μm) present in the zero-minute hold sample in Figure 4.2.4 a).

In general, good agreement between the LR parameters of the cyclic and interrupted data sets was achieved, except for the y-intercept. The interpreted t_{IS} and ISZ due to IBU obtained from the liquid width and MBC plots agreed very well for the cyclic series. Obtaining an t_{IS} of 247 minutes and 38 μm of ISZ due to IBU from both Figure 4.3.2 and Figure 4.3.3. In terms of the interrupted series, there was some discrepancy in terms of t_{IS} and width of ISZ due to IBU predicted from the $2w_t$ and MBC plot. Figure 4.3.2 predicted 205 minutes and 39 μm, while Figure 4.3.3 predicted 219 and 45 μm for t_{IS} and IBU width. Better agreement between the cyclic and interrupted data sets for the y-intercept was achieved in Figure 4.3.2, while better agreement for predicted t_{IS} and slope were achieved in Figure 4.3.3.

The discrepancy was due to the multiple samples (14 in total) associated with the interrupted series. Each of these interrupted experiments had a separate FM and base metal sample, where the cyclic test used one filler and base metal sample to construct the entire curve. By using a single sample instead of multiple samples to build the MBC plot, a large degree of sample to sample variability is removed and the linearity of the MBC plot is improved. Differences in the degree of BM wetting are thought to be the biggest contributor to the variability in the interrupted set of experiments.

4.4 Comparison to Literature and Theory

Pouranvari et al. have conducted multiple studies on the TLPB of IN718 using BNi-2 using the traditional approach described in Section 1.0. Figure 4.4.1 plots MBC versus the square root of liquid duration for the current study, as well as that conducted by Pouranvari et al. [36]. The work completed by Pouranvari et al. [36] had the closest experimental conditions to the current study (1050°C; 50 μm BNi-2 foil as a full joint; cast IN718 BM with a similar grinding surface preparation), and directly measured and plotted the width of the ISZ or MBC versus braze time.

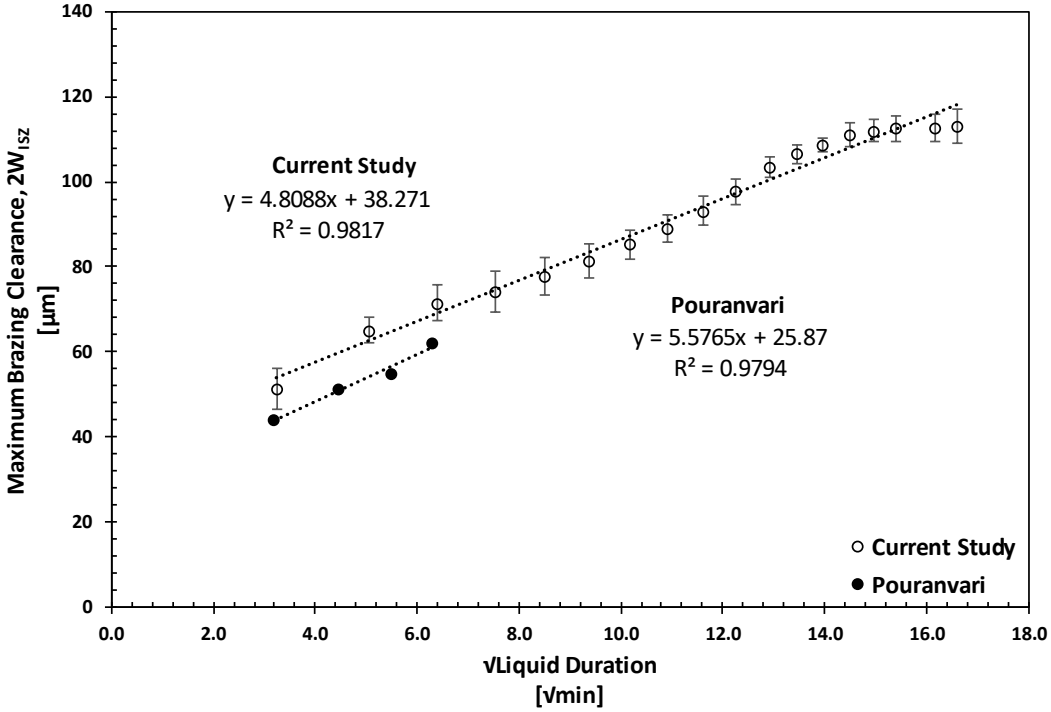

Figure 4.4.1 - Comparison of MBC for IN718/BNi-2 between current study and Pouranvari et al. [36]

It should be noted that the data taken from literature is plotted as the square root of hold time rather than the square root of liquid duration. Also, the BM used in the current study was wrought IN718. Agreement between the two data sets in terms of k_{IS}, the width of IS layer present at zero minutes liquid duration, and t_{IS} was very good considering these differences.

Physical modelling of the TLPB process has typically focused on the IS stage, and two different approaches have been commonly used. Both approaches apply analytical models to predict the diffusion controlled two phase moving boundary problem using time dependent diffusion equations based on Fick's second law [15]. The first approach is termed the migrating S/L interface model, and is simplified to the following expression [7]:

$$\sqrt{\mathbf{t}_{IS}} = \frac{2w_i}{4\gamma\sqrt{D_{B-IN718}}} \qquad \textbf{Eq. (4.4.1)}$$

where t_{IS} is the time required for complete IS, $2w_i$ is initial liquid width, $D_{B\text{-}IN718}$ is the diffusion coefficient of B in Ni, and γ is a dimensionless parameter that takes the moving interface into account. γ can be calculated using Equation 4.4.2;

$$\frac{C_S - C_M}{C_L - C_S} = \gamma\sqrt{\pi}e^{\gamma^2}\left(1 + erf(\gamma)\right) \qquad \textbf{Eq. (4.4.2)}$$

where C_s is the solute concentration in the solid phase at the S/L interface, C_M is the concentration of B in the base metal initially, and C_L is the solute content of the liquid phase at the interface.

The second approach is termed the solute distribution law or B diffusion model [7]. Analytical solutions to Fick's second law for unsteady state diffusion from a 2W thick source into a semi-infinite substrate were first proposed by Crank [66], and in the case of TLPB of Ni-based superalloys, can be simplified and expressed as;

$$\sqrt{t_{IS}} = \frac{2w_i}{4erf^{-1}\left(\frac{C_S}{C_0}\right)\sqrt{D_{B-Ni}}} \qquad \textbf{Eq. (4.4.3)}$$

where t_{IS} is the time required for complete IS, $2w_i$ is initial liquid width, C_s is the B concentration of the solid phase at the S/L interface, C_0 is the initial B concentration present in the interlayer, and $D_{B\text{-}Ni}$ is the diffusion coefficient of B in Ni. Values used for various solute concentrations in Equation 4.4.2 and 4.4.3 are found in Table 4.4.1. Using the values in Table 4.4.1 and Equation 4.4.2, the theoretical dimensionless parameter γ was calculated to be equal to 0.011.

Table 4.4.1 - Various solute concentrations of interest

Variable	Concentration [at% B]	Reference
C_s	0.3	[67]
C_M	0	---
C_L	13.16	[68]
C_0	14.45	[8]

Figure 4.4.2 contains a log-log plot of the time predicted for completion of IS versus the diffusion coefficient of B in Ni. The time was calculated via Equation 4.4.2 and 4.4.3, using diffusion coefficients on the order of magnitude of those cited in literature (1.0E-11 – 1.0E-9 m^2/s) [7], [21], [22], [32], [69]. The y-intercept for the cyclic data set in Figure 4.3.2 was used as $2w_i$ in Equation 4.4.2 and 4.4.3.

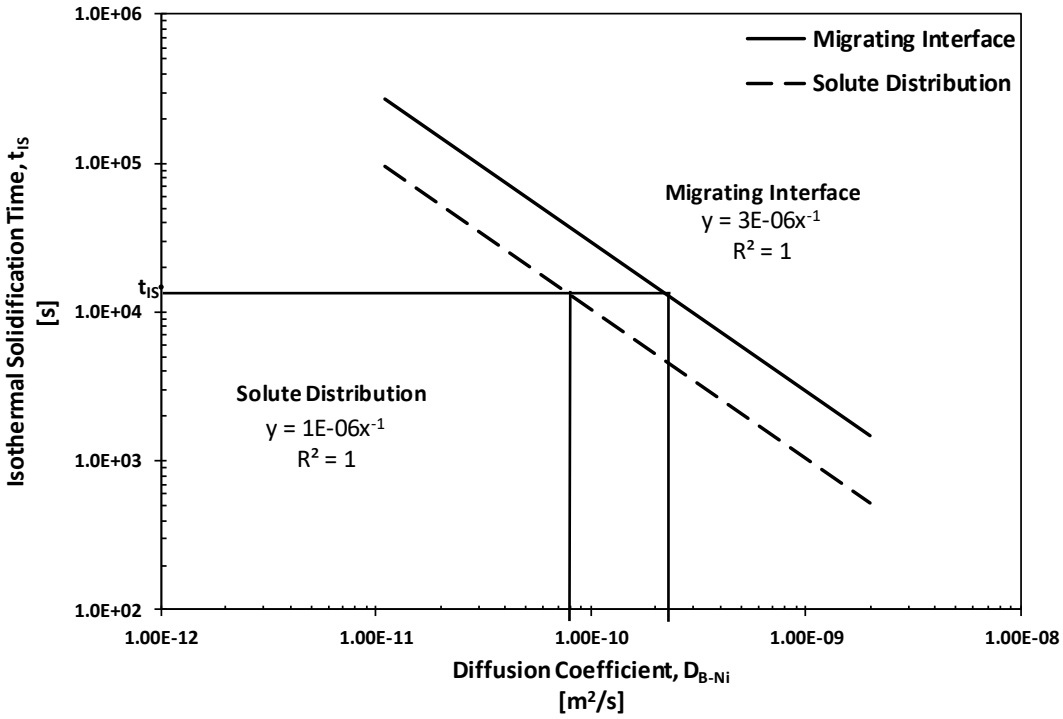

Figure 4.4.2 - Diffusion coefficient vs. IS time predicted from the migrating interface and solute distribution models

For a given diffusivity value, the prediction for t_{IS} was three times higher using the migrating interface model compared to the solute distribution model. Both models predict an inverse linear dependence of t_{IS} on the magnitude of diffusivity. Using the range of diffusivities found in literature, t_{IS} for a $2w_i$ = 75 μm varied widely from under 16 minutes to over 1600 minutes. The experimentally determined t_{IS} from the cyclic data set is shown as a horizontal line on Figure 4.4.2, and the $D_{B\text{-}IN718}$ predicted from both models are depicted as vertical lines on Figure 4.4.2. Recall that brazing was carried out at 1050°C, and thus t_{IS} and $D_{B\text{-}IN718}$ are for that specific T_B. The $D_{B\text{-}IN718}$ values that best correlated with the t_{IS} determined from Figure 4.4.2 using the migrating interface and solute distribution models were approximately 2.0E-10 m^2/s and 6.8E-11 m^2/s respectively.

Using experimental data for t_{IS} at different T_B values , Pouranvari et al. [21] estimated $D_{B\text{-}IN718}$ to be 2.4E-10 m^2/s. Using a similar approach, Ojo et al. [32] used two methods to estimate $D_{B\text{-}IN738}$ to be 3.4E-10 or 6.7E-11 m^2/s at 1050°C. Consequently, the diffusivities determined in the current study were very close to those used by other researchers. Given that Pouranvari studied IN718 brazed with BNi-2, it was concluded that the migrating interface model is most applicable to the current investigation.

The DSC methodology allowed for determination of a more accurate starting liquid width since it provides the liquid width after dissolution, wetting, and IBU occurred. By using the initial liquid width determined via DSC and metallography in analytical models, wetting phenomena, dissolution, and ISZ growth due to IBU can all be incorporated into determining the kinetics. Using a more accurate starting liquid width leads to obtaining more accurate predictions for t_{IS}. The increase in liquid width due to poor wetting and dissolution is captured by the metallographic measurement of $2w_o$, while the ISZ growth due to IBU is inherently built into the liquid width and MBC plots. If a starting initial liquid width of 100 μm (two times nominal width of BNi-2 foil) was used in either the migrating interface or solute distribution models, the time for the IS process to complete would be inaccurate, as effects of dissolution and IBU on kinetics of IS would not have been accounted for.

CHAPTER 5 Surface Characterization

Once the kinetic behaviour of the TLPB process for IN718 using BNi-2 and an ISP treatment was determined, the surface of P&WC samples was characterized. This was accomplished via OM, FE-SEM, and LSCM.

5.1 Optical Microscopy

Figure 5.1.1 contains stereo images of the surface prepared P&WC samples in the as-received condition. The AC and No Prep samples had a similar appearance, the difference being that the surface of the AC sample appeared more degraded as a result of the AC process. The AC+NiCr, AC+NiCr+Ni(F), and AC+NiCr+Ni(B) samples also had similar appearances, and the general visual appearance at this magnification was likely controlled by the roughening step present. The appearance of the AC+Ni(F) sample resembled that of the AC sample, but the presence of the Ni plating had removed the degraded appearance caused by the AC process

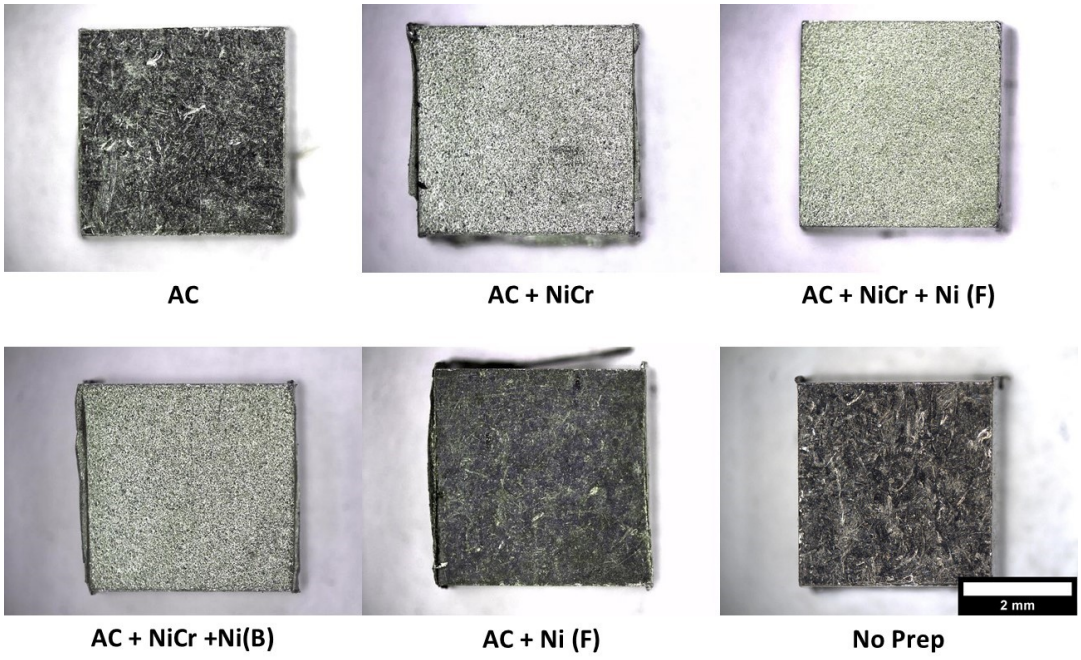

Figure 5.1.1 - Stereoscopic micrographs of the as-received surface prepared samples

Optical micrographs of polished cross sections for the surface prepared P&WC samples in the as-received condition are in Figure 5.1.2. The surface of the AC sample is relatively

flat compared to the other surface processing routes. The samples containing a roughening step were characterised by a wavy surface imposed by the Nicroblast^{TM} grit. A continuous and relatively even layer of Ni plating was observed on samples subject to a Ni(F) step. This plating was also present on both sides of the ingot. No distinct and continuous layer of plating was documented on the Ni brush plating samples. This was likely due to the localised nature of the brush plating process, as opposed to the more continuous electrolytic flash plating process. The plating is presumably present but is only present locally in very small thicknesses on the surface. The plating could also potentially be absent at the depth to which the brush plated sample was polished in the micrograph in Figure 5.1.2.

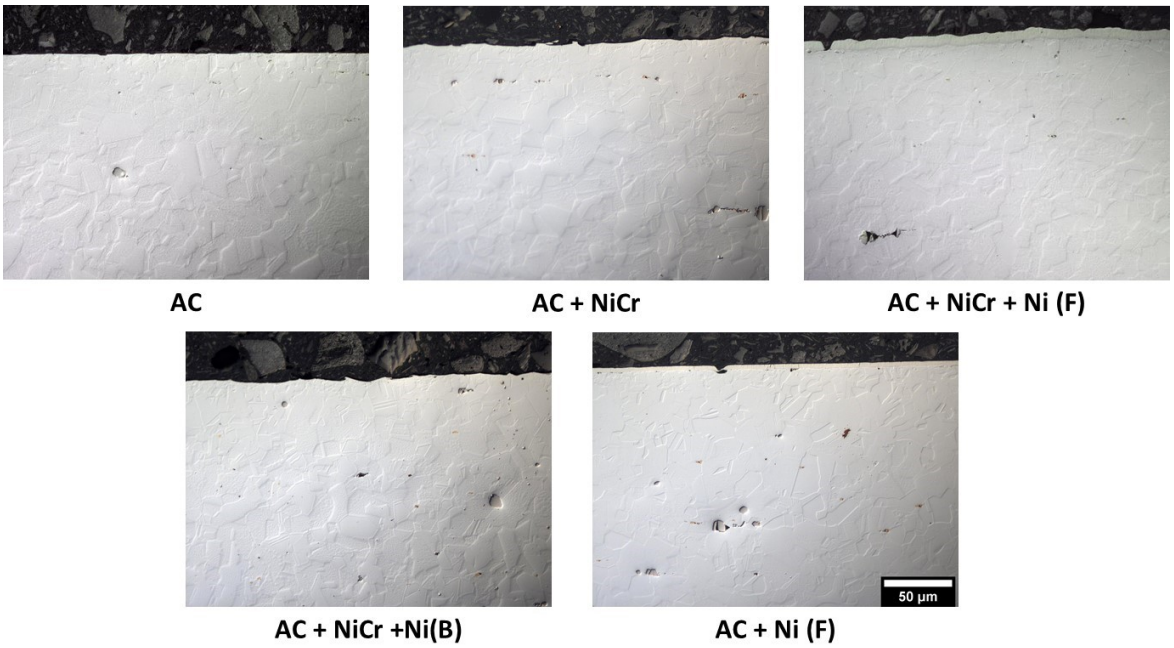

Figure 5.1.2 - Optical micrographs of polished cross sections for as-received surface prepared samples.

Figure 5.1.3 contains higher magnification micrographs of as-received Ni(F) samples. The thickness of the Ni(F) coating was determined by means of 30 equidistant measurements across the surface of the ingot. The average plating thickness for the AC+NiCr+Ni(F) substrate was 8 ± 1 µm, while the AC+Ni(F) sample was 4 ± 1 µm. Some defects were observed in the Ni coating in both flash plated sample types, in the form of perpendicular cracks through the coating, as well as pores at the coating/BM interface. The composition of the coating was measured using EDS for the Ni(F) samples, and the results are present

in Table 5.1.1. The Ni(F) layer for both sample types were mostly Ni, with minor amounts of Fe present.

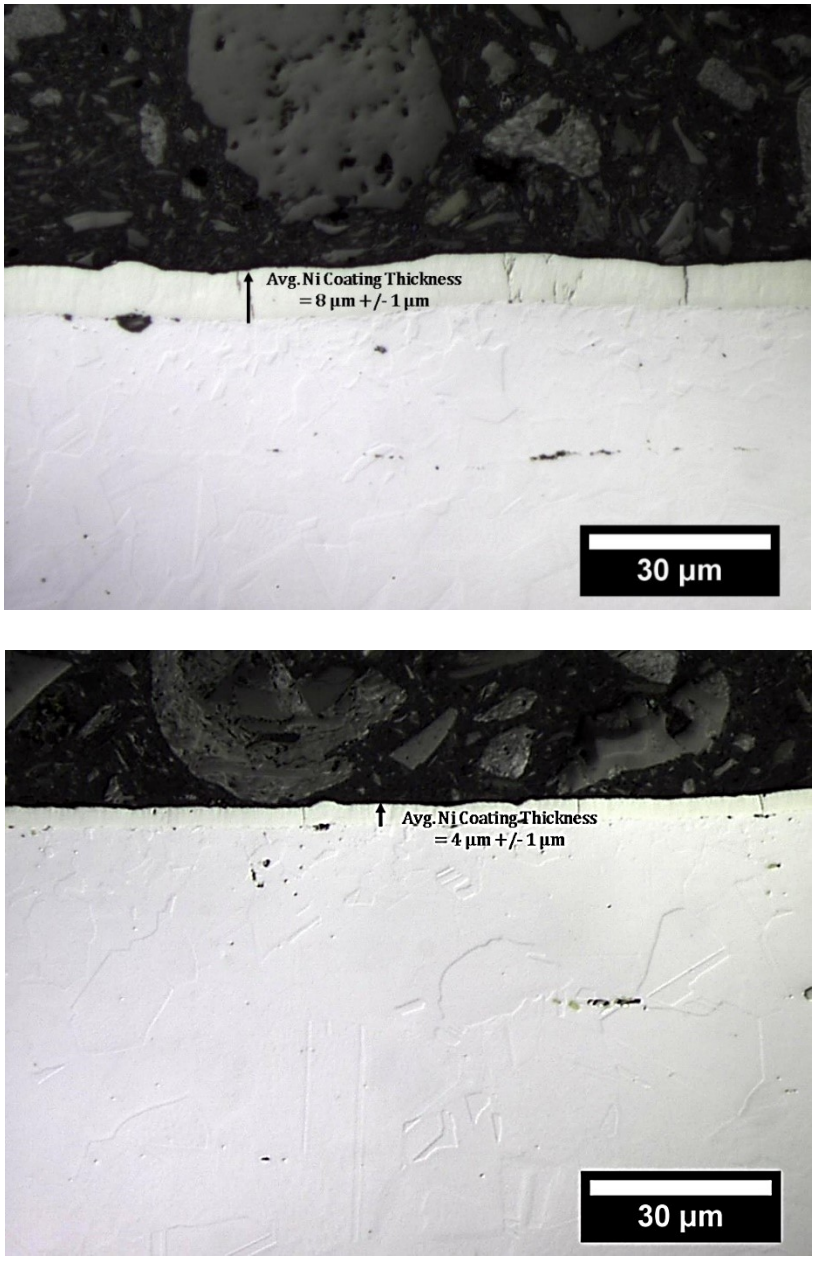

Figure 5.1.3 - Optical micrographs of polished cross sections for Ni(F) substrates in as-received condition: a) AC+NiCr+Ni(F), b) AC +Ni(F)

Table 5.1.1 - Chemical composition of Ni coating in Ni(F) samples

Sample Type	Chemical Composition [wt.]	
	Ni	Fe
AC+NiCr+Ni(F)	99.2	0.8
AC+Ni(F)	99.5	0.5

5.2 Scanning Electron Microscopy

An FE-SEM micrograph of the surface was taken for each of the different surface preparations studied. Figure 5.2.1 contains the FE-SEM micrograph for the AC sample type. The FE-SEM micrographs revealed that for the AC type substrate, the surface was characterised by striations caused from the AC process. The striations were randomly oriented and varied in size.

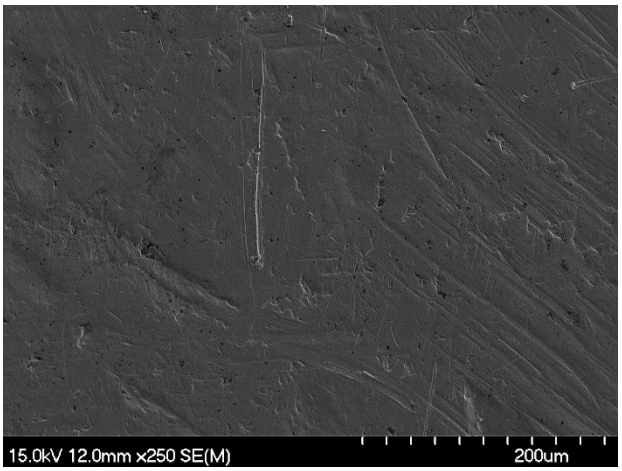

Figure 5.2.1 - FE-SEM micrograph of the surface for AC sample

The FE-SEM micrograph for the AC+NiCr sample is present in Figure 5.2.2. The surface of this sample type was characterised in Figure 5.2.2.

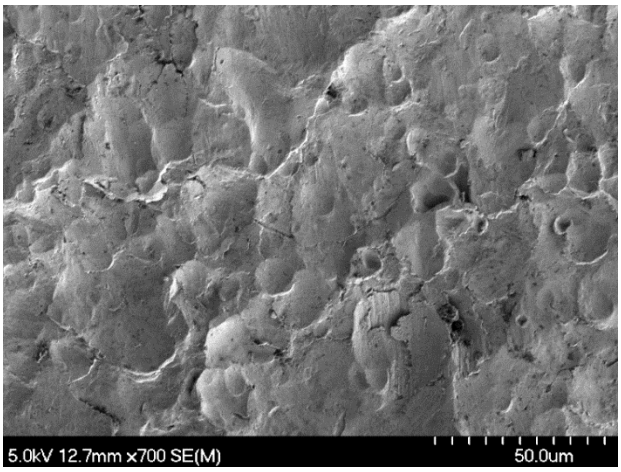

Figure 5.2.2 - FE-SEM micrograph of the surface for AC+NiCr sample

Observation of the FE-SEM micrograph for AC+NiCr+Ni(F) sample, Figure 5.2.3, revealed that the surface of the Ni(F) sample has a dendritic morphology. The electrolytic plating process resulted in the growth of a dendritic Ni coating on the surface of the IN718 BM. The cracks visible in Figure 5.1.3 a) were also seen in Figure 5.2.3, and there was also the presence of growth defects in the form of craters on the surface. The cracks in the coating were observed to travel through the crater-like defects.

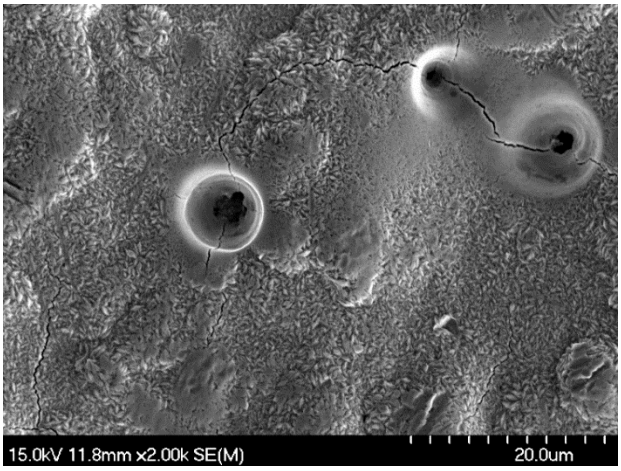

Figure 5.2.3 - FE-SEM micrograph of the surface for AC+NiCr+Ni(F) sample

Figure 5.2.4 contains an FE-SEM micrograph for the AC+NiCr+Ni(B) sample. The general topography of the surface resembled that of the AC+NiCr sample, in terms of the wavy and dimpled appearance. The dendritic morphology present in Ni(F) samples was absent for brush plated samples. There did appear to be some foreign particles present on the

surface of the brush plated sample, that were not present in the AC+NiCr sample. These particles may either be blast media embedded in the surface from the NiCr step or may be localised plating from the brush plating process.

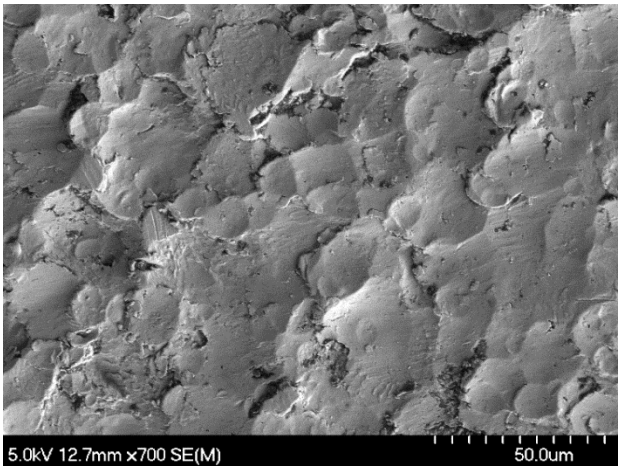

Figure 5.2.4 - FE-SEM micrograph of the surface for AC+NiCr+Ni(B) sample

Figure 5.2.5 contains an FE-SEM micrograph of the AC+Ni(F) sample. The surface of this sample type was near identical to the other Ni(F) substrate. Appendix B contains additional FE-SEM micrographs of the surface prepared substrates.

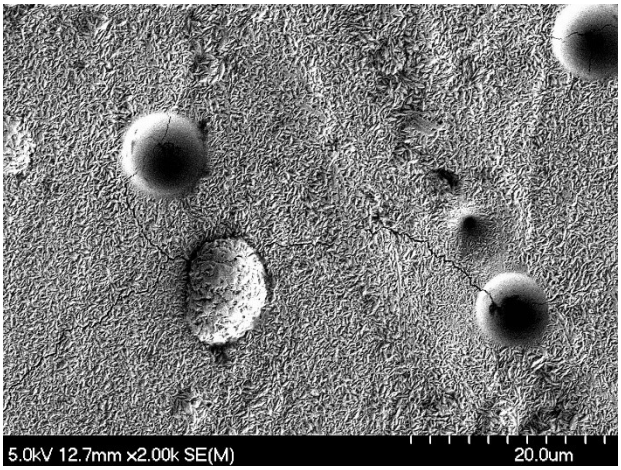

Figure 5.2.5 - FE-SEM micrograph of the surface for AC+Ni(F) sample

5.3 Laser Scanning Confocal Microscopy

Figure 5.3.1 contains the measured surface roughness for the surface prepared IN718. The error bars represent the standard deviation for ten measurements. Laser + optical

micrographs and height maps can be found in Appendix C. The AC+NiCr+Ni(B) sample had the highest roughness. Samples that were subject to a NiCr step had very similar roughness values. Samples absent of a roughening step had comparable roughness values. The No Prep sample also had a relatively high standard deviation.

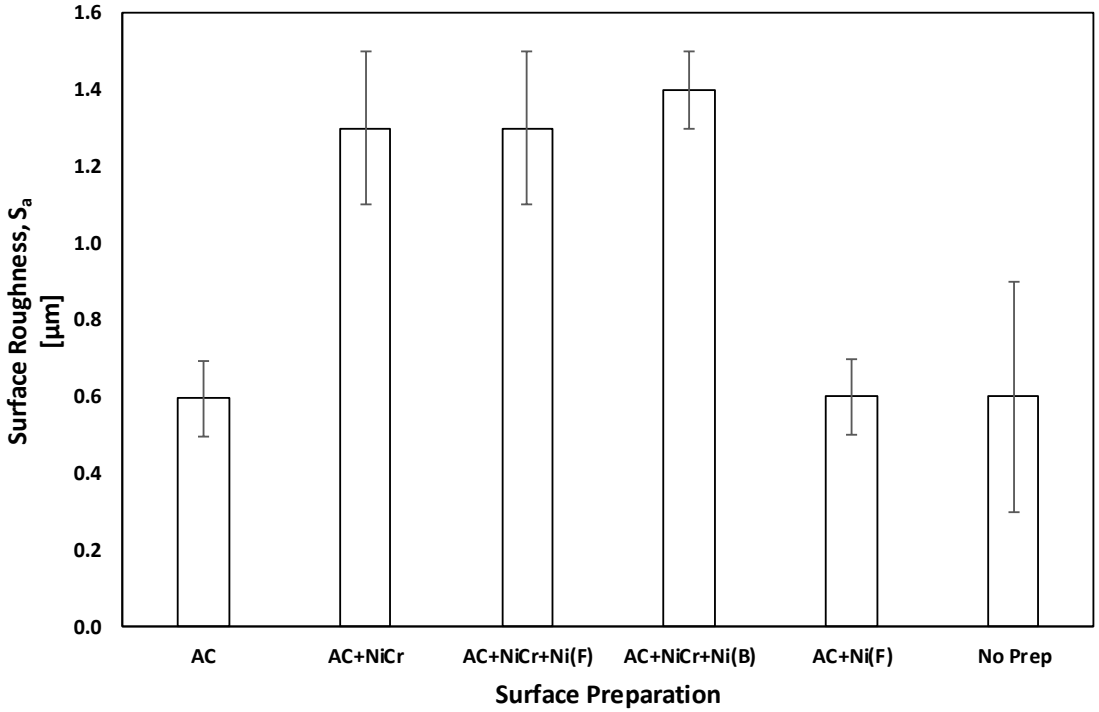

Figure 5.3.1 - Measured surface roughness (S_a) of surface prepared substrates

CHAPTER 6 Influence of Surface Preparation on Wetting & Spreading of Molten BNi-2 on Inconel 718

6.1 Thermal Analysis

Typical DSC traces obtained from an undersized foil experiment using AC+NiCr and an AC+NiCr+Ni(F) BM are found in Figure 6.1.1. Appendix D contains examples of DSC traces from undersized foil TLPB half joints using remaining base metal types.

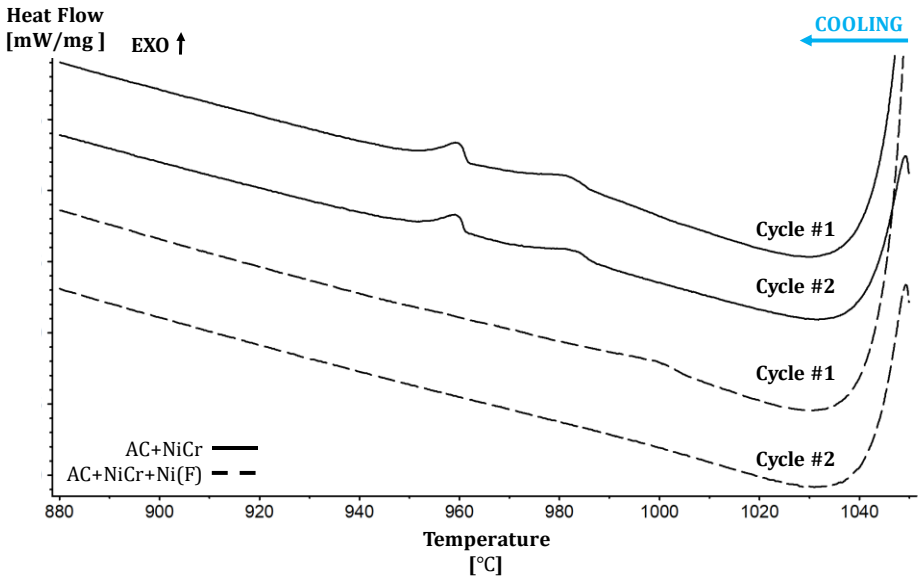

Figure 6.1.1 - DSC traces of AC+NiCr & AC+NiCr+Ni(F) samples using undersized foil

The DSC traces belonging to the AC+NiCr sample contained two broad exothermic peaks present on each cooling segment. As previously mentioned, these peaks are associated with the athermal solidification of the residual liquid into binary and ternary eutectic phases on cooling. With increased cycling there is a reduction in the size of the exothermic peak, which is evidence of decreased liquid fraction (progression of IS) [56]. Since there was liquid remaining on the final cooling segment, it can be deduced that the IS process was incomplete. DSC traces of base metal surface processing routes that omitted a Ni(F) step also had exothermic peaks remaining on cooling to room temperature.

Ni(F) samples showed a single, much broader exothermic peak on the first cooling segment. On the second cooling segment, there was no evidence of an exothermic peak indicating that the liquid had completely isothermally solidified at T_B. The Ni(F) samples resulted in complete IS after just two cycles.

6.2 Spreading Index

Figure 6.2.1 contains stereo micrographs of the undersized foil DSC experiments. Samples that were subject to AC, AC+NiCr, and No Prep exhibited poor wetting. The shape of the FM was constant before and after the experiment. The AC+NiCr+Ni(B) sample was subject to some degree of wetting by the molten BNi-2. The Ni(F) samples showed superior wetting and spreading after brazing. The shape of the spreading front differs from the initial foil shape, and the FM contact area after brazing was significantly increased.

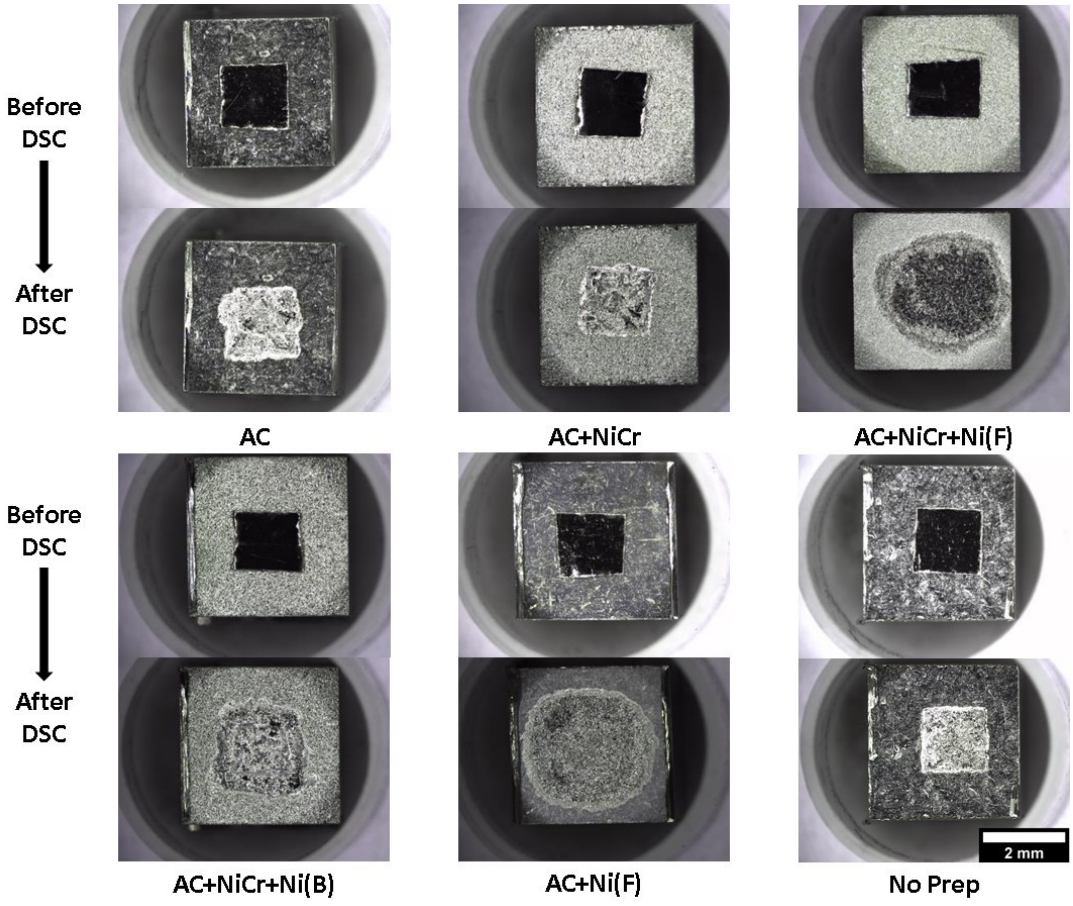

Figure 6.2.1 - Stereo micrographs of undersized foil TLPB half joints before and after DSC testing

The FM contact area was measured on the stereomicrographs both before and after brazing. The spreading index, N, is a simple measure of FM wettability and is calculated as the ratio of FM contact area after brazing A_f, divided by the initial contact area A_o. A large N value represents high wettability of the molten FM. The spreading index is plotted for the base metal surface preparation methods of interest in Figure 6.2.2. The error bars represent the standard deviation amongst the three trials.

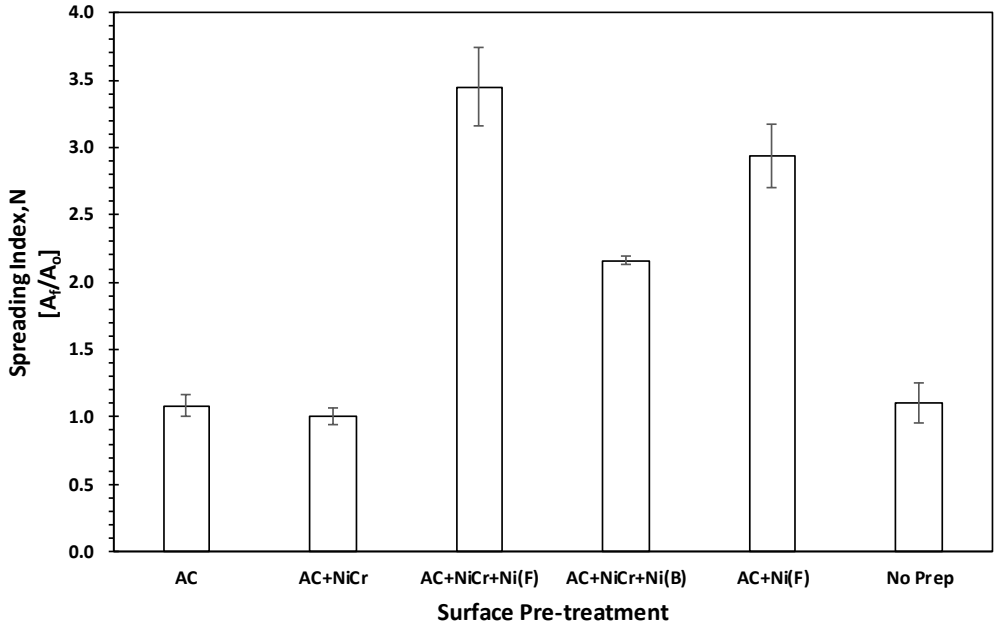

Figure 6.2.2 - Spreading index for various IN718 surface processing routes

Samples absent of a Ni plating showed poor wetting and spreading behaviour compared to samples that had a Ni plating present. The shape and area of the BNi-2 FM remained more or less constant after heating and holding at T_B. Superalloys are subject to what is known as selective oxidation. Despite Ni being the primary element in most superalloys, oxide scales other than NiO develop during exposure to high temperatures [5]. The type of oxide present is affected by the alloy composition, the atmospheric service conditions, and surface condition [70]. Alloys that possess low amounts of Al and high amounts of Cr, such as IN718, exhibit Group II oxide scales. Group II oxide scales involve an external scale of Cr_2O_3 and internal precipitation of Al_2O_3 sub-scale. The thermodynamic stability of the Al_2O_3 and Cr_2O_3 oxide is much greater than NiO, and thus the chromia and alumina scales dominate at high temperature [5]. As mentioned earlier in Chapter 1.5.3, liquid

metals possess generally poor wettability on metal-oxides. The work of adhesion is less than the work of cohesion, and thus wetting and spreading is inhibited.

Samples containing a Ni(F) step exhibited superior wetting, and therefore had a high spreading index compared to other surface pre-treatments tested. The variability in spreading was higher for Ni(F) samples than for other sample types. The presence of a Ni(F) plating resulted in an increase in adhesive forces between the liquid FM and the BM substrate.

A block flow diagram of the surface processing routes used in TLPB on IN718 with BNi-2 FM is found in Figure 6.2.3. The surface roughness and spreading index are included within each chart element to compare the influence each processing step has. Upon analysis of Figure 6.2.1, Figure 6.2.2, and Figure 6.2.3, it was determined that the highest degree of base metal wettability was achieved using a Ni(F) step process. Surface roughness was determined to play a minor role in increasing the wettability of the IN718 substrate, and no direct relation between wettability and surface roughness was observed. The increased roughness from the NiCr step provided only a minor increase in wettability compared to the Ni(F) sample with the roughening step absent. Therefore, it can be postulated that the requirement for a blasting step prior to Ni(F) plating may not entirely be necessary to ensure full wetting through the joint gap. Ni brush plating provided increased wettability compared to samples absent of a Ni plating, but to a lesser extent than Ni(F) plating did. The third row of possible process routes shown in Figure 6.2.3 was the only combination where increased roughness resulted in increased wettability. From this analysis, it was determined that wettability of the surface was controlled more by the presence of a protective Ni(F) layer than changes in surface roughness.

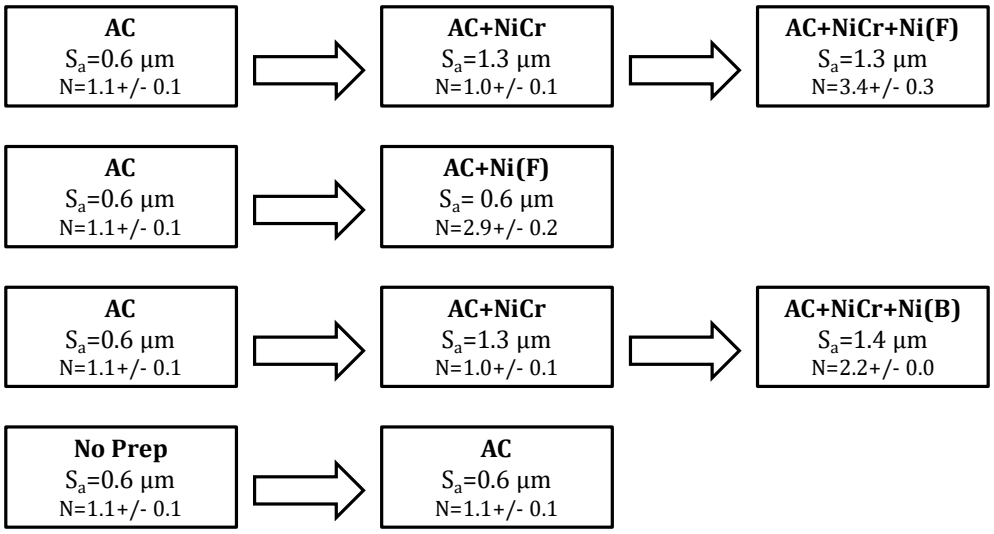

Figure 6.2.3 - Block flow diagram depicting the impact of BM surface processing on surface roughness and FM wettability

Figure 6.2.4 contains a graphic illustrating the two extreme cases of wetting and spreading behavior displayed by BNi-2 on the various surface prepared IN718 BM ingots. Note that the dimensions of the FM and BM are not to scale. Case A represents the situation where poor wetting conditions existed and little to no spreading of the FM across the faying surface occurred. Whereas Case B is the state where excellent wetting conditions were present and significant spreading of the molten FM across the faying surface occurred. Case A results in the final gap width, w_o, being approximately equal to the starting width of the foil, w_{foil}. Case A half-joints have a spreading index, N, close to unity and approximately equal FM contact area before and after the two cycle DSC experiment. Case B results in a significantly smaller final gap width than the original foil width, and a spreading index much greater than unity.

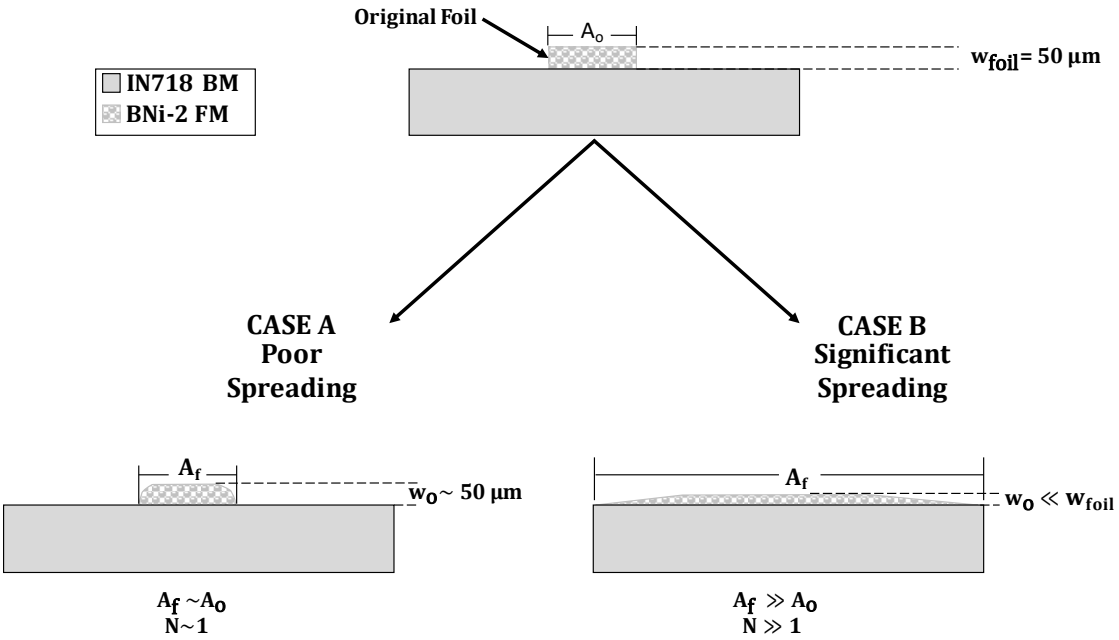

Figure 6.2.4 - Schematic depicting the two extreme cases of wetting and spreading behavior exhibited in an IN718/BNi-2 half-joint using an undersized FM foil

IN718 base metal surface preparation routes investigated in this study that exhibited Case A wetting and spreading behaviour include the AC, AC+NiCr, and No Prep base metals. Both Ni(F) substrates displayed Case B wetting and spreading behaviour. The Ni(B) sample type was intermediate between both cases. In the Case B situation of the Ni(F) samples, the molten FM can wet and spread across the faying surface, resulting in a reduced w_o. Since the w_o was much smaller in Case B samples, complete IS was able to occur within the 25 minutes liquid duration experienced, as evidenced by the DSC results in Figure 6.1.1. In terms of Case A, the w_o after the melting of the FM remains close to the nominal thickness of the amorphous foil. Since the w_o is much larger, complete IS does not occur within the liquid duration experienced during the DSC test. The presence of an exothermic peak on the final cooling segment of the DSC trace for the AC+NiCr sample in Figure 6.1.1 is confirmation that complete IS did not occur.

6.3 Microstructural Examination

w_o was measured for the undersized foil experiments using surface prepared IN718 using the same approach taken in as described in Chapter 4.2. The average w_o for the three undersized foil trials is plotted versus the spreading length in Figure 6.3.1. The spreading

length is simply the length of BM that is in contact with the FM. The error bars represent the standard deviation amongst the three trials.

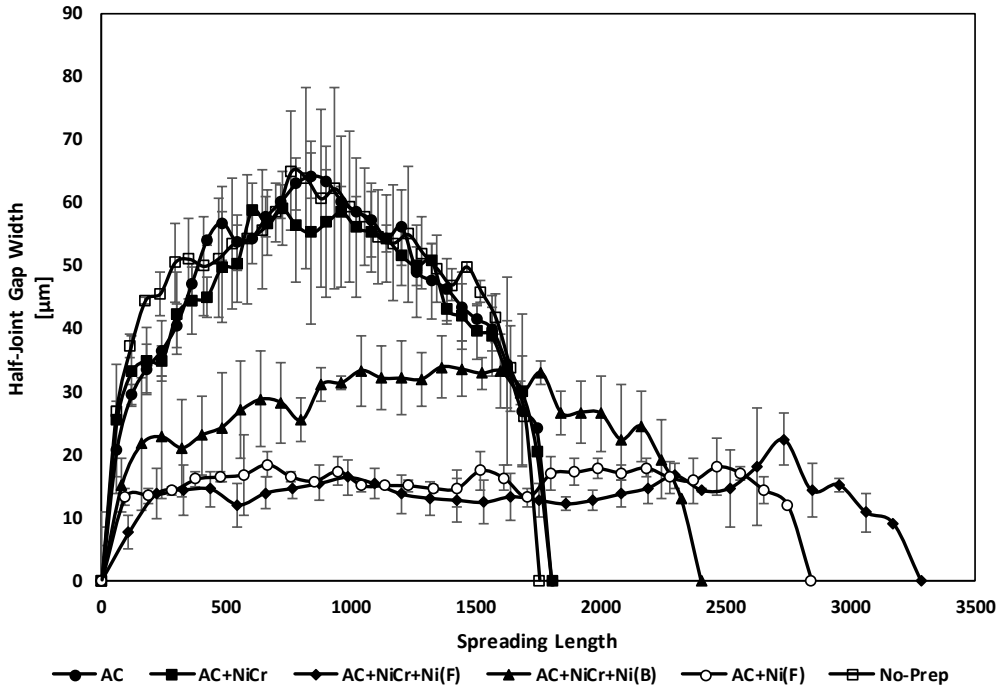

Figure 6.3.1 - Plot of half-joint width vs. spreading length for undersized foil DSC experiments

Micrographs taken at the center of the joint for select undersized foil experiments are presented in Figure 6.3.2. The complete set of micrographs, including micrographs of joint extremities are found in Appendix E.

a)

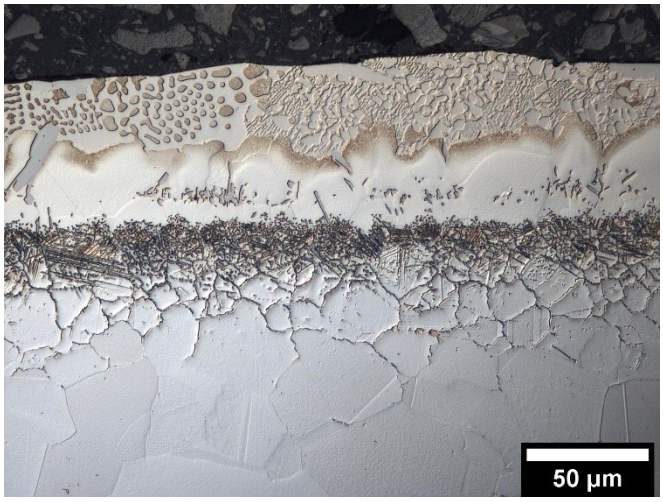

b)

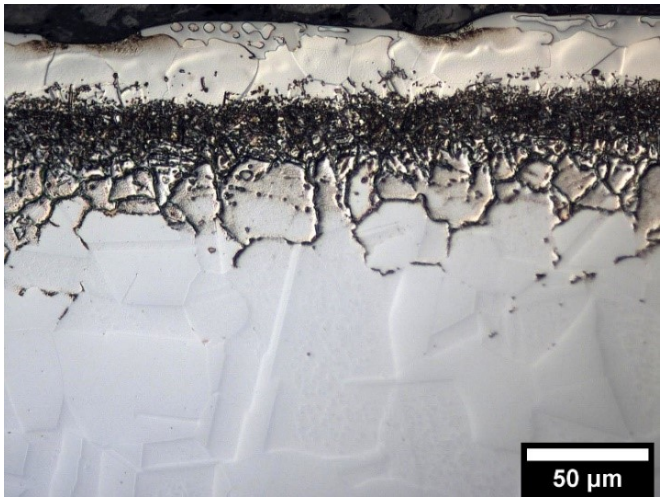

c)

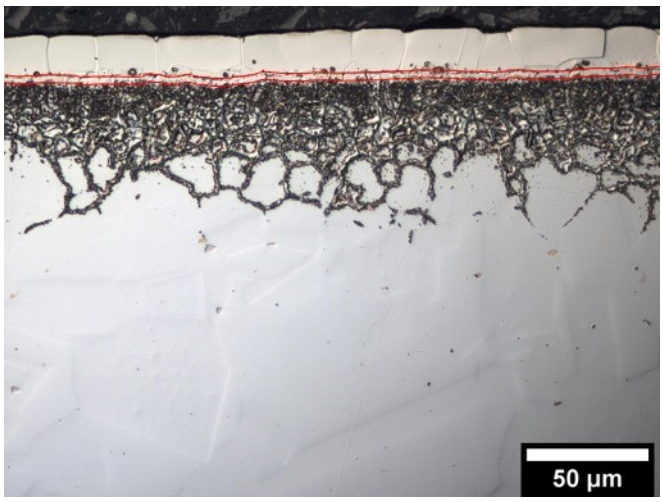

Figure 6.3.2 - Post DSC micrographs of polished cross sections from select undersized foil experiments subject to 2 cycles (1050°C – 5min-870°C); a) AC+NiCr, b) AC+NiCr+Ni(B), c) AC+Ni(F) (etched)

Table 6.3.1 - Average w_o for surface prepared IN718/BNi-2 half-joints

Sample Type	w_o [μm]
AC	47 ± 13
AC+NiCr	46 ± 11
AC+NiCr+Ni(F)	13 ± 4
AC+NiCr+Ni(B)	27 ± 6
AC +Ni(F)	15 ± 4
No Prep	47 ± 10

The microstructure present within the TLPB half-joints from undersized foil experiments was as described in Chapter 4.2 for the ISP experiments. The same microstructural regions (ASZ, ISZ, DAZ, and BM) were observed, as seen in Figure 6.3.2. Samples subject to poor wetting and spreading, such as AC+NiCr, had a larger w_o value, and were subject to more variation in w_o as indicated by Figure 6.3.1 and Table 6.3.1. A larger liquid width was present on samples that exhibited poor wetting (i.e. AC+NiCr). Since the liquid width (i.e. w_o) was larger, a significant ASZ region remained in these samples. The presence of an ASZ in the AC+NiCr sample validates the conclusion that the solidification peak present on the final cooling segment of the DSC trace (Figure 6.1.1) was due to incomplete IS. A smaller width of ASZ is present in the AC+NiCr+ Ni(B) sample as the FM spread to a smaller initial liquid width, as seen in Figure 6.3.1 and Figure 6.3.2.

Ni(F) samples resulted in a smaller liquid width due to superior spreading. Only an isothermally solidified region was present for these samples after just two cycles, and no ASZ was present in the microstructure. The microstructure observed for the Ni(F) sample supports the conclusion determined from Figure 6.1.1 that the Ni(F) sample had been completely isothermally solidified. Note there was also the presence of microporosity located at the interface between the Ni plating and the IN718 BM. Some microporosity was also observed in the as-received condition, but the extent of microporosity was increased compared to the as-received condition. The increased degree of porosity observed after brazing could be due to the Kirkendall effect. As will be outlined below, interdiffusion between the plating and the parent metal occurs during heating. This mass transfer may lead to an imbalance of diffusion and the formation of Kirkendall pores.

There was also the presence of a denuded zone in Ni(F) samples. The two red lines in Figure 6.3.2 c) indicate the boundaries of the denuded zone. Sample types that did not contain a Ni(F) layer did not have a denuded zone present, and the DAZ started at the BM/FM interface. Figure 6.3.3 contains optical micrographs taken at various locations along the length of an AC+Ni(F) IN718/BNi-2 half-joint.

a)

b)

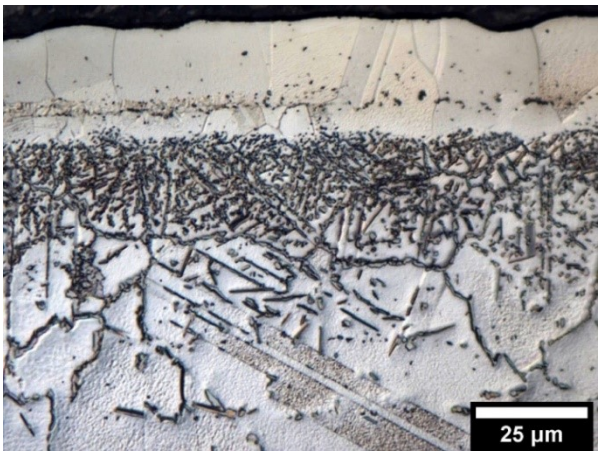

c)

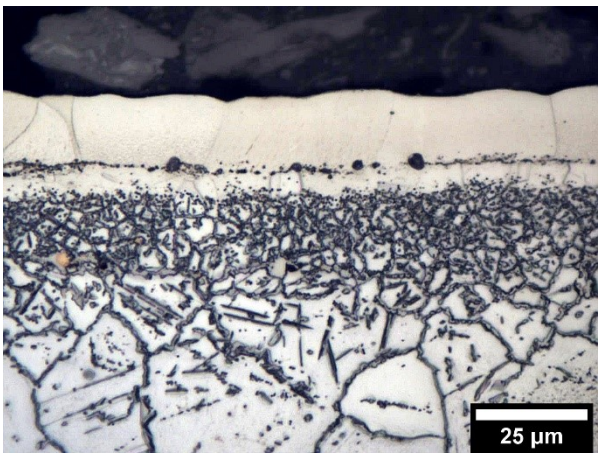

Figure 6.3.3 - a) LHS of an AC+Ni(F) IN718/BNi-2 half-joint, b) further toward the center of the half-joint, c) center of the half-joint (etched)

Figure 6.3.3 a) shows that near the spreading front of the FM there is ISZ, an intact Ni plating, a denuded zone, DAZ, and IN718 BM regions. Figure 6.3.3 b) and c) revealed that

as the thickness of FM above the plating increases (i.e. at a location towards the center of the half-joint) the distinct layer associated with a Ni plating is no longer visible. This behaviour was also displayed for the AC+NiCr+Ni(F) samples.

Figure 6.3.4 shows FE-SEM micrographs of the AC+NiCr+Ni(F) and AC+Ni(F) samples captured at a location away from the FM /BM interface after DSC cycling. The presence of voids at the BM/plating interface in both Ni(F) sample types was observed. EDS point scans were conducted within the plated region shown in Figure 6.3.4 a) and b), and the results are summarised in Figure 6.3.5.

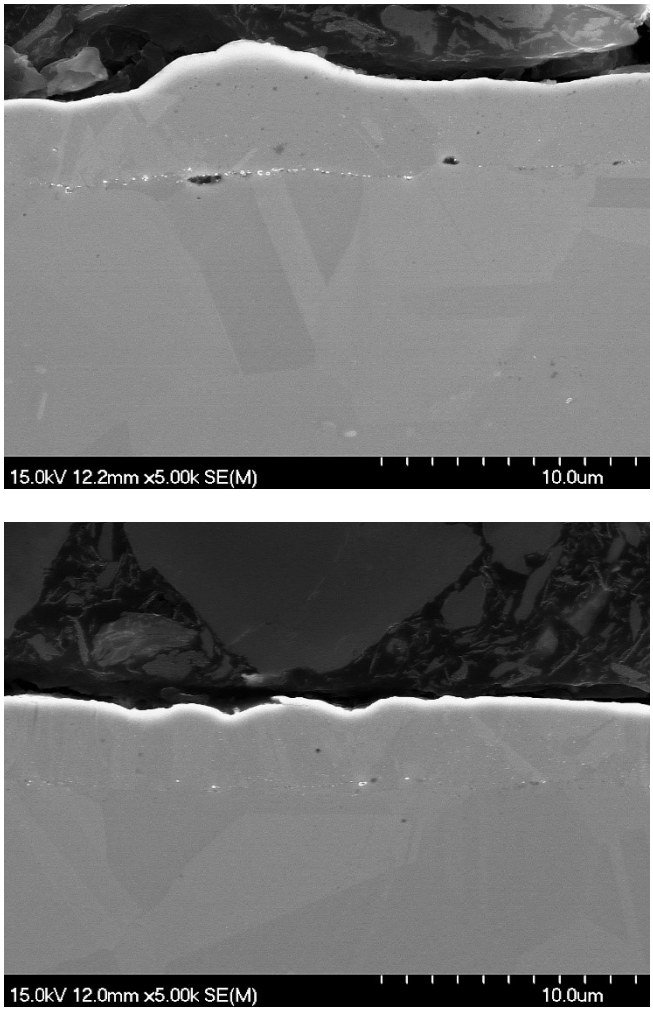

Figure 6.3.4 - FE-SEM micrograph of undersized foil half-joint taken away from the FM /BM interface: a) AC+NiCr+Ni(F), b) AC+Ni(F)

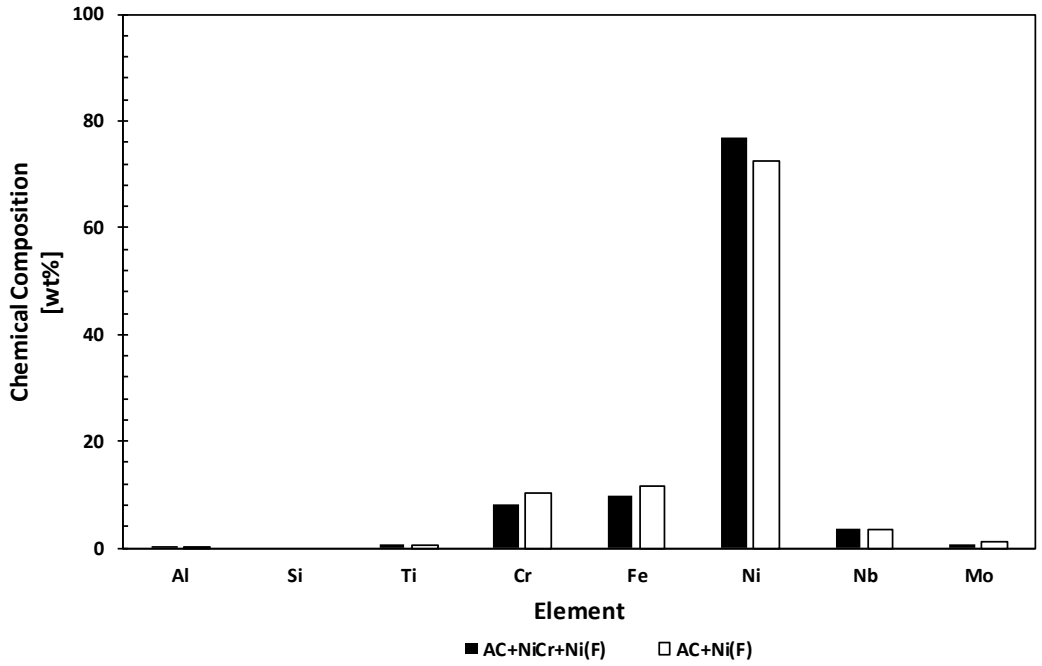

a)

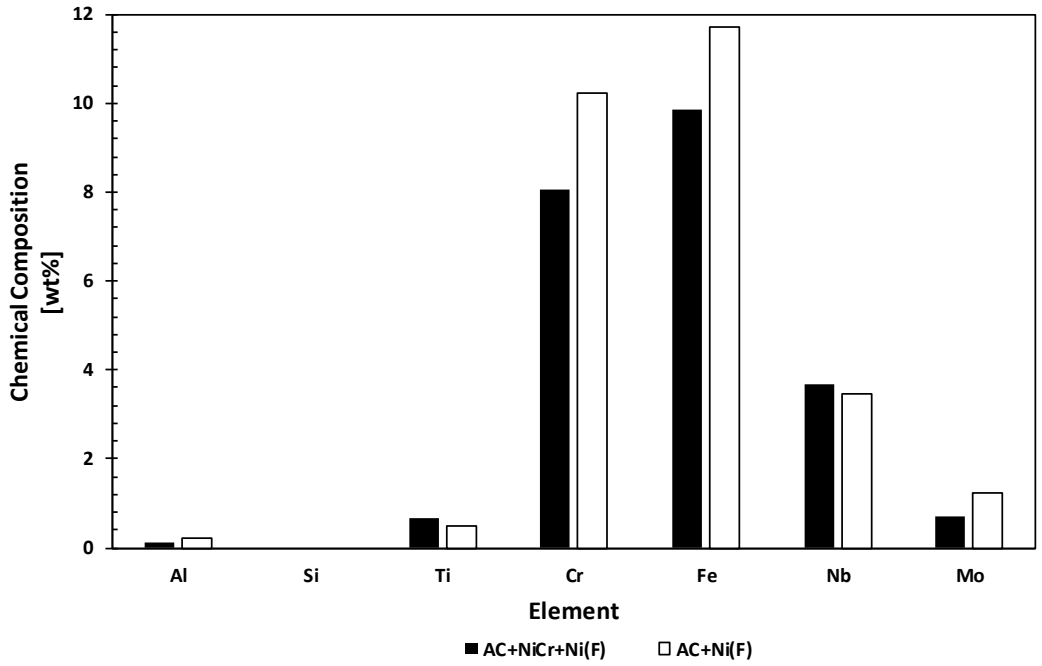

b)

Figure 6.3.5 – a) EDS point scan results of average plating composition after heating for two cycles (approx. 25 mins liquid duration), b) Ni data removed

The Ni plating is clearly visible adjacent to the base metal surface in both Figure 6.3.4 a) and b). Note there is no presence of a DAZ in these images, which serves as further

evidence that this region contains no FM, and the distinct layer above the BM is the Ni plating. In both Ni(F) samples, the EDS scans revealed that the plating region had the presence of BM elements that were not initially present within the Ni plating. During heating to T_B and during the brazing cycle, solid-state interdiffusion resulted in alloying of the plated layer with BM elements. Despite the introduction of Cr into the plated layer, the amount of Cr is significantly reduced compared to the IN718 BM.

The amount of Cr present at the surface was reduced, such that a Cr_2O_3 layer was not able to form on the surface of the Ni-plated IN718. It is postulated that the oxidation on the Ni-plated substrates was a Group I oxidation, where the scale is NiO with an internal sub-scale of Cr_2O_3, Al_2O_3, and/or $Ni(Al, Cr)_2O_4$ [5]. According to Gale & Wallach, localized reduction of Ni based substrate oxide close to a droplet of B containing FM can occur by the B initially present within FM [71]. According to Gale and Wallach [71], B is capable of reducing NiO by the following chemical reaction:

$$\boldsymbol{NiO + \frac{2}{3}B = Ni + \frac{1}{3}B_2O_3} \qquad \textbf{Eq. (6.3.1)}$$

The reduction of the NiO results in production of fresh metallic Ni that the FM can flow over. The work of adhesion is increased compared to when the NiO is present, and FM flow is reinitiated.

Figure 6.3.6 a) shows an FE-SEM micrograph of the same sample shown in Figure 6.3.4, but the image was taken at the location where the FM stopped spreading. The circles embedded within Figure 6.3.6 represent the approximate location of the EDS scans. On the left-hand side of Figure 6.3.6, there are four different regions of interest; the ISZ, the plating, the DAZ, and a region termed the denuded zone in between the DAZ and the Ni plating. The denuded zone forms as a result of the solid-state diffusion between the BM and the Ni plating. The average compositions of the denuded zone and the FM /plating regions determined by EDS are shown in Figure 6.3.6. The average chemical compositions for both IN718 and BNi-2 listed in Table 3.1.2 are also included in Figure 6.3.6 for comparison.

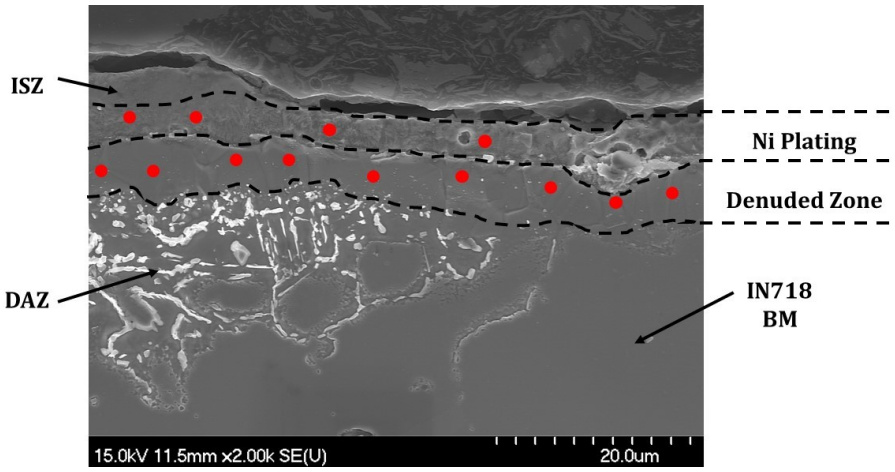

a)

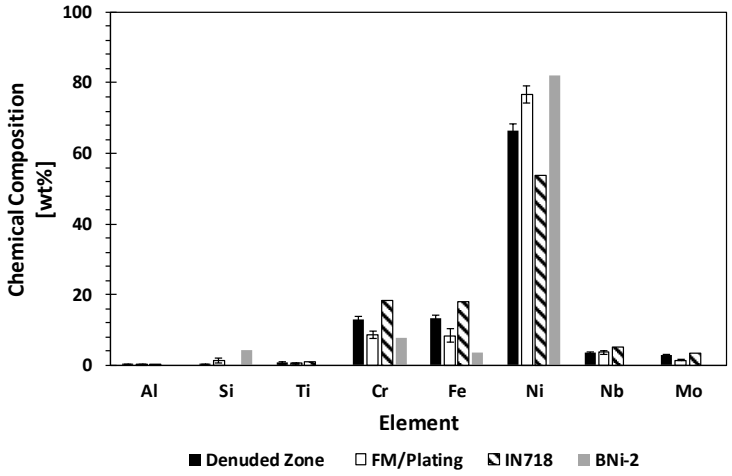

b)

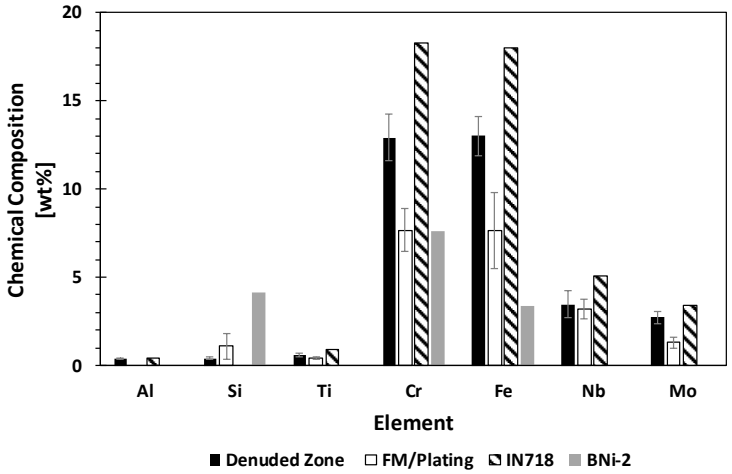

c)

Figure 6.3.6 – a) FE-SEM micrograph of AC+NiCr+Ni(F) half-joint taken at location where FM stopped spreading, b) EDS results, c) Ni data removed (etched)

The EDS results in Figure 6.3.6 showed that the denuded zone was depleted of BM elements such as Cr, Fe, Nb, and Mo. The denuded zone was also enriched in Ni. Since the plating was in contact with the FM on the left-hand side, this introduced Si, which is not present in the BM or the plating originally. The denuded zone also had Si present, but much less than was present in the plating or FM. Scans conducted in the alloyed Ni-plated region, were enriched in Cr, Fe, Al, Ti, Nb, and Mo. Another interesting feature observed in Figure 6.3.6, was that the DAZ precipitated at a location below the denuded zone.

According to Pouranvari et al. [8], in-situ precipitation of borides within the DAZ relies on short range diffusion of boron and boride-former elements from the adjacent surrounding superalloy matrix. This creates a region local to the boride precipitate that is depleted of boron. The B depleted zone can then act as a B sink, increasing the B concentration gradient and associated B diffusion flux into the BM [8]. Boride precipitation at T_B results in a reduction of t_{IS}, and thus more boride formers present in the BM results in shorter t_{IS}. The sum of the boride former elements (Cr + Mo + Nb + Ta +W), or in other words the boride former index, is related to t_{IS}. The larger the total sum of boride formers present within the BM, the larger the diffusive flux will be due to boride precipitation.

The denuded zone is depleted of boride formers present in the BM (such as Cr, Nb, and Mo). Therefore, precipitation of the DAZ starts at a location in the BM that contains an appropriate amount of boride former to initiate precipitation of the DAZ.

Figure 6.3.7 shows an FE-SEM micrograph of the same sample shown in Figure 6.3.4, but the image was taken near the center of the half-joint where the plating was completely covered by FM. There are three different regions of interest namely the ISZ, the DAZ, and the denuded zone. Unlike the region near the edge of the spreading filler described above, a plated layer is no longer distinguishable at the joint center. The average compositions of the denuded zone and the ISZ(or FM)/plating regions at the center of the half-joint determined by EDS are also shown in Figure 6.3.7, including the standard deviation. As in the case of Figure 6.3.6, the nominal compositions of IN718 and BNi-2 are also included for comparison.

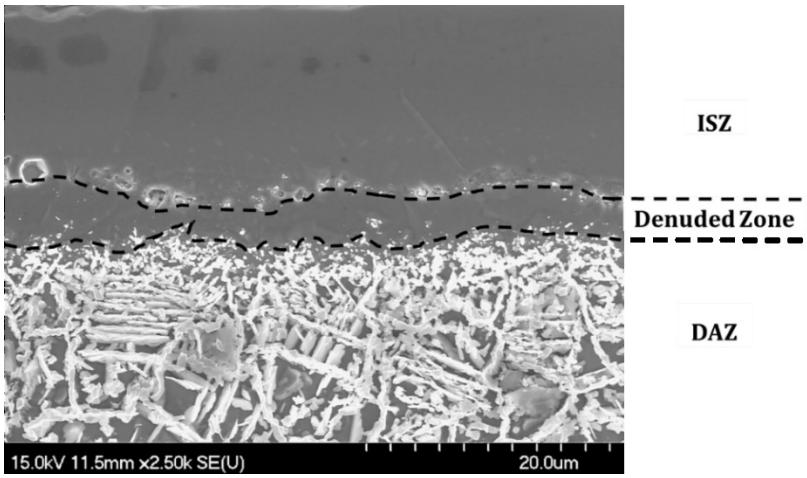

a)

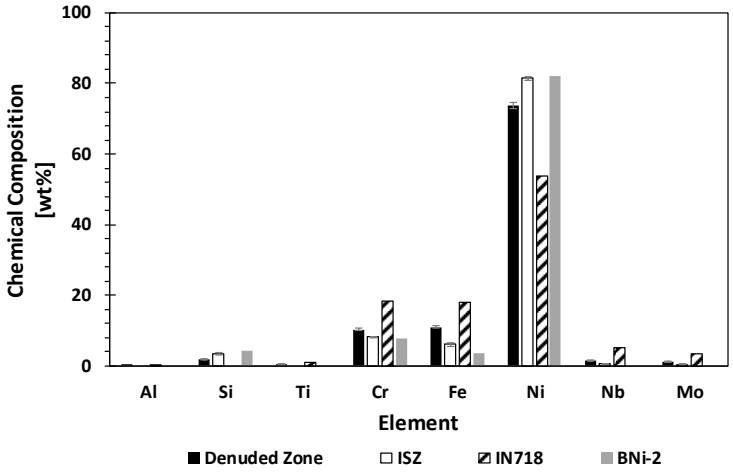

b)

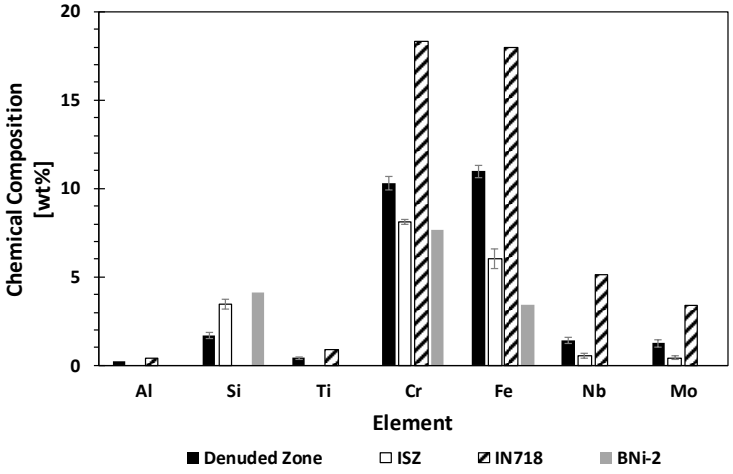

c)

Figure 6.3.7 – a) FE-SEM micrograph of AC+NiCr+Ni(F) half-joint taken at location near center of half-joint, b) EDS results, c) Ni data removed (etched)

Within the center of the joint, the chemical composition of the denuded zone was depleted of BM elements such as Al, Ti, Cr, Fe, Nb, Mo. The denuded zone had higher amounts of those BM elements than the FM /Plating region, but was lower in Si. Overall, the composition of the FM /plated region approached the nominal composition of BNi-2 (without B included) with the presence of some Nb and Mo. The amount of Fe present in the FM /Plating region was also slightly higher than nominally present in the FM . Since the w_o was larger in the center of the half-joint, the overall composition of the FM region was more homogeneous than regions at the extremity of the half-joint. The FM /plating regions at the edge of the half-joint, where the FM stopped spreading, had higher amounts of Fe, Nb, and Mo than in the center of the half-joint. The AC+Ni(F) sample showed similar behavior as the AC+NiCr+Ni(F) sample, and associated FE-SEM micrograph and EDS results can be found in Appendix F.

Figure 6.3.8 contains a schematic diagram of the proposed concentration profile that develops during heating to T_B in a Ni(F) IN718/BNi-2 half-joint.

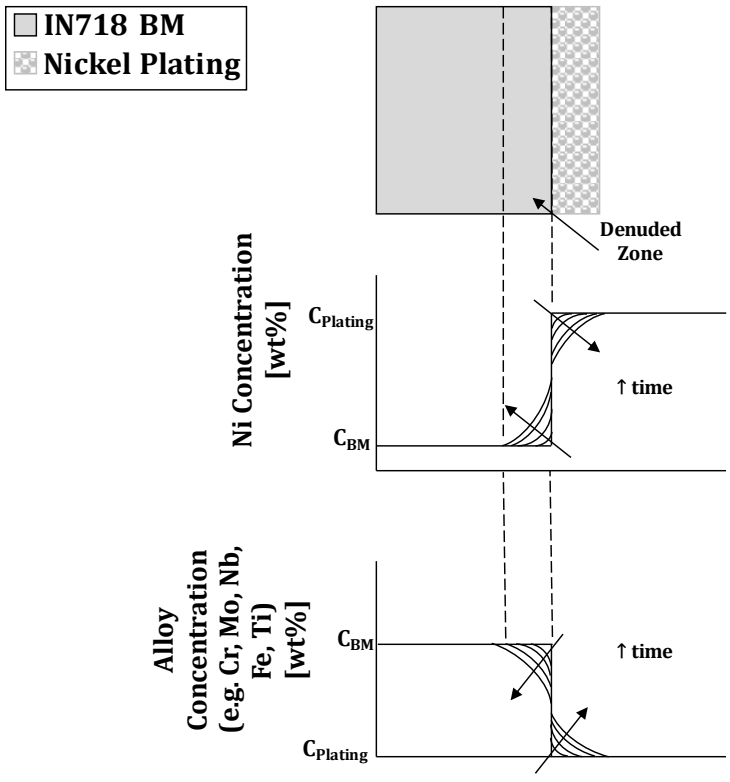

Figure 6.3.8 - Schematic diagram of development of concentration profile existing in a Ni(F) IN718 sample just prior to reaching the BNi-2 melting range

What the figure points out is that a chemical gradient is developed at the faying surface of the BM as a result of the Ni plating treatment. B diffusion and DAZ formation needs to occur in a chemical gradient. Since there is a gradient in the concentration of boride former elements in the denuded zone, the DAZ needs to form at a location with sufficient amounts of those particular elements. The impact of this chemical gradeint of the TLPB beahviour of a braze joint will be examined in Chapter 7.

CHAPTER 7 Effect of Surface Preparation on Transient Liquid Phase Bonding Behaviour of Inconel 718/BNi-2

After the wetting and spreading behaviour was characterized, cyclic DSC testing using half-joints was conducted on surface prepared IN718 BM to determine the influence of surface preparation on the kinetics of IS. Note that the No Prep sample type was not included in this chapter. It exhibited very poor wetting behaviour and a situation where no surface preparation is done on IN718 prior to brazing is not reflective of practical brazing procedures.

7.1 Thermal Analysis

As previously mentioned, vital steps in determining the kinetics of a TLPB couple using DSC were to measure the solidification enthalpy of the FM alone and in thermal contact with the BM (diffusion barrier run), this was done as described in Chapter 4.1.1.

7.1.1 BNi-2 Foil Only and Diffusion Barrier Experiments

The average solidification enthalpy of the BNi-2 foil was measured as 235 ± 12 J/g (two trials), while the diffusion barrier run using a fully Nicrobraz coated AC 3.9 x 3.9 x 1.92 mm square BM resulted in a solidification enthalpy of 211 ± 11 J/g (three trials). In general, the shape and number of peaks present in the cooling DSC traces resembled those discussed in Chapter 4.1.1.Stereo images of the half-joints using various surface prepared IN718 ingots are found in Figure 7.1.1.

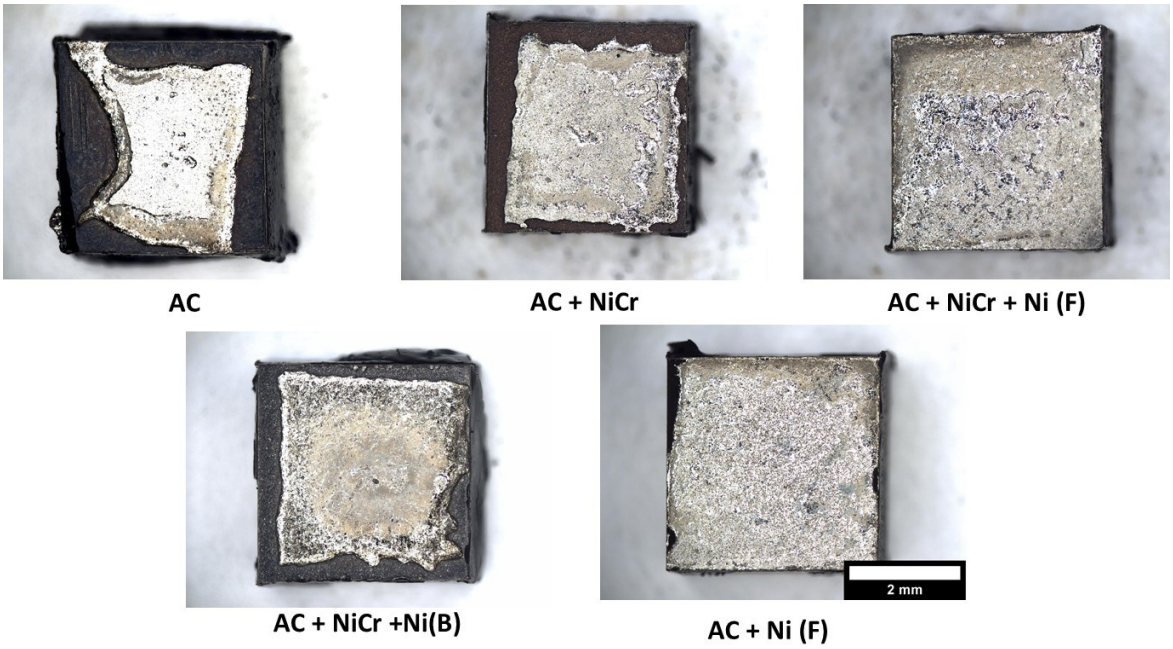

Figure 7.1.1 - Stereo images of TLPB half-joints using various Ni-plated IN718 ingots and BNi-2 foil (post DSC testing)

IN718 ingots subject to a Ni-flash plating process, both resulted in complete wetting and spreading of the BM. The Ni(B) sample did not result in complete wetting and spreading. The average percentage of FM coverage area was approximately 85 ± 7% for the AC+NiCr+Ni(B) sample. BM types that omitted Ni plating operations resulted in poor wetting and spreading. The wetting behavior observed for these surface prepared BM was as expected, based on results from the experiments described in Chapter 6.2.

Typical DSC traces obtained from the first five cooling segments from a full coverage experiment using an AC+NiCr+Ni (F) base metal sample are found in Figure 6.1.1. Appendix G contains examples of the first five DSC traces on cooling from full coverage TLPB half joints made using the remaining surface prepared BM types.

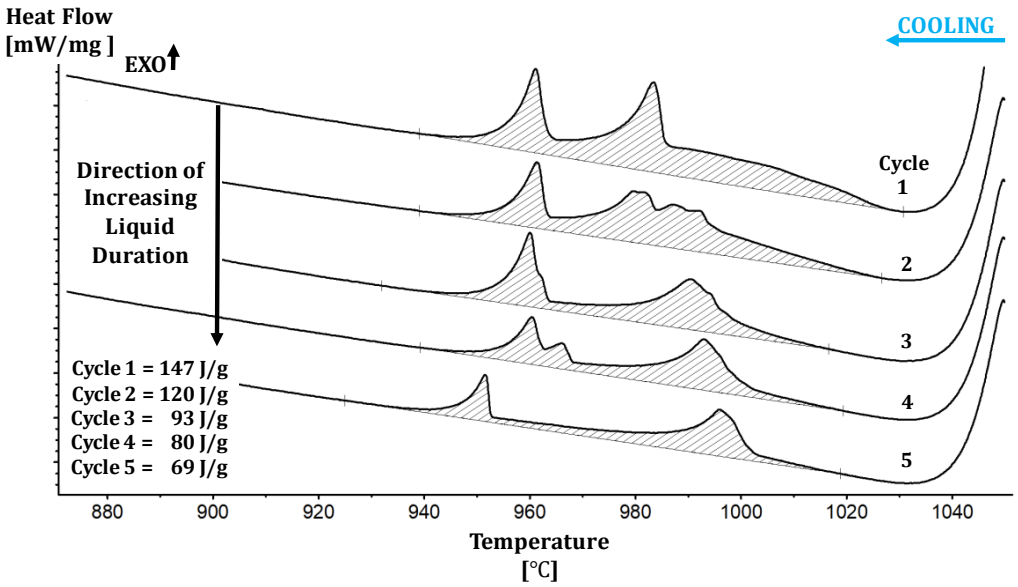

Figure 7.1.2 - First five cooling segments obtained after cyclic DSC testing of IN718/BNi-2 TLPB half-joint using an AC+NiCr+Ni(F) BM

As in other cases, the peaks observed on cooling were associated with the athermal solidification of the residual liquid into binary and ternary eutectic phases on cooling. As expected, with increasing number of cycles (i.e. liquid duration time), the magnitude of the solidification enthalpy decreases. Figure 7.1.3 compares the first cooling segment measured on the DSC trace for various surface prepared IN718/BNi-2 half-joints subjected to a cyclic thermal profile.

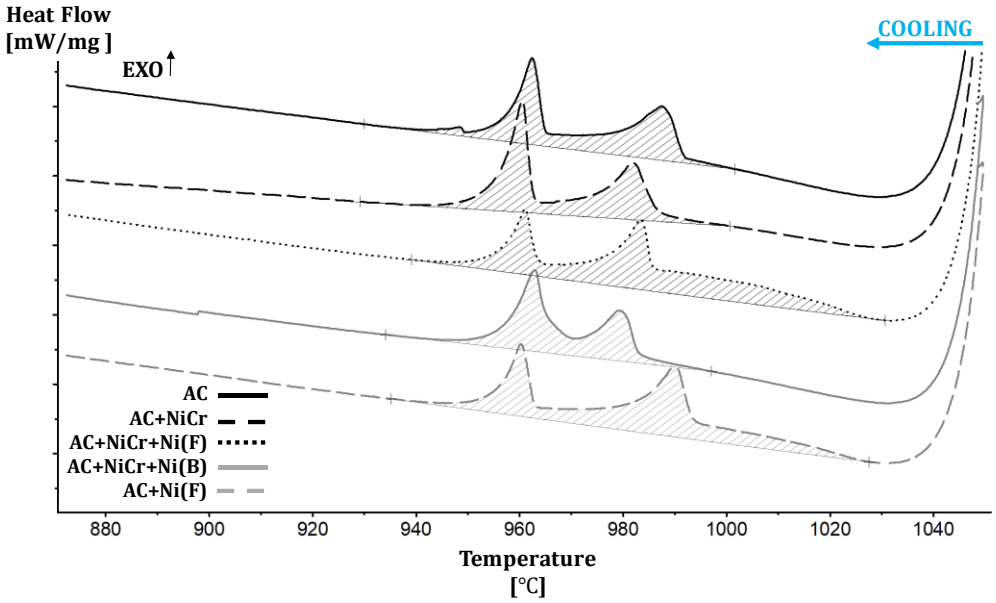

Figure 7.1.3 - DSC traces on first cooling segment for surface prepared IN718/BNi-2 half-joints using full size foil subject to cyclic thermal profile

Upon investigation of Figure 7.1.3, it was observed that sample types absent of a Ni(F) step only had two exothermic peaks present during the first cooling segment. The onset of solidification for these sample types was approximately within the range of 1000 – 1005°C. For the Ni(F) step samples, a broad exothermic peak was detected at approximately 1030°C. This broad high temperature peak is similar in character to that observed in the BNi-2 foil only and barrier experiment discussed in Chapter 4.1.1. The implications of this observation will be discussed later.

The solidification enthalpy is plotted against the square root of liquid duration for the surface prepared samples in Figure 7.1.4. The error bars represent the standard deviation in the measured solidification enthalpy amongst two trials for each surface preparation type.

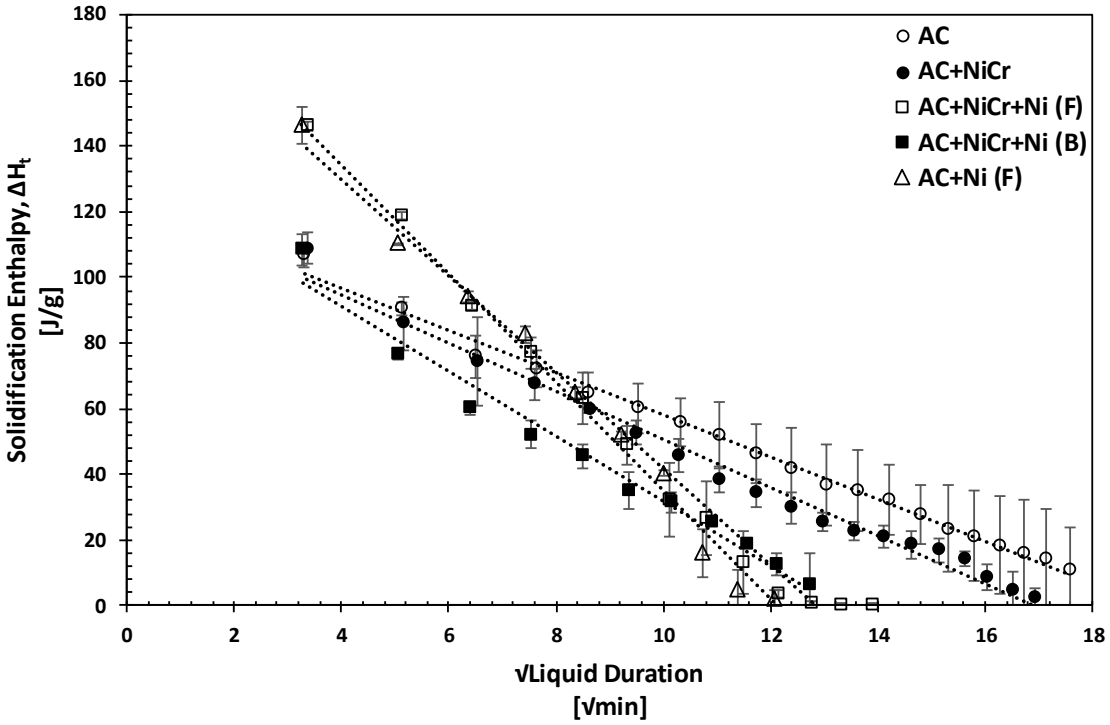

Figure 7.1.4 - Average solidification enthalpy vs. square root liquid duration for the surface prepared IN718/BNi-2 TLPB couples

The AC+Ni(F) sample type resulted in a larger solidification enthalpy than in the case of the AC sample on the first cooling segment. The AC+Ni(F) substrate also resulted in a steeper slope than the AC base metal. These same two remarks are also true for the AC+NiCr+Ni(F) sample shown in Figure 7.1.4. The AC+NiCr+Ni(B) sample shown in Figure 7.1.4 had a slightly lower initial enthalpy, and steeper slope than the AC+NiCr. As anticipated, a linear relationship was observed between the solidification enthalpy and the square root of liquid duration. The standard deviation in enthalpy measurements was largest for the AC and AC+NiCr samples, while the Ni-plated substrates showed a much smaller standard deviation. This is due to the fact that the Ni(F) samples consistently exhibited full spreading of the molten filler. The AC and AC+NiCr samples exhibited incomplete spreading which varied slightly from sample to sample.

7.2 Microstructural examination

7.2.1 Cyclic DSC experiments

Representative micrographs of TLPB half-joints using surface prepared BM are found in Figure 7.2.1 and Figure 7.2.2.

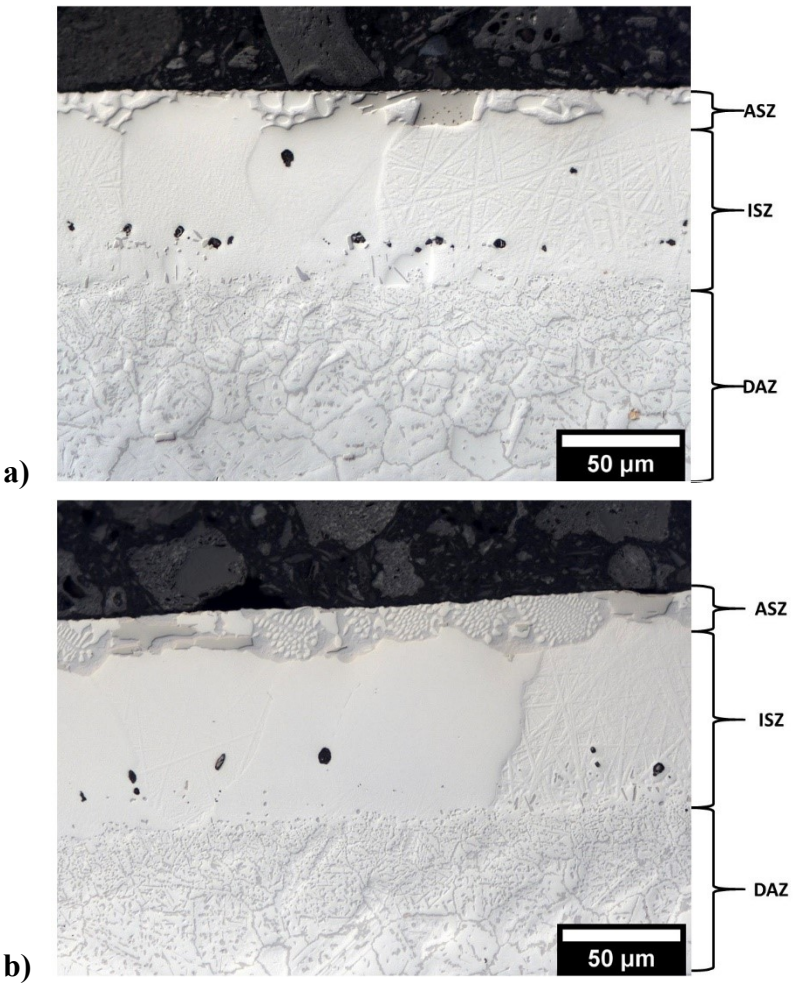

Figure 7.2.1 - Optical micrographs for surface prepared IN718/BNi-2 TLPB half-joints after 20 cycle DSC testing: a) AC, b) AC+Ni(F)

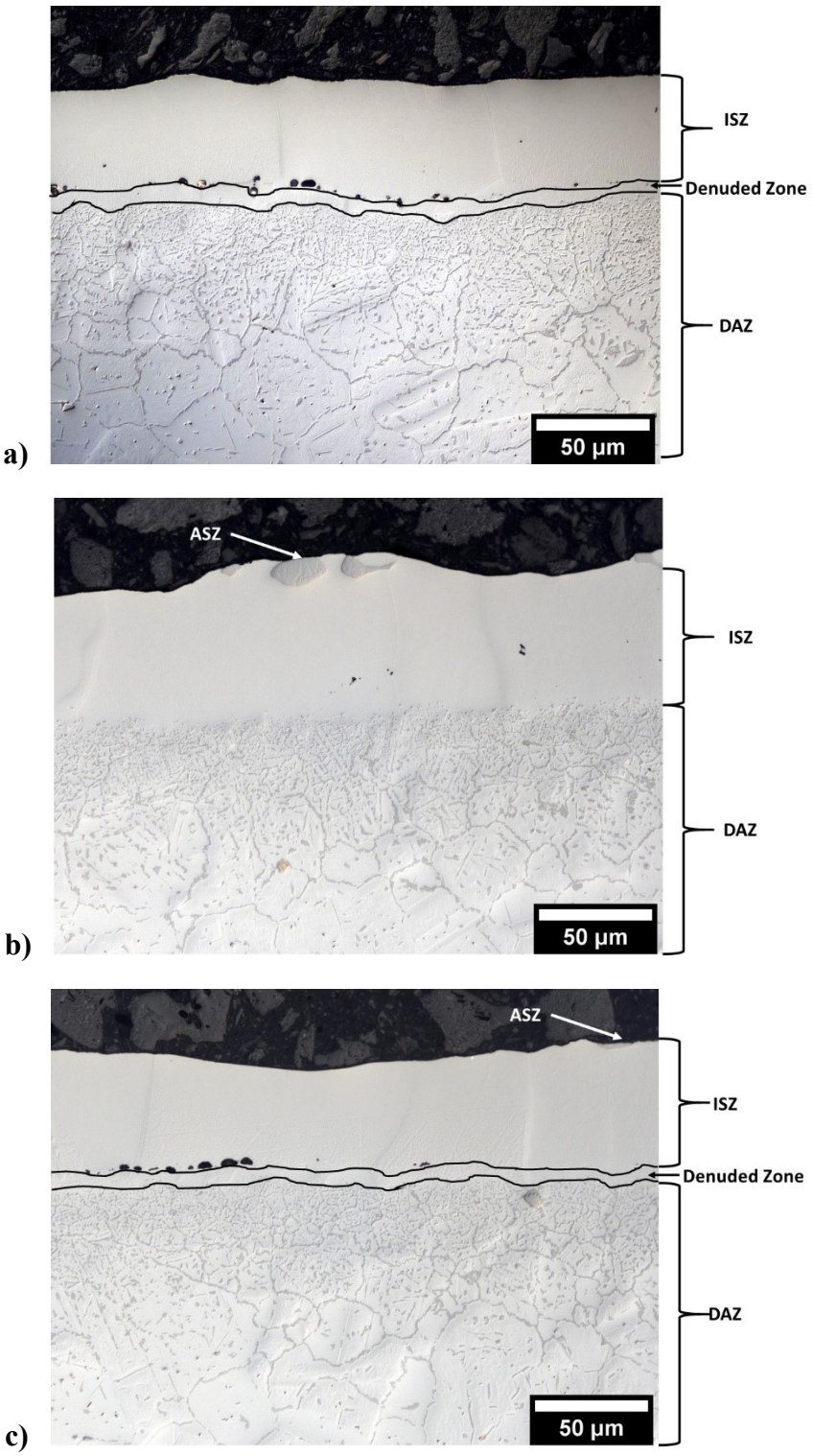

Figure 7.2.2 - Optical micrographs for surface prepared IN718/BNi-2 TLPB half-joints after 20 cycle DSC testing: a) AC+NiCr, b) AC+NiCr+Ni(F), c) AC+NiCr+Ni(B)

In terms of half-joints made using an AC base metal, the microstructure after the 20 cycle DSC test was characterised by mostly ISZ and DAZ. This sample also had a small layer of ASZ present. Since the AC samples were subject to poor wetting, the average $2w_o$ was increased. Due to this increased initial liquid width, IS did not go to completion after the cyclic DSC test. The microstructure had some ASZ present due to liquid remaining prior to cooling to room temperature, confirming incomplete IS. The ASZ present in the microstructure was also confirmed by the DSC measurements of Figure 7.1.4, as the AC sample never reaches 0 J/g of enthalpy. The phases present within the microstructure for the AC + NiCr sample type were similar to the AC type. Both of these surface preparation types also resulted in some amount of solidification enthalpy, as seen in Figure 7.1.4. Porosity within the ISZ of these sample types was also visible in Figure 7.2.1 and Figure 7.2.2. It should also be noted, that samples subject to poor wettability resulted in the largest standard deviation $2w_o$.

The microstructure of the Ni(B) sample was mostly ISZ and DAZ. Compared to the AC and AC+NiCr samples, the brush plated sample had a much smaller amount of ASZ observed. The localised application of the Ni plating in the AC+NiCr+Ni(B) sample resulted in some minor improvement in wetting and spreading as discussed in Chapter 6.2. Both Ni(F) sample types resulted in complete IS, and the microstructure consisted of an ISZ and a DAZ only. As in the case of the Ni(B) sample, in some cases a very minor amount of ASZ was observed that was not detected on DSC traces. Both types of samples containing a Ni(F) step resulted in full wetting of the base metal by the molten FM. This improvement of wetting and spreading observed in plated samples resulted in a reduction of the initial liquid width. Since the liquid was able to spread out to a smaller width, IS occurred to a greater extent during the cyclic DSC test. This was part of the reason for little or no solidification enthalpy and ASZ present in the room temperature microstructure. However, the raw enthalpy data of Figure 7.1.4 also indicated k_{IS} was higher in plated samples. This observation as well as efforts to account for different starting $2w_o$ values will be described in more detail below.

As seen in Figure 7.2.1 b) and Figure 7.2.2 b), the Ni(F) substrates had the presence of pores in the ISZ close to the ISZ/DAZ interface. These pores were also observed along the BM/plating interface of Ni(F) ingots in the as-received condition. As mentioned in Chapter

6.3, these pores enabled determination of the original BM/plating interface, which brought to light the presence of a denuded base metal region beneath the BM/plating interface for the undersized foil experiments. The feature of a denuded zone is also present in the full sized foil experiments, as seen in Figure 7.2.1 b) and Figure 7.2.2 b). The approximate width of the denuded base metal region was 9 ± 3 μm and 8 ± 2 μm for the AC+NiCr+Ni(F) and AC+Ni(F) samples respectively. There appears to be no clear indication of a plated layer above the denuded zone, potentially serving as evidence the plating has been homogenized through interdiffusion and alloying with adjacent BM and FM as a result of prolonged hold time at T_B.

The average percentage of faying surface area covered by the FM, width of the ISZ, and $2w_o$ for the two trials of each type of surface prepared half-joint are listed in Table 7.2.1. The percentage of faying surface area covered by the FM was measured using stereo micrographs like those in Figure 7.1.1. The average $2w_o$ and width of ISZ were measured using optical micrographs such as those found in Figure 7.2.1 and Figure 7.2.2. In the case of Ni(F) samples, the denuded zone was not included in $2w_o$ measurements or ISZ measurements as that region is actually BM. The labels in both Figure 7.2.1 b) and Figure 7.2.2 b) indicate how the bounds for various microstructural zones of interest were determined. The standard deviation in the various measurements listed in Table 7.2.1 are also included for the two cyclic DSC trials of each base metal type.

Table 7.2.1 - Metallographic measurements for various surface prepared IN718/BNi-2 half-joints subject to cyclic DSC testing (20 cycles)

Sample Type	Average Percentage FM Coverage [%]	Average $2w_o$ [μm]	Average $2w_{ISZ}$ [μm
AC	69 ± 12	160 ± 24	135 ± 12
AC+NiCr	72 ± 1	142 ± 10	125 ± 10
AC+NiCr+Ni(F)	98 ± 2	98 ± 5	89 ± 14
AC+NiCr+Ni(B)	85 ± 7	111 ± 3	109 ± 5
AC+Ni(F)	100 ± 0	92 ± 14	91 ± 8

Sample types that exhibited poor wetting, such as AC and AC+NiCr, developed larger $2w_o$, resulting in a larger amount of liquid remaining after the brazing hold time. Interestingly, the AC and AC+NiCr samples had the largest width of ISZ present after the cyclic DSC

test. The implications of this observation will be discussed below. Samples subject to a Ni(B) step resulted in intermediate wetting and spreading, and thus had thinner gap and ISZ widths. The measured width of the ISZ was closer to the $2w_o$ value for Ni-plated samples, indicating that they were closer to a fully isothermally solidified TLPB half-joint. The average $2w_o$ for Ni(F) substrates was less than 100 μm due to using a slightly undersized foil in some trials.

Figure 7.2.3 and Figure 7.2.4 contain results obtained from EDS scans conducted on surface prepared TLPB half-joints. The EDS scans were conducted within a rectangular area located in the ISZ of the various half-joints. This was done to determine the bulk or average composition within the ISZ region. Comparison of this value with the original composition of the BNi-2, allows an assessment of the amount of dissolution/interdiffusion of the base metal. The composition of the BNi-2 FM, determined by ICP-OES, is also included in Figure 7.2.3 and Figure 7.2.4 for comparison purposes. Since the EDS technique has difficulty quantifying B, the composition for the FM has been normalised to exclude B in both Figure 7.2.3 and Figure 7.2.4.

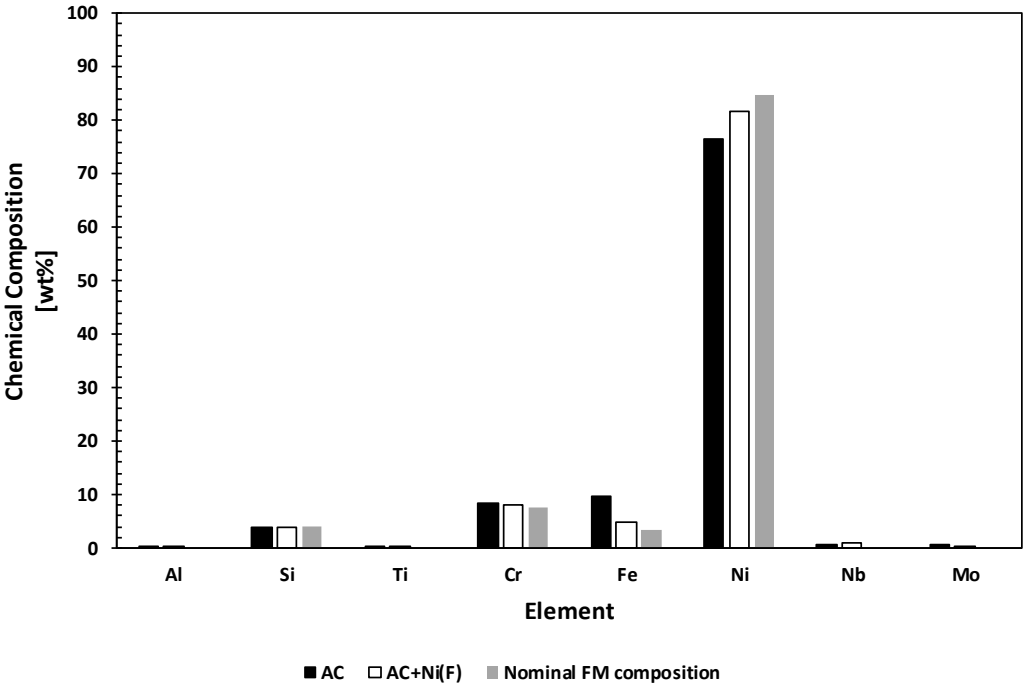

a)

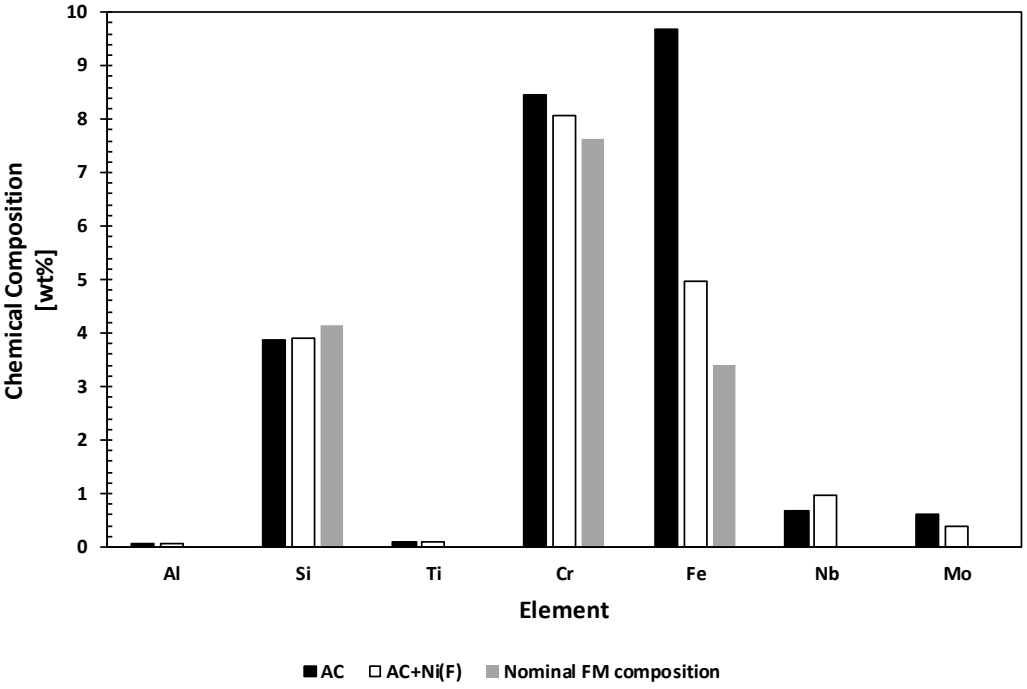

b)

Figure 7.2.3 – a) Bulk chemistry of ISZ determined via FE-SEM-EDS for cleaned & plated IN718/BNi-2 half-joints subject to cyclic DSC testing, b) Ni data removed

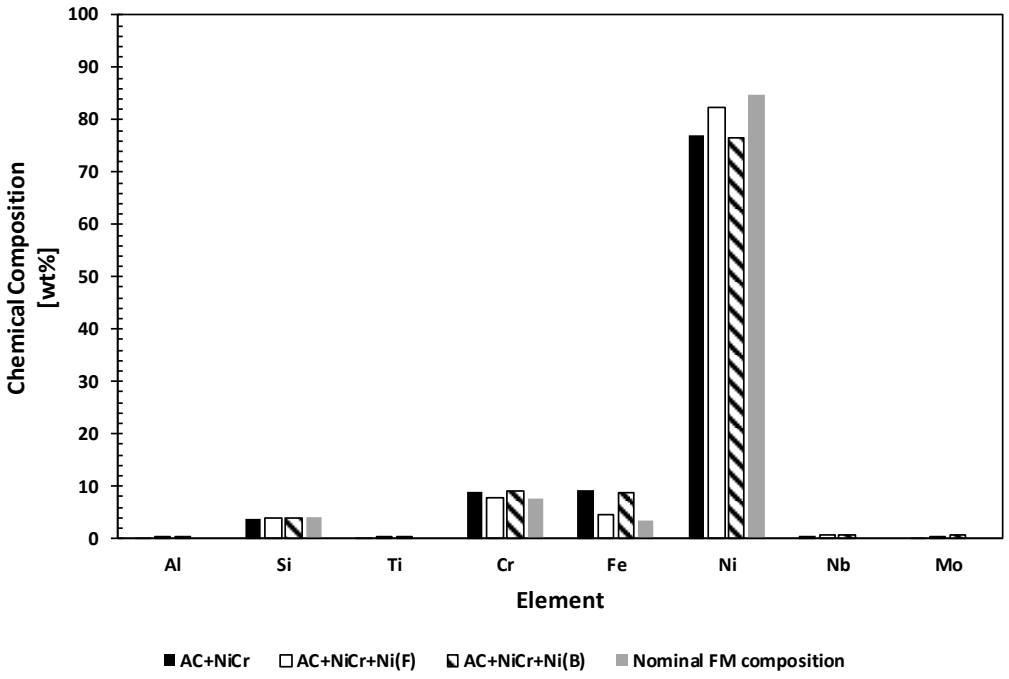

a)

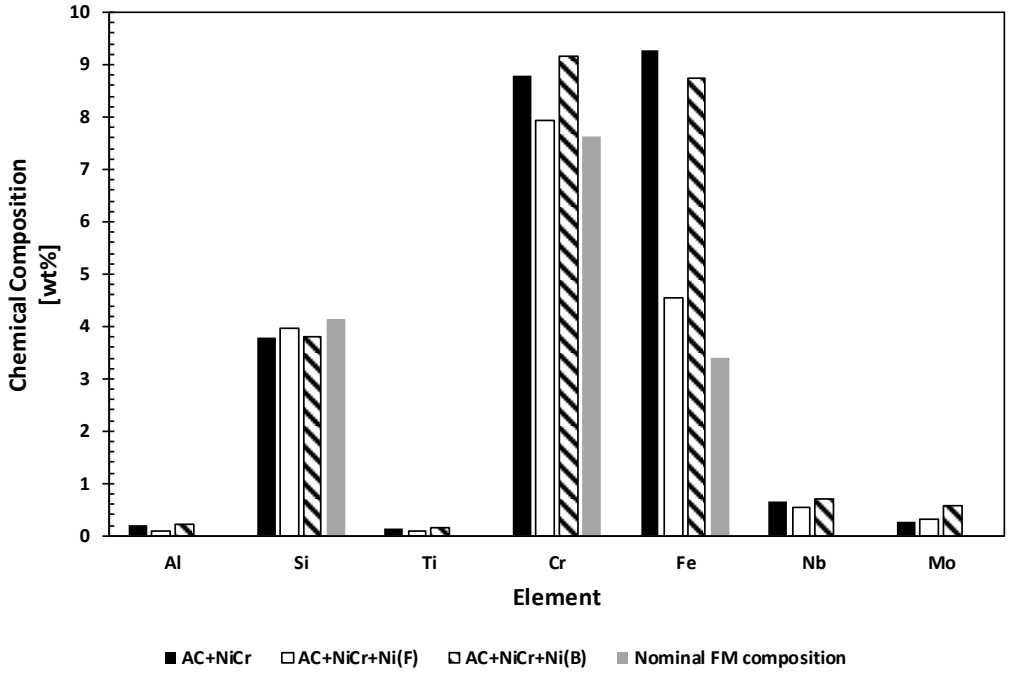

b)

Figure 7.2.4 - a) Bulk chemistry of ISZ determined via FE-SEM-EDS for cleaned, roughened, and plated IN718/BNi-2 half-joints subject to cyclic DSC testing, b) Ni data removed

Since the BM contains less Ni and more Cr and Fe than the FM, dissolution/interdiffusion would result in a decreasing level of Ni and increasing level of Cr and Fe in the ISZ. It would also introduce Ti, Nb, Mo and Al which were not originally present in BNi-2. Furthermore, since no Si is contained within the BM, its concentration in the ISZ should decrease with dissolution. The chemical composition of the ISZ after the 20 cycle DSC test in an AC+Ni(F) sample was closest to that of the FM, indicating the lowest level of dissolution/interdiffusion. The Ni content in the ISZ was higher and the Fe and Cr content lower for the AC+Ni(F) sample than the AC sample. This coupled with less reduction in Si and lower levels of Ti, Nb, Mo, and Al, in the AC+Ni(F) all support less dissolution/interdiffusion in the presence of a Ni plating.

The ISZ of Ni(F) samples had the highest Ni content, and the amount of Ni present was closest to the nominal FM value. The amount of Cr and Fe present in the ISZ for the AC+NiCr+Ni(F) sample was also lower than the other sample types in Figure 7.2.4. The presence of base metal elements not originally found within the FM was also detected in the ISZ of the AC+NiCr+Ni(F). For the AC+NiCr+Ni(F) sample, the content of base metal elements within the ISZ was lower and the Si content higher than the other two sample types in Figure 7.2.4. The amount of Cr and Fe present in the ISZ of all sample types in Figure 7.2.4 was higher than the nominal amount in the FM. However, this increase was the lowest for the AC+NiCr+Ni(F) sample.

All of this evidence suggests less dissolution/interdiffusion between the molten FM and base metal in the presence of the Ni(F) plating. ISZ compositions for the AC+NiCr AC+NiCr+Ni(B) were nominally the same indicating that the brush Ni coating did not alter dissolution/interdiffusion to a significant extent. An FE-SEM micrograph of an AC+NiCr+Ni(F) sample subject to a 20 cycle DSC test is shown in Figure 7.2.5.

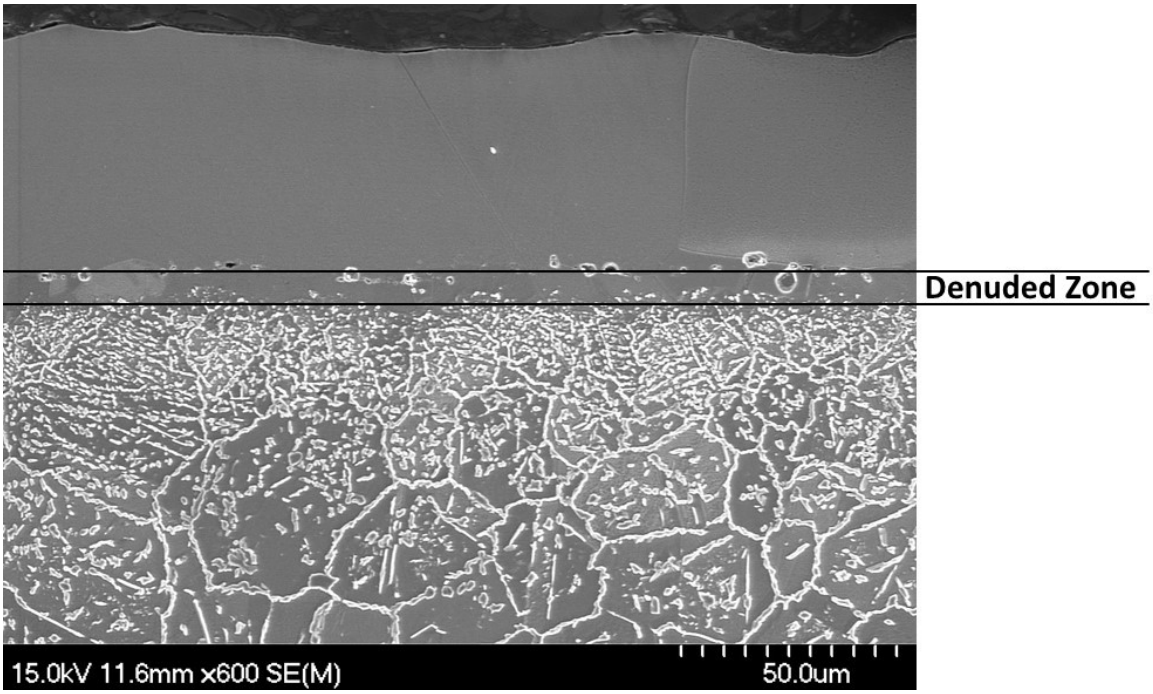

Figure 7.2.5 - SEM micrograph of AC+NiCr+Ni(F) IN718/BNi-2 half-joint subject to cyclic DSC testing (etched)

Figure 7.2.6 contains EDS results of bulk scans taken within the denuded zone of both types of NI(F) substrates. The nominal composition of both the FM and the BM are also included in Figure 7.2.6 for comparison purposes.

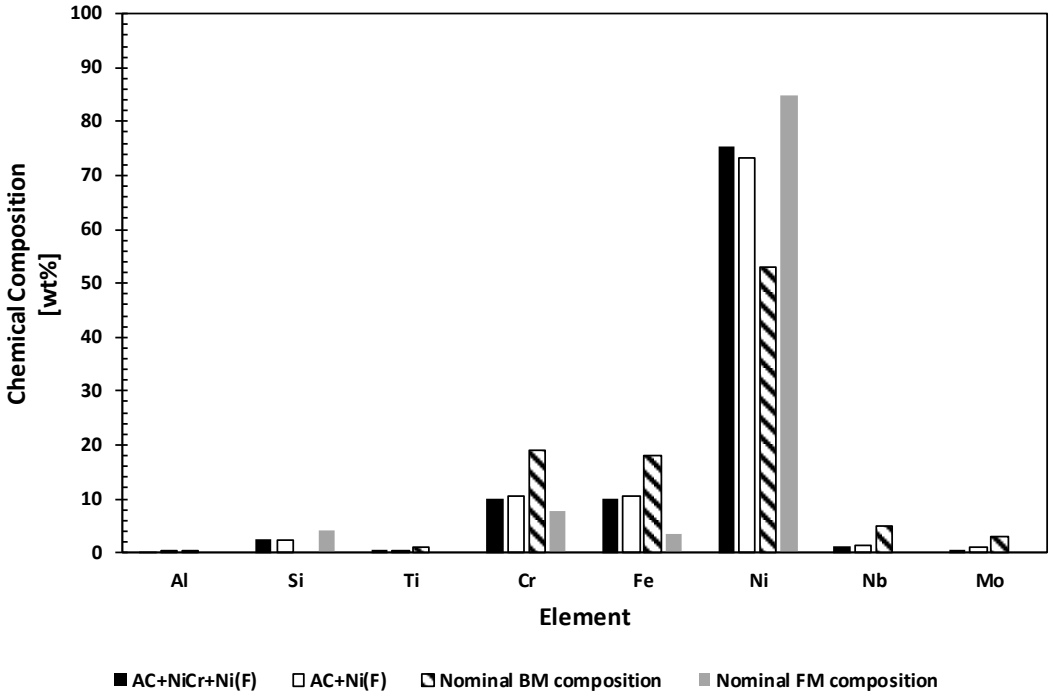

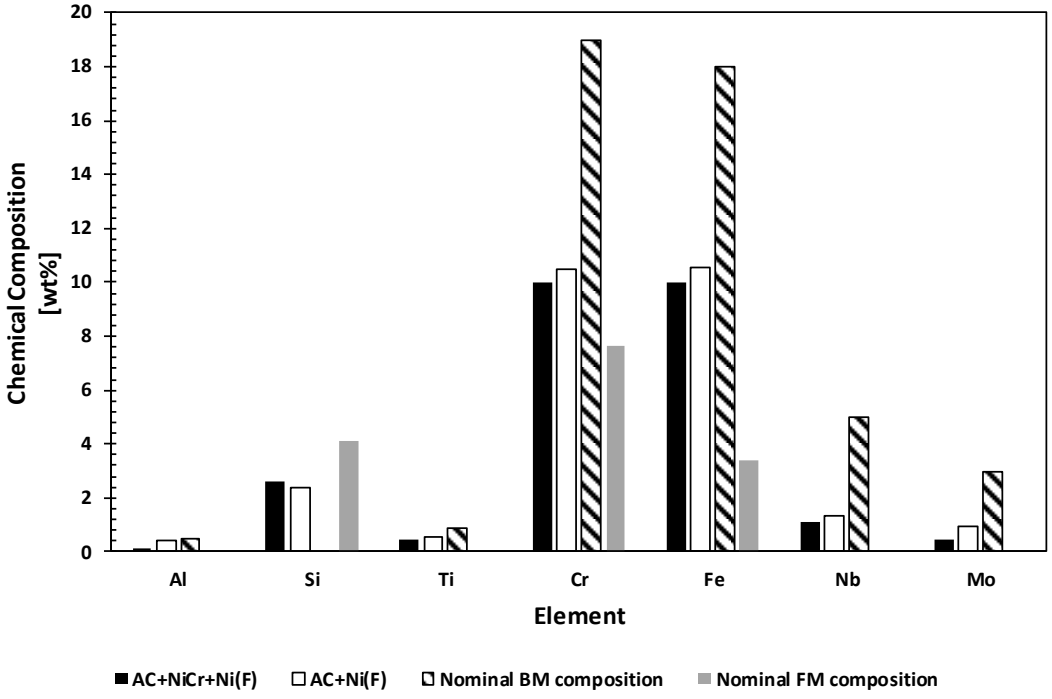

a)

Figure 7.2.6 - a) Bulk chemistry of denuded zone determined via FE-SEM-EDS for Ni(F) IN718/BNi-2 half-joints subject to cyclic DSC testing, b) Ni data removed

The denuded zone present in both Ni(F) substrates was Ni rich and contained more Ni than nominally present within IN718. The amount of other base metal elements such as Cr, Fe, Nb, Mo, Al, and Ti were significantly lower than nominally present within IN718. A higher amount of the aforementioned base metal elements was present in the AC+Ni(F) sample than the sample containing a roughening step. This denuded zone persists throughout the brazing hold time, and a region of base metal with altered base metal chemistry is created. There was also Si detected within the denuded region, indicating diffusion of Si from the FM had occurred. When the bulk chemistry of the ISZ and denuded zone are compared, the ISZ is more Ni rich than the denuded zone. Base metal elements such as Fe and Cr were present in higher proportions in the denuded zone than in the ISZ. There was a greater quantity of Si detected within the ISZ than the denuded zone. Therefore, the concentration gradient described in the wetting and spreading study also persists through the brazing time.

Figure 7.2.7 and Figure 7.2.8 contain the results of EDS line scans conducted across the ISZ for the various surface prepared IN718/BNi-2 half-joints. The AC and AC+NiCr+Ni(F) samples were chosen for discussion as they represent the two general cases observed in terms of chemical composition gradients across the ISZ.

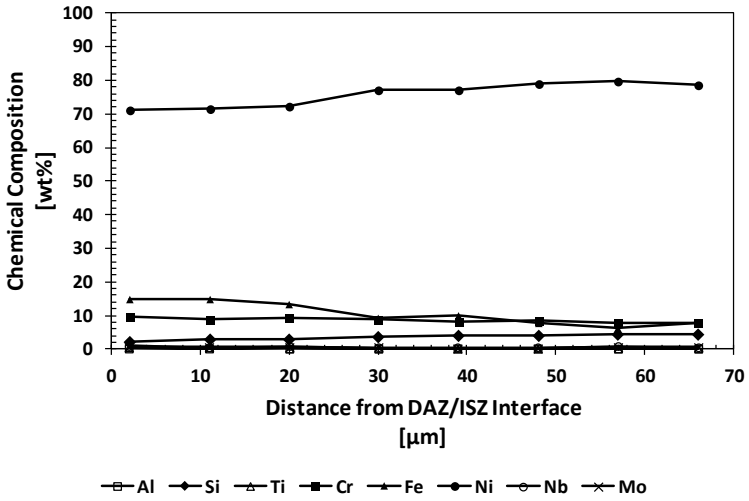

a)

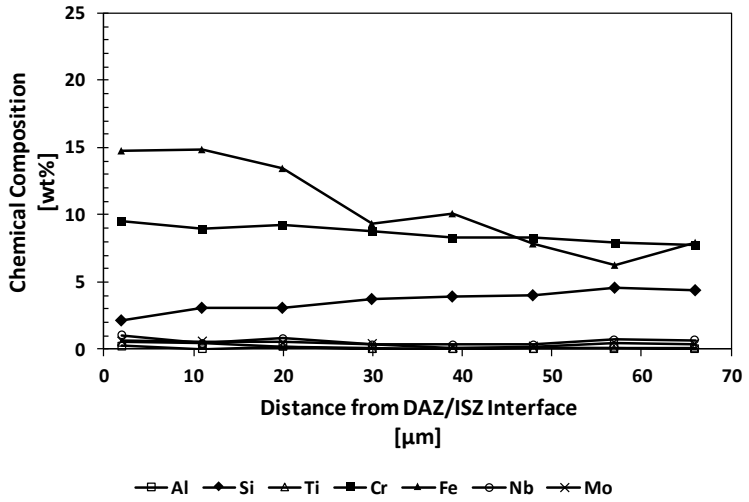

b)

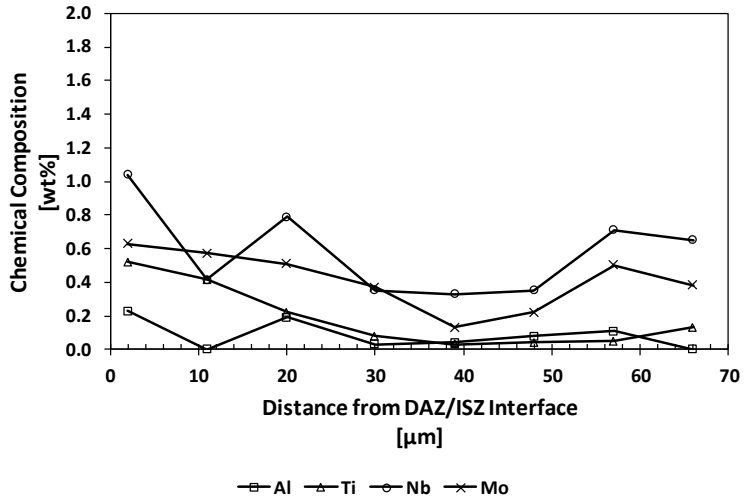

c)

Figure 7.2.7 – a) EDS line scan of ISZ taken on an AC sample subject to cyclic DSC testing, b) Ni data removed, c) Fe and Cr data removed

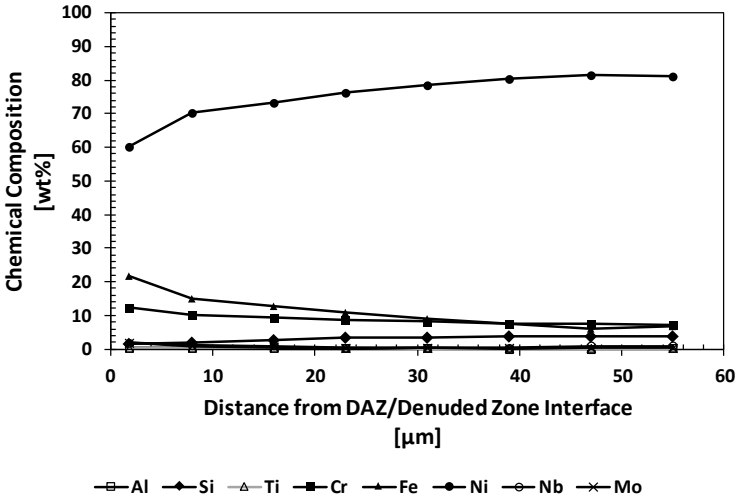

a)

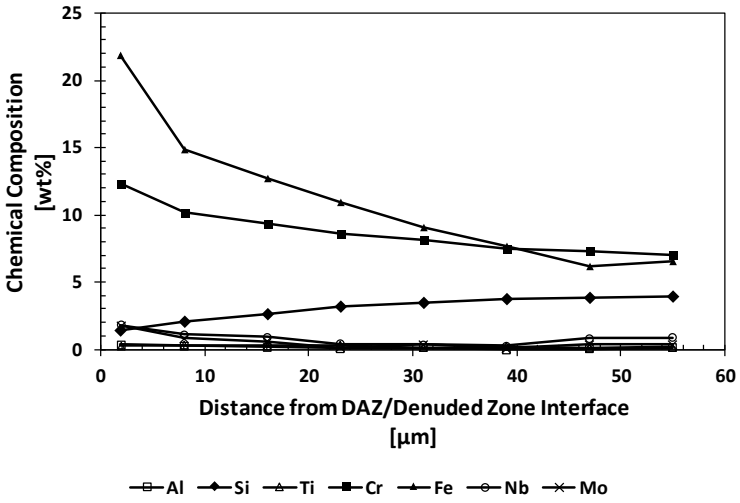

b)

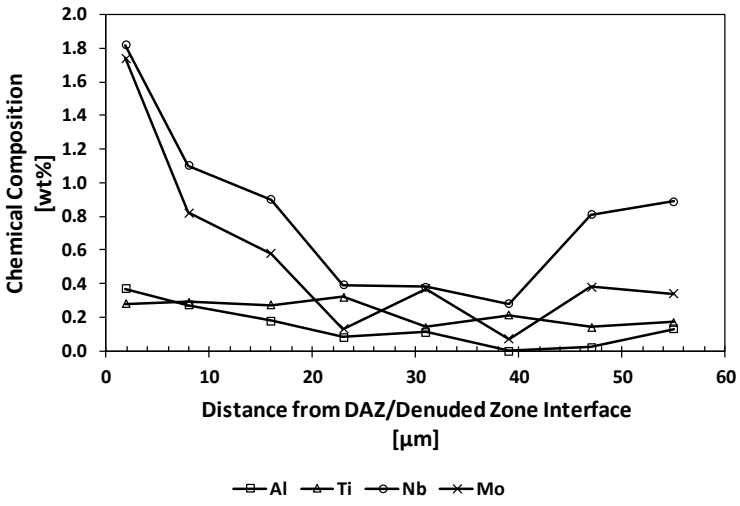

c)

Figure 7.2.8 - a) EDS line scan of ISZ taken on an AC+NiCr+Ni(F) sample subject to cyclic DSC testing, b) Ni data removed, c) Fe and Cr data removed

Both the AC and AC+NiCr+Ni(F) samples had a positive Ni gradient as the distance from the DAZ/ISZ interface was increased. The Ni(F) sample had a much steeper Ni gradient than the AC sample, ranging from 60 to 81 wt.% Ni. Both sample types also had a positive Si gradient across the ISZ, with the AC+NiCr+Ni(F) sample possessing a steeper gradient. The remaining elements present in the ISZ of both samples had a negative composition gradient as the distance from the DAZ/ISZ interface was increased. In the case of the Ni(F) substrates, the chemical gradient for elements such as Fe, Cr, Nb, Mo, Al, and Ti were much steeper than the AC sample. The change in chemical composition across the first 10 μm for the plated sample was also much steeper than in the case of the AC sample. The denuded zone is included within the first 10 μm of the Ni(F) samples, meaning that the formation of the denuded zone results in a significant chemical gradient being initiated close to the interface. This was also observed in the AC+Ni(F) sample shown in Appendix F. An interesting feature observed in Figure 7.2.8 c) was that the presence of two chemical gradients existed. A negative chemical gradient was observed for Al, Ti, Nb, and Mo until approximately 30 μm away from the DAZ/ISZ interface. After 30 μm, the sign of the chemical gradient became positive. This behavior was also observed for other surface prepared IN718/BNi-2 half-joints, as well as the ISP samples discussed in Chapter 4.2. Elements such as Al, Ti, Nb, and Mo tend to enrich the melt, and thus after a certain width has been isothermally solidified, those elements have no where to migrate to and form solid solution gamma within the ISZ as their amounts are within solid solubility limits [36].

Overall the differences in compositional profiles between the AC and AC+NiCr+Ni(F) further support the lower levels of dissolution/interdiffusion in the presence of a Ni(F) plating.

7.2.2 Samples held at 1050°C for 60 minutes

The AC, AC+NiCr+Ni(F), and AC+Ni(F) samples were heated to 1050°C and held for 60 minutes. The purpose of these samples was to provide an intermediate brazing time so that the development of the microstructure and the change in chemical composition of the ISZ could be analysed as a function of increased brazing time. Optical micrographs of the AC, AC+NiCr+Ni(F), and AC+Ni(F) samples held at 1050°C for 60 minutes are found in Figure 7.2.9.

a)

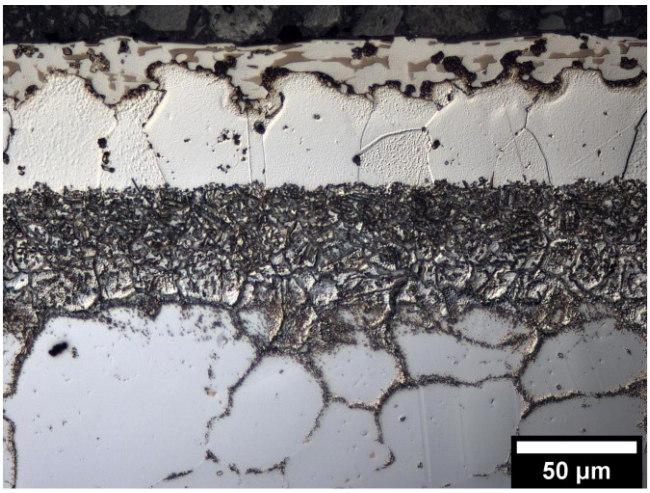

b)

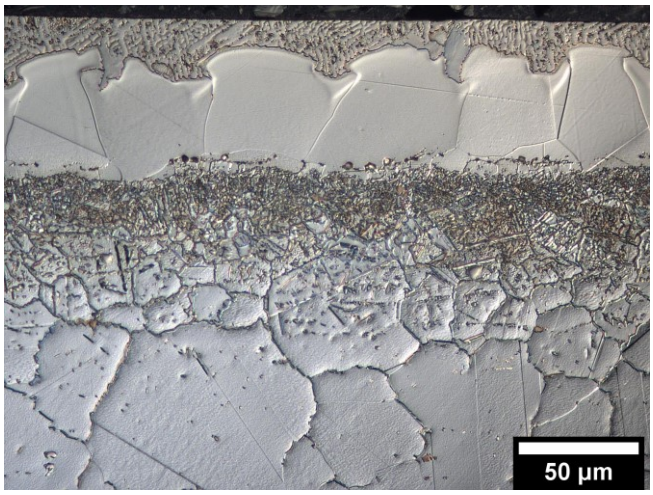

c)

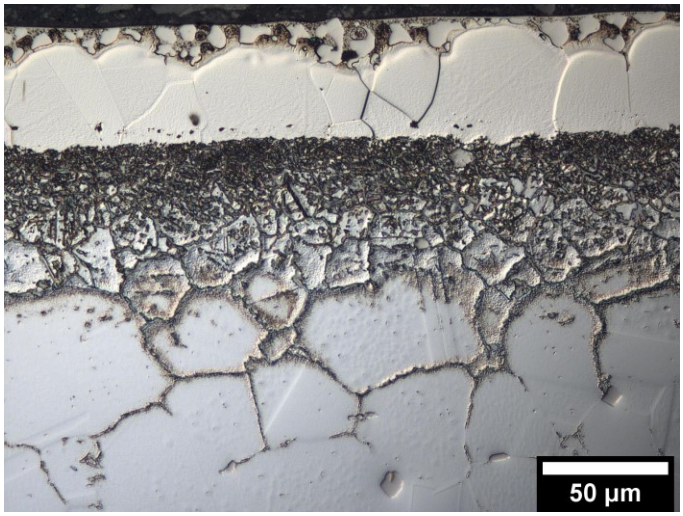

Figure 7.2.9 - Micrographs of half-joints heated to 1050°C and held for 60 min: a) AC, b) AC+NiCr+Ni(F), c) AC+Ni(F) (etched)

All three of the surface prepared half-joints displayed an ASZ, ISZ, and DAZ. The AC sample exhibited some distributed and isolated porosity within the ISZ. Both Ni(F) samples had an ASZ remaining after a 60-minute hold at 1050°C. As in all other Ni(F) samples shown thus far, there was the presence of the denuded zone and porosity at the interface of the denuded zone and the ISZ. Table 7.2.2 contains the average $2w_o$ and average width of ISZ for the samples held at 1050°C for 60 minutes. The standard deviation in the measured width is also included in Table 7.2.2.`

Table 7.2.2 - Metallographic measurement of select surface prepared IN718/BNi-2 half-joints held for 60 minutes at 1050°C

Sample Type	$2w_o$ [µm]	$2w_{ISZ}$ [µm
AC	116 ± 11	86 ± 10
AC+NiCr+Ni(F)	114 ± 17	74 ± 11
AC+Ni(F)	106 ± 16	72 ±11

Bulk EDS scans were also completed for the 60-minute hold samples. The bulk composition of the ISZ for the AC, AC+NiCr+Ni(F) sample is plotted for three different brazing holds in Figure 7.2.10 and 7.2.11. The AC+Ni(F) sample was omitted as the chemical composition of the ISZ was very similar to the sample that included a roughening step.

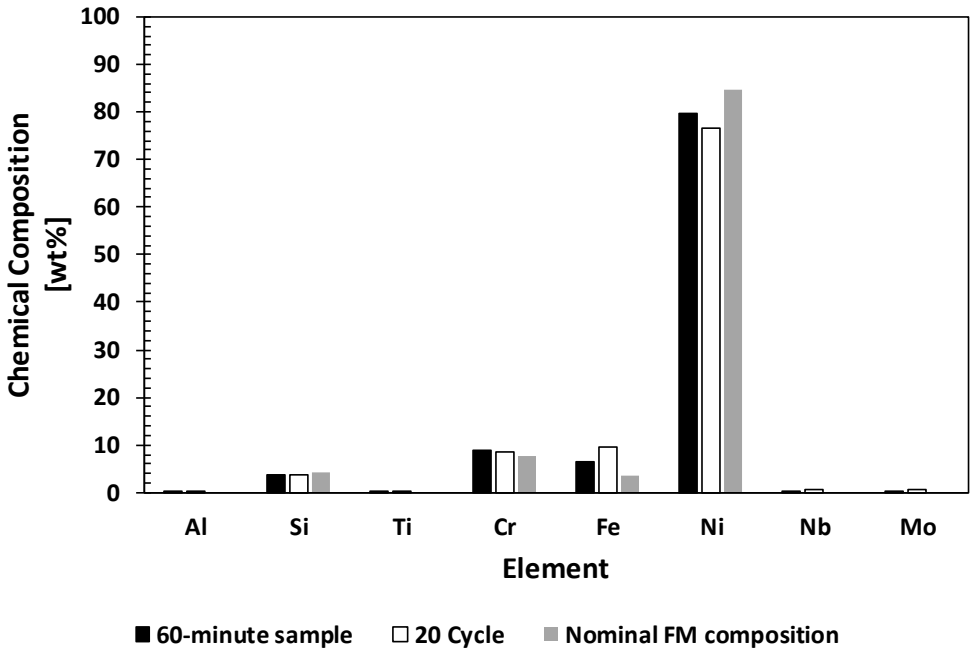

a)

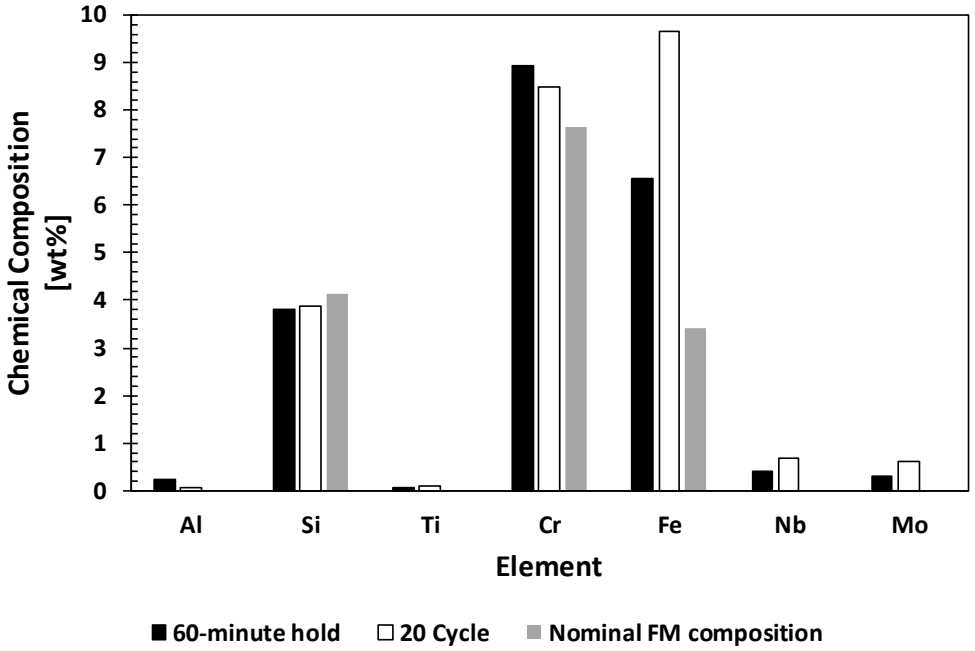

b)

Figure 7.2.10 - a) Bulk composition of the ISZ present in an AC IN718/BNi-2 half-joints as a function of hold time; b) Ni data removed

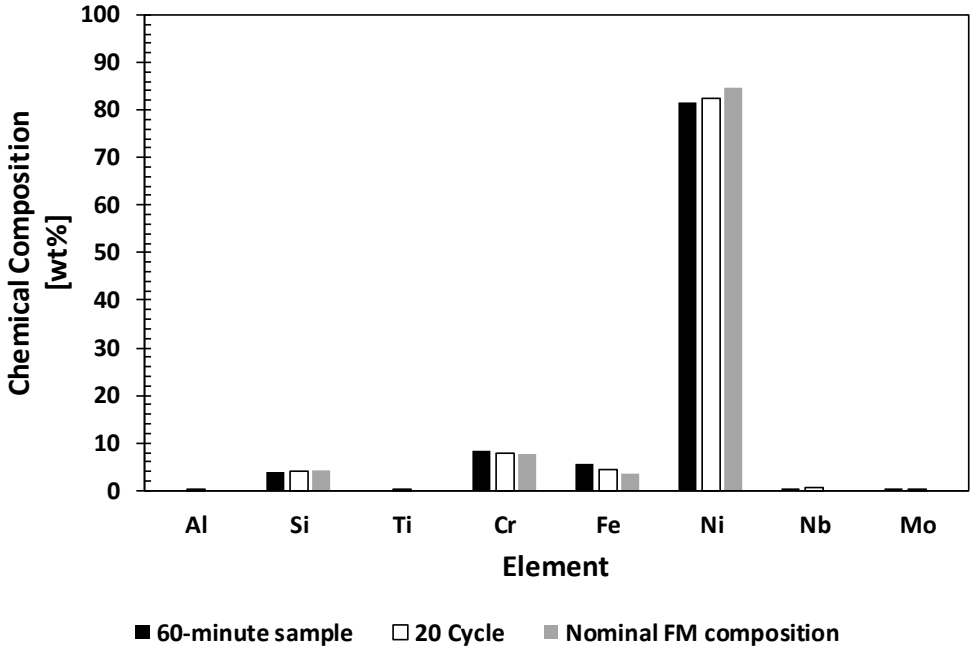

a)

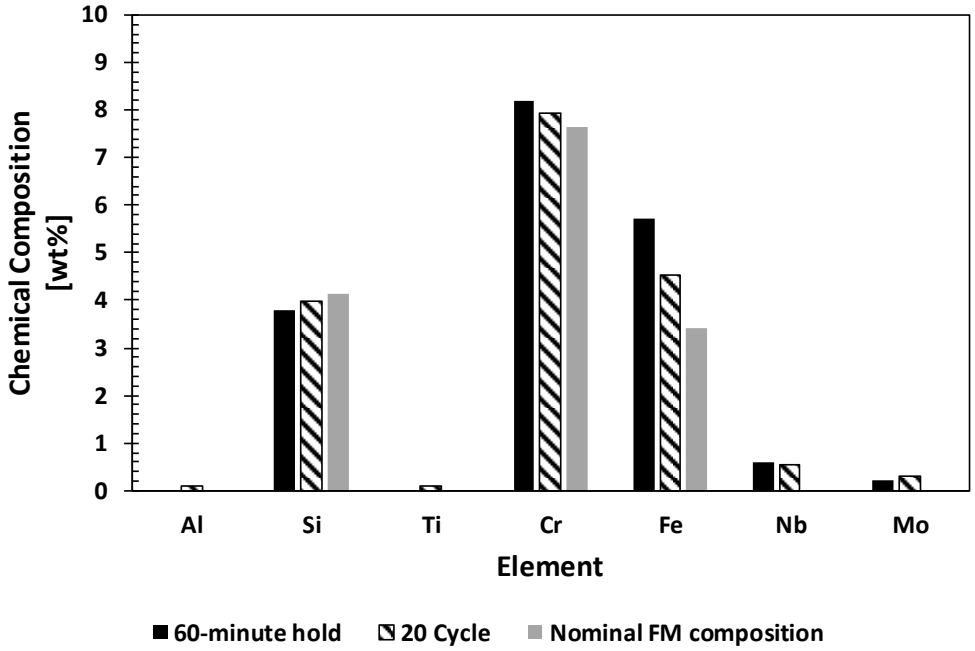

b)

Figure 7.2.11 - a) Bulk composition of the ISZ present in an AC+NiCr+Ni(F) IN718/BNi-2 half-joints as a function of hold time; b) Ni data removed

In both the AC and the AC+NiCr+Ni(F) samples, the Nb and Mo increased with increasing hold time. The Si content in the AC sample remained constant at 4 wt.%, which is close to the composition of the FM (normalised without B). The Ni(F) sample started with a slightly

lower Si content than nominally present within the FM, before increasing to 4 wt.% Si. After a 20 Cycle DSC test, both the AC and Ni(F) sample had approximately the same amount of Cr present. Both sample types had a large increase in Cr occur for the 60-minute hold sample. The largest difference between the two sample types was that the AC sample had an increase in the Fe content after 20 cycles (from 8 to about 9.5 wt.% Fe), whereas the Fe in the AC+NiCr+Ni(F) sample decreased from 8 to 5 wt.%. Note that Ni was present in the samples but is not shown in Figure 7.2.10, as it dwarfed the rest of the elemental data. The general trend for Ni content in the AC sample was that the Ni content decreased as a function of increased hold time (from 81 to 77 wt.% Ni). The Ni content remained constant at around 83 wt.% Ni for the Ni(F) substrates. This is believed to be due to the addition of Ni from the incorporation of the plating.

7.3 Rate of Isothermal Solidification and Maximum Brazing Clearance

The liquid fraction plot for the surface prepared IN718/BNi-2 TLPB half-joints is found in Figure 7.3.1. The liquid fraction was determined as described in Chapter 4.3. The error bars represent the standard deviation in the experimentally determined liquid fraction for each of the different surface prepared IN718/BNi-2 half-joints.

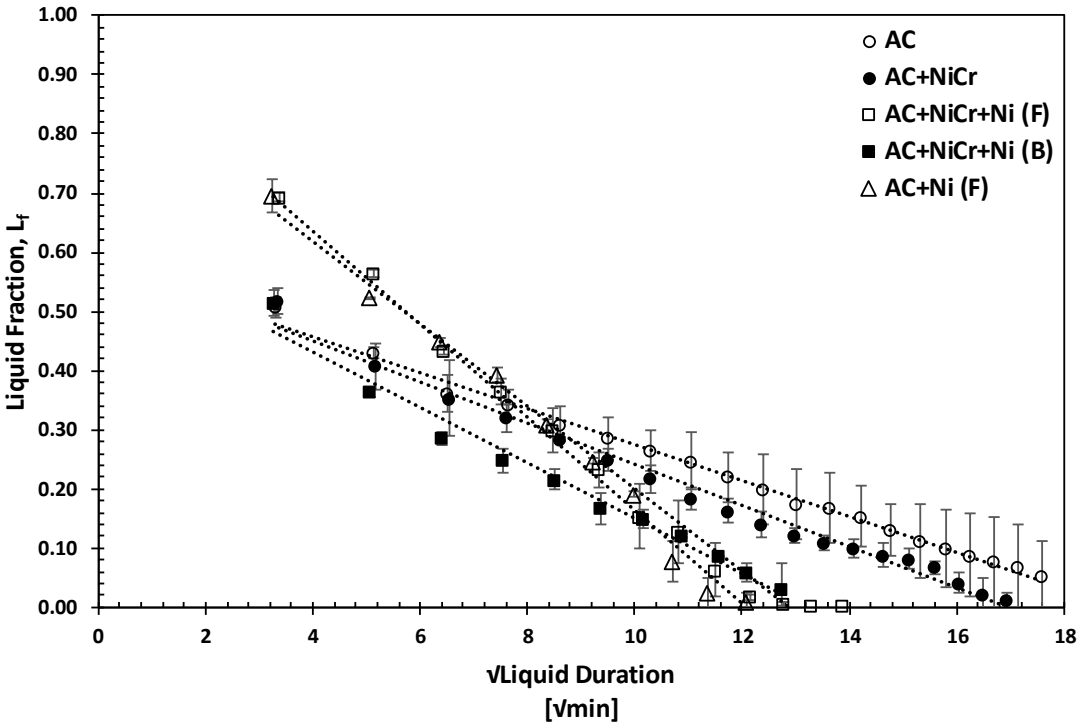

Figure 7.3.1 - Liquid fraction vs. square root of liquid duration for surface prepared IN718/BNi-2 TLPB couples

The trends observed in the liquid fraction plot were the same as those observed in the plot of solidification enthalpy versus square root of liquid duration. The most notable difference amongst the various surface prepared half-joints was the significant increase in slope and in y-intercept observed in Figure 7.3.1 for the Ni(F) samples. The AC+Ni(F) sample in Figure 7.3.1 had the steepest slope and highest y-intercept value out of the various sample types tested. The slope of the AC+Ni(F) sample was more than double that of the AC and AC+NiCr samples. The AC+NiCr+Ni(F) sample also had a relatively steep slope and high y-intercept compared to samples omitting a Ni(F) step. The slope for the AC+NiCr+Ni(F) sample was up to two times larger than surface preparation routes omitting a Ni(F) in Figure 7.3.1. The Ni(B) sample had a slightly larger y-intercept and steeper slope than the AC and AC+NiCr sample.

As discussed previously, the y-intercept of a liquid fraction plot represents the liquid fraction present at the onset of melting. As mentioned in Chapter 4.3, the width of ISZ present once T_B is first achieved represents a more physically meaningful prediction for

the growth of the ISZ due to IBU. Thus, the interpretation of the y-intercept (ISZ present at zero minutes liquid duration) will be omitted for this chapter. The liquid fraction present at T_B (2.2 $\sqrt{min}$ liquid duration) represents the liquid fraction present after wetting, dissolution, and IBU have taken place.

The initial liquid fraction present at T_B (2.2 $\sqrt{min}$ liquid duration) for the AC, AC+NiCr, and AC+NiCr+Ni(B) samples was approximately 0.51, indicating that 49% of the liquid had been consumed due to IBU. The initial liquid fraction present at T_B (2.2 $\sqrt{min}$ liquid duration) for the AC+NiCr+Ni(F) and AC+Ni(F) samples in Figure 7.3.1 was 0.74 and 0.78 respectively. This implies that approximately 26-28% of the liquid fraction was consumed by the time T_B was reached. The presence of a Ni(F) step appears to result in a reduction of the ISZ growth due to IBU. The reduced initial liquid fraction present in the AC, AC+NiCr, and AC+NiCr+Ni(B) samples occurs through interdiffusion between the FM and base metal. Consequently, the DSC results of Figure 7.3.1 are consistent with the compositional analysis presented in Chapter 7.2, where interdiffusion was observed to be reduced for the Ni plated samples.

$2w_t$ is plotted against the square root of liquid duration for the surface prepared samples in Figure 7.3.2. $2w_t$ was determined in the same manner as previously described in Chapter 4.3. The only exception is, that the $2w_o$ was measured from the approximate location of the denuded zone/FM interface to the end of the ASZ for samples that were Ni(F). Since the denuded zone and ISZ have a similar appearance under the optical microscope, it was difficult to determine the exact location of the denuded zone/FM interface. The porosity that was initially present at the Ni plating/IN718 interface was used as an aid in determining where to begin the $2w_o$ measurement. The error bars represent the standard deviation in $2w_t$ for two trials of each surface preparation type.

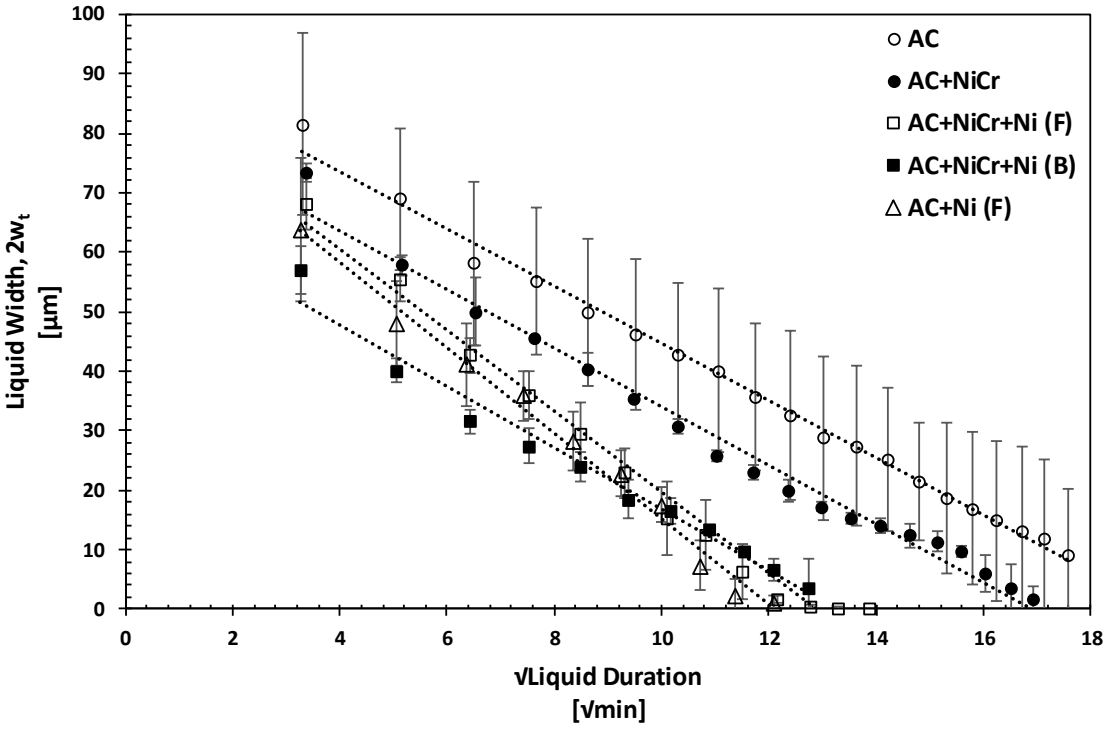

Figure 7.3.2 – $2w_t$ vs. square root of liquid duration for surface prepared IN718/BNi-2 TLPB couples

Relevant LR parameters extracted from the $2w_t$ plot are found in Table 7.3.1. The aforementioned variables are all determined in the same manner as in Chapter 4.3 using the $2w_t$ plot in Figure 7.3.2.

Table 7.3.1 - LR parameters extracted from $2w_t$ plot for surface prepared IN718/BNi-2 half-joints

Sample Type	R^2	k_{IS} $\left[\frac{\mu m}{\sqrt{min}}\right]$	$2w_i$ [µm]	$2w_{\sqrt{2.2\ min}}$ [µm]	t_{IS} [min]
AC	0.99	-4.8	93	82	373
AC+NiCr	0.99	-4.9	83	72	288
AC+NiCr+Ni(F)	0.98	-6.8	88	73	166
AC+NiCr+Ni(B)	0.98	-5.2	68	57	175
AC+Ni(F)	0.99	-7.2	87	71	147

t_{IS} estimated by Figure 7.3.2 was the longest for the AC. As previously mentioned, the t_{IS} is simply the x-intercept on the $2w_t$ plot and is related to the initial liquid width. t_{IS} estimated by Figure 7.3.2 was the shortest for the AC+Ni(F) sample. The Ni(F) samples were able to fully wet the base metal, resulting in a reduction of $2w_o$. A larger initial liquid width is expected for samples that resulted in poor wetting and therefore a longer t_{IS} as seen in Figure 7.3.2.

As in Figure 7.1.4 and 7.3.1, k_{IS} for the Ni(F) samples was increased compared to other samples. The standard deviation of the $2w_t$ as a function of the square of liquid duration was much larger for the AC sample than other samples. Since the AC sample had exhibited poor wetting behavior, there was more variation in the percentage of base metal faying surface covered by the FM. The fluctuation in the wetting behavior led to a wider range of initial liquid width amongst the two trials for the AC sample type. The liquid width of the Ni(F) samples had much less variation than the AC sample type.

The MBC is plotted against the square root of liquid duration for the surface prepared samples in Figure 7.3.3. The error bars present in both MBC plots represent the standard deviation in predicted MBC amongst two trials for each surface preparation route. Relevant LR parameters extracted from Figure 7.3.3 are found in Table 7.3.2.

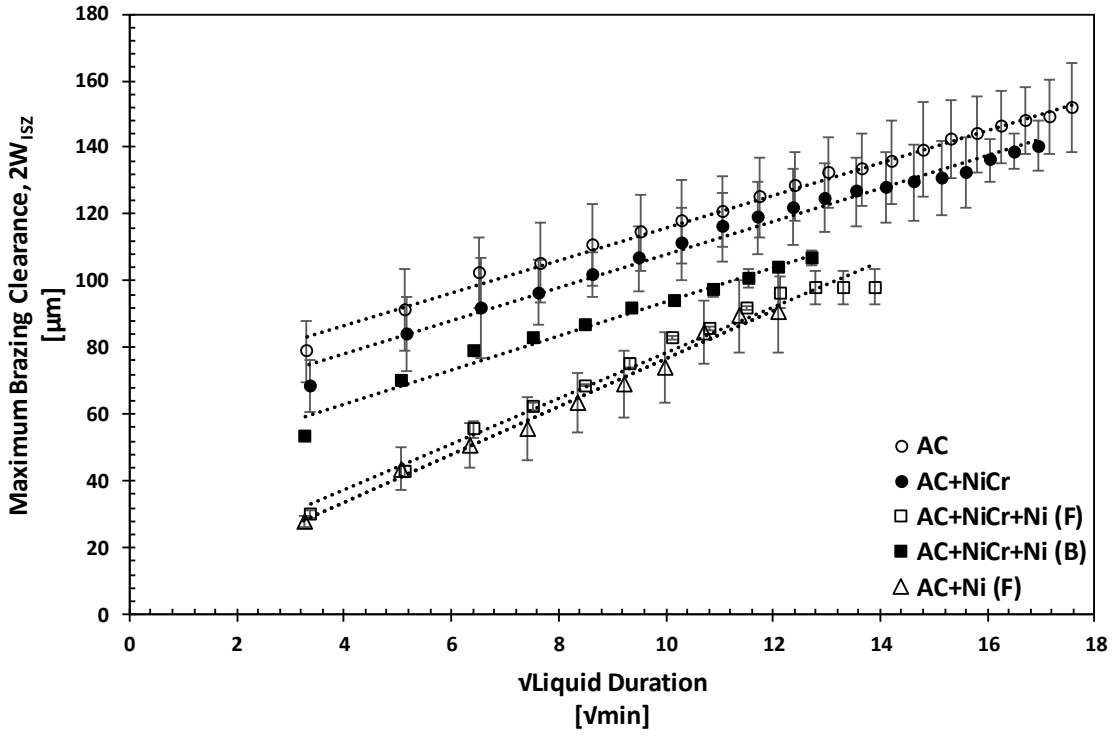

Figure 7.3.3 - MBC vs. square root of liquid duration for surface prepared IN718/BNi-2 TLPB couples

Table 7.3.2 - LR parameters from MBC plots for surface prepared IN718/BNi-2 half-joints

Sample Type	R^2	k_{IS} $\left[\frac{\mu m}{\sqrt{min}}\right]$	$2w_{ISZ,0}$ [µm]	$2w_{ISZ,\sqrt{2.2\ min}}$ [µm]	t_{IS} [min]
AC	0.99	4.9	67	78	365
AC+NiCr	0.99	4.9	59	69	287
AC+NiCr+Ni(F)	0.98	6.8	10	25	166
AC+NiCr+Ni(B)	0.98	5.2	42	53	176
AC+Ni(F)	0.99	7.2	5	20	146

The MBC predicted at 2.2 $\sqrt{min}$ liquid duration using the LR data in Figure 7.3.3 was largest for the AC sample. Other samples that omitted a Ni(F) operation also had relatively large width of ISZ present at 2.2 $\sqrt{min}$ liquid duration. Both the Ni(F) specimens had comparatively smaller width of ISZ once T_B was first reached. This width of ISZ at T_B corresponds to IBU. As indicated in Table 7.3.2, the presence of a Ni(F) step resulted in a reduction of the %IBU. The lower level of IBU in the Ni(F) samples was consistent with

the above observations that interdiffusion between the filler and BM was reduced by the presence of the Ni plating. In addition to the differences in the extent of IBU, the Ni(F) samples had a faster k_{IS} than samples omitting a Ni(F) step. Sample types absent of a Ni(F) step resulted in the longest t_{IS} for their respective $2w_o$. These samples were subject to poor wetting and spreading, and therefore had initially larger $2w_o$ and longer t_{IS}. Since Ni(F) samples were able to fully spread over the faying surface, their starting $2w_o$ was smaller and therefore so was t_{IS}.

The advantage of the MBC plot is its predictive capability and use in TLPB process design. For example, it can determine how the differences in IBU and k_{IS} imposed by the surface preparations relate to t_{IS} for different starting $2w_o$. This will be further discussed below in Chapter 7.3.1.

The actual measured ISZ widths present after a 60-minute isothermal hold for the AC, AC+NiCr+Ni(F), and AC+Ni(F) samples were 43 ± 6 µm (86 ± 11 µm on a full joint basis), 37 ± 6 µm (74 ± 11 µm on a full joint basis), and 35 ± 6 µm (71 ± 11 µm on a full joint basis) respectively. A 60-minute isothermal hold corresponds to 70 minutes liquid duration ($8.4\sqrt{\text{min}}$). The MBC present after $8.4\sqrt{\text{min}}$ predicted by Figure 7.3.3 for the AC, AC+NiCr+Ni(F), and AC+Ni(F) samples was 108 µm, 67 µm, and 65 µm. The predicted MBC for the AC sample was outside of the of the standard deviation of the actual measured ISZ for the AC sample, while both Ni(F) samples had a predicted MBC that fell within the standard deviation of the actual measured ISZ. Despite the overestimation of the AC sample, predicted MBC values are still in relatively good agreement with those measured on micrographs.

7.3.1 Predictability of MBC curves

Recall from Chapter 5.3, that samples subject to a roughening step had higher surface roughness than sample types omitting a roughening step. Keeping this in mind, analysis of Table 7.3.2 revealed that there was no significant relationship between surface roughness and MBC parameters such as $2w_{ISZo}$ and k_{IS}. The larger impact on MBC parameters is the presence or absence of a Ni plating step and associated boride former potential.

Recall from Chapter 6.3, the denuded zone observed in Ni(F) samples had a reduced amount of boride formers present. It was stated in Chapter 6.3 that t_{IS} is inversely related

to the boride precipitation potential of the BM. Increasing the potential for boride precipitation results in enhanced diffusion flux of B and IBU formation. Since there was a reduced amount of boride formers present within the denuded zone, the B had to diffuse to a location within the BM below the denuded zone, where boride former concentration was sufficient to initiate boride precipitation. The presence of the denuded zone essentially results in an apparent increase in the diffusion distance required for boride precipitation. This increased diffusion distance can potentially explain the reduced IBU exhibited by Ni-plated samples.

The target gap width (or MBC) must be considered when determining the optimum base metal surface preparation route for brazing IN718 using BNi-2 FM. Figure 7.3.4 contains the same MBC plot shown in Figure 7.3.3, but three lines have been added to the figure. The vertical red line is placed at $2.2\sqrt{\text{min}}$, the time when T_B is first reached. The purpose of this line is to serve as a visual marker for the IBU that has occurred during initial melting. The two horizontal black lines are placed at two different MBC values, 50 and 100 μm. The purpose of these lines is to illustrate the effects of surface preparation on freezing two different values of $2w_o$.

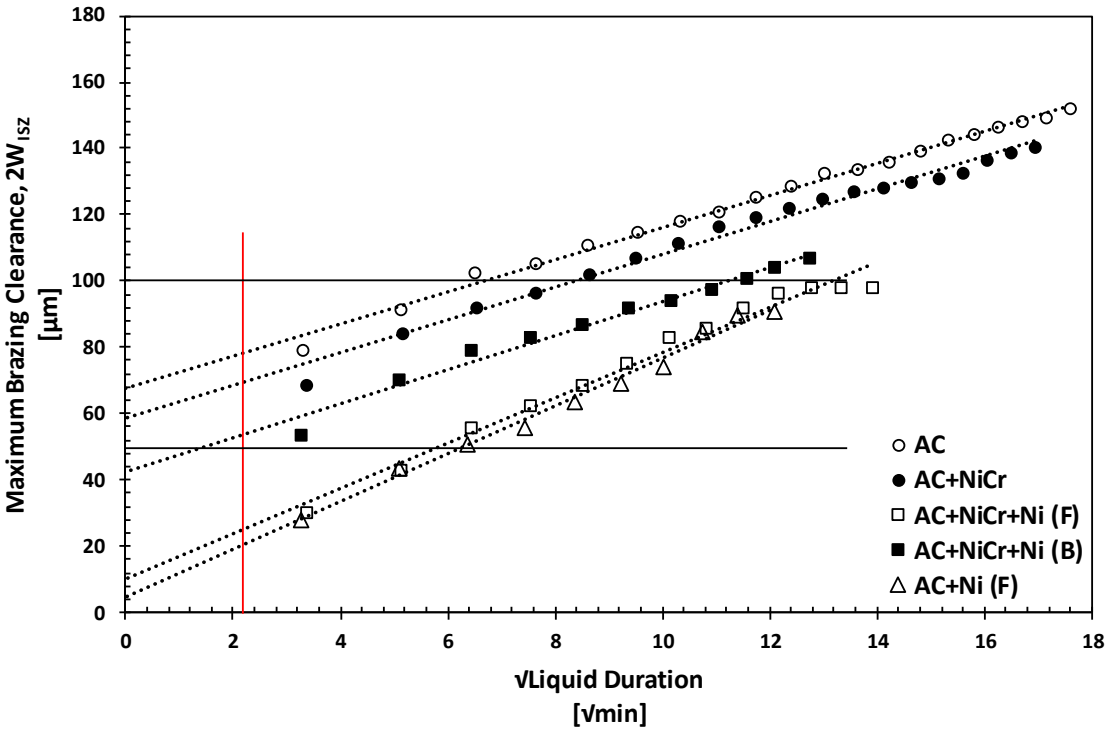

Figure 7.3.4 - MBC plot for IN718/BNi-2 half-joints illustrating the impact of surface preparation on t_{IS} for a narrow and wide $2w_o$

If the desired $2w_o$ value was 50 µm, the sample types omitting a Ni(F) step will have already achieved complete IS by the time T_B is first reached. In terms of the Ni(F) samples, they will reach completion of IS around 6.0-6.4 $\sqrt{min}$ (36-41 minutes) liquid duration. If the desired $2w_o$ value was 100 µm, the samples omitting a Ni(F) step will reach completion of IS faster. Despite the increased k_{IS} exhibited by the Ni(F) specimens, the large degree of IBU experienced by samples such as the AC type ends up being the limiting factor in terms of t_{IS}. Inspection of Figure 7.3.4 indicates that a gap of 160 µm would be required for the higher IS rate in the Ni(F) samples to result in a shorter t_{IS} compared to samples without a Ni(F) step.

FM placement method and spreading index must also be considered when determining the optimum base metal surface preparation route for brazing IN718 using BNi-2 FM.

If a dynamic placement method is to be used, the spreading index and width of ISZ grown due to IBU are of great importance. The spreading index needs to be high in a dynamic brazing process, as the molten FM needs to freely flow into the joint clearance. If the

spreading index is low, that insinuates that the FM has poor wettability when that surface preparation method is used.

If the brazing process used a preplaced FM foil, then the IBU would not have as much of an effect on gap filling. Although capillary force will assist in pulling the liquid into the gap, if there exists poor wettability of the filler on the faying surfaces, flow through the joint could be halted early and areas not wet by FM can create porosity. If the target $2w_o$ is smaller than the predicted MBC at $2.2\sqrt{\text{min}}$, then gap filling issues could potentially arise. The FM could freeze before travelling the full joint length, and growth of large ISZ dendrites into the melt could potentially act to choke off the flow of the metal through the joint.

7.4 Comparison to Literature and Theoretical Predictions

Arafin et al. [7] have studied the TLPB of IN718 with BNi-2 FM using a Ni-plated IN718 substrate like that used in the current study. The parent metal was first subject to a NiCr step, and then subsequently AC. Once the cleaning procedures were complete, the faying surface of the base metal was plated using a Ni(F) operation. Arafin et al. [7] measured the MBC as a function of isothermal hold time. A wedge type base metal configuration was used to allow for a variable gap size across the length of the joint. Similar experimental conditions employed in the current study were used by Arafin et al. [7]. The largest differences were that brazing was conducted in a vacuum atmosphere using BNi-2 paste.

The results from the study performed by Arafin et al. [7] are compared to the current study in Figure 7.4.1. Note that the data taken from the Arafin et al. [7] study is plotted as the square root of isothermal hold time, while the data from the current study is plotted as the square root of liquid duration. Considering the differences in the experimental conditions, good agreement was achieved between the MBC plot of Ni(F) half-joints and those used in the study done by Arafin et al. [7].

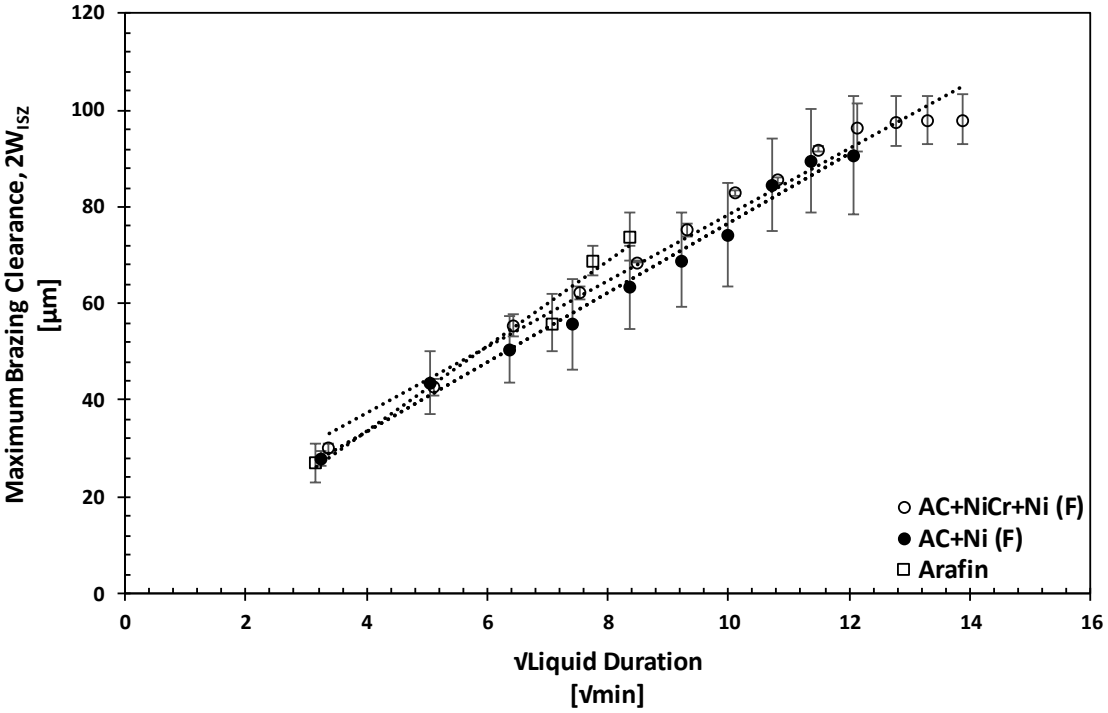

Figure 7.4.1 - Comparison of MBC plot for IN718/BNi-2 half-joints using Ni(F) substrates and Arafin [4] study

The approach taken in Chapter 4.4 to determine the apparent diffusion coefficient of boron in the base metal was employed on the surface prepared half-joints. Only the migrating interface model was applied to determine the diffusion coefficient at 1050°C that best correlated with the predicted t_{IS} from thermal analysis. The k_{IS} determined from a $2w_t$ or MBC plot can be expressed in the following manner.

$$k_{IS} = 4\gamma\sqrt{D_{B\text{-}IN718}} \qquad \text{Eq. (7.4.1)}$$

The same value of 0.011 used in Chapter 4.4 was used here to determine k_{IS}, and values determined by Eq. 7.4.1 and from the MBC plot are found in Table 7.4.1. The diffusion coefficient that correlated with the average t_{IS} from DSC was used in Eq. 7.4.1 and is also included in Table 7.4.1.

Table 7.4.1 - Comparison of k_{IS} determined via modelling and thermal analysis

Sample Type	$D_{B\text{-}IN718}$ $\left[\frac{m^2}{s}\right]$	k_{IS} $\left[\frac{\mu m}{\sqrt{min}}\right]$	From MBC Plot	
			k_{IS} $\left[\frac{\mu m}{\sqrt{min}}\right]$	$t_{IS,\,MBC}$ [min]
AC	1.8E-10	4.6	4.9	365
AC+NiCr	2.3E-10	5.2	4.9	287
AC+NiCr+Ni(F)	4.0E-10	6.8	6.8	168
AC+NiCr+Ni(B)	3.8E-10	6.6	5.2	175
AC+Ni(F)	4.5E-10	7.3	7.2	146

The apparent diffusion coefficients for samples absent of any Ni plating were very close to the value of 2.0E-10 m^2/s determined in Chapter 4.4 for the ISP samples. This makes sense as the ISP sample is a comparable type of surface pre-treatment to the AC and AC+NiCr surface preparation routes. k_{IS} predicted using the migrating interface model and the MBC plots in Figure 7.3.3 agreed very well for the Ni(F) samples. The presence of a Ni plating step results in an increase in the apparent diffusion coefficient, up to 4.5E-10 m^2/s for the AC+Ni(F) sample.

CHAPTER 8 Summary & Conclusions

8.1 Using Differential Scanning Calorimetry to Study the Transient Liquid Phase Bonding Behavior of IN718/BNi-2

The application of the cyclic DSC method allows for measurement of important aspects related to the TLPB of IN718 with a BNi-2 FM. DSC combined with metallographic analysis can be a useful tool to characterize the kinetics of a TLPB couple. The use of a cyclic thermal profile allows for the entire IS curve to be obtained using a single sample and DSC test.

For the cyclic testing, k_{IS} for IN718/BNi-2 couple was determined to be 4.8 μm/$\sqrt{\text{min}}$ and t_{IS} required to obtain an MBC of 114 μm was predicted to be 247 minutes. Interrupted DSC testing determined the k_{IS} for IN718/BNi-2 couple to be 4.6 μm/$\sqrt{\text{min}}$ and t_{IS} to obtain an MBC of 114 μm was predicted to be 219 minutes. Interrupted testing to validate the cyclic method determined that the two approaches agree well with each other. Some degree of variability between the two approaches was still observed.

Rapid diffusion of boron during heating resulted in a portion of the liquid freezing before T_B was reached. This was confirmed both microstructurally and from the analysis of the various plots generated from the DSC data for both cyclic and interrupted testing.

Variability caused by poor wetting and dissolution can be accounted for by converting the liquid width plot to an MBC plot. The liquid width at zero hold time (10 minutes liquid duration) estimated from cyclic DSC data set was 62 ± 4 μm, suggesting that approximately 52 ± 4 μm (26 μm ± 2 for a half-joint) had already solidified by the time the half-joint reached the liquidus temperature. The MBC at 10 minutes liquid duration predicted by thermal analysis was 51 ± 5 μm for the cyclic series. Although these predictions from the DSC data were slightly higher than the actual measured ISZ width for the 0-minute hold sample of 20 ± 5 μm (40 μm ± 10 for a full joint), relatively good agreement was still achieved considering the cyclic series was made up of six different sets of filler and base metal samples. Experimental and theoretical predictions found in the literature agreed well with the DSC predictions.

8.2 Surface Characterization

The surface of samples that omitted a NiCr step produced very similar S_a values, and the physical appearance of the samples under the stereomicroscope was also very similar. Samples that were subject to the NiCr step had a very wavy appearance and comparable S_a values. Randomly oriented striations of varying size were produced on the AC and AC+Ni(F) samples. The surface of AC+NiCr and AC+NiCr(B) were very similar in the sense that they had a ductile and dimpled surface imposed by the roughening step. The NiCr process resulted in smearing and deformation of the faying surface for those two sample types.

The thickness of the Ni(F) layer was 8 ± 1 μm for the AC+NiCr+Ni(F) and was 4 ± 1 for the AC+Ni(F) sample. The Ni(F) coating was determined to be composed of mostly Ni with minor amounts of Fe present. There was no confirmation of a continuous layer of Ni on AC+NiCr+Ni(B) due to the localized application of the nickel coating via a brush. High magnification FE-SEM micrographs revealed the nickel coating on both the Ni(F) samples had a dendritic morphology. This dendritic morphology was absent in AC+NiCr+Ni(B) substrates. The FE-SEM micrographs also showed that the Ni(F) coating had the presence of cracks and crater-like defects. The cracks formed a network in the coating and travelled through the crater defects.

8.3 Influence of Surface Preparation on Wetting & Spreading of Molten BNi-2 on Inconel 718

The absence of exothermic peaks on DSC traces during the final cooling segment for Ni(F) samples indicated that IS went to completion. Sample types that did not contain a Ni(F) step did not reach completion of IS, as indicated by the exothermic peaks observed on the final cooling trace. The exothermic peaks observed on cooling for samples such as the AC+NiCr sample were associated with the athermal solidification of residual liquid during cooling to room temperature. The presence of liquid on cooling to room temperature was an indicator that IS did not reach completion for those samples.

The AC, AC+NiCr, and No Prep samples were subject to poor wetting and spreading behavior. The shape of the FM was constant before and after brazing, as was the area of FM coverage. The spreading index for these samples was approximately equal to unity.

These sample types demonstrated Case A wetting behavior. Case A is the situation where poor wetting occurred, resulting in a w_o that was very close to the nominal foil thickness, the area of FM coverage being constant, and the spreading index equal to unity.

Ni(F) samples showed the most promising behavior from a wetting and spreading perspective. The presence of a Ni(F) step resulted in significant wetting and spreading of the FM over the faying surface of the BM. In fact, Ni(F) samples exhibited the highest degree of BM wettability out of the various surface conditions tested. The presence of the NiCr step in the AC+NiCr+Ni(F) sample provided minor increases in wettability compared to the AC+Ni(F) sample. This could potentially serve as evidence that the NiCr step is not really required, at least from a wettability perspective. The shape of the FM was different than the original shape, and the area of FM coverage was increased significantly. The spreading index for these samples was greater than 3.0. Ni(F) samples demonstrated a Case B wetting behavior, where the w_o was much smaller than the nominal foil thickness, the area covered by the FM was much greater than the original foil area, and the spreading index was much greater than unity. AC+NiCr+Ni(B) samples showed wetting behavior that lied between Case A and B. The shape and area of the FM changed somewhat after brazing, and the spreading index was 2.0.

It was postulated that samples absent of the Ni(F) step were subject to different oxidation behavior. Samples such as the AC+NiCr type resulted in formation of an external scale of Cr_2O_3 and precipitation of an internal subscale of Al_2O_3. The FM was not able to wet the oxide surface of the BM as liquid metals demonstrate poor wettability on metal oxides. The thermodynamically stable Cr_2O_3 scale resulted in an overall increase in the $\gamma_{S/L}$ resulting in an apparent increase in the work of adhesion and contact angle, and therefore causing the spreading process to be inhibited. Although the Ni(F) layer had increased Cr due to interdiffusion between plating and BM, the Cr present was insufficient to form the Cr_2O_3 layer. It was believed that the Ni(F) layer acted to protect the "virgin" IN718 BM surface from forming the Cr_2O_3 layer and instead formed a NiO layer. This NiO layer was able to be reduced by the B contained within the FM, and the wetting and spreading process could reinitiate on the freshly created Ni surface. The Ni(F) layer resulted in a reduction of the $\gamma_{S/L}$ and increased the cohesive force between the liquid FM and the BM faying surface.

Surface roughness was determined to have a minor role on the wettability of the various surfaces investigated. No direct relationship between surface roughness and wettability was observed, except for in the case of the AC+NiCr+Ni(B) sample. The Ni(B) sample seen an increase in both surface roughness and wettability compared to the AC and AC+NiCr samples. In general, wettability was controlled by the presence of the protective Ni(F) layer as opposed to changes in surface roughness imposed by the various surface preparation methods studied.

The microstructure of Ni(F) samples confirmed the conclusions determined from DSC results, that completion of IS was achieved. This was evidenced by the absence of an ASZ in the microstructure. Ni(F) samples were able to spread out over the faying surface, resulting in a reduction in w_o. Since w_o was reduced, the Ni(F) samples were able to reach completion of IS within the given brazing time. Samples subject to poor wetting and spreading, such as the AC+NiCr samples, resulted in a larger w_o value than Ni(F) samples. Since the w_o was larger, IS was not able to reach completion in these samples, resulting in the presence of an ASZ within the microstructure and detection of an exothermic peak on cooling in the DSC.

Some other very interesting observations were revealed by conducting metallography on the samples. Optical microscopy revealed that the Ni(F) plating becomes alloyed and homogeneous with the FM after two cycles (approximately 25 minutes at 1050°C). It was determined that both types of the Ni(F) samples were subject to microporosity. This microporosity was located at the interface between the Ni plating and the IN718 BM. There was some microporosity observed in the as-received condition, but the amount of microporosity was increased after brazing. The increased porosity was thought to occur due to the Kirkendall effect. It was determined that Ni(F) samples had a denuded BM region located adjacent to the Ni(F) plating. Interdiffusion between the BM and the plating resulted in BM elements migrating into the plating. This resulted in a layer beneath the plating that was termed the denuded zone. The boride former potential of the denuded zone was lowered due to reduced amounts of Nb, Cr, and Mo. This inhibited the precipitation of borides in the denuded zone and caused the DAZ to form in the BM adjacent to the denuded zone.

8.4 Effect of Surface Preparation on Transient Liquid Phase Bonding Behavior of Inconel 718/BNi-2

Two exothermic peaks were observed on the first cooling segment of DSC traces belonging to samples without a Ni(F) plating. The onset temperature of the first peak was 1000-1005°C. Samples that were subject to a Ni(F) sample had a third exothermic peak present on the first cooling segment. This additional peak present on Ni(F) samples was a broad peak that had an onset temperature around 1030°C. The character of cooling trace for samples containing a Ni(F) step resembled that of the BNi-2 foil alone and the diffusion barrier experiment. The standard deviation in enthalpy measurements for Ni(F) was smaller than other sample types and was related to the extent of wetting and spreading.

As in SET II, AC and AC+NiCr samples were subject to poor wetting and spreading. This resulted in an increase in the starting $2w_o$, which meant that those samples were unable to reach completion of IS during the 20 cycle DSC test. Therefore, liquid remained during cooling and an exothermic peak was present on the DSC trace. The conclusion of incomplete IS was verified by the presence of an ASZ within the microstructure of these samples. The opposite behavior was observed for samples with a Ni(F) plating, where IS was completed and no ASZ remained in the microstructure of those samples. The AC+NiCr+Ni(B) sample demonstrated intermediate wetting behavior, and therefore only had a very minor amount of ASZ present in the microstructure. The microstructural observations confirmed conclusions made based on DSC results for the various surface prepared samples.

The denuded zone present in Ni(F) samples during SET II experiments was persistent and existed after the 20 cycle DSC test. The microporosity observed in the Ni(F) samples also persisted after the longer brazing time was allotted. The denuded zone was 9 ± 3 μm for the AC+NiCr+Ni(F) sample, while it was 8 ± 2 μm for the AC+Ni(F) sample.

Chemical composition of the ISZ for the Ni(F) samples was the closest to the nominal FM composition. This was an indication that interdiffusion and dissolution was less for the Ni(F) samples. The amount of Cr, Fe, Nb, Mo was increased for samples omitting a Ni(F) step. The presence of a Ni(B) step had no marked influence on the dissolution and interdiffusion behavior. There was a steep chemical gradient of BM elements formed in

the denuded zone. Differences observed between the compositional profiles of samples with and without Ni(F) further supported the conclusion of less interdiffusion and dissolution occurring in the Ni(F) samples.

In terms of the kinetics determined from DSC analysis, the presence of a Ni(F) step resulted in an increase in k_{IS} and a reduction in the IBU. The opposite conclusion was drawn for samples that did not contain a Ni(F) layer. In fact, the absence of a Ni(F) step can result in up to 50% of the starting $2w_o$ being solidified due to IBU. The reduced extent of IBU was consistent with conclusion of less interdiffusion occurring in these samples. Samples without a Ni(F) present resulted in the longest t_{IS} for their respective $2w_o$. The $2w_o$ of samples with Ni(F) was inherently larger due to poor wetting and spreading, resulting in the increase t_{IS} value. Despite this, those samples were able to grow a significant ISZ layer by the time T_B was first reached due to IBU.

Ni(F) samples had a reduced quantity of boride formers present compared to the BM. A higher boride former potential within the BM means that a shorter t_{IS} can be achieved. Since the Ni(F) substrates had a reduced boride precipitation potential within the denuded zone, the t_{IS} for those samples was increased compared to other sample types. The denuded zone resulted in an increase in the required diffusion distance for B to be able to precipitate borides and initiate the growth of IS. The increase in diffusion distance can explain the sluggish IBU process exhibited by Ni(F) samples.

The target gap width (or MBC) must be considered when determining the optimum base metal surface preparation route for brazing IN718 using BNi-2 FM. Despite the increased k_{IS} exhibited by the Ni(F) specimens, the large degree of IBU experienced by samples such as the AC type ends up being the limiting factor in terms of t_{IS}.

In order for the molten FM to flow freely and fill the entire gap without creating porosity, the spreading index needs to be considered. If the spreading index is low, that implies that the FM has poor wettability when that surface preparation method is used. FM flow through a joint with a BM that has low spreading index could be halted early and areas not wet by FM can create porosity. If the target $2w_o$ is smaller than the predicted MBC at $2.2\sqrt{\min}$, then gap filling issues could potentially arise. The FM could freeze before travelling the

full joint length, and growth of large ISZ dendrites into the melt could potentially act to choke off the flow of the metal through the joint.

Actual width of ISZ for 60-minute isothermal hold tests agreed well with predictions of ISZ made by MBC plot. The best agreement was achieved for Ni(F) substrates. Agreement between Ni(F) samples and the Arafin study also agreed very well.

8.5 Future Work

An investigation into how the various surface preparations would influence dynamic gap filling would certainly compliment this study. As indicated in this study, surface preparation on IN718 can have a great effect on the wettability of the faying surface and the kinetics of IS.

It would be very interesting to produce lap joints using the various surface conditions included in this study. Examining how the differences in IBU and other kinetic parameters imposed by the surface condition impact the overall joint quality and microstructure. It would also be worthwhile conducting mechanical testing on the lap joints to understand how fracture occurs within the joints. Quantifying how the denuded zone and the microporosity observed in Ni(F) samples influence the mechanical properties. These features could serve as potential sites for crack nucleation and growth for a joint prepared with a Ni(F) treatment.

It would also be meaningful to investigate whether the microporosity observed in Ni(F) samples can be alleviated in some manner. Potentially these pores could be remedied via an SSH treatment conducted post brazing. Determining how the SSH treatment influences re-melt temperature for Ni(F) samples would also be valuable. The SSH study could be accomplished using a DSC.

References

[1] M. M. Schwartz, *Brazing*, 2nd ed. Materials Park, OH: ASM International, 2003.

[2] D. S. Duvall, W. A. Owczarski, and D. F. Paulonis, "Tlp Bonding: a New Method for Joining Heat Resistant Alloys.," *Weld. J. (Miami, Fla)*, vol. 53, no. 4, pp. 203–214, 1974.

[3] "Brazing Handbook," 5th ed., Miami, Fl: American Welding Society, 2006, p. 110.

[4] W. F. Smith, *Structure and Properties of Engineering Alloys*. Montreal, QC: McGraw-Hill Book Company, 1981.

[5] R. C. Reed, *Superalloys - Fundamentals and Applications*, 1st ed. New York: Cambridge University Press, 2006.

[6] M. J. Donachie and S. Donachie, *Superalloys - A Technical Guide*, 2nd ed. Materials Park, OH: ASM International, 2002.

[7] M. A. Arafin, M. Medraj, D. P. Turner, and P. Bocher, "Transient liquid phase bonding of Inconel 718 and Inconel 625 with BNi-2: Modeling and experimental investigations," *Mater. Sci. Eng. A*, vol. 447, no. 1–2, pp. 125–133, 2007.

[8] M. Pouranvari, A. Ekrami, and A. H. Kokabi, "Role of base-metal composition in isothermal solidification during diffusion brazing of nickel-based superalloys," *Sci. Technol. Weld. Join.*, vol. 23, no. 1, pp. 13–18, 2018.

[9] M. M. Schwartz, *Welding, brazing and soldering*, vol. 6. Materials Park, OH: ASM International, 1993.

[10] W. F. Gale and D. A. Butts, "Transient Liquid Phase Bonding," *Sci. Technol. Weld. Join.*, vol. 9, no. 4, pp. 283–300, 2004.

[11] J. Barone and R. Page, "Heat Exchanger Panel and Manufacturing Method Therof Using Transient Liquid Phase Bonding Agent and Vacuum Compression Brazing," US20090049794, 2009.

[12] W. MacDonald and T. Eagar, "Transient liquid phase bonding," *Annu. Rev. Mater. ...*, vol. 1, no. 1, pp. 23–46, 1992.

[13] Y. Wang, "Transient Liquid Phase Joining of Carbon and Stainless Steels to Aluminium Alloy Using Gallium Metal," University of Illinois at Chicago, 2015.

[14] G. O. Cook and C. D. Sorensen, "Overview of Transient Liquid Phase and Partial Transient Liquid Phase Bonding," *J. Mater. Sci.*, vol. 46, no. 16, pp. 5305–5323, 2011.

[15] Y. Zhou, W. F. Gale, and T. H. North, "Modelling of Transient Liquid Phase Bonding," *Int. Mater. Rev.*, vol. 40, no. 5, pp. 181–196, 1995.

[16] N. S. Bosco and F. W. Zok, "Critical Interlayer Thickness for Transient Liquid Phase Bonding in the Cu-Sn System," *Acta Mater.*, vol. 52, no. 10, pp. 2965–2972, 2004.

[17] D. M. Jacobson and G. Humpston, "Principles of Brazing," 1st ed., Materials Park, OH: ASM International, 2005, p. 268.

[18] H. Ikawa, Y. Nakao, and T. Isai, “Theoretical Considerations on the Metallurgical Process in T.L.P. Bonding of Nickel-Base Superalloys,” *Trans. Japan Weld. Soc.*, vol. 10, no. 1, pp. 24–29, 1979.

[19] Y. Nakao, K. Nishimoto, K. Shinozaki, and C. Kang, “Theoretical Research on Transient Liquid Insert Metal Diffusion Bonding of Nickel Base Alloys,” in *Superalloys 1988*, 1989, pp. 775–783.

[20] I. Tuah-Poku, M. Dollar, and T. B. Massalski, “A Study of the Transient Liquid Phase Bonding Process Applied to a Ag/Cu/Ag Sandwich Joint,” *Metall. Trans.*, vol. 19A, pp. 675–686, 1988.

[21] M. Pouranvari, A. Ekrami, and A. H. Kokabi, “Diffusion induced isothermal solidification during transient liquid phase bonding of cast IN718 superalloy,” *Can. Metall. Q.*, vol. 53, no. 1, pp. 38–46, 2014.

[22] W. F. Gale and E. R. Wallach, “Influence of Isothermal Solidification on Microstructural Development in Ni-Si-B Filler Metals,” *Mater. Sci. Technol.*, vol. 7, no. December, pp. 1143–1148, 1991.

[23] H. Nakagawa, C. H. Lee, and T. H. North, “Modeling of base metal dissolution behavior during transient liquid-phase brazing,” *Metall. Trans. A*, vol. 22, no. 2, pp. 543–555, 1991.

[24] M. Pouranvari, A. Ekrami, and A. H. Kokabi, “Diffusion brazing of cast INCONEL 718 superalloy utilising standard heat treatment cycle,” *Mater. Sci. Technol.*, vol. 30, no. 1, pp. 109–115, 2014.

[25] American Welding Society (AWS) A5 Committee on Filler Metals and Allied Materials, “Specification for Filler Metals for Brazing and Braze Welding, AWS A5.8M:2004,” Miami, Fl, 2004.

[26] T. Tokunaga, K. Nishio, and M. Hasebe, “Thermodynamic Study of Phase Equilibria in the Ni-Si-B System,” *J. Phase Equilibria*, vol. 22, no. 3, pp. 291–299, 2001.

[27] M. Pouranvari, A. Ekrami, and A. H. Kokabi, “TLP bonding of cast IN718 nickel based superalloy: Process-microstructure-strength characteristics,” *Mater. Sci. Eng. A*, vol. 568, pp. 76–82, 2013.

[28] N. P. Wikstrom, A. T. Egbewande, and O. A. Ojo, “High temperature diffusion induced liquid phase joining of a heat resistant alloy,” *J. Alloys Compd.*, vol. 460, no. 1–2, pp. 379–385, 2008.

[29] M. Pouranvari, A. Ekrami, and A. H. Kokabi, “Effect of bonding temperature on microstructure development during TLP bonding of a nickel base superalloy,” *J. Alloys Compd.*, vol. 469, no. 1–2, pp. 270–275, 2009.

[30] Y. Nakao, K. Nishimoto, K. Shinozaki, and C. Kang, “Theoretical Research on Transient Liquid Insert Metal Diffusion Bonding of Nickel Base Alloys,” *Trans. Japan Weld. Soc.*, vol. 20, no. 1, pp. 60–65, 1989.

[31] A. Ghoneim and O. A. Ojo, “Microstructure and mechanical response of transient liquid phase joint in Haynes 282 superalloy,” *Mater. Charact.*, vol. 62, no. 1, pp. 1–7, 2011.

[32] O. A. Ojo, N. L. Richards, and M. C. Chaturvedi, “Isothermal solidification during transient liquid phase bonding of Inconel 738 superalloy,” *Sci. Technol. Weld. Join.*, vol. 9, no. 6, pp. 532–540, 2004.

[33] B. Zhang *et al.*, “Precipitation and evolution of boride in diffusion affected zone of TLP joint of Mar-M247 superalloy,” *J. Alloys Compd.*, vol. 695, pp. 3202–3210, 2017.

[34] K. Nishimoto, K. Saida, D. Kim, and the late Y. Nakao, “Transient Liquid Phase Bonding of Ni-base Single Crystal Superalloy, CMSX-2.,” *ISIJ Int.*, vol. 35, no. 10, pp. 1298–1306, 1995.

[35] S. K. Tung, L. C. Lim, and M. O. Lai, “Solidification phenomena in nickel base brazes containing boron and silicon,” *Scr. Mater.*, vol. 34, no. 5, pp. 763–769, 1996.

[36] M. Pouranvari, a Ekrami, and a H. Kokabi, “Diffusion Brazing Metallurgy of IN718/Ni-Cr-Si-B-Fe/IN718,” *Weld. Res.*, vol. 93, no. February, 2014.

[37] R. H. Parker, “Interfacial Phenomena,” in *An Introduction to Chemical Metallurgy*, 2nd ed., Oxford, England: Pergamon International Library, 1978, pp. 212–261.

[38] H. D. Solomon, R. E. Delair, and J. Thyssen, “The High-Temperature Wetting Balance and the Influence of Grit Blasting on Brazing of IN718,” no. October, 2003.

[39] A. M. Nikitinskii, “Problem of wetting and surface tension,” *Weld. Int.*, vol. 13, no. 7, pp. 563–566, 1999.

[40] N. Eustathopoulos, “Wetting by Liquid Metals—Application in Materials Processing: The Contribution of the Grenoble Group,” *Metals (Basel).*, vol. 5, no. 1, pp. 350–370, 2015.

[41] W. F. Gale, “Transient Liquid Phase Bonding of Intermetallic Compounds,” *Mater. Sci. Forum*, vol. 426, no. 3, pp. 1891–1896, 2003.

[42] R. C. Tucker and P. S. T. Inc, *Surface Engineering*. ASM International, 1993.

[43] American Welding Society (AWS) C3 Committee on Brazing and Soldering, “Specification for Furnace Brazing 3.6M 2016.” American Welding Society, Miami, Fl, p. 18, 2015.

[44] M. B. Johnson and M. A. White, “Thermal Methods,” in *Multi Length-Scale Characterisation*, D. W. Bruce, D. O’Hare, and R. L. Walton, Eds. Wiley, 2014, pp. 63–119.

[45] M. E. Brown, *Introduction to Thermal Analysis: Techniques and Applications*, 3rd ed., vol. 1. New York, NY: Kluwer Academic Publishers, 2004.

[46] Netzsch, “Functional principle of a heat flux DSC.” [Online]. Available: https://www.netzsch-thermal-analysis.com/en/landing-pages/principle-of-a-heat-flux-dsc/. [Accessed: 22-May-2019].

[47] W. J. Boettinger, U. R. Kattner, and J. H. Perepezko, *DTA and Heat-flux DSC Measurements of Alloy Melting and Freezing*. Washington, DC: National Institure of Standards and Technology, 2006.

[48] Netzsch, “Differential Scanning Calorimetry - DSC 404 F1/F3 Pegasus - Method, Technique, Applications,” *Technical Brochure*, 2016. .

[49] S. Knappe, I. Sales, and A. Manager, “Analyzing & Testing Business Unit Quality Control and Failure Analysis of Polymers by Differential Scanning Calorimetry (DSC).” .

[50] J. Ruiz-Vargas, N. Siredey-Schwaller, N. Gey, P. Bocher, and A. Hazotte, “Microstructure development during isothermal brazing of Ni/BNi-2 couples,” *J. Mater. Process. Technol.*, vol. 213, pp. 20–29, 2013.

[51] J. Ruiz-Vargas, N. Siredey-Schwaller, N. Gey, P. Bocher, and A. Hazotte, “First melting stages during isothermal brazing, of Ni/BNi-2 couples,” *J. Mater. Process. Technol.*, vol. 213, no. 12, pp. 2074–2080, 2013.

[52] M. L. Kuntz, B. Panton, S. Wasiur-Rahman, Y. Zhou, and S. F. Corbin, “An Experimental Study of Transient Liquid Phase Bonding of the Ternary Ag-Au-Cu System Using Differential Scanning Calorimetry,” *Metall. Mater. Trans. A*, vol. 44, no. 8, pp. 3708–3720, 2013.

[53] M. L. Kuntz, Y. Zhou, and S. F. Corbin., "A study of transient liquid-phase bonding of Ag-Cu using differential scanning calorimetry," *Metall. Mater. Trans. A Phys. Metall. Mater. Sci.*, vol. 37, no. 8, pp. 2493–2504, 2006.

[54] N. Weyrich and C. Leinenbach, "Characterization of the isothermal solidification process in the Ni / Au – Ge layer system," pp. 3835–3844, 2015.

[55] S. F. Corbin, S. Winkler, D. R. Turriff, and M. Kozdras, "Analysis of fluxless, reactive brazing of al alloys using differential scanning calorimetry," *Metall. Mater. Trans. A Phys. Metall. Mater. Sci.*, vol. 45, no. 9, pp. 3907–3915, 2014.

[56] D. C. Murray and S. F. Corbin, "Determining the kinetics of transient liquid phase bonding (TLPB) of inconel 625/BNi-2 couples using differential scanning calorimetry," *J. Mater. Process. Technol.*, vol. 248, no. December 2016, pp. 92–102, 2017.

[57] J. T. Niemann and R. A. Garrett, "Eutectic Bonding of Boron-Aluminum Structural Components," *Weld. J. Res. Suppl.*, vol. 1, pp. 175–184, 1974.

[58] D. M. Turriff, S. F. Corbin, and M. Kozdras, "Diffusional solidification phenomena in clad aluminum automotive braze sheet," *Acta Mater.*, vol. 58, no. 4, pp. 1332–1341, 2010.

[59] *ASME B46.1-2009: Surface Texture (Surface Roughness, Waviness, and Lay)*. New York, NY: American Society of Mechanical Engineers.

[60] A. Davoodi Jamaloei, A. Khorram, and A. Jafari, "Characterization of microstructure and mechanical properties of dissimilar TLP bonding between IN718/IN600 with BNi-2 interlayer," *J. Manuf. Process.*, vol. 29, pp. 447–457, 2017.

[61] M. Pouranvari, A. Ekrami, A. H. Kokabi, and H. N. Han, "Microstructural characteristics of a cast IN718 superalloy bonded by isothermal solidification," *Met. Mater. Int.*, vol. 19, no. 5, pp. 1091–1099, 2013.

[62] V. Jalilvand, H. Omidvar, H. R. Shakeri, and M. R. Rahimipour, "Microstructural evolution during transient liquid phase bonding of Inconel 738LC using AMS 4777 filler alloy," *Mater. Charact.*, vol. 75, pp. 20–28, 2013.

[63] O. A. Ojo, N. . Richards, and M. C. Charturvedi, "Effect of gap size and process parameters on diffusion brazing of Inconel 738," *Sci. Technol. Weld. Join.*, vol. 9, no. 3, pp. 209–220, 2004.

[64] E. Lugscheider and K.-D. Partz, "High Temperature Brazing of Stainless Steel with Nickel-Base Filler Metals BNi-2 BNi-5 BNi-7," *Weld. J. WRS*, pp. 160-164s, 1983.

[65] E. Moreau and S. Corbin, "Predicting MBC from DSC analysis of IN625 BNi2 braze joints," "In submission stage," 2019.

[66] J. (John) Crank 1916-, "The mathematics of diffusion / John Crank.," pp. viii, 414 p., 1975.

[67] ASM Alloy Phase Diagrams Committee, "Alloy Phase Diagrams," in *ASM Handbook*, 3rd ed., vol. 3, no. 11, H. Baker, Ed. ASM Handbook, 1992, pp. 1–1741.

[68] S. LEBAILI and S. HAMAR-THIBAULT, "Equilibres Liquide-Solide Dans Le Systeme Ni-B-Si Dans La Region Riche En Nickel," *Acta Met.*, vol. 35, no. 3, pp. 701–710, 1987.

[69] M. A. Arafin, M. Medraj, D. P. Turner, and P. Bocher, "Optimization of process variables during TLP bonding of nickel superalloys," in *Aerospace Materials & Manufacturing: Emerging Materials,*

Processes and Repair Terchniques, 2006, pp. 301–313.

[70] V. Shukla, R. Jayaganthan, and V. Tewari, “Oxidation and Hot Corrosion Behaviour of Ni-based Superalloy Inconel 718 in Na2SO4 - 0.75 V2O5 Environment at Elevated Temperature,” *J. Mater. Eng. Perform.*, vol. 3, no. 1, pp. 20–24, 2003.

[71] W. F. Gale and E. R. Wallach, “Wettability of Nickel Alloys by Ni-Si-B fillers: influence of substrate oxide reduction and isothermal solidifcation,” *J. Mater. Sci.*, vol. 27, pp. 5653–5660, 1992.

Appendix A Example of Full Set of Traces from a Cyclic DSC Experiment

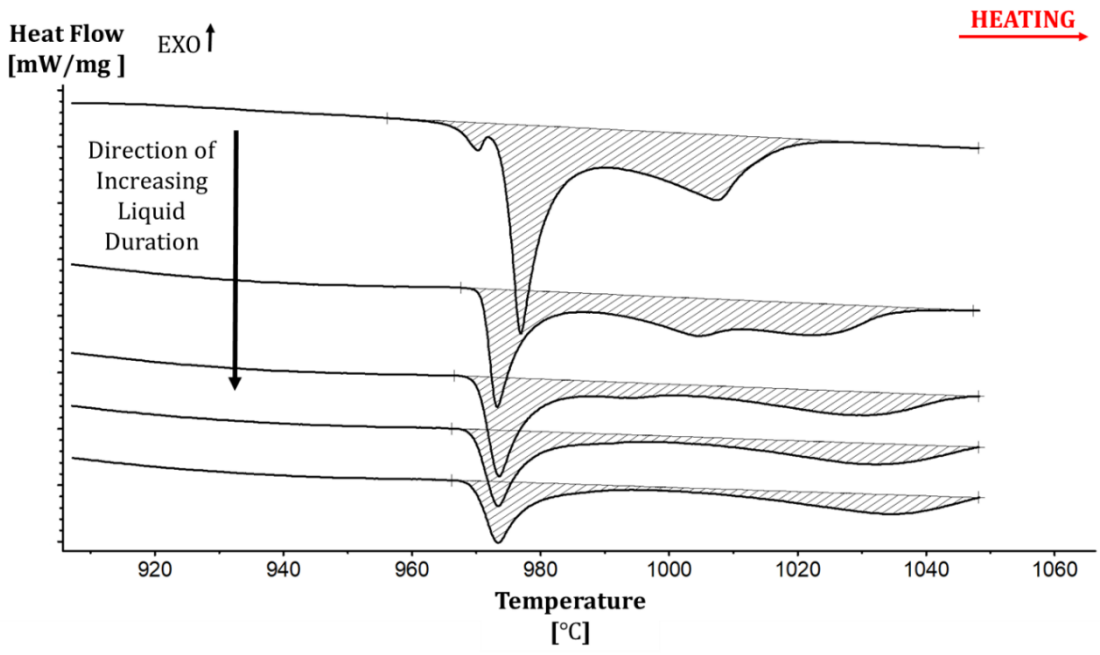

Figure A.1 - DSC traces for IN718/BNi-2 TLPB half-joint using ISP sample (Cycle #1 - 5)

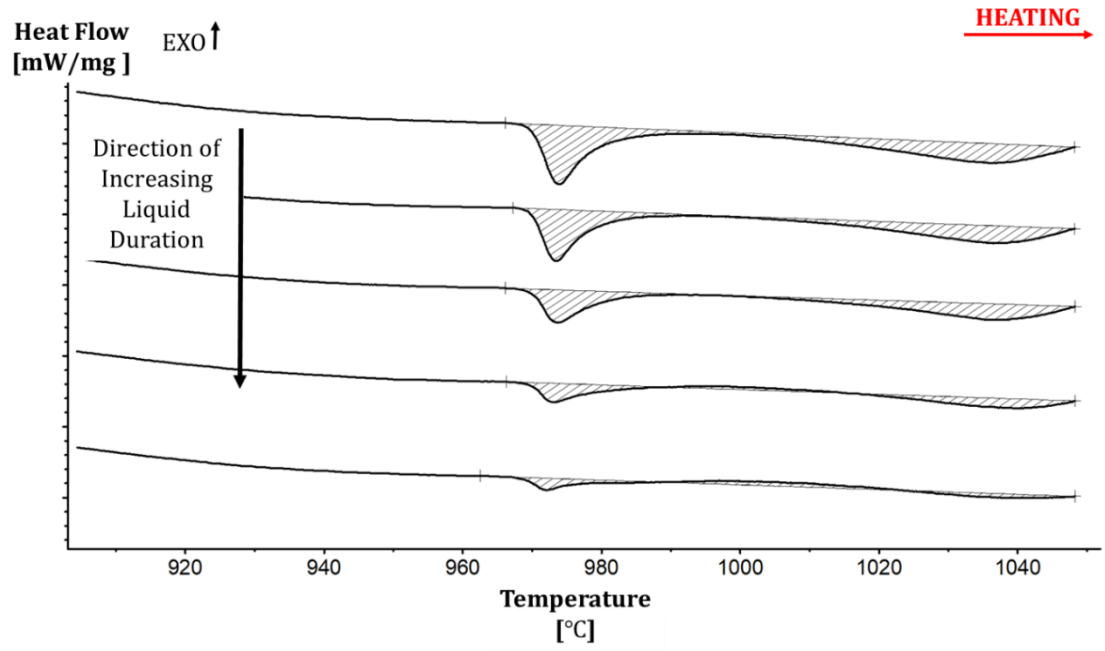

Figure A.2 - DSC traces for IN718/BNi-2 TLPB half-joint using ISP sample (Cycle #6 - 10)

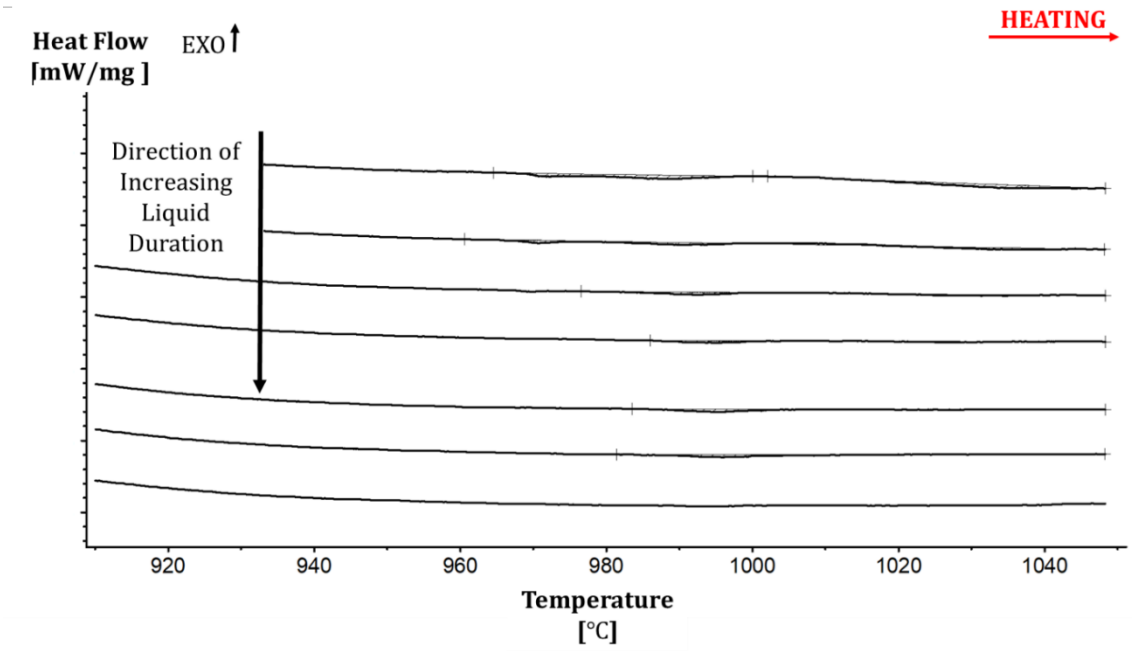

Figure A.3 - DSC traces for IN718/BNi-2 TLPB half-joint using ISP sample (Cycle #11 - 17)

***Note: Cycle #1-5 are located in Section 4.1.2**

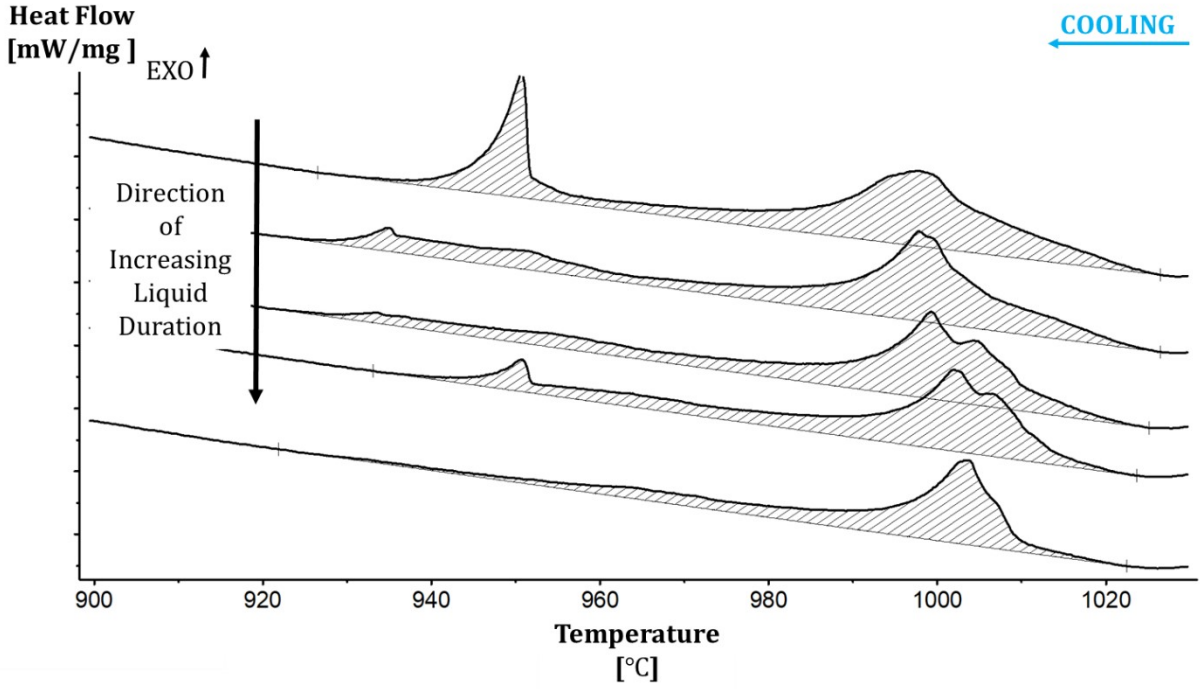

Figure A.4 - DSC traces for IN718/BNi-2 TLPB half-joint using ISP sample (Cycle #6 - 10)

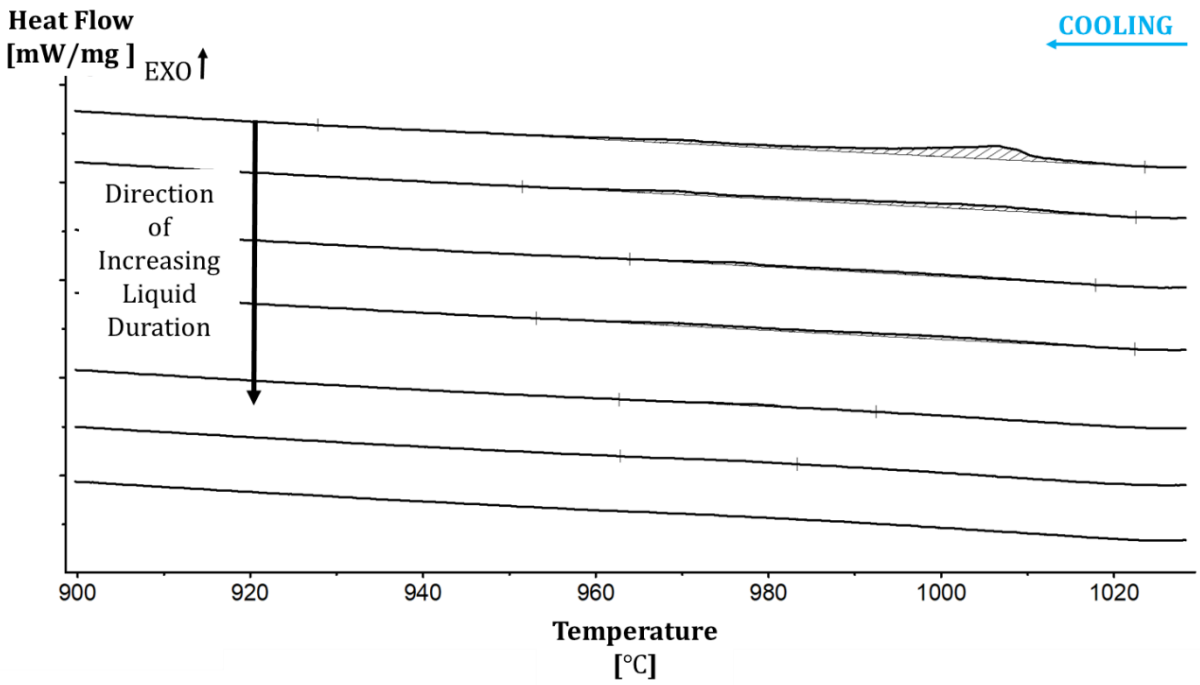

Figure A.5 - DSC traces for IN718/BNi-2 TLPB half-joint using ISP sample (Cycle #11 - 17)

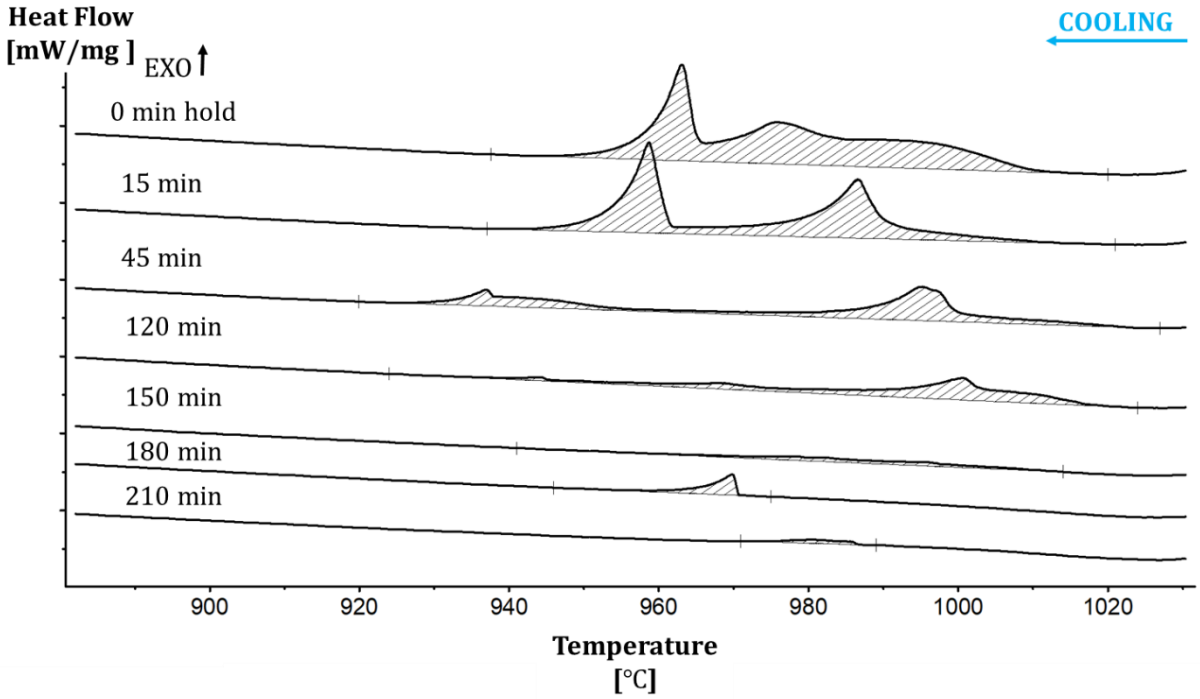

Figure A.6 - DSC traces for IN718/BNi-2 TLPB half-joint using ISP sample (isothermal hold)

Appendix B Additional Scanning Electron Micrographs of As-received Surface Prepared Inconel 718 Base Metal

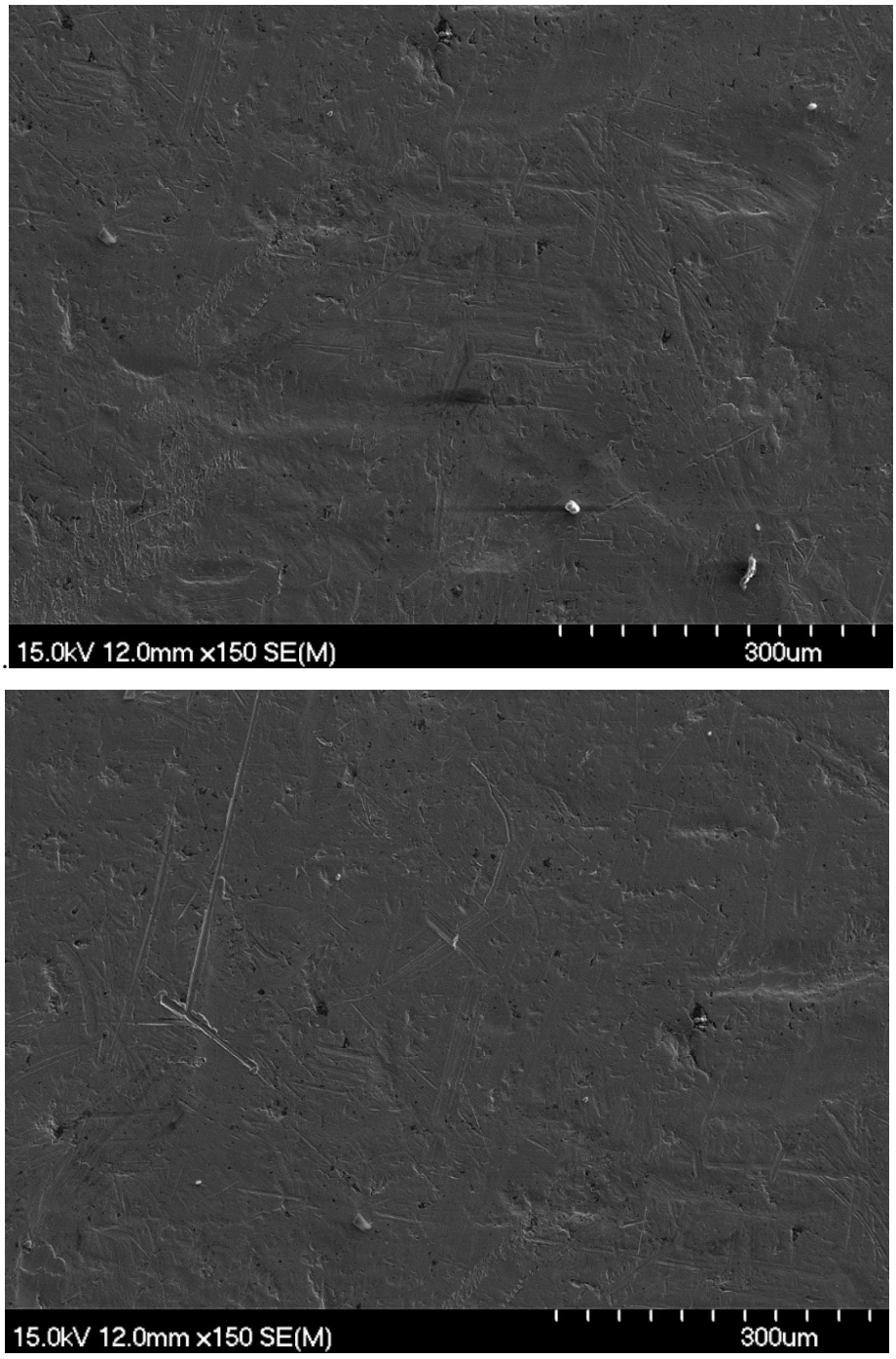

Figure B.1 - Additional FE-SEM Micrographs of As-received AC IN718 BM

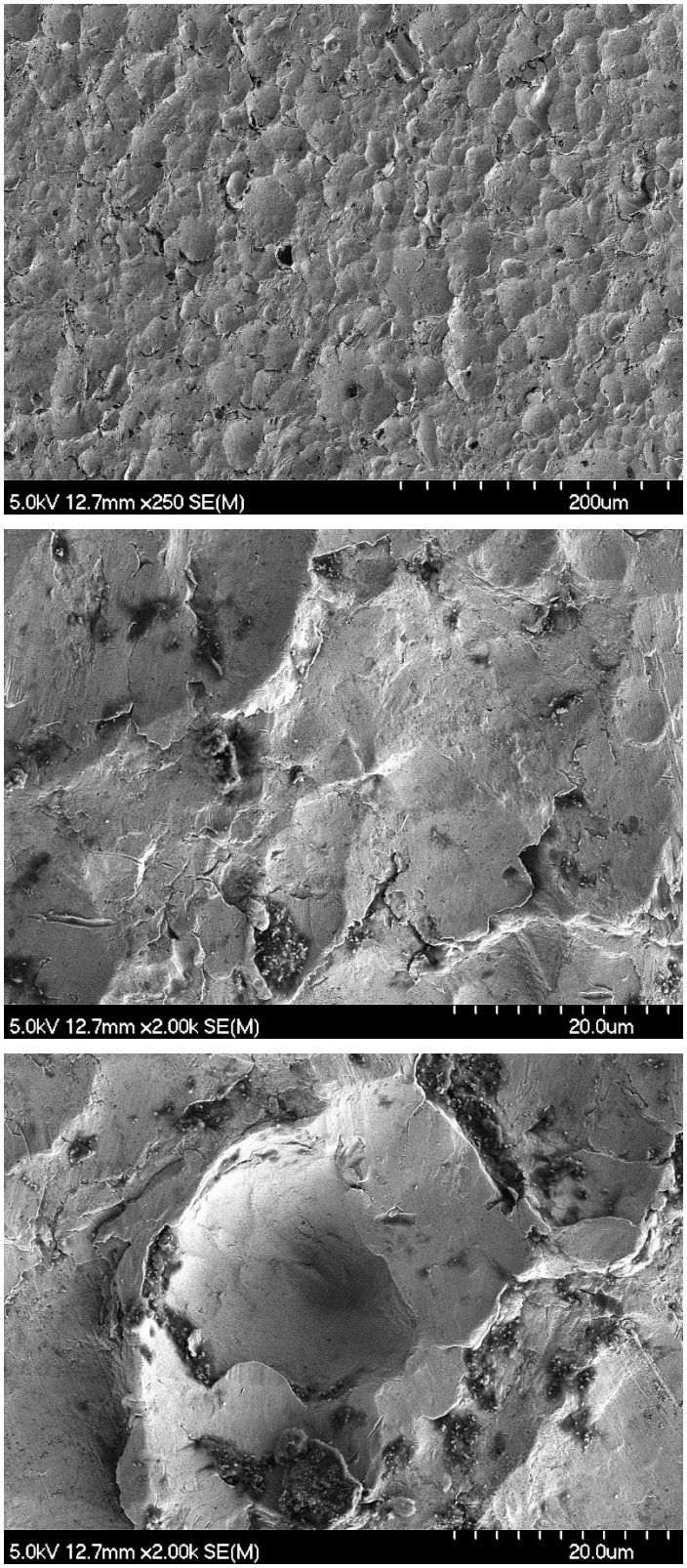

Figure B.2 - Additional FE-SEM Micrographs of As-received AC+NiCr IN718 BM

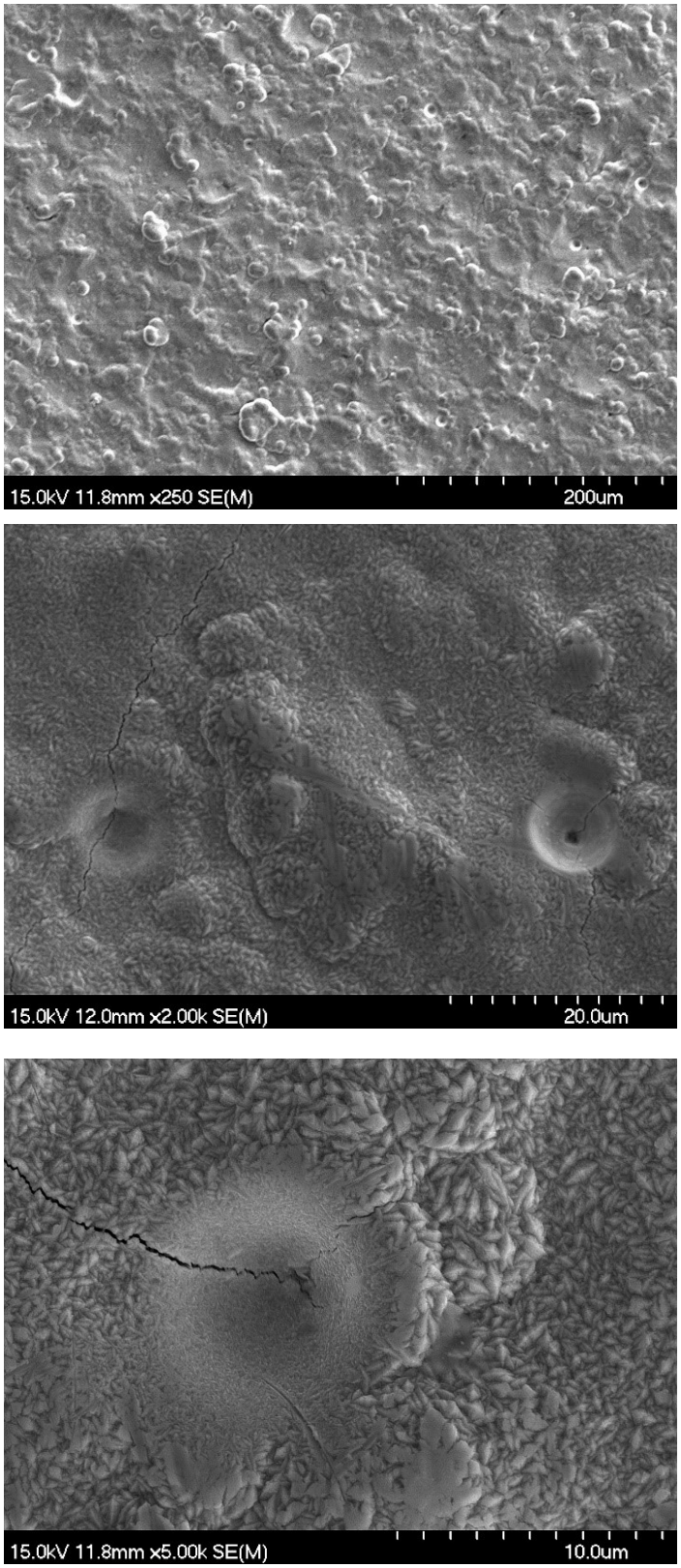

Figure B.3 - Additional FE-SEM Micrographs of As-received AC+NiCr+Ni(F) IN718 BM

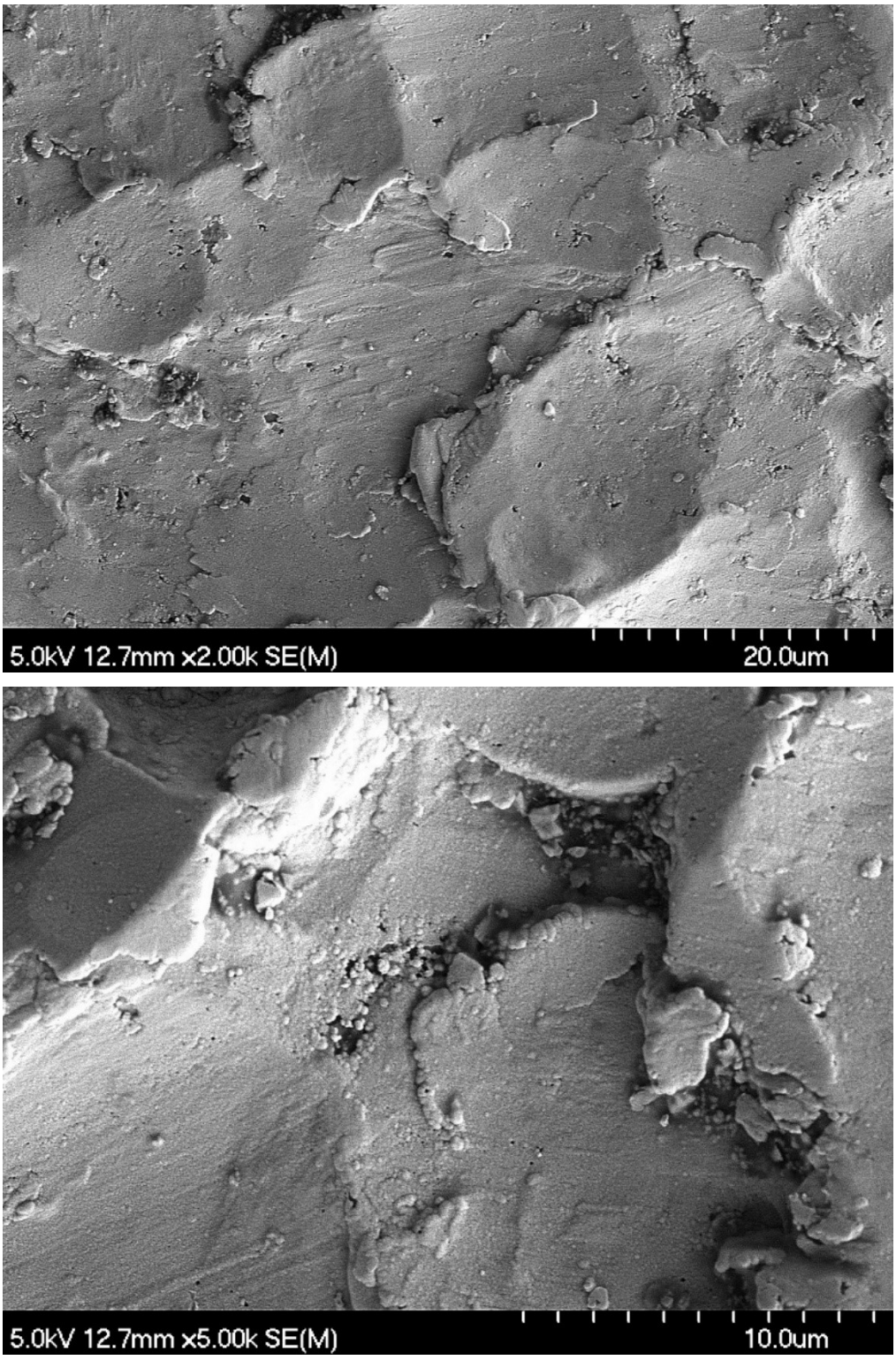

Figure B.4 - Additional FE-SEM Micrographs of As-received AC+NiCr+Ni(B) IN718 BM

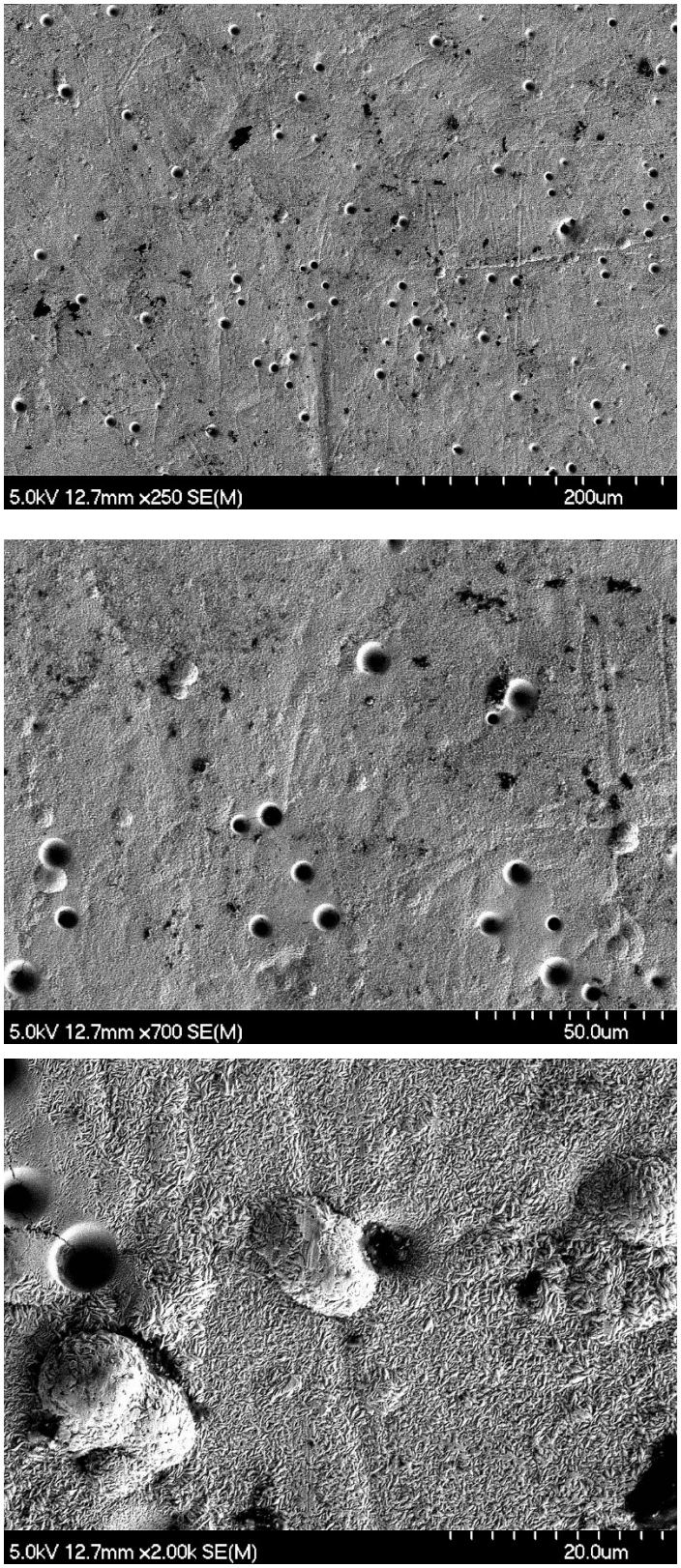

Figure B.5 - Additional FE-SEM Micrographs of As-received AC+Ni(F) IN718 BM

Appendix C Additional Micrographs & Height Maps of Surface Prepared Inconel 718 Base Metal Generated Using Laser Scanning Confocal Microscopy

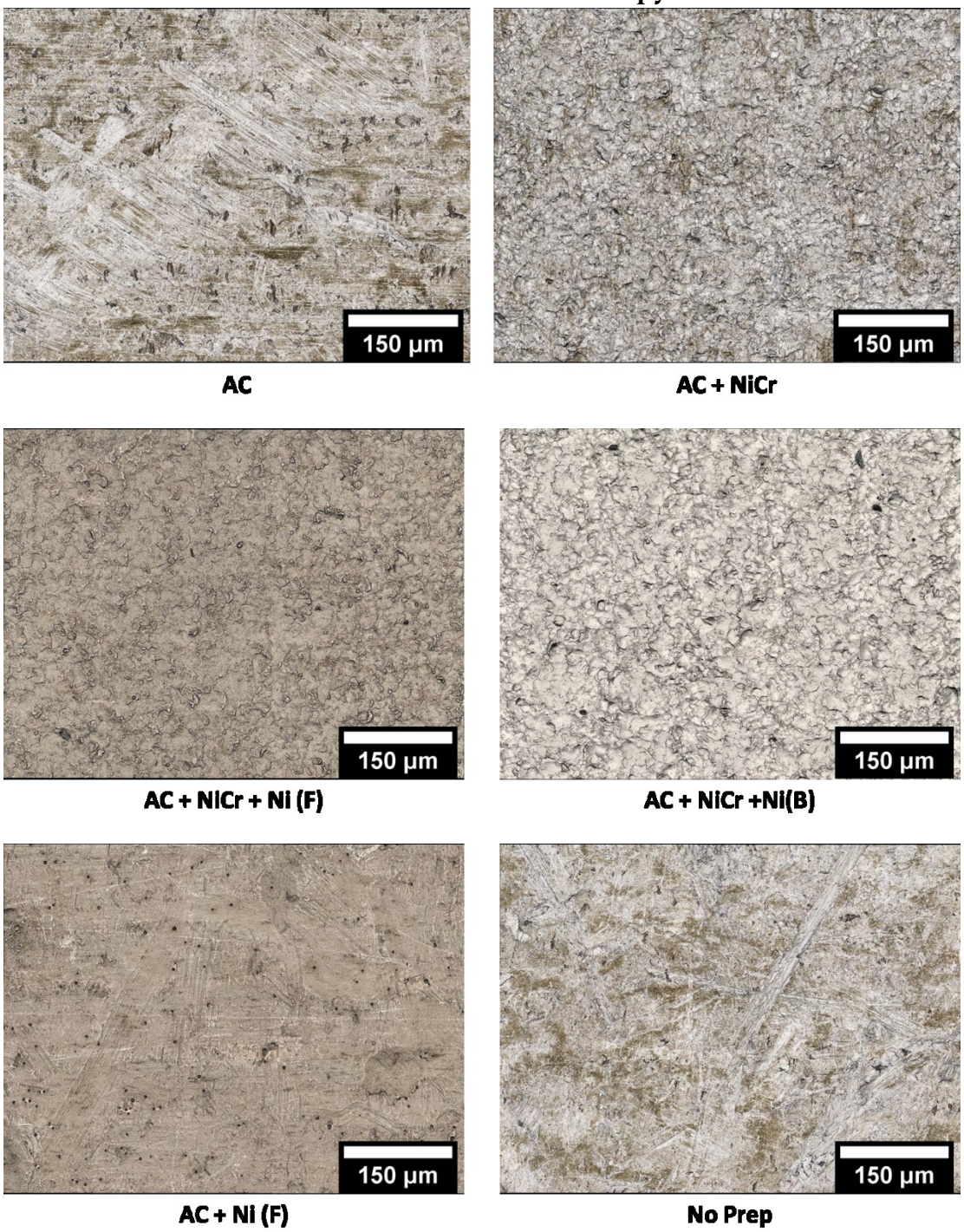

Figure C.1 – Laser + Optical Micrographs of Surface Prepared IN718 BM

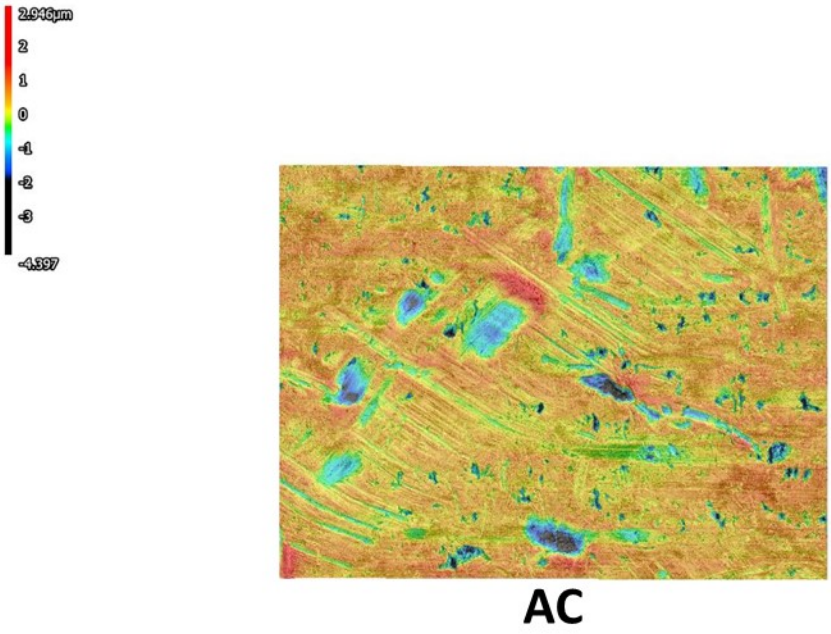

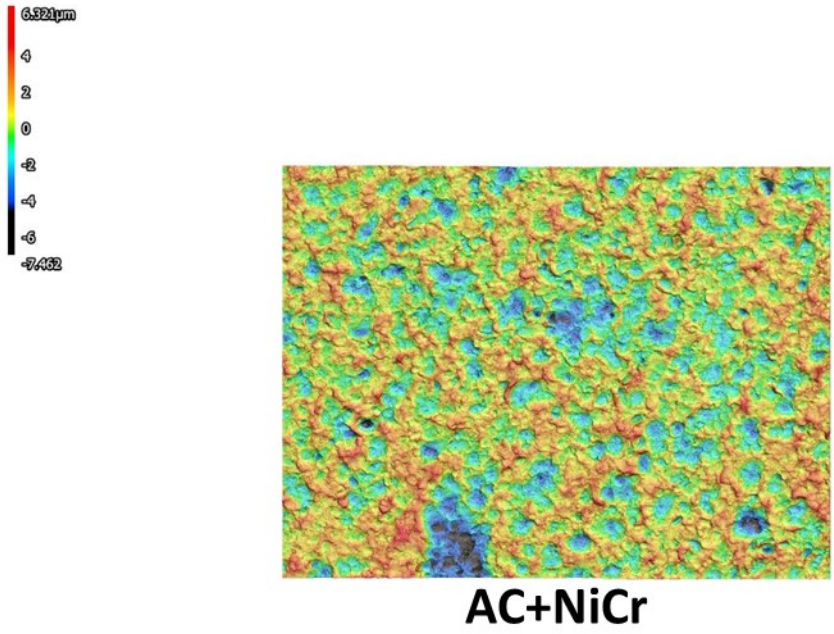

Figure C.2 - Height maps for AC & AC+NiCr samples

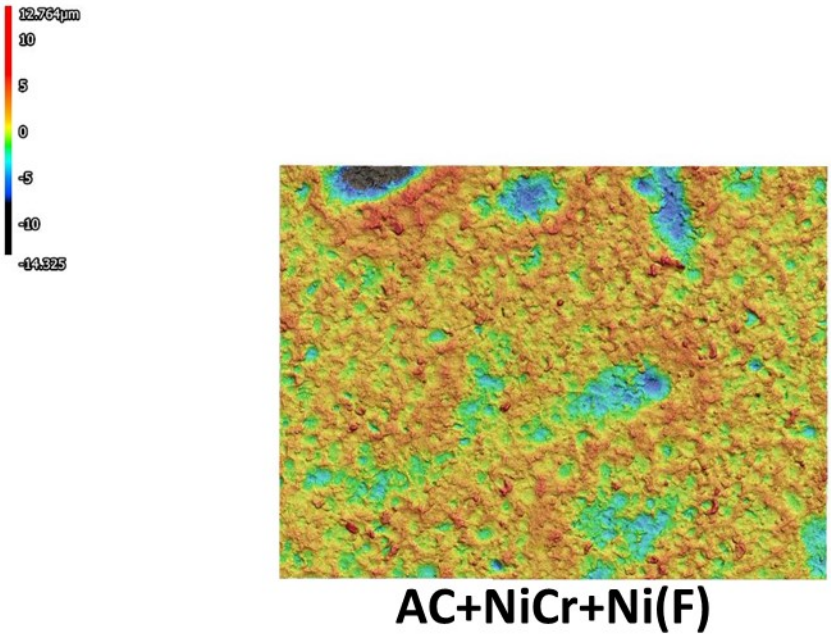

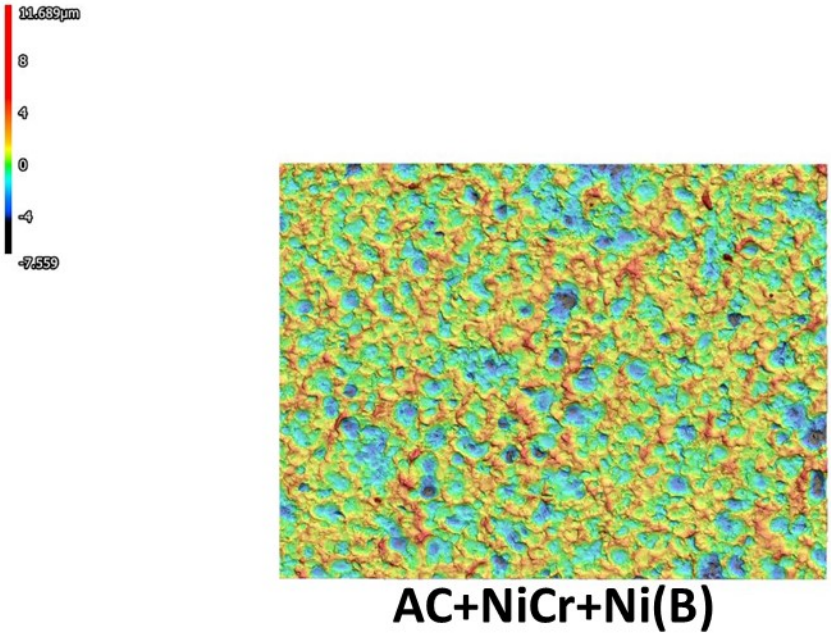

Figure C.3 - Height maps for AC+NiCr+Ni(F) & AC+NiCr+Ni(B) samples

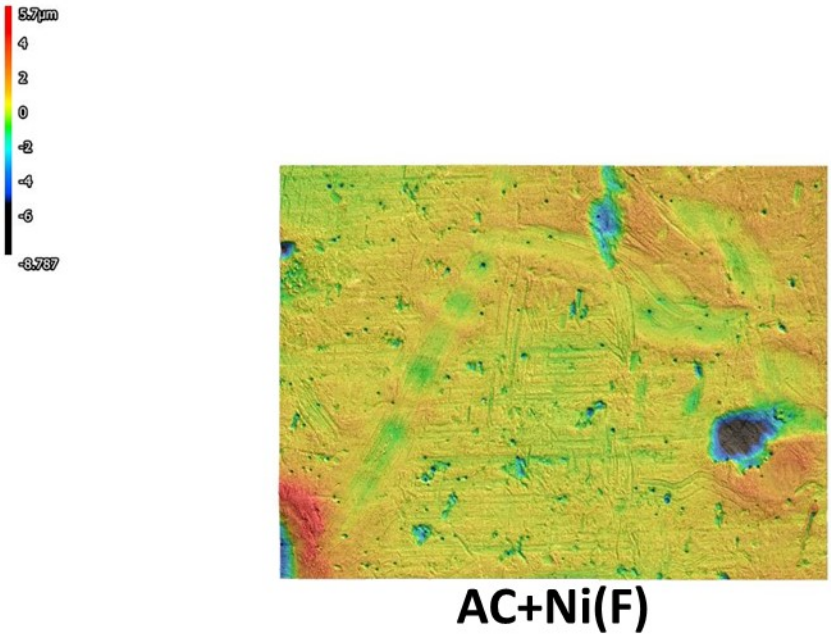

Figure C.4 - Height maps for AC +Ni(F) & No Prep samples

Appendix D Additional DSC Traces for Undersized BNi-2 Foil Experiments

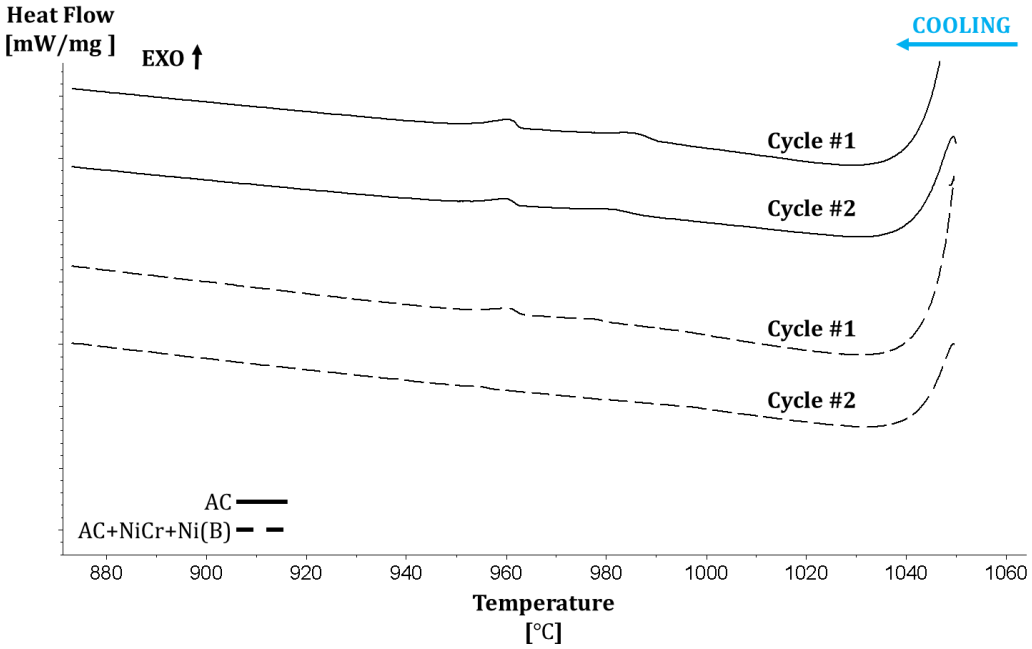

Figure D.1 - DSC traces of AC & AC+NiCr+Ni(B) samples using undersized foil

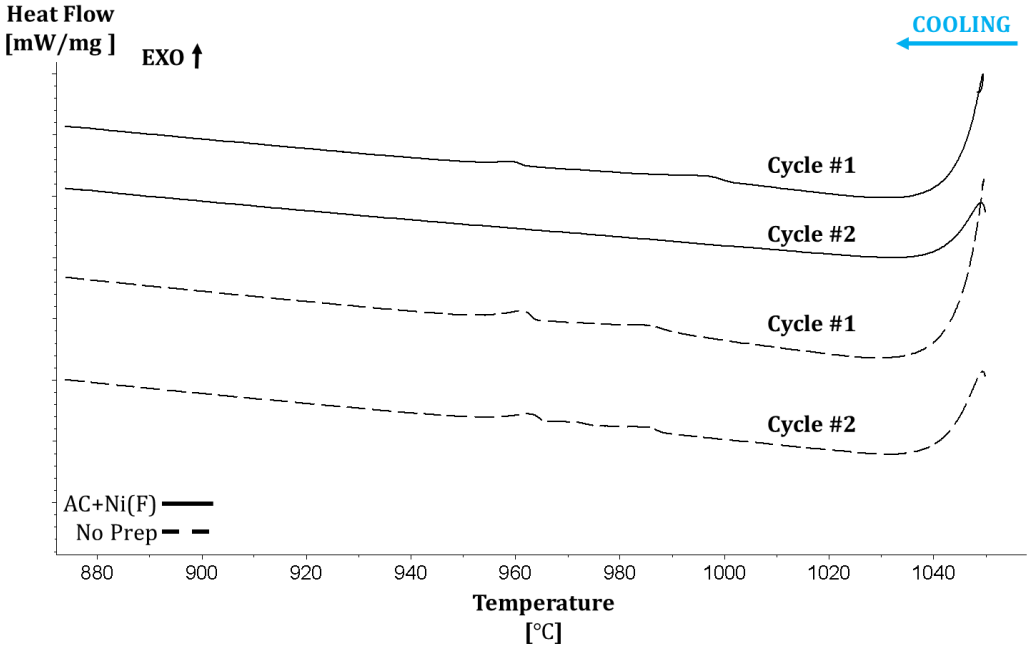

Figure D.2 - DSC traces of AC+Ni(F) & No Prep samples using undersized foil

Appendix E Additional Micrographs of Undersized BNi-2 Foil Experiments

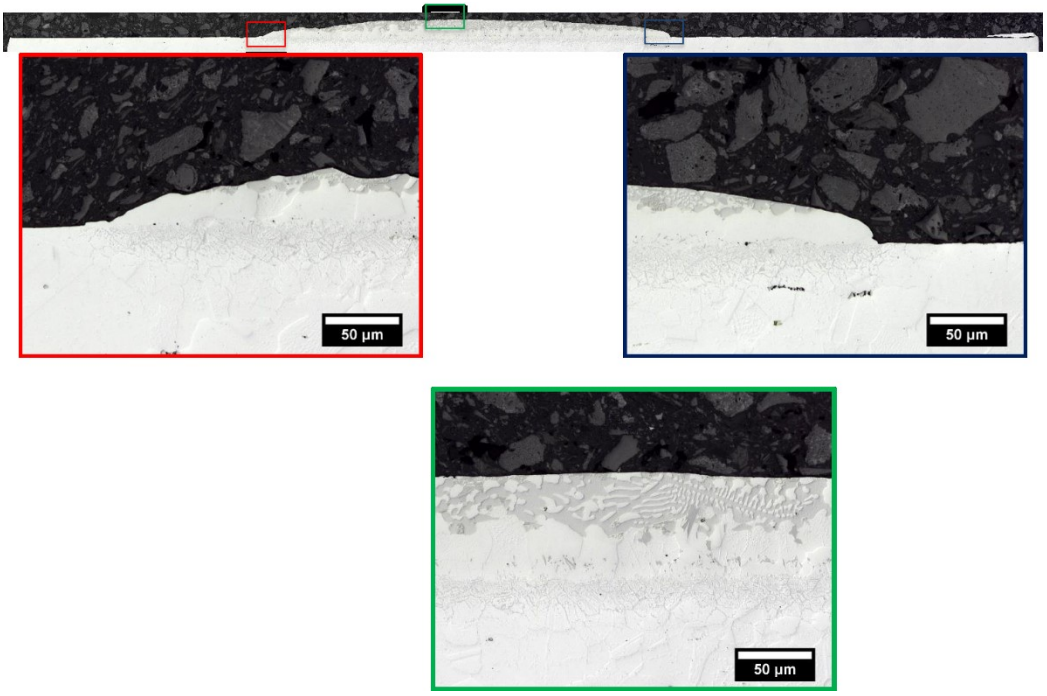

Figure E.1 - Optical micrograph of AC half-joint using undersized BNi-2 foil

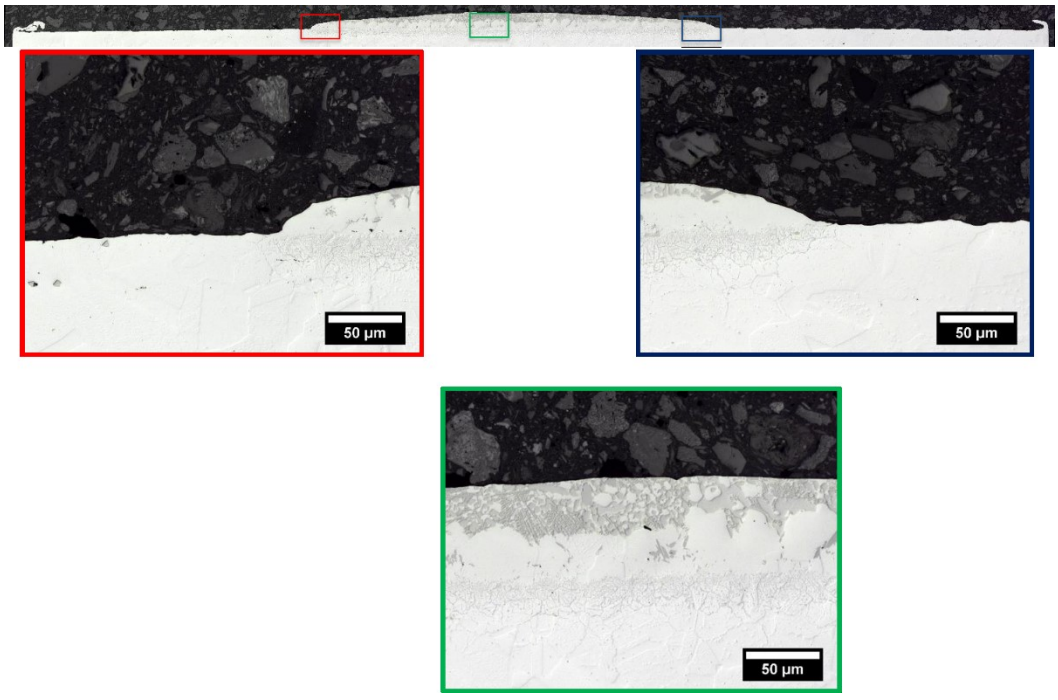

Figure E.2 - Optical micrograph of AC+NiCr half-joint using undersized BNi-2 foil

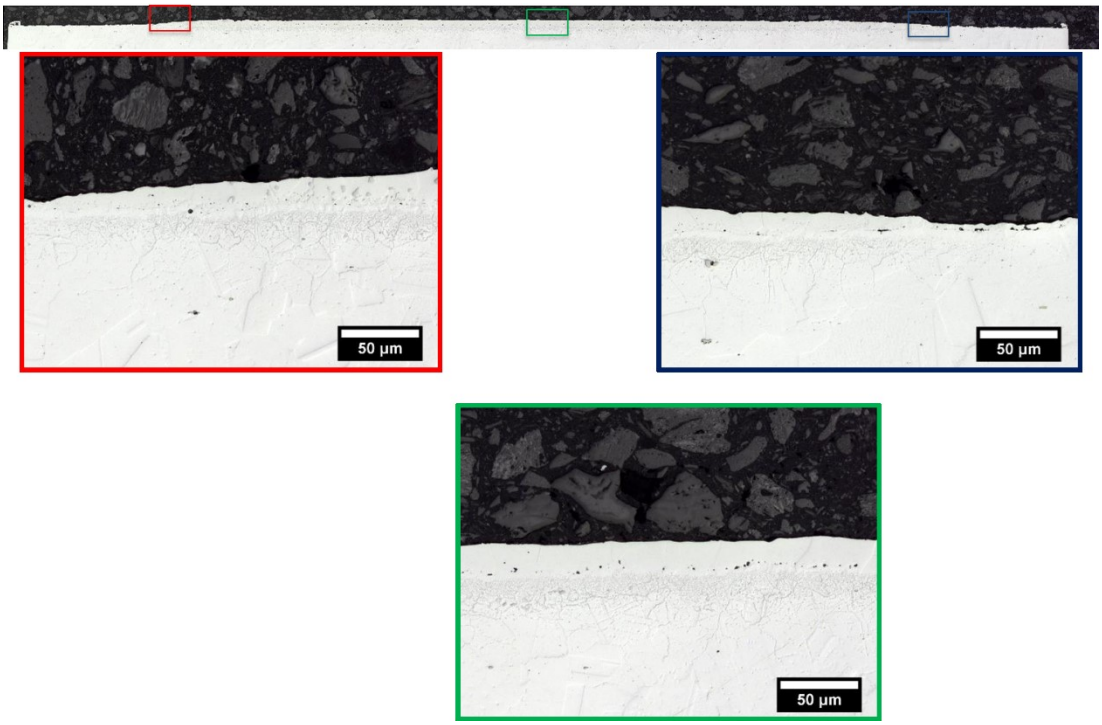

Figure E.3 - Optical micrograph of AC+NiCr+Ni(F) half-joint using undersized BNi-2 foil

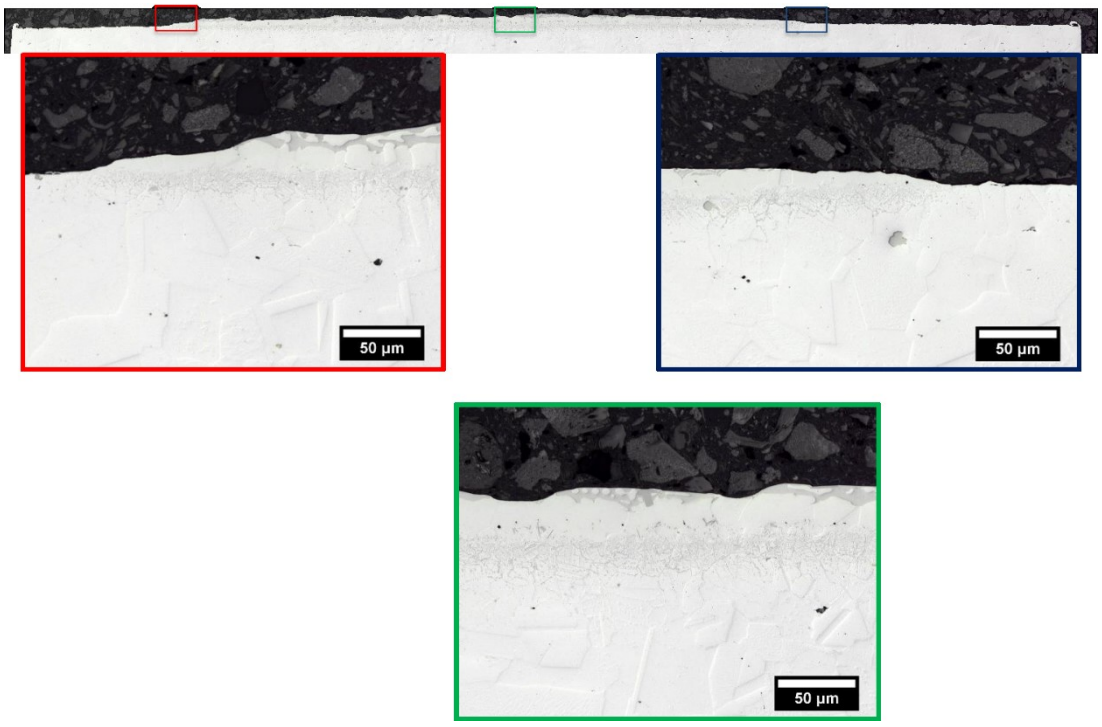

Figure E.4 - Optical micrograph of AC+NiCr+Ni(B) half-joint using undersized BNi-2 foil

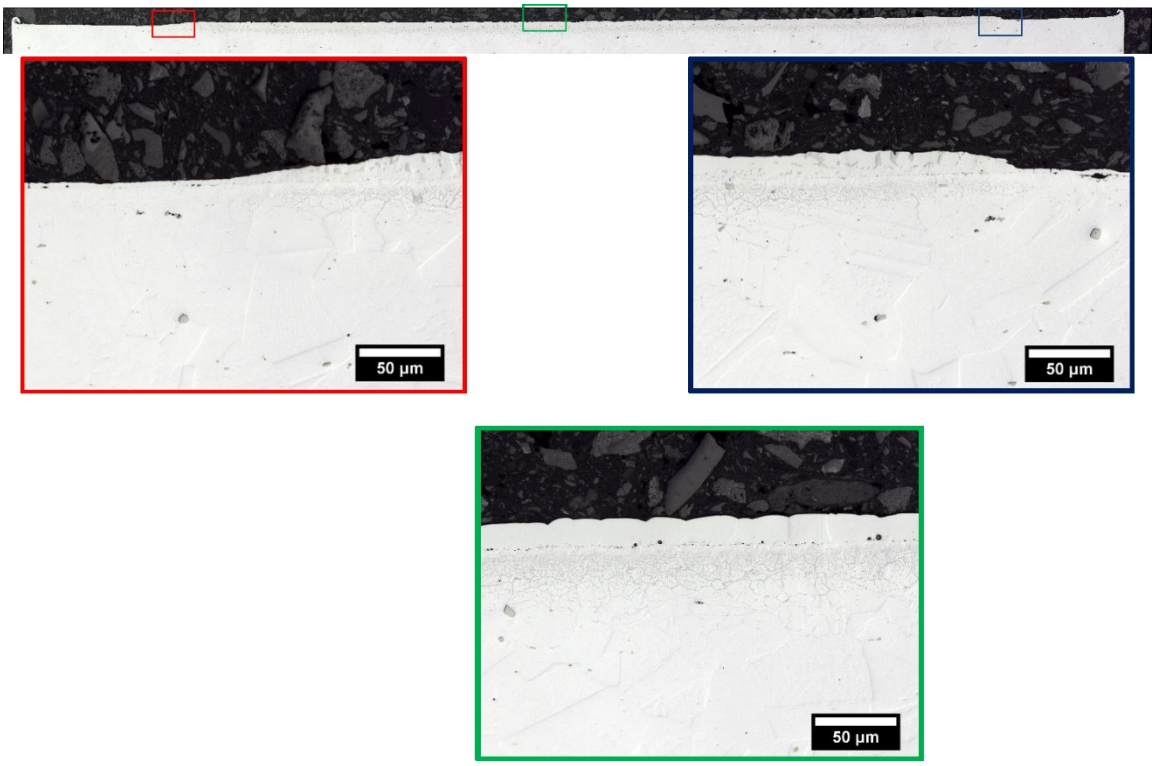

Figure E.5 - Optical micrograph of AC+Ni(F) half-joint using undersized BNi-2 foil

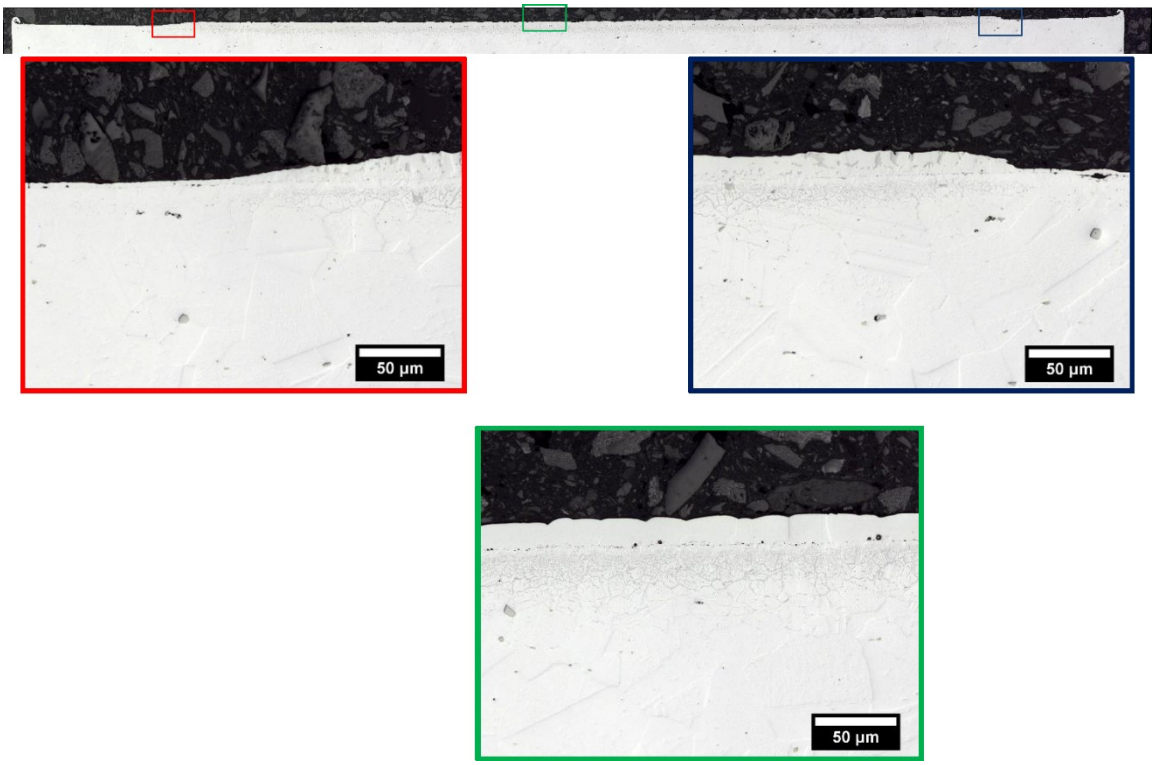

Figure E.6 - Optical micrograph of No Prep half-joint using undersized BNi-2 foil

Appendix F Additional EDS Results for AC+Ni(F) IN718/BNi-2 Half-joint Using Undersized Foil

a)

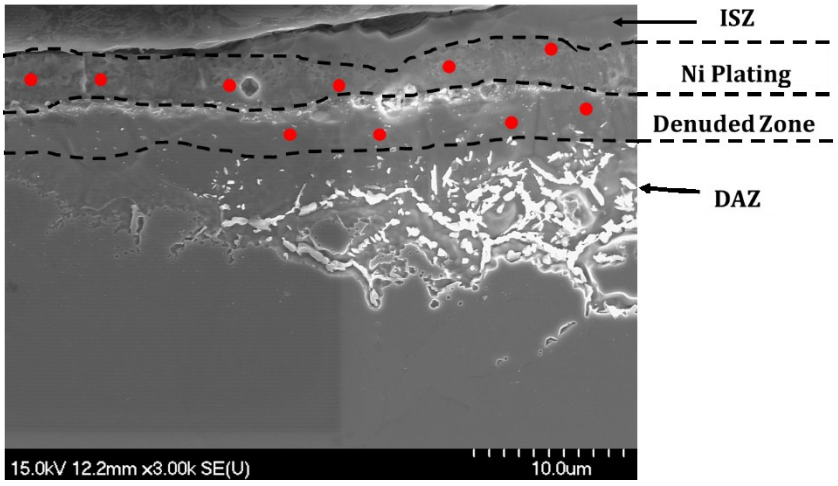

b)

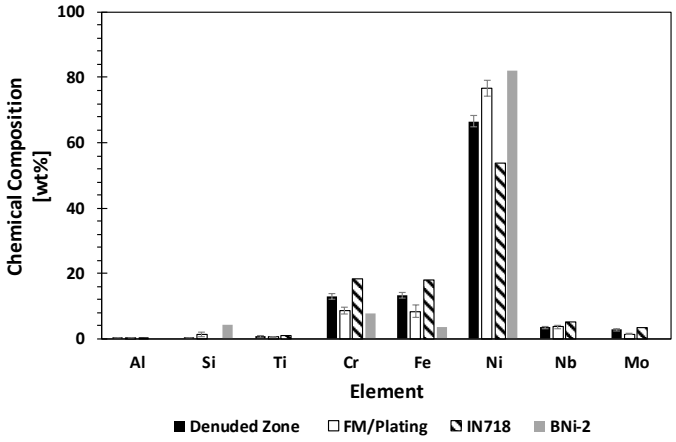

c)

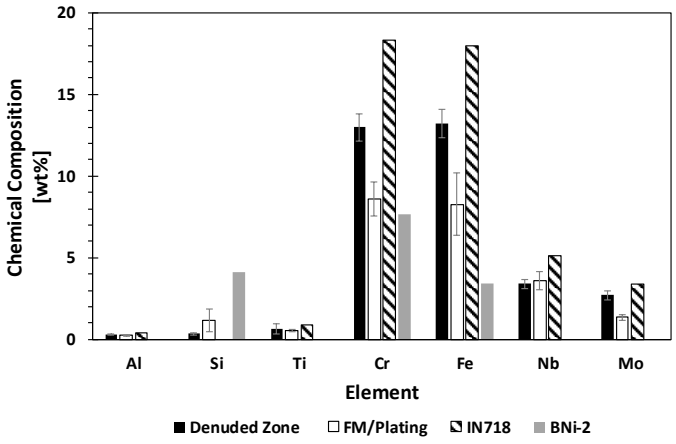

Figure F.1 – a) FE-SEM micrograph of AC+Ni(F) half-joint taken at location where FM stopped spreading, b) EDS results, c) Ni data removed

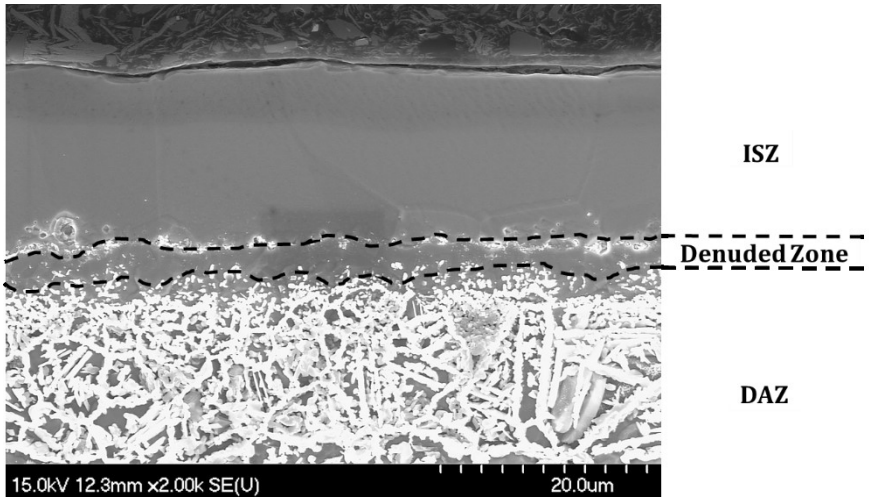

a)

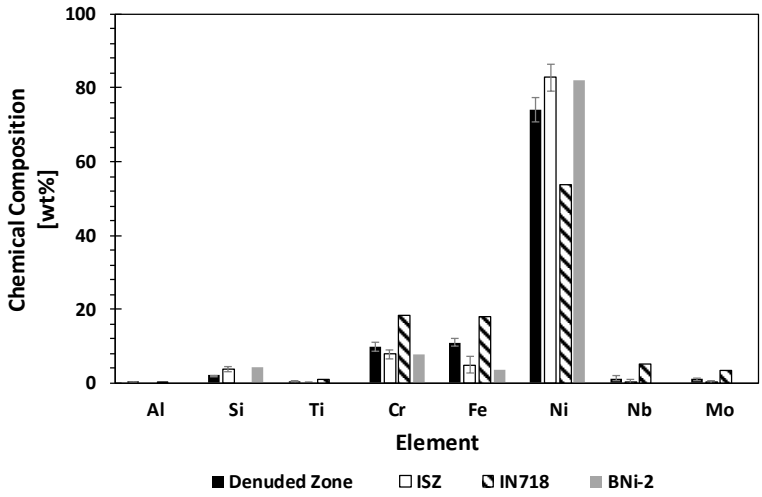

b)

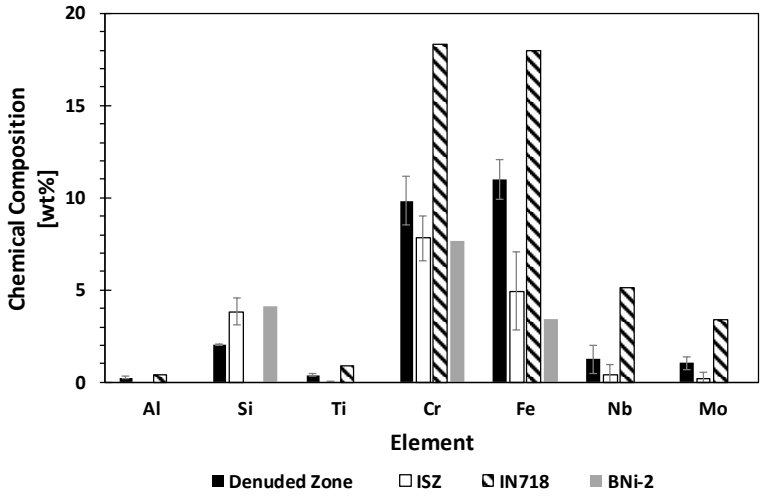

c)

Figure F.2 - a) FE-SEM micrograph of AC+Ni(F) half-joint taken at location at location near center of half-joint, b) EDS results, c) Ni data removed

Appendix G Additional Cyclic DSC Traces for IN718/BNi-2 Half-joints Made Using Surface Prepared Base Metal

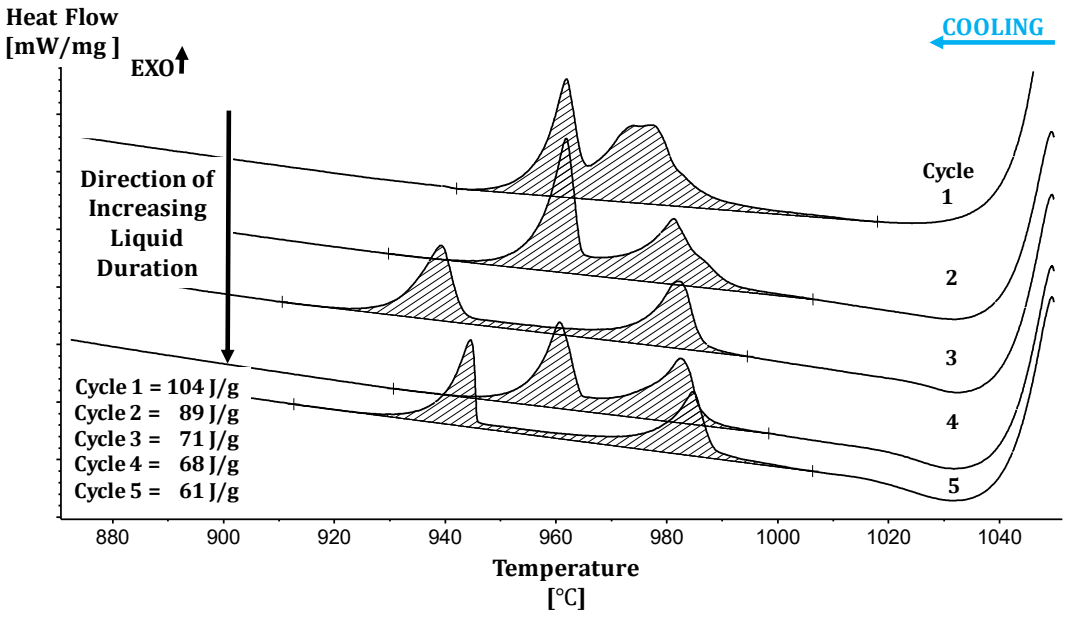

Figure G.1 - First five cooling segments obtained after cyclic DSC testing of IN718/BNi-2 TLPB half-joint using an AC BM

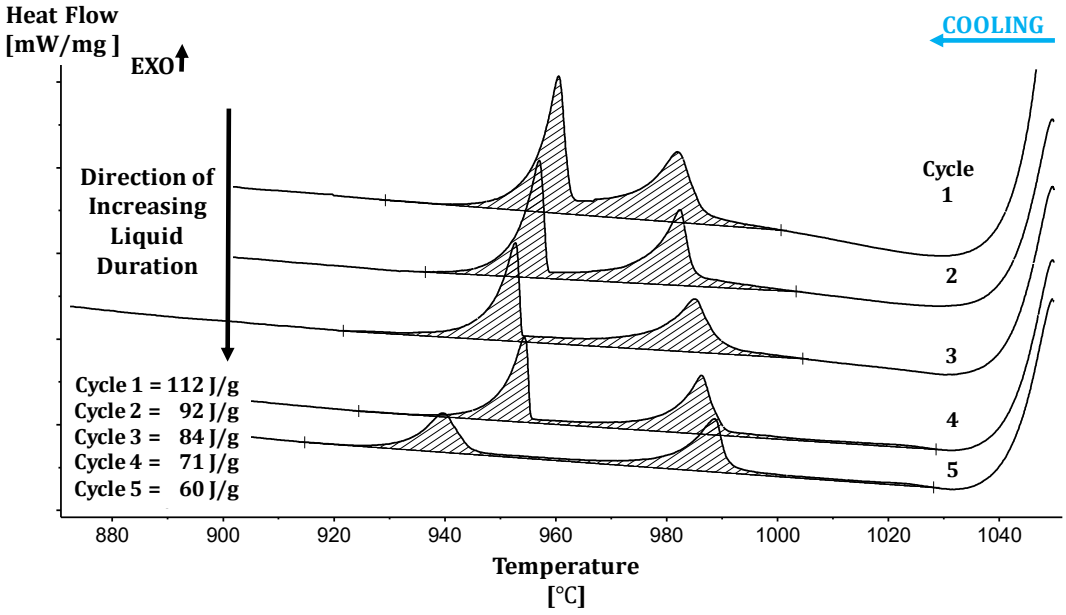

Figure G.2 - First five cooling segments obtained after cyclic DSC testing of IN718/BNi-2 TLPB half-joint using an AC+NiCr BM

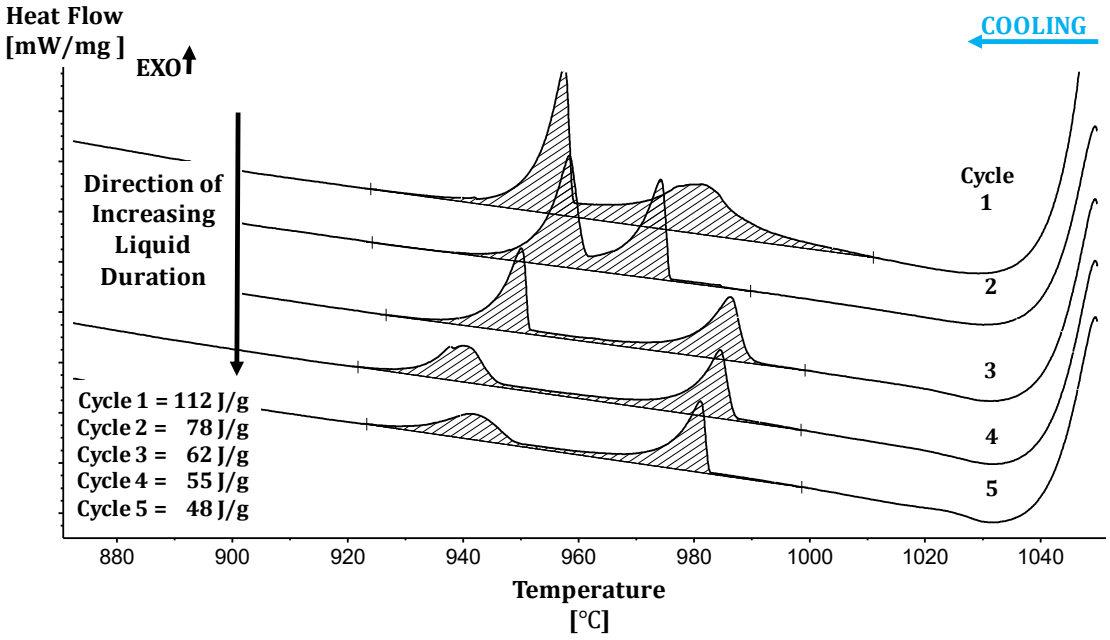

Figure G.3 - First five cooling segments obtained after cyclic DSC testing of IN718/BNi-2 TLPB half-joint using an AC+NiCr+Ni(B) BM

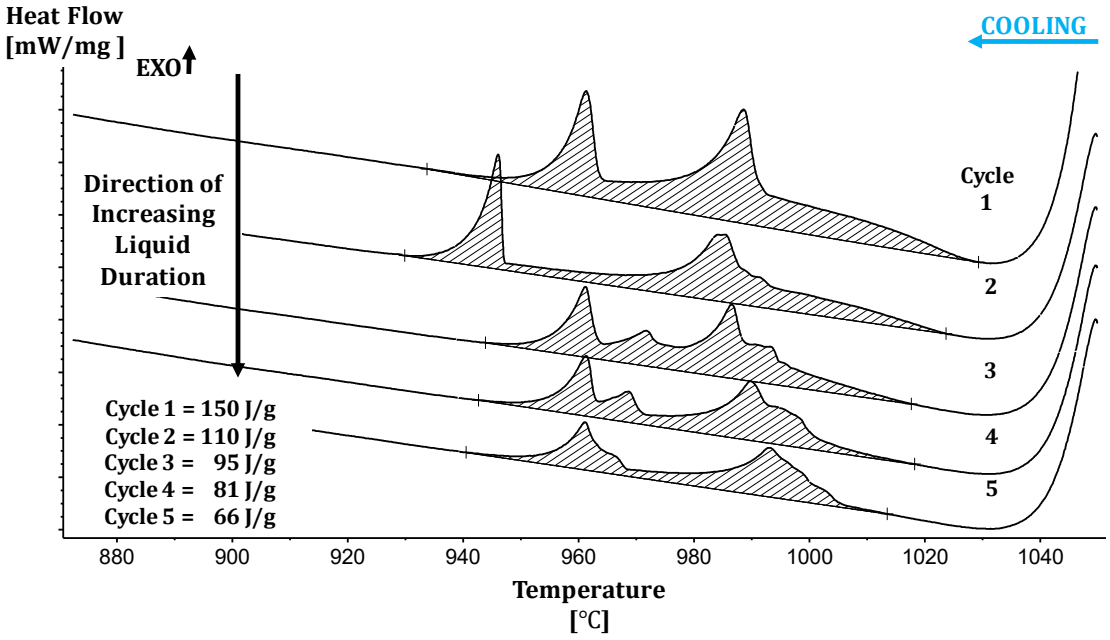

Figure G.4 - First five cooling segments obtained after cyclic DSC testing of IN718/BNi-2 TLPB half-joint using an AC +Ni(F) BM

Appendix H Representative EDS Line Scan Across the ISZ taken on an AC+Ni(F) IN718/BNi-2 Half-joint Subject to Cyclic DSC Testing

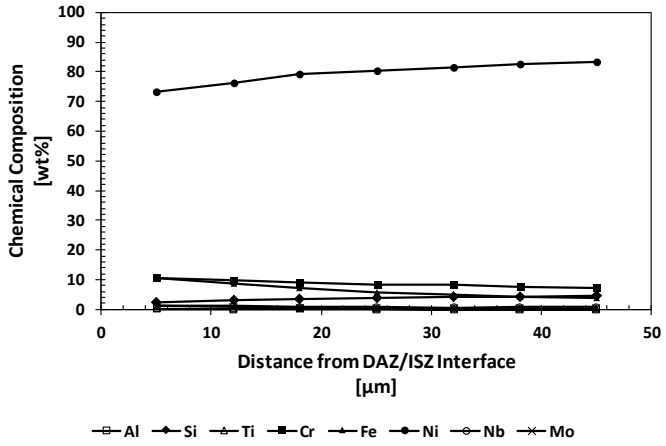

a)

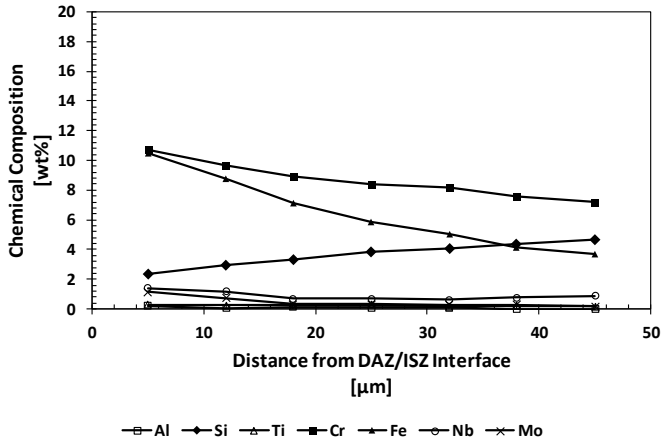

b)

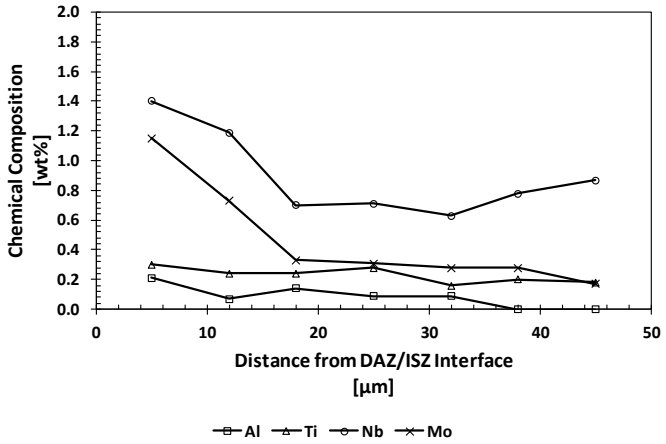

c)

Figure H.1 - a) EDS line scan of ISZ taken on an AC+Ni(F) sample subject to cyclic DSC testing, b) Ni data removed, c) Fe and Cr data removed